Charles University in Prague
Faculty of Mathematics and Physics

DOCTORAL THESIS

Jan Zemen

Magnetic anisotropies in (Ga,Mn)As and metallic multilayers with strong spin-orbit coupling

Institute of Physics ASCR, v.v.i.

Supervisor: Dr. Tomáš Jungwirth
Study programme: Physics
Study field: Condensed Matter Physics and Material Research

Acknowledgement

I would like to thank in particular to my supervisor Dr. Tomáš Jungwirth for the insightful guidance and inspiring discussions, to Dr. Jan Mašek for the invaluable assistance when implementing the tight-binding approximation, to Dr. Karel Výborný for the extensive practical advice, to Dr. Jan Kučera for the efficient technical support, to Jan Mol and Pavel Motloch for their kind help with developing the tight-binding code, and to all my colleagues from the Department of Spintronics and Nanoelectronics for creating such a friendly working environment.

I declare that I wrote my doctoral thesis independently and exclusively with the use of the cited sources. I agree with lending the thesis.

Prohlašuji, že jsem svou disertační práci napsal samostatně a výhradně s použitím citovaných pramenů. Souhlasím se zapůjčováním práce.

Prague, 19th August 2010 Jan Zemen

Title: Magnetic anisotropies in (Ga,Mn)As and metallic multilayers with strong spin-orbit coupling

Author: Jan Zemen
Department: Institute of Physics ASCR, v.v.i.
Supervisor: Dr. Tomáš Jungwirth
Supervisor's e-mail address: jungw@fzu.cz

Abstract: The thesis presents a numerical study of magnetocrystalline anisotropies in dilute ferromagnetic semiconductors and transition metal systems intended to advance the current understanding of the microscopic origins of this relativistic effect and to contribute to the development of spintronic devices with new functionalities.

The major part of the work surveys magnetocrystalline anisotropies in (Ga,Mn)As epilayers and compares the calculations to available experimental data. Our model is based on an envelope function description of the valence band holes and a spin representation for their kinetic-exchange interaction with localised electrons on Mn^{2+} ions, treated in the mean-field approximation. For epilayers with growth induced lattice-matching strains we study in-plane to out-of-plane easy axis reorientations as a function of Mn local-moment concentration, hole concentration, and temperature. Next we focus on the competition of in-plane cubic and uniaxial anisotropies. We add an in-plane shear strain to the effective Hamiltonian in order to capture measured data in bare, unpatterned epilayers, and we provide microscopic justification for this approach. The model is then extended by an in-plane uniaxial strain and used to directly describe experiments with magnetisation direction controlled by strains due to postgrowth lithography or an attached piezo-electric stressor. We also study magnetisation switchings induced electrostatically in a field-effect transistor. The calculated easy axis directions and anisotropy fields are in semiquantitative agreement with experiment in a wide parameter range.

The second part of this work builds upon the experience gained in modelling magnetic anisotropies in (Ga,Mn)As and explores analogous spin-orbit coupling induced phenomena in ferromagnetic transition metal alloys. Our description of these systems is based on the tight-binding approximation with a realistic Slater-Koster parametrisation. We compare the predicted band structures, densities of states and magnetic anisotropy energies to ab-initio calculations first for elemental metals and then for CoPt and FePt ordered alloys. Qualitative agreement of ab-initio and tight-binding predictions is observed for the bimetallic structures. The applied formalism and the corresponding newly developed code allow for modelling magnetic anisotropies in systems with broken symmetry due to a finite multilayer structure, elastic strains or applied electric fields. Our work also provides practical basis for further research in this direction, in particular for studies of relativistic magnetotransport anisotropies by means of local Green's function formalism which is directly compatible with our tight-binding approach.

Keywords: Ferromagnetic semiconductor, transition metals, magnetic anisotropy, Kohn-Luttinger Hamiltonian, kinetic-exchange interaction, tight-binding approximation, spin-orbit interaction.

Název práce: Magnetické anizotropie v (Ga,Mn)As a v kovových multivrstvách se silnou spin-orbitální interakcí

Autor: Jan Zemen
Katedra (ústav): Fyzikální ústav AVČR, v.v.i.
Vedoucí disertační práce: Dr. Tomáš Jungwirth
e-mail vedoucího: jungw@fzu.cz

Abstrakt: V této disertační práci jsou prezentovány numerické výpočty magnetokrystalických anisotropií ve feromagnetických polovodičích a přechodových kovech se zameřením na mikroskopický původ těchto relativistických jevů i na vývoj spintronických součástek s novou funkcionalitou.

Převážná část práce je věnována výzkumu magnetických anisotropií v (Ga,Mn)As epivrstvách a srovnání výpočtu s dostupnými experimentálními daty. Náš model popisuje valenční díry pomocí šestipásové obálkové funkce a jejich kinetickou výměnnou interakci s lokalizovanými manganovými momenty započítává v přiblížení středního pole. Nejprve studujeme otáčení magnetické snadné osy ze směru kolmého k vrstvě do směru paralelního v závislosti na koncentraci Mn iontů, koncentraci děr a teplotě v epivrstvách s elastickým napětím způsobeným různou mřížkovou konstantou substrátu a epivrstvy. Pak se zaměřujeme na vzájemnou velikost kubické a uniaxiální komponenty magnetické anisotropie v rovině vzorku. Do našeho efektivního Hamiltoniánu je vloženo uniaxiální napětí v rovině vzorku za účelem modelování anisotropií měřených v neupravených souvislých epivrstvách a zároveň je poskytnuto mikroskopické odůvodnění tohoto postupu. Model je pak rozšířen o uniaxiální napětí podle libovolného směru v rovině vzorku a používán pro popis experimentů, kde je směr magnetizace určen napětím indukovaným litografickou úpravou vzorku nebo piezo-elekrickým členem. Dále studujeme přepínání směru magnetizace v tranzistoru řízeném elektrickým polem. Vypočtené směry magnetické snadné osy a velikosti anisotropních polí se shodují semikvatitativně s experimentem na široké škále parametrů.

Druhá část práce staví na zkušenostech získaných při studiu magnetických anisotropií v (Ga,Mn)As a zkoumá analogické jevy s původem ve spin-orbitalní interkaci ve slitinách feromagnetických přechodových kovů. Náš popis těchto systemů je založen na přiblížení těsné vazby s realistickou Slaterovou-Kosterovou parametrizací. Vypočtené pásové struktury, hustoty stavů a magnetické anisotropní energie porovnáváme s dostupnými ab-initio výsledky pro jednoprvkové kovy a pro uspořádané slitiny CoPt a FePt. V případě bimetalických struktur pozorujeme kvalitativní shodu výsledků obou metod. Použitý formalismus a odpovídající nově vyvinutý kód umožňují modelování magnetických anisotropií v systémech se symetrií porušenou vrstevnatou strukturou slitiny, elastickým napětím mřížky nebo přiloženým elektrickým polem. Naše práce také poskytuje dobrý základ pro další výzkum relativistických transportních anisotropií ve formalismu lokálních Greenových funkcí, který je s přiblížením těsné vazby kompatibilní.

Klíčová slova: Feromagnetické polovodiče, transitivní kovy, magnetická anisotropie, Kohnův-Luttingerův Hamiltonián, kinetická výměnná interakce, přiblížení těsné vazby, spin-orbitální interakce.

Contents

1 Introduction **1**
1.1 Magnetic Anisotropies in Spintronics . . . 1
1.2 Overview of the thesis . . . 2
1.3 Ferromagnetic semiconductors . . . 4
1.3.1 Impurity properties . . . 5
1.3.2 Origin of ferromagnetism and magnetic anisotropy . . . 6
1.3.3 Effective Hamiltonian model . . . 6
1.4 Metallic multilayers . . . 8
1.4.1 Origin of magnetic anisotropy . . . 8
1.4.2 Tight-binding model . . . 9

2 Theoretical framework **10**
2.1 Magnetocrystalline anisotropy of (Ga,Mn)As . . . 10
2.1.1 Tetrahedral symmetry of the host semiconductor . . . 11
2.1.2 Symmetry lowering mechanisms . . . 16
2.2 Magnetocrystalline anisotropy in metals . . . 22
2.2.1 Slater-Koster approach . . . 23
2.2.2 Finite systems . . . 26
2.2.3 Parametrisation . . . 27
2.2.4 Modelling of magnetic anisotropy . . . 30
2.2.5 Integration in k-space . . . 32
2.3 Shape anisotropy . . . 33

3 Results and analysis **35**
3.1 Overview of theoretical results in (Ga,Mn)As and comparison to experiments 35
3.1.1 In-plane vs. out-of-plane magnetic easy axis . . . 35
3.1.2 In-plane anisotropy: Competition of cubic and uniaxial components 39
3.1.3 Anisotropy fields . . . 48
3.1.4 Samples with post-growth controlled strains . . . 61
3.2 Controlling magnetic anisotropy in (Ga,Mn)As - devices . . . 71
3.2.1 Field Effect Transistor . . . 72
3.2.2 Relaxation in arrays of microbars . . . 78
3.2.3 Relaxation in L-shaped microbars . . . 96
3.2.4 Piezo-electric stressing . . . 101
3.2.5 Domain wall width and angle . . . 105
3.3 Overview of results in transition metal systems . . . 112

3.3.1 Bulk elemental metals 112
3.3.2 Bimetallic multilayers 117

4 Summary **125**
4.1 Effective Hamiltonian model 125
4.2 Tight-binding model 127

A Used constants **128**
A.1 Cubic anisotropy coefficients 128
A.2 Effective Hamiltonian parameters 129
A.3 Tight-binding parameters 129

Chapter 1

Introduction

1.1 Magnetic Anisotropies in Spintronics

In this work we study magnetocrystalline anisotropies in dilute moment ferromagnetic semiconductors and ordered metallic alloys with the intention to advance our understanding of the microscopic origins of this relativistic effect and to contribute to the development of spintronic devices with new functionalities.

Spintronics is a field of research that investigates the spin of the electron as well as its charge, combining the magnetic and electrical properties of materials, and aiming for applications in information storage and processing. The first generation spintronic devices such as hard drive read heads based on the Giant Magneto-Resistance (GMR) or Tunnel Magneto-Resistance (TMR) effects and Magnetic Random Access Memories (MRAM) are metallic structures [17]. In MRAMs, the magnetic state of the memory bit is manipulated by electrical current-induced magnetic field or spin transfer torque. This approach suffers from high energy dissipation and limited scalability.

One possible solution to these problems is the electric-field control of magnetic properties which was first demonstrated in the ferromagnetic semiconductor (In,Mn)As [81, 20]. Consequently, we have seen an intense experimental and theoretical exploration of the magnetic properties of (III,Mn)V ferromagnetic systems and their dependence on the tuneable material parameters. Rich phenomenology has been discovered including the sensitivity of the magnetic state to the concentration of magnetic Mn dopants and of charge carriers, temperature, and lattice matching strains. Large share of the phenomena is due to the strong spin-orbit coupling (SOC) in the host semiconductors such as GaAs or InAs which gives rise to magnetic anisotropy of the ground state and transport properties. The Anisotropic Magneto-resistance (AMR) [7] as well as the Tunnelling Anisotropic Magneto-resistance (TAMR) [37] have been observed in Dilute Magnetic Semiconductors (DMSs). Our work focuses primarily on the magnetocrystalline anisotropy in (Ga,Mn)As which has become an archetypal example of DMSs.

Magnetocrystalline anisotropy is the dependence of the energy of a ferromagnet on the magnetisation orientation with respect to crystallographic axes. It originates in the coupling of the spin and orbital degrees of freedom derived from the Dirac equation. In the $(v/c)^2$ order of the expansion of the Dirac equation beyond the non-relativistic form a new term arises which captures this SOC. Contrary to the shape anisotropy arising from the magnetic dipole-dipole interaction, the magnetocrystalline anisotropy is of quantum-

relativistic origin. The band structure dependence on the magnetisation direction through the SOC offers the opportunity to control the alignment of the magnetic easy axis by external electric field [19, 89], lattice strain [35, 93, 147, 149], or via temperature dependent exchange-splitting of the bands also by temperature [110, 109]. Such ability to manipulate the magnetisation direction has many potential applications in non-volatile memory devices. Moreover, the functionality of a spintronic transistor has been demonstrated in (Ga,Mn)As nanostructure where the Fermi energy is manipulated by magnetisation reorientation resulting in the Coulomb Blockade Anisotropic Magnetoresistance Effect (CBAMR) [150]. During the past five years the author of this thesis has contributed to the theoretical investigation of the dependence of magnetocrystalline anisotropies in (Ga,Mn)As on doping, temperature, electric fields, and lattice strains. His results are summarised in papers [89, 59, 149, 101, 130, 155] and in this thesis.

After a decade of research, which has led to discoveries of fundamental physics phenomena, the desired spintronic functionality is still not available at room temperature in DMSs [87, 144]. There have been attempts recently to take advantage of the experience with SOC phenomena gained in magnetic semiconductors and to search for analogous spintronic behaviour in ordered metallic alloys. The key idea is that one type of atom contributes the magnetic moment and maintains ferromagnetic order above the room temperature whereas the the other type of atom possesses strong SOC making the band structure of the compound strongly dependent on the magnetisation direction in analogy to DMSs. So far, the TAMR effect has been demonstrated in CoPt multilayer [95] or in Fe/GaAs/Au heterostructure [77] and the CBAMR effect in Co-based metallic nanostructures [8]. The direct electric field control of magnetic anisotropy in materials with metallic carrier densities is a delicate effect. However, the presence of this effect has been recently reported in a MgO/Fe/Au multilayer structure [70]. A detailed experimental exploration and theoretical microscopic understanding of these phenomena is still required. A complementary strand of this doctoral work is devoted to calculations of the magnetocrystalline anisotropy energy (MAE) and the anisotropic density of states (ADOS) in CoPt and FePt multilayers.

1.2 Overview of the thesis

After mentioning briefly the broader scientific context of the thesis we will now comment on the main aspects and structure of this doctoral research in more detail. The work is theoretical and consists of two parts which differ in the applied methods as well as in studied materials. The first and more extensive part investigates the dependence of magnetocrystalline anisotropies of (Ga,Mn)As epilayers on Mn doping, hole density, temperature, and strain. The context of our research in the field of DMSs is introduced in Sec. 1.3. The virtual-crystal $\boldsymbol{k} \cdot \boldsymbol{p}$ approximation for hole states and mean-field treatment of their exchange interaction with Mn d-shell moments allow for efficient numerical simulations [26, 1, 55]. Our theoretical method is described in more detail in Sec. 2.1. Special attention is given to mechanisms breaking the cubic symmetry of an ideal zincblende (Ga,Mn)As crystal. Microscopic mechanism which breaks the remaining in-plane square symmetry in unpatterned epilayers is modelled by introducing an additional uniaxial in-plane strain in the Hamiltonian. In Subsec. 2.1.2 we have demonstrated the

correspondence of this effective approach and a generic $\boldsymbol{k} \cdot \boldsymbol{p}$ Hamiltonian with the lowered symmetry of the p-orbital states which form the top of the spin-orbit coupled valence band.

We have systematically explored the reliability of the effective Hamiltonian model in predicting the magnetocrystalline anisotropies of (Ga,Mn)As epilayer and micro-devices. Comparison of our results with experiment is not straightforward due to the presence of unintentional compensating defects in (Ga,Mn)As epilayers. In Sec. 3.1 we take advantage of the large amount of experimental data on magnetic anisotropy in (Ga,Mn)As which has accumulated over the past years and test the relevance of our model over a wide parameter range. We focus on general trends rather than on matching results directly to an isolated experimental sample. The text of the whole section is an edited version of a review-like paper [155]. The work presented in Sec. 3.2 has involved close collaboration with experimental teams listed at the end of this section. It provides a more detailed description of five combined experimental and theoretical projects focused on the control of magnetocrystalline anisotropies in (Ga,Mn)As-based nano-devices by electric field [89], temperature [130], lattice mismatch relaxation due to post-growth lithography [149, 59], and piezo-electric straining [101]. Results of these projects have been published (or submitted to Physical Review **B** in case of [59]). The author of this thesis has contributed to the joint research by the microscopic numerical simulations and the analysis and interpretation of the experimental results. For this he has made significant extensions to the pre-existing library of DMS routines, in particular to include systems with general strain tensors. The author has also linked the DMS library to outputs of elastic theory simulations of lattice deformation effects in (Ga,Mn)As.

The second part of the thesis is devoted to a study of SOC phenomena in ordered metallic alloys. The motivation, context, and strategy of this research is briefly introduced in Sec. 1.4. We apply the standard tight-binding formalism using the Slater-Koster approach and include the atomic SOC term and the ferromagnetic exchange splitting. Our formalism together with three realistic parametrisations is presented in Sec. 2.2. The author of the thesis has developed a numerical code implementing the microscopic model, compared the calculated band structures, densities of states and magnetic anisotropy energies to ab-initio calculations, and performed internal consistency checks. All results are presented in Sec. 3.3 and corresponding publications are currently under preparation. The current version of our model and code represents the first stage of developing a coherent description of magnetocrystalline and magneto-transport anisotropies in metallic multilayers with strong SOC which we intend to complete in future. This is the topic of UK EPSRC Postdoctoral Fellowship granted to the author of this thesis which starting date is January 2011.

The following paragraphs introduce the individual institutions forming the closest scientific environment of my reserach: The Department of Spintronics and Nanoelectronics at the Institute of Physics AS CR, v. v. i., the host of these doctoral studies, has broad expertise in modelling the band structure, transport and micromagnetic properties of ferromagnetic semiconductor materials and devices. The effective Hamiltonian model used in this doctoral research has one of its origins in this group [1]. Complementary to the research of ground state properties presented in this thesis, Dr. Karel Výborný has conducted a parallel research of the transport anisotropies in (Ga,Mn)As building on the same effective Hamiltonian model [103, 49]. Note that AMR is an important experimental

means of determining the magnetic state and magnetocrystalline anisotropies of a conducting sample which has been utilised for example in subsection 3.2.4. In the second part of the doctoral studies when developing a tight-binding code to calculate the electronic structure of the ordered metallic alloys, the author of this thesis has collaborated closely with Dr. Jan Mašek from the Department of Condensed Matter Theory of the Institute.

Even though the main expertise of the author of this thesis is in theory, he has enjoyed numerous interactions with experimentalists resulting in six joint publications. He has collaborated closely with the experimental group in the Department of Spintronics and Nanoelectronics, mentioned above, which specialises in the growth of DMS epilayers using the Molecular Beam Epitaxy (MBE) technique and in the fabrication of semiconductor nanostructures using electron-beam and optical lithography. Our joint projects have focused on the dependence of magnetocrystalline anisotropy in (Ga,Mn)As on lattice strains and temperature [155, 59] and external electric fields [89].

The author has enjoyed the collaboration with Prof. Václav Holý and Lukáš Horák from the Department of Condensed Matter Physics of the Charles University in Prague. We have studied magnetic anisotropies in (Ga,Mn)As microbars with lattice mismatch relaxation determined from high resolution x-ray diffraction measurements [149, 59].

Hitachi Cambridge Laboratory focuses on research into magnetic and spintronic devices for data storage and information processing and has a long track record in the development of devices with new functionalities including the demonstration of single electron memory cells and single electron logic circuits. The joint research with the group has led to joint publications on magnetocrystalline anisotropy induced by the growth strain relaxation in a nanometer wide channels [149] and by gating of thin films [89]. The author is a co-inventor of a new magnetoresistive memory device holding several international patents: EP2015307, KR20090007201, US2009016098, JP2009021586, CN101345079. The collaboration has been extended also to Hitachi Advanced Research Laboratory in Japan which has led to a publication on the temperature dependence of magnetic domain wall properties in (Ga,Mn)As epilayers [130].

The Experimental Condensed Matter Group at the School of Physics and Astronomy in at the University of Nottingham has expertise in the study of magnetism and electrical transport phenomena in DMSs. The collaboration with this group has led to joint papers on the magnetocrystalline anisotropy controlled by a piezo-electric stressor attached to the ferromagnetic epilayer [101] and to a detailed systematic study of anisotropy effects in strain-relaxed (Ga,Mn)As microstructures [59].

1.3 Ferromagnetic semiconductors

(Ga,Mn)As studied in the first part of the thesis is one of the most experimentally explored $III_{1-x}Mn_xV$ DMSs. The synergy of ferromagnetic and semiconducting properties has attracted much attention of both basic and applied research ever since the discovery of carrier-mediated ferromagnetism in $III_{1-x}Mn_xV$ [82, 83]. For typical doping levels 1%-10% of Mn the magnetic dipole interactions and corresponding shape anisotropies are 10-100 times weaker in (Ga,Mn)As than in conventional dense-moment ferromagnets. Consequently, magnetocrystalline anisotropy plays a decisive role in the process of magnetisation reversal. Despite the low saturation magnetisation the magnetic anisotropy

fields reach $\sim$ 10-100mT due to the large SOC.

1.3.1 Impurity properties

Before establishing the microscopic model of the doped semiconductor, the properties of the doping impurities must be considered. The extended x-ray absorption fine structure studies [118] show that the Mn ions are distributed randomly in (Ga,Mn)As grown by the Low-Temperature MBE technique. The elements in the (Ga,Mn)As compound have an atomic structure [Ar]$3d^{10}4s^2 4p^1$ for Ga, [Ar]$3d^5 4s^2$ for Mn, and [Ar]$3d^{10}4s^2 4p^3$ for As. It implies that the most stable and, therefore, most common position of Mn in the GaAs host lattice is on the Ga site where its two $4s$-electrons can participate in the crystal bonding in the same way as the two Ga $4s$-electrons. Because of the missing valence p-electron the Mn_{Ga} impurity acts as an acceptor which is the key difference as compared to Mn-doped II-VI DMSs. The binding energy of the acceptor centre $E_b = 112.4$ meV inferred from the infra-red (IR) spectroscopy [16, 64] is consistent with the Scanning Tunnelling Microscope (STM) measurement [151, 152] and ranks Mn among moderately shallow acceptors in GaAs whose band gap is $E_g = 1.52$ eV. The moderately low binding energy and random distribution of impurities allow us to use the effective kinetic-exchange and the virtual-crystal approximation in our modelling [55].

The weakly bound hole occupies one of the three antibonding $sp - d$ levels with dominant As $4p$ character. The Electron Paramagnetic Resonance (EPR) and Ferromagnetic Resonance (FMR) experiments confirmed the presence of the positively ionised Mn_{Ga} acceptor centres in (Ga,Mn)As [4, 131, 107]. The $S = 5/2$ local moment on Mn was detected through a resonance line centred at Lánde g-factor $g = 2$ and, in low Mn-density samples, through a sextet splitting of the line due to the hyperfine interaction with the ^{55}Mn nuclear spin $I = 5/2$. In addition, the small energy difference in the hole spin oriented parallel or antiparallel to the Mn moment $\Delta\varepsilon = 8 \pm 3$ meV [64] reveals that the hole does not reside in the d-shell or form a Zhang-Rice-like singlet but occupies an effective-mass Bohr orbit [27]. Therefore, it can be classified as a charge-transfer insulator [26] in agreement with photo emission spectroscopy [85, 84].

Note that the electronic structure is strongly dependent on the Mn concentration as discussed in Ref. [54, 74]. The hole binding energy of an isolated substitutional Mn impurity is produced by the long-range Coulomb potential of the single-acceptor and by the short-range central cell and $p - d$ kinetic-exchange potentials [9]. At very weak doping, the Fermi level resides inside a narrow impurity band (assuming some compensation), separated from the valence band by an energy gap of magnitude close to the impurity binding energy. In this regime, strong electronic correlations are an essential element of the physics and a single-particle picture has limited utility. In the metallic state at Mn-doping larger than 1%, on the other hand, the impurities are sufficiently close together, and the long-range Coulomb potentials which contribute to the binding energy of an isolated impurity are sufficiently screened, the system is best viewed as an imperfect crystal with disorder-broadened and shifted host Bloch bands. In this regime, electronic correlations are usually less strong and a single-particle picture often suffices. Our modelling of magnetocrystalline anisotropies in (Ga,Mn)As is based on the Bloch valence band theory and has therefore merit on the metal side of the metal-insulator transition (MIT).

1.3.2 Origin of ferromagnetism and magnetic anisotropy

Ferromagnetism in (III,Mn)V DMSs was first described ten years ago [24, 50, 27, 26, 1]. The direct exchange between the holes near the top of the valence-band and the localised Mn d-electrons is weak since the top of the GaAs valence band is dominated by $4p$-states more heavily weighted on As than on Ga sites. (Mn_{Ga} and As belong to different sublattices.) Therefore, the antiferromagnetic kinetic-exchange whose microscopic origin is the $p - d$ hybridisation dominates.

Zener [156] first proposed a model of ferromagnetism driven by the kinetic-exchange coupling of the carriers and the localised spins to explain magnetic behaviour of transition metal ferromagnets. According to the model, spin polarisation of the localised spins leads to spin splitting of the bands, which results in the lowering of the carrier energy. At sufficiently low temperatures, this lowering overcompensates the increase of the free energy caused by the decrease of entropy, that is associated with the polarisation of localised spins. However, the Zener model was later abandoned, as neither the itinerant character of the magnetic electrons nor the quantum (Friedel) oscillations of the electron spin polarisation around the localised spins were taken into account, and both of these are now established to be critical ingredients of the theory of magnetic metals. In particular, the resulting competition between ferromagnetic and antiferromagnetic interactions in metals leads rather to a spin-glass than to a ferromagnetic ground state. In the case of (Ga,Mn)As, however, the magnetic moments are strongly localised and dilute and the coupling between them is mediated by itinerant carriers of comparable or lower density. Under such conditions, the kinetic-exchange model is well applicable. An important aspect of our model is that it can take into account the SOC contribution to the carrier-mediated exchange interaction. Note that in III-V nitrides or II-VI oxides the $p - d$ hybridisation is strong enough to bind the hole [28] making our model not suitable for these compounds.

We also remark that the extended or weakly localised holes mediate the interaction between local Mn moments on both sides of the MIT. According to the two-fluid model [90] of the Anderson-Mott MIT in doped semiconductors, the conversion from itinerant electrons to singly occupied impurity states occurs gradually as the system crosses the MIT.The localisation radius decreases rather slowly from infinity at the MIT towards the Bohr radius deep in the insulator phase so the wave functions retain an extended character at length scales comparable to the inter-impurity distance even on the insulating side of the MIT. This is consistent with the experimentally observed onset of ferromagnetism in strongly insulating (Ga,Mn)As at $\sim 1\%$ Mn-doping while the MIT occurs at higher doping $\sim 1.5\%$.

1.3.3 Effective Hamiltonian model

Let us mention the spin density functional theory (SDFT) first as it is an established tool to study origins of ferromagnetism. As an ab-initio approach it has the advantage of involving no phenomenological parameters. In metals, the exchange-correlation energy functional can be successfully approximated by the local spin-density approximation (LSDA). Unfortunately, in the DMSs with strongly localised magnetic d-electrons the LSDA leads to underestimation of energy splitting between the occupied and empty d-states, to an unrealistically large partial density of states (DOS) near the top of the valence

band, and consequently to an overestimate of the strength of the $p-d$ hybridisation. The widely used corrections such as the LDA+U improve the resulting DOS but can have to some extent an uncontrollable effect on the total energy of the system and therefore also on the magnetocrystalline anisotropy. To the best of our knowledge, ab-initio calculations of magnetic anisotropies in DMSs have not been published to date, likely also due to additional difficulties related to the random positions of Mn impurities in the lattice.

Our effective Hamiltonian approach [26, 1] focuses only on the low-energy degrees of freedom while the core states enter via parameters of this less microscopic model. We concentrate on the top of the valence band occupied by holes mediating the ferromagnetism. Moreover, the holes are localised or weakly bound as mentioned earlier so the $\boldsymbol{k}\cdot\boldsymbol{p}$ envelope function approximation is appropriate. We use the six-band Kohn-Luttinger (KL) Hamiltonian [60] reflecting the tetrahedral symmetry of the zinc-blende lattice of the semiconductor host (neglecting the lack of inversion symmetry). The SOC and lattice strains can be incorporated efficiently within this formalism. We use the established KL parameters [138] for describing the host electronic structure.

The relatively weak hybridisation V_{pd} of the host valence band holes and Mn moments can be incorporated perturbatively using the Shriefer-Wolff transformation [112]. The Anderson Hamiltonian [5] including the Coulomb correlation integral of the localised states is transformed to a form where the valence band interacts with the localised d-states only via a spin-spin term. The kinetic-exchange interaction can be described by a single parameter:

$$J_0 = 2|V_{pd}|^2 \frac{U}{\epsilon_d(\epsilon_d + U)} \ , \tag{1.1}$$

where ϵ_d is the single-particle atomic-level energy of the occupied d-state measured from the top of the valence band, and $\epsilon_d + U$ is the energy cost of adding the opposite-spin d-orbital electron. (To better illustrate the physics we wrote the explicit form of Eq. (1.1) for a case of a single localised orbital.) The k-vector dependence of J_0 is neglected since the valence band states of interest are near the Brillouin zone centre. In the rest of the thesis we use $J_{pd} = J_0\Omega_{u.c.}$ where $\Omega_{u.c.}$ is the unit cell volume. The kinetic-exchange results in an antiferromagnetic coupling of the localised and itinerant spins which can be understood based on a simple level-repulsion picture as shown in Fig. 1.1

Finally, the long range nature of the carrier mediated magnetism allows us to use the virtual-crystal mean-field treatment of the Mn local moments. The model ignores disorder and spin-wave fluctuations of the magnetic system. Despite these approximations, the approach has proven useful for describing many thermodynamic and magneto-transport properties of (Ga,Mn)As samples with metallic conductivities [55], such as the measured transition temperatures [27, 51, 52, 57], the anomalous Hall effect [56, 53, 29, 121], anisotropic magneto resistance [56, 49, 29, 121, 104, 103, 102], spin-stiffness [61], ferromagnetic domain-wall widths [25, 130], Gilbert damping coefficient [122, 123, 34], and magneto-optical coefficients [26, 124, 122, 62, 121]. In this thesis we demonstrate the qualitative and often semi-quantitative reliability of the effective model in predicting the magnetocrystalline anisotropies of (Ga,Mn)As epilayers and micro-devices.

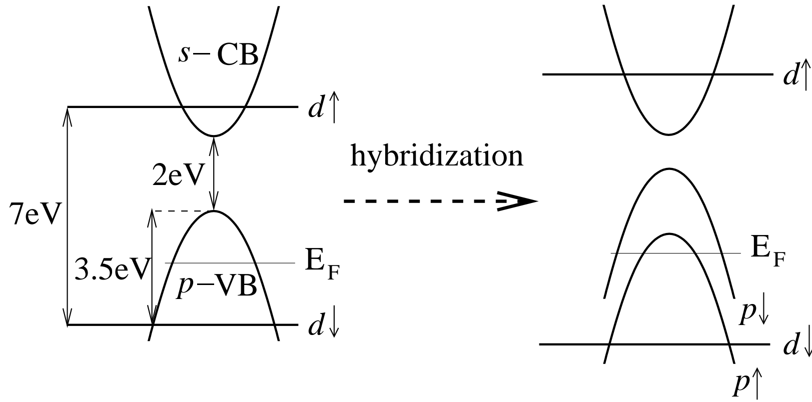

Figure 1.1: Schematics of the splitting of the valence-band due to the $p-d$ hybridisation in the electron picture. For the filled Mn d-shell level deep in the valence band and the empty d-level in the conduction band, the hybridisation pushes the energy of the spin-down valence band states up relative to the energy of the spin-up valence band states resulting in the antiferromagnetic coupling of the localised and itinerant spins.

1.4 Metallic multilayers

Having gained valuable experience with SOC effects in DMSs, one potential route to achieving the desired spintronic functionalities at room temperature is to exploit analogous relativistic phenomena in metallic alloys, multilayers or nanostructures. At the same time, recent progress in fabrication and characterisation of the magnetic nanoparticles and thin films based on the ordered $L1_0$ CoPt and FePt alloys, renewed interest in understanding the mechanisms contributing to the large magnetocrystalline anisotropy of these materials [116]. Moreover, TAMR effect has been demonstrated in CoPt multilayer [95]. These factors have motivated us to start developing a description of magnetocrystalline and magneto-transport anisotropies in metallic alloys and layered structures with strong SOC.

1.4.1 Origin of magnetic anisotropy

The relevant metallic alloys combine at least two types of atoms where one type contributes the magnetic moment and maintains ferromagnetic order above the room temperature whereas the the other type of atom possesses SOC in analogy to (Ga,Mn)As where the host semiconductor has strong SOC in the valence band and Mn contributes the large magnetic moment. In this work we focus on typical magnetic transition metal elements ferromagnets, iron and cobalt, and on the heavy noble metal platinum. Note that Pt has SOC two orders of magnitude stronger than Fe or Co. Hybridisation of states of the magnetic Fe or Co and non-magnetic but strongly spin-orbit coupled Pt can significantly enhance magnetic anisotropies compared to pure Fe or Co. The ferromagnetic order is maintained in the alloy even though the Curie temperature is lowered, e.g., $T_C \approx 800$ K in a 100 nm thick annealed CoPt film [99] as compared to $T_C \approx 1388$ K in bulk Co.

1.4.2 Tight-binding model

The $\boldsymbol{k} \cdot \boldsymbol{p}$ method which we use in case of DMSs is not suitable for describing the complex electronic structure of transition metals with many bands crossing the Fermi level. Moreover, the envelope function approximation is not appropriate for structures whose properties vary on a length scale comparable to the lattice constant as, e.g., in ultra-thin films or stacks of alternating few-monolayer films of different materials. For the transition metal systems we therefore employ the tight-binding scheme which has been previously used successfully to predict magnetocrystalline anisotropies in transition-metal monolayers [14]. Another advantage of the tight-binding model, as compared to the delocalised-basis $\boldsymbol{k} \cdot \boldsymbol{p}$ or ab-initio approaches, is the possibility to combine it in a straightforward way with the Landauer-Büttiker transport formalism in the framework of one-particle Green's functions, taking advantage of the localised basis used in the tight-binding scheme. This combined approach has proven useful recently for example in the study of spin-dependent tunnelling in (Ga,Mn)As [106, 105]. Due to its semi-phenomenological nature and the consideration of short range interactions only, the tight-binding approximation allows in principle for the description of complicated multilayer structures and for developing physical understanding of the studied magnetic anisotropy phenomena including their dependence on lattice strains or external electric fields.

We start with choosing a suitable realistic tight-binding parametrisation, compare results of the newly developed code to ab-initio calculations and check the internal consistency of our numerical predictions focusing on magnetocrystalline anisotropies. We restrict this work to cobalt, platinum and iron since their compounds have been studied both experimentally and theoretically by a relativistic full-potential Linearised Augmented Plain Wave (LAPW) methods [115, 116] providing a valuable benchmark for our modelling and code.

After comparing all parametrisations on the level of bulk monoatomic crystals, we calculate the DOS and MAE for CoPt and FePt ordered alloys, both for bulk crystals and for thin films. We test the numerical convergence of the calculations and then compare to available ab-initio data. We conclude this part of the work by evaluating local MAE and ADOS of a thin film which is a quantity directly related to TAMR.

Chapter 2

Theoretical framework

In this chapter we review briefly the two methods of modelling, electronic structures, and magnetocrystalline anisotropies in semiconductor and metallic systems with strong SOC. Section 2.1 presents the key elements of our effective Hamiltonian model including its symmetries which are particularly important for the studied magnetic anisotropy. Section 2.2 presents the standard tight-binding formalism in the Slater-Koster approach, discusses three realistic parametrisations which we implement and again details the symmetry lowering mechanisms.

2.1 Magnetocrystalline anisotropy of (Ga,Mn)As

We use the effective Hamiltonian approach to calculate the magnetocrystalline anisotropy energy of a system of itinerant carriers exchange coupled to Mn local moments. The $\boldsymbol{k}\cdot\boldsymbol{p}$ approximation is well suited for the description of hole states near the top of the valence band in a (III,Mn)V semiconductor. The strong SOC makes the band structure sensitive to the direction of the magnetisation. The Hamiltonian reads

$$\mathcal{H} = \mathcal{H}^{KL} + J_{pd}\sum_{I}\mathbf{S}_I\cdot\hat{\mathbf{s}}(\mathbf{r})\delta(\mathbf{r}-\mathbf{R_I}) + \mathcal{H}^{str}. \tag{2.1}$$

$\mathcal{H}^{KL}$ is the six-band Kohn-Luttinger Hamiltonian [68] including the SOC (see Eq. (2.19)). We use GaAs values for the Luttinger parameters [138]. $\mathcal{H}^{str}$ is the strain Hamiltonian discussed in the following subsection. The second term in Eq. (2.1) is the short-range antiferromagnetic kinetic-exchange interaction between localised spin $\mathbf{S}_I$ ($S=5/2$) on the Mn^{2+} ions and the itinerant hole spin $\hat{\mathbf{s}}$, parametrised by a constant [138] $J_{pd}=55$ meVnm^3. In the virtual-crystal mean-field approximation it becomes $J_{pd}N_{Mn}\langle S\rangle\hat{\mathbf{M}}\cdot\hat{\mathbf{s}}$. The explicit form of the 6×6 spin matrices $\hat{\mathbf{s}}$ is given in Ref. [1]. $\hat{\mathbf{M}}$ is the magnetisation unit vector and $N_{Mn}=4x/a_0^3$ is the concentration of Mn atoms in $Ga_{1-x}Mn_xAs$ (a_0 is the lattice constant). Note that the Fermi temperature in the studied systems is much higher than the Curie temperature so the smearing of the Fermi-Dirac distribution function is negligible. Therefore, finite temperature enters our model only in the form of decreasing the magnitude of magnetisation $|\mathbf{M}|=SB_S(J_{pd}\langle\hat{\mathbf{s}}\rangle/k_BT)$, where B_S is the Brillouin function and $\langle\hat{\mathbf{s}}\rangle$ is the hole spin-density calculated from the virtual-crystal mean-field form of Eq. (2.1).

We recall that the above model description is based on the canonical Schrieffer-Wolf transformation of the many-body Anderson Hamiltonian. For (Ga,Mn)As the transformation replaces the microscopic hybridisation of Mn d-orbitals with As and Ga sp-orbitals by the effective spin-spin kinetic-exchange interaction of $L = 0, S = 5/2$ local Mn-moments with host valence band states [55]. Therefore, the local moments in the effective model carry zero SOC and the magnetocrystalline anisotropy is entirely due to the spin-orbit coupled valence-band holes. The $\hat{\mathbf{M}}$-dependent total energy density, which determines the magnetocrystalline anisotropy, is calculated by summing one-particle energies for all occupied hole states in the valence band,

$$E_{tot}(\mathbf{M}) = \sum_{n=1}^{m} \int E_n(\mathbf{k}, \mathbf{M}) f(E_n(\mathbf{k}, \mathbf{M})) d^3k, \tag{2.2}$$

where $1 \leq m \leq 6$ is the number of occupied bands and $f(E_n(\mathbf{k}))$ is the Fermi distribution function taken at zero temperature as explained above.

2.1.1 Tetrahedral symmetry of the host semiconductor

The symmetry of the host crystal plays an important role in the derivation of the model Hamiltonian. The zinc-blende structure has a space group denoted by $F\overline{4}3m$ or T_d^2. Its point group T_d has tetrahedral symmetry.

In a general crystal approximated by a periodic potential V_0 the $\boldsymbol{k} \cdot \boldsymbol{p}$ method can be derived from the one-electron Schrödinger equation

$$\left(\frac{p^2}{2m} + V_0 \right) |\Phi_{n\boldsymbol{k}}\rangle = \epsilon_{n\boldsymbol{k}} |\Phi_{n\boldsymbol{k}}\rangle, \tag{2.3}$$

where we assume the solution in the form of Bloch wave functions $|\Phi_{n\boldsymbol{k}}\rangle = e^{i\boldsymbol{k}\cdot\boldsymbol{r}}|n\boldsymbol{k}\rangle$. $|n\boldsymbol{k}\rangle$ is the lattice periodic function, m is the free electron mass, n is the band index, and $\boldsymbol{k}$ lies within the first Brillouin zone. We obtain the equation

$$\left(\frac{p^2}{2m} + V_0 + \frac{\hbar}{m} \boldsymbol{k} \cdot \boldsymbol{p} \right) |n\boldsymbol{k}\rangle = \left(\epsilon_{n\boldsymbol{k}} - \frac{\hbar^2 k^2}{2m} \right) |n\boldsymbol{k}\rangle, \tag{2.4}$$

which simplifies in the centre of the Brillouin zone, the Γ point, to:

$$\left(\frac{p^2}{2m} + V_0 \right) |n0\rangle = \epsilon_{n0} |n0\rangle. \tag{2.5}$$

The solutions $|n0\rangle$ form a complete and orthogonal set of basis functions so the $\frac{\hbar}{m}\boldsymbol{k} \cdot \boldsymbol{p}$ term with finite k-vectors can be treated as a perturbation of Eq. (2.5). The larger the part of the Brillouin zone that should be covered, the more basis states should be used in the approximation.

At this point we focus on the triply degenerate top of the valence band which has the Γ_4 symmetry [154] in zinc-blende structures. Γ_4 (in the Koster notation) is one of the irreducible representations of the zinc-blende point group at the Γ point and its three wave functions are typically denoted by $|X\rangle$, $|Y\rangle$, and $|Z\rangle$. We assume the first-order correction to the energy ϵ_{n0}, a term linear in k, to vanish since ϵ_{n0} is an extremum. (The k linear

term is in general nonzero due to the lack of inversion symmetry; however, it vanishes in the basis relevant to our model as mentioned later.) The second-order correction involves summation over all neighbouring energy levels and corresponding states $|m0\rangle$. Their contribution to the series depends on two factors:

- The wave function $|m0\rangle$ can couple to $|n0\rangle$ only if the matrix element $\langle m0|\boldsymbol{p}|n0\rangle$ does not vanish. The operator $\boldsymbol{p}$ has Γ_4 symmetry in zinc-blende structures so according to the matrix theorem [154] (p. 46), the function $|m0\rangle$ has to belong to one of the irreducible representations in the direct sum $\Gamma_4 \otimes \Gamma_4 = \Gamma_4 \oplus \Gamma_5 \oplus \Gamma_3 \oplus \Gamma_1$ in order to give nonzero product with $\boldsymbol{p}|n0\rangle$.

- The relative importance if the coupling depends on the energy separation $\epsilon_{n0} - \epsilon_{m0}$. In addition, bands with energies higher than ϵ_{n0} tend to decrease the effective mass of the perturbed band leading eventually to concave dispersions for example in case of the top of the valence band of zinc-blende structures.

The two lowest conduction bands with energies closest to the valence band are formed by functions belonging to the Γ_1 and Γ_4 irreducible representations. Therefore, it is sufficient to write the second-order correction $\mathcal{W}$ of Eq. (2.5) considering the two lowest conduction bands (denoted by Γ_1^c and Γ_4^c) in the summation:

$$\mathcal{W}_{ij} = \frac{\hbar^2 k^2}{2m}\delta_{i,j} + \frac{\hbar^2}{m^2} \sum_{l \in \{\Gamma_1^c, \Gamma_4^c\}} \frac{\langle i|\boldsymbol{k}\cdot\boldsymbol{p}|l\rangle\langle l|\boldsymbol{k}\cdot\boldsymbol{p}|j\rangle}{\epsilon_i - \epsilon_l}, \tag{2.6}$$

where the basis functions $|i\rangle$ and $|j\rangle$ belong to the valence band Γ_4^v as mentioned above and share the same energy $\epsilon_i = \epsilon_{n0}$.

The basis functions are not known and cannot be calculated within our theory but we can limit the number of unknown Hamiltonian matrix elements using the high symmetry of the host crystal. As a result of the three-fold rotational symmetries of the zinc-blende crystal the following holds [154] (p. 103) for the only nonzero momentum operator expectation values relevant to Eq. (2.6):

$$\langle X|p_y|\Gamma_4^c(z)\rangle = \langle Y|p_z|\Gamma_4^c(x)\rangle = \langle Z|p_x|\Gamma_4^c(y)\rangle, \tag{2.7}$$

$$\langle X|p_x|\Gamma_1^c\rangle = \langle Y|p_y|\Gamma_1^c\rangle = \langle Z|p_z|\Gamma_1^c\rangle, \tag{2.8}$$

where $|X\rangle$, $|Y\rangle$, and $|Z\rangle$ belong to Γ_4^v. Due to the reflection symmetry with respect to the (110) planes it holds also

$$\langle X|p_y|\Gamma_4^c(z)\rangle = \langle Y|p_x|\Gamma_4^c(z)\rangle. \tag{2.9}$$

Now we can write the second-order correction to the valence band of the zinc-blende structure in a matrix form using only three distinct parameters:

$$\mathcal{W} = \begin{bmatrix} Ak_x^2 + B(k_y^2 + k_z^2) & Ck_xk_y & Ck_xk_z \\ Ck_yk_x & Ak_y^2 + B(k_x^2 + k_z^2) & Ck_yk_z \\ Ck_zk_x & Ck_zk_y & Ak_z^2 + B(k_x^2 + k_y^2) \end{bmatrix}, \tag{2.10}$$

where the reference energy ϵ_{n0} is set to zero, the electron spin is neglected for the moment and the parameters are constructed as:

$$A = \frac{\hbar^2}{2m} + \frac{\hbar^2}{m^2} \sum_{l \in \{\Gamma_1^c, \Gamma_4^c\}} \frac{|\langle X|p_x|l\rangle|^2}{\epsilon_i - \epsilon_l}, \tag{2.11}$$

$$B = \frac{\hbar^2}{2m} + \frac{\hbar^2}{m^2} \sum_{l \in \{\Gamma_1^c, \Gamma_4^c\}} \frac{|\langle X|p_y|l\rangle|^2}{\epsilon_i - \epsilon_l}, \tag{2.12}$$

$$C = \frac{\hbar^2}{m^2} \sum_{l \in \{\Gamma_1^c, \Gamma_4^c\}} \frac{\langle X|p_x|l\rangle\langle l|p_y|Y\rangle + \langle X|p_y|l\rangle\langle l|p_x|Y\rangle}{\epsilon_i - \epsilon_l}. \tag{2.13}$$

Note that due to the choice of the basis Γ_4^v the resulting perturbation has cubic symmetry, point group O_h, which includes the tetrahedral symmetry of the crystal and the space inversion symmetry. (In the electron picture when the conduction band is higher in energy than the valence band, the parameters A, B, and C are negative.)

When incorporating the spin of the electron, we have to consider the coupling of spin and orbital degrees of freedom which is of relativistic origin. The atomic SOC is given by

$$\mathcal{W}^{so} = \frac{1}{2m^2c^2}\left(\boldsymbol{S} \times \nabla V_a\right) \cdot \boldsymbol{p} = \frac{1}{2m^2c^2r}\frac{dV_a}{dr}\boldsymbol{S} \cdot \boldsymbol{L}, \tag{2.14}$$

where $\boldsymbol{S}$ is the electron spin operator, $\boldsymbol{L}$ is the electron orbital angular momentum, V_a is the radial atomic potential neglecting the symmetry of the crystal at this stage, and c is the speed of light in vacuum. We also remark that the single group (symmetry operations of spinless wave functions) of the Γ-point with five irreducible representations becomes a double group with eight irreducible representations after incorporating the electron spin.

Instead of using the group theory to find out the band splitting due to $\mathcal{W}^{so}$, we can use the relation of the functions $|X\rangle$, $|Y\rangle$, and $|Z\rangle$ to the atomic p wave functions corresponding to orbital angular momentum $l = 1$. The six degenerate states can be chosen as eigenstates of the z-component of the orbital momentum, $L_z|l\ s\ m_l\ m_s\rangle = \hbar m_l|l\ s\ m_l\ m_s\rangle$ with quantum numbers $m_l = 1, 0, -1$, and the z-component of spin, $S_z|l\ s\ m_l\ m_s\rangle = \hbar m_s|l\ s\ m_l\ m_s\rangle$ with $m_s = \pm 1/2$. The eigenstates of $\mathcal{W}^{so}$ diagonalise the total angular momentum operator $\boldsymbol{J} = \boldsymbol{S} + \boldsymbol{L}$ and its component J_z. They can be denoted by $|l\, s; j\, m_j\rangle$ and expressed in terms of the $\boldsymbol{S}$ and $\boldsymbol{L}$ eigenstates:

$$|l\ s; j\ m_j\rangle = \sum_{m_l, m_s} |l\ s\ m_l\ m_s\rangle\langle l\ s\ m_l\ m_s|l\ s; j\ m_j\rangle, \tag{2.15}$$

where $\langle l\ s\ m_l\ m_s|l\ s; j\ m_j\rangle$ are the Clebsch-Gordan coefficients and the summation runs through the eigenstates of the S_z and L_z operators. The quantum numbers of $\boldsymbol{J}$ can take values $j = l + s = 3/2$ or $j = l - s = 1/2$. To relate these results back to our Γ_4^v functions, we can define $(l = 1)$-like states in the zinc-blende structure:

$$\begin{aligned} |1, -1\rangle &= (|X\rangle - i|Y\rangle)/\sqrt{2}, \\ |1, 1\rangle &= -(|X\rangle + i|Y\rangle)/\sqrt{2}, \\ |1, 0\rangle &= |Z\rangle. \end{aligned} \tag{2.16}$$

Note that this association of Γ_4^v with the atomic functions explains the absence of the first-order correction to energy in our basis. In addition to the selection rules based on crystal symmetry mentioned above, the matrix element $\langle\Gamma_4|\boldsymbol{p}|\Gamma_4\rangle$ vanishes for atomic functions with definite parity: $\langle\boldsymbol{r}|X\rangle \propto xf(r)$, $\langle\boldsymbol{r}|Y\rangle \propto yf(r)$, and $\langle\boldsymbol{r}|Z\rangle \propto zf(r)$.

The transformation (2.15) then gives the following functions labelled by the eigenvalues j and m_j of the total angular momentum and its projection:

$$
\begin{aligned}
|3/2,3/2\rangle &= -\frac{1}{\sqrt{2}}\big(|X,\uparrow\rangle + i|Y,\uparrow\rangle\big), \\
|3/2,-1/2\rangle &= \frac{1}{\sqrt{6}}\big(|X,\uparrow\rangle - i|Y,\uparrow\rangle\big) + \sqrt{\frac{2}{3}}\,|Z,\downarrow\rangle, \\
|3/2,1/2\rangle &= -\frac{1}{\sqrt{6}}\big(|X,\downarrow\rangle + i|Y,\downarrow\rangle\big) + \sqrt{\frac{2}{3}}\,|Z,\uparrow\rangle, \\
|3/2,-3/2\rangle &= \frac{1}{\sqrt{2}}\big(|X,\downarrow\rangle - i|Y,\downarrow\rangle\big), \\
|1/2,1/2\rangle &= \frac{1}{\sqrt{3}}\big(|X,\downarrow\rangle + i|Y,\downarrow\rangle\big) + \frac{1}{\sqrt{3}}\,|Z,\uparrow\rangle, \\
|1/2,-1/2\rangle &= -\frac{1}{\sqrt{3}}\big(|X,\uparrow\rangle - i|Y,\uparrow\rangle\big) + \frac{1}{\sqrt{3}}\,|Z,\downarrow\rangle.
\end{aligned}
\tag{2.17}
$$

The ($j = 3/2$)-like and ($j = 1/2$)-like states are four-fold and two-fold degenerate, respectively. Their energy separation at the Γ point is the so called spin-orbit splitting $\Delta_{so} = \frac{3}{4m^2c^2r}\frac{dV_a}{dr}$. Based on the characters of the double group representations for the E and S_4 symmetry operations we can conclude that the ($j = 3/2$)-like states belong to the Γ_8 representation and ($j = 1/2$)-like states to the Γ_7 representation [154] (p. 74).

The correction $\mathcal{W}$ introduced in Eq. (2.6) combined with $\mathcal{W}^{so}$, can be written in the basis of Eq. (2.17) as follows:

$$
\mathcal{H}^{KL} = \left[\begin{array}{cccc|cc}
\mathcal{H}_{hh} & -c & -b & 0 & \frac{b}{\sqrt{2}} & c\sqrt{2} \\
-c^* & \mathcal{H}_{lh} & 0 & b & -\frac{b^*\sqrt{3}}{\sqrt{2}} & -d \\
-b^* & 0 & \mathcal{H}_{lh} & -c & d & -\frac{b\sqrt{3}}{\sqrt{2}} \\
0 & b^* & -c^* & \mathcal{H}_{hh} & -c^*\sqrt{2} & \frac{b^*}{\sqrt{2}} \\
\hline
\frac{b^*}{\sqrt{2}} & -\frac{b\sqrt{3}}{\sqrt{2}} & d^* & -c\sqrt{2} & \mathcal{H}_{so} & 0 \\
c^*\sqrt{2} & -d^* & -\frac{b^*\sqrt{3}}{\sqrt{2}} & \frac{b}{\sqrt{2}} & 0 & \mathcal{H}_{so}
\end{array}\right].
\tag{2.18}
$$

This form of the effective $\boldsymbol{k}\cdot\boldsymbol{p}$ Hamiltonian in a diamond- or zinc-blende-type structure is known as the Kohn-Luttinger Hamiltonian [68] which is the fundamental constituent of our model. The four-band Hamiltonian relevant at the lowest hole densities is highlighted.

The matrix elements of $\mathcal{H}^{KL}$ depend on the Kohn-Luttinger parameters [1]:

$$\begin{aligned}
\mathcal{H}_{hh} &= \frac{\hbar^2}{2m}\big((\gamma_1+\gamma_2)(k_x^2+k_y^2)+(\gamma_1-2\gamma_2)k_z^2\big),\\
\mathcal{H}_{lh} &= \frac{\hbar^2}{2m}\big((\gamma_1-\gamma_2)(k_x^2+k_y^2)+(\gamma_1+2\gamma_2)k_z^2\big),\\
\mathcal{H}_{so} &= \frac{\hbar^2}{2m}\big(\gamma_1(k_x^2+k_y^2+k_z^2)\big)+\Delta_{so},\\
b &= \frac{\sqrt{3}\hbar^2}{m}\gamma_3 k_z(k_x-ik_y),\\
c &= \frac{\sqrt{3}\hbar^2}{2m}\big(\gamma_2(k_x^2-k_y^2)-2i\gamma_3k_xk_y\big),\\
d &= -\frac{\sqrt{2}\hbar^2}{2m}\gamma_2(2k_z^2-k_x^2-k_y^2).
\end{aligned} \tag{2.19}$$

Figure 2.1 shows schematically the band structure of GaAs near the Γ point and provides intuitive explanation of the notation used for the elements of $\mathcal{H}^{KL}$. The band with smaller(larger) dispersion is referred to as the heavy(light) hole band and labelled by $hh(lh)$ in Eqs. (2.19); the split-off band (labelled by so) is separated by the SOC. Instead of working with valence band electrons with negative effective masses, we switch

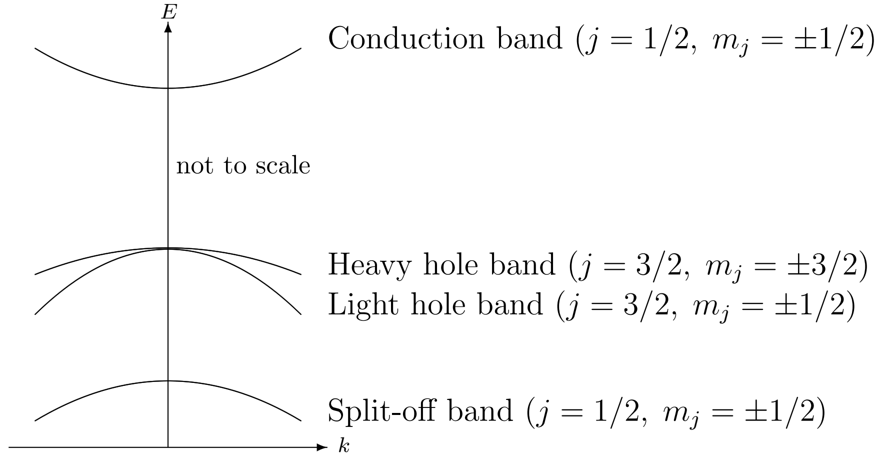

Figure 2.1: Schematic overview of the energy dispersions near the Brillouin zone centre (in the electron picture). The valence bands are solutions of the Kohn-Luttinger Hamiltonian given in Eq. (2.18). Each band is two-fold degenerate in m_j at $k = 0$.

to the hole picture in Eqs. (2.19) where the valence band effective masses are positive. Eqs. (2.19) assume positive values of γ_i which can be expressed in terms of the parameters of the spin-degenerate Hamiltonian (with A, B, and C in the electron picture):

$$\begin{aligned}
\gamma_1 &= -\frac{2m}{3\hbar^2}\left(A+2B\right),\\
\gamma_2 &= -\frac{m}{3\hbar^2}\left(A-B\right),\\
\gamma_3 &= -\frac{m}{3\hbar^2}C.
\end{aligned} \tag{2.20}$$

The parameters γ_i are tabulated in Ref. [138]. We have used the values listed in Table A.1.

2.1.2 Symmetry lowering mechanisms

The magnetocrystalline anisotropy components studied in this work originate in the tetrahedral symmetry of the host zinc-blende structure and in additional symmetry breaking mechanisms. In the first part of this subsection, we describe the most common mechanism, the lattice strain, which is introduced during the growth of the samples on substrates with slightly different lattice constant or by a particular post-growth treatment of the thin film. In the second part of this subsection, we mention a symmetry breaking mechanism assuming an in-plane microscopic potential which does not cause a macroscopic lattice distortion.

The $\boldsymbol{k} \cdot \boldsymbol{p}$ method provides straightforward means of incorporating elastic strains [26, 11, 21] which we now discuss in more detail. Small deformation of the crystal lattice can be described by a transformation of coordinates:

$$r'_\alpha = r_\alpha + \sum_\beta e_{\alpha\beta} r_\beta, \tag{2.21}$$

where $e_{\alpha\beta}$ is the strain tensor. According to the theory of elastic medium [48] we can define six independent stresses: X_x, Y_y, Z_z, Y_z, Z_x, X_y, which are forces per unit area, the capital letters denote their directions, and the subscripts denote the normals to the faces of the cell at which they are applied. Equal forces are assumed to act on opposite sides of the cell to maintain equilibrium. We omit stresses Z_y, X_z, Y_x as we are not interested in forces producing pure rotations. In elastic bodies there is linear dependence between the stress and strain components and in case of cubic symmetry we can write:

$$\begin{bmatrix} X_x \\ Y_y \\ Z_z \\ Y_z \\ Z_x \\ X_y \end{bmatrix} = \begin{bmatrix} c_{11} & c_{12} & c_{12} & 0 & 0 & 0 \\ c_{12} & c_{11} & c_{12} & 0 & 0 & 0 \\ c_{12} & c_{12} & c_{11} & 0 & 0 & 0 \\ 0 & 0 & 0 & c_{44} & 0 & 0 \\ 0 & 0 & 0 & 0 & c_{44} & 0 \\ 0 & 0 & 0 & 0 & 0 & c_{44} \end{bmatrix} \begin{bmatrix} e_{xx} \\ e_{yy} \\ e_{zz} \\ e_{yz} \\ e_{zx} \\ e_{xy} \end{bmatrix}, \tag{2.22}$$

where c_{ij} are the elastic moduli, e.g., the off-diagonal element $c_{12} = \frac{\partial^2 U}{\partial e_{xx} \partial e_{yy}} = \frac{\partial X_x}{\partial e_{yy}}$ where U is the elastic energy per unit volume of the body. Focusing on the thin films grown on thick substrates, we expect zero net force acting perpendicular to the interface: $Z_z = c_{12} e_{xx} + c_{12} e_{yy} + c_{11} e_{zz} = 0$; and equal strain along the main in-plain axes: $e_{xx} = e_{yy} \equiv e_0$. Therefore, we can determine the out-of-plane strain component from the in-plane components as $e_{zz} = -2\frac{c_{12}}{c_{11}} e_0$.

Expressing $\mathcal{H}^{KL}$ in the $\mathbf{r}'$ coordinates introduced in Eq. (2.21) leads to extra terms dependent on the strain that can be treated perturbatively [21]. The derivation of the strain Hamiltonian starts by expanding the differential operators. Ignoring all terms of order $O(e^2)$ or higher, we can write

$$\frac{\partial}{\partial r'_\alpha} = \sum_\beta \frac{\partial r_\beta}{\partial r'_\alpha} \frac{\partial}{\partial r_\beta} = \sum_\beta \frac{1}{\delta_{\alpha\beta} + e_{\alpha\beta}} \frac{\partial}{\partial r_\beta} \cong \sum_\beta \left(\delta_{\alpha\beta} - e_{\alpha\beta}\right) \frac{\partial}{\partial r_\beta} \tag{2.23}$$

and correspondingly

$$\frac{\partial^2}{\partial r_\alpha'^2} \cong \frac{\partial^2}{\partial r_\alpha^2} - 2\sum_\beta e_{\alpha\beta}\frac{\partial^2}{\partial r_\alpha \partial r_\beta}, \quad (2.24)$$

$$k_\alpha p_\alpha' \cong k_\alpha p_\alpha - \sum_\beta e_{\alpha\beta} k_\alpha p_\beta, \quad (2.25)$$

$$V_0(r') \cong V_0(r) + \sum_{\alpha\beta} e_{\alpha\beta}\frac{\partial V_0(r')}{\partial e_{\alpha\beta}} = V_0(r) + \sum_{\alpha\beta} e_{\alpha\beta} V_{\alpha\beta}. \quad (2.26)$$

Inserting these expansions into Eq. (2.4), we obtain

$$\sum_\alpha \left(\frac{p_\alpha^2}{2m} - \frac{1}{m}\sum_\beta p_\alpha p_\beta e_{\alpha\beta} + \frac{\hbar}{m} k_\alpha p_\alpha - \frac{\hbar}{m}\sum_\beta k_\alpha p_\beta e_{\alpha\beta} \right) |n\boldsymbol{k}\rangle =$$
$$= \left(\epsilon_{n\boldsymbol{k}} - \frac{\hbar^2 k^2}{2m} - V_0 - \sum_{\alpha\beta} e_{\alpha\beta} V_{\alpha\beta} \right) |n\boldsymbol{k}\rangle. \quad (2.27)$$

The term combining two small quantities k_α and $e_{\alpha\beta}$ can be neglected. The remaining terms due to strain can be treated as a perturbation of Eq. (2.5). In contrast to the $\boldsymbol{k}\cdot\boldsymbol{p}$ term where the first-order correction linear in momentum vanishes due to the parity of functions $|X\rangle$, $|Y\rangle$, and $|Z\rangle$, here, the first order-correction is quadratic in $\boldsymbol{p}$ so it is nonzero.

$$\begin{aligned}
\mathcal{W}_{ij}^{str} &= \sum_{\alpha\beta} \left(V_{\alpha\beta}\delta_{i,j} - \frac{1}{m}\langle i|p_\alpha p_\beta|j\rangle \right) e_{\alpha\beta}, \\
&= \sum_{\alpha\beta} \left(V_{\alpha\beta}\delta_{i,j} - \frac{1}{m}\sum_{l\notin\ \Gamma_4^v} \langle i|p_\alpha|l\rangle\langle l|p_\beta|j\rangle \right) e_{\alpha\beta}, \\
&= V_s\delta_{i,j} - \frac{1}{m}\sum_{\alpha\beta}\sum_{l\notin\ \Gamma_4^v} \langle i|p_\alpha|l\rangle\langle l|p_\beta|j\rangle e_{\alpha\beta}, \quad (2.28)
\end{aligned}$$

where we defined the constant $V_s \equiv \sum_{\alpha\beta} V_{\alpha\beta} e_{\alpha\beta}$ and inserted the unity operator $\sum_l |l\rangle\langle l|$. The summation over l runs through the complete and orthogonal set of solutions of Eq. (2.5) at $k=0$. The valence band states of Γ_4^v are left out explicitly as their contribution is zero, again due to their parity. Note that equations (2.6) and (2.28) have the same form when $e_{\alpha\beta}$ is associated with $k_\alpha k_\beta$. The summation over neighbouring states in Eq. (2.6) is restricted to the conduction band owing to the larger energy separation of other bands but the structure of $\mathcal{W}$ shown in Eq. (2.10) is given by the symmetry of the crystal. Based on the observed formal analogy of the $\mathcal{W}$ and $\mathcal{W}^{str}$, taking advantage of the tetrahedral symmetry of our system, we can write the spin-degenerate matrix:

$$\mathcal{W}^{str} = \begin{bmatrix} A^s e_{xx} + B^s(e_{yy}+e_{zz}) & C^s e_{xy} & C^s e_{xz} \\ C^s e_{yx} & A^s e_{yy} + B^s(e_{xx}+e_{zz}) & C^s e_{yz} \\ C^s e_{zx} & C^s e_{zy} & A^s e_{zz} + B^s(e_{xx}+e_{yy}) \end{bmatrix}, \quad (2.29)$$

where we omit the shift of the reference energy ϵ_{n0} by V_s:

$$A^s = \frac{1}{m} \sum_{l \notin \Gamma_4^v} |\langle X|p_x|l\rangle|^2, \tag{2.30}$$

$$B^s = \frac{1}{m} \sum_{l \notin \Gamma_4^v} |\langle X|p_y|l\rangle|^2, \tag{2.31}$$

$$C^s = \frac{1}{m} \sum_{l \notin \Gamma_4^v} \left(\langle X|p_x|l\rangle\langle l|p_y|Y\rangle + \langle X|p_y|l\rangle\langle l|p_x|Y\rangle\right). \tag{2.32}$$

Although the numerical values of the parameters A^s, B^s, and C^s are not related to their counterparts from $\mathcal{W}$ in a simple way, the structure of $\mathcal{W}^{str}$ allows us to write matrix elements of the six-band strain Hamiltonian $\mathcal{H}^{str}$ in the basis of total angular momentum only by making the following replacements in Eq. (2.19):

$$k_\alpha k_\beta \to e_{\alpha\beta} \tag{2.33}$$
$$-\frac{\hbar^2}{2m}\gamma_1 \to a_1, \quad -\tfrac{\hbar^2}{2m}\gamma_2 \to \tfrac{a_2}{2}, \quad -\frac{\hbar^2}{2m}\gamma_3 \to \frac{a_3}{2\sqrt{3}},$$

where a_1, a_2, and a_3 are the elastic constants. We obtain the elements of $\mathcal{H}^{str}$ (in the hole picture):

$$\begin{aligned}
\mathcal{H}^s_{hh} &= -\left(a_1 + \frac{a_2}{2}\right)(e_{xx}+e_{yy}) - (a_1 - a_2)e_{zz} \\
\mathcal{H}^s_{lh} &= -\left(a_1 - \frac{a_2}{2}\right)(e_{xx}+e_{yy}) - (a_1 + a_2)e_{zz} \\
\mathcal{H}^s_{so} &= -a_1(e_{xx}+e_{yy}+e_{zz})
\end{aligned}$$

$$\begin{aligned}
b^s &= -a_3(e_{zx} - ie_{zy}) \\
c^s &= \frac{a_2}{2}\sqrt{3}(e_{yy}-e_{xx}) + ia_3 e_{xy} \\
d^s &= \frac{\sqrt{2}}{2} a_2 \left(2e_{zz} - (e_{xx}+e_{yy})\right).
\end{aligned} \tag{2.34}$$

Since the matrix $\mathcal{H}^{str}$ has the same structure as $\mathcal{H}^{KL}$ we will write explicitly only two particular examples for strain tensors typically occurring in the MBE-grown epilayers. The lattice matching strain induced by the epitaxial growth breaks the symmetry between in-plane and out-of-plane cubic axes. Corresponding non-zero components of the strain tensor read $e_{xx} = e_{yy} \equiv e_0 = -\frac{c_{11}}{2c_{12}} e_{zz} = (a_s - a_0)/a_0$ where a_s and a_0 are the lattice constant of the substrate and the relaxed epilayer, respectively. Typical magnitudes are $e_0 \sim 10^{-4} - 10^{-2}$. The corresponding strain Hamiltonian entering Eq. (2.1) reads (in the hole picture):

$$\mathcal{H}^{str}(e_0) = a_2 e_0 \frac{c_{11}+2c_{12}}{c_{11}} \begin{bmatrix} 0 & 0 & 0 & 0 & 0 & 0 \\ 0 & 2 & 0 & 0 & 0 & \sqrt{2} \\ 0 & 0 & 2 & 0 & -\sqrt{2} & 0 \\ 0 & 0 & 0 & 0 & 0 & 0 \\ 0 & 0 & -\sqrt{2} & 0 & 1 & 0 \\ 0 & \sqrt{2} & 0 & 0 & 0 & 1 \end{bmatrix} \equiv \varepsilon_s \mathbf{h}_g, \tag{2.35}$$

where we introduced the deformation potential $\varepsilon_s = a_2 e_0 \frac{c_{11}+2c_{12}}{c_{11}}$ and the growth strain matrix $\mathbf{h}_g$.

As we discuss in Subsec. 3.1.4, relaxing the growth strain in microbars in transverse direction produces a uniaxial symmetry breaking in the plane, described by a combination of $e_{xx} \neq e_{yy}$ and e_{xy} strains, depending on the crystal orientation of the microbar [147, 46, 149, 93]. The magnitudes range between zero and the growth strain. Additional in-plane uniaxial anisotropy effects can be also induced by piezo-stressors [35, 10, 101, 88]. The typical magnitude achieved by commercial stressors [113] at low temperature is of the order of 10^{-4}. The strain Hamiltonian corresponding to a strain tensor with a single nonzero component e_{xy} reads (in the hole picture):

$$\mathcal{H}^{str}(e_{xy}) = a_3 e_{xy} \begin{bmatrix} 0 & -i & 0 & 0 & 0 & i\sqrt{2} \\ i & 0 & 0 & 0 & 0 & 0 \\ 0 & 0 & 0 & -i & 0 & 0 \\ 0 & 0 & i & 0 & i\sqrt{2} & 0 \\ 0 & 0 & 0 & -i\sqrt{2} & 0 & 0 \\ -i\sqrt{2} & 0 & 0 & 0 & 0 & 0 \end{bmatrix} \equiv a_3 e_{xy} \mathbf{h}_s. \qquad (2.36)$$

An unpatterned bulk (Ga,Mn)As epilayer can also show broken in-plane symmetry, most frequently between the [110] and [1$\bar{1}$0] directions [109, 110, 142, 146, 145, 39, 126, 133, 94, 36]. For convenience and for direct comparison with effects mentioned in the previous paragraph we model this “intrinsic” in-plane uniaxial anisotropy by an effective shear strain e_{xy}^{int}. We fix its sign and magnitude for a given wafer by fitting to the corresponding measured anisotropy coefficients. To narrow down the number of fitted values for e_{xy}^{int} in the extensive set of experimental data which we analyse, we assume that e_{xy}^{int} describes effectively a symmetry-breaking mechanism induced during growth and its value does not change upon the post-growth treatments, including annealing, hydrogenation, lithography or piezo-stressing.

We point out that an in-plane strain has not been detected experimentally in the bare unpatterned (Ga,Mn)As epilayers. It is indeed unlikely to occur as the substrate imposes the cubic symmetry. The possibility of transfer of the shear strain from the substrate to the epilayer was ruled out by the following test experiment. A 50 nm (Ga,Mn)As film was grown on GaAs substrate. An identical film was grown on the opposite side of the neighbouring part of the same substrate. Both samples developed uniaxial magnetic anisotropy along a diagonal but the easy axes were orthogonal to each other. If there were a uniaxial strain in the substrate responsible for the uniaxial anisotropy in the epilayer, the easy axes in the two samples would be collinear. Nevertheless, we argue below that the effective modelling via e_{xy}^{int} provides a meaningful description of the “intrinsic” uniaxial anisotropy.

In the second part of this subsection the original contribution of the author of this thesis to the modelling is presented. We compare the effective Hamiltonian corresponding to the e_{xy}^{int} strain with a $\boldsymbol{k}\cdot\boldsymbol{p}$ Hamiltonian in which, without introducing the macroscopic lattice distortion, the [$\bar{1}$10]/[110] symmetry is broken. We recall that the derivation of the Kohn-Luttinger Hamiltonian involves a summation over the Γ_1 and Γ_4 states of the two lowest conduction bands in the second-order correction of Eq. (2.5). The symmetries of the tetrahedron point group T_d narrow down the number of non-vanishing independent

matrix elements in Eq. (2.6) and determine the structure of the resulting Kohn-Luttinger Hamiltonian.

If the tetrahedral symmetry of the GaAs lattice is broken the number of independent matrix elements increases. Let us consider a perturbation to the crystal potential that removes two of the C_2 elements of group T_d (rotations by 180° about the [100] and [010] axes). The corresponding potential takes a form $V = xy\xi$, which mixes the Γ_1 and $\Gamma_4(z)$ states of the conduction band considered in the summation in Eq. (2.6) and leaves $\Gamma_4(x)$ and $\Gamma_4(y)$ states unchanged. (ξ is a fast decreasing radial function.) Such inter-mixing of surrounding states represents the local symmetry lowering experienced by the valence band states. The summation over the perturbed states, $\alpha\Gamma_1 + \beta\Gamma_4(z)$, $-\beta\Gamma_1 + \alpha\Gamma_4(z)$, $\Gamma_4(x)$, $\Gamma_4(y)$ in Eq. 2.6 gives rise to extra terms in the Hamiltonian $\tilde{\mathcal{W}}$. (The original form $\mathcal{W}$ is given in Eq. (2.10).) Assuming a weak local potential V, $\alpha \gg \beta$, we can neglect terms of quadratic and higher-order dependence on V and obtain:

$$\tilde{\mathcal{W}} = \begin{bmatrix} Ak_x^2 + B(k_z^2 + k_y^2) + 2Dk_xk_y & Ck_xk_y + D(k_x^2 + k_y^2) & Ck_xk_z + Dk_yk_z \\ Ck_yk_x + D(k_x^2 + k_y^2) & Ak_y^2 + B(k_z^2 + k_x^2) + 2Dk_xk_y & Ck_yk_z + Dk_xk_z \\ Ck_zk_x + Dk_zk_y & Ck_zk_y + Dk_zk_x & Ak_z^2 + B(k_x^2 + k_y^2) \end{bmatrix} \tag{2.37}$$

where

$$\begin{aligned} D &= \zeta\langle X|p_y|\Gamma_4(z)\rangle\langle\Gamma_1|p_x|X\rangle, \\ \zeta &= \frac{\hbar^2}{m^2}\alpha\beta\left[\frac{1}{\epsilon_v - (\epsilon_{c1} + \Delta)} - \frac{1}{\epsilon_v - (\epsilon_{c4} - \Delta)}\right]. \end{aligned} \tag{2.38}$$

ϵ_{c1} and ϵ_{c4} are the energies of the conduction band Γ_1 and Γ_4 states, respectively. The small energy Δ is quadratically dependent on the size of the potential V but we include it to express the shift of the perturbed energy levels.

Elements containing the parameter D change the dependence of the original $\boldsymbol{k}\cdot\boldsymbol{p}$ Hamiltonian on the k-vector. However, the structure of the $\mathcal{W}$ is preserved similarly to the strain Hamiltonian. The transformation of basis given in Eq. (2.15) results in a modified six-band Kohn-Luttinger Hamiltonian $\tilde{\mathcal{H}}^{KL}$. It has the structure shown in Eq. (2.18) and its matrix elements are derived from the original ones given in Eq. (2.19) as follows:

$$\begin{aligned} \tilde{\mathcal{H}}_{hh} &= \mathcal{H}_{hh} + \frac{3\hbar^2}{m}\gamma_4k_xk_y, & \tilde{b} &= b + \frac{\sqrt{3}\hbar^2}{2m}\gamma_4k_z(k_y - ik_x), \\ \tilde{\mathcal{H}}_{lh} &= \mathcal{H}_{lh} + \frac{\hbar^2}{m}\gamma_4k_xk_y, & \tilde{c} &= c - i\frac{\sqrt{3}\hbar^2}{2m}\gamma_4(k_x^2 + k_y^2), \\ \tilde{\mathcal{H}}_{so} &= \mathcal{H}_{so} + \frac{2\hbar^2}{m}\gamma_4k_xk_y, & \tilde{d} &= d + \frac{\sqrt{2}\hbar^2}{m}\gamma_4k_xk_y, \end{aligned} \tag{2.39}$$

where we add a new parameter $\gamma_4 = -\frac{2m}{3\hbar^2}D$ to the three Kohn-Luttinger parameters listed in Eq. (2.20).

The correspondence of the new Hamiltonian components induced by the microscopic potential $V = xy\xi$ to the strain Hamiltonian derived earlier in this subsection remains to be show explicitly. We focus on the in-plane effects and neglect the matrix element $\tilde{b}$ dependent on k_z. Then we can write the extension of the Kohn-Luttinger Hamiltonian

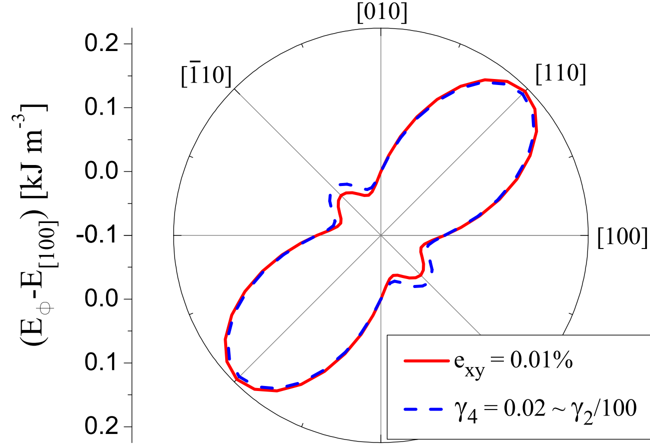

Figure 2.2: Modification of the originally cubic in-plane magnetic anisotropy by adding a uniaxial anisotropy due to the shear strain e_{xy} or due to the local potential $V = xy\xi$. $e_0 = -0.3\%$, $p = 3 \times 10^{20}$ cm^{-3}, $x = 3\%$, γ_2 and γ_4 are the Kohn-Luttinger parameters.

$\mathcal{H}^V = \tilde{\mathcal{H}}^{KL} - \mathcal{H}^{KL}$ using the matrices $\mathbf{h}^g$ and $\mathbf{h}^s$ introduced in Eqs. (2.35) and (2.36):

$$\mathcal{H}^V = -\frac{\sqrt{3}\hbar^2}{2m}\gamma_4(k_x^2 + k_y^2)\mathbf{h}_s - \frac{\hbar^2}{m}\gamma_4 k_x k_y \left(\mathbf{h}_g - 3\mathbf{I}\right), \tag{2.40}$$

where $\mathbf{I}$ is a unit matrix. Note that the first term corresponds directly to the effective shear strain Hamiltonian if we replace the deformation potential $a_3 e_{xy}^{int}$ in Eq. (2.36) with the factor $-\frac{\sqrt{3}\hbar^2}{2m}\gamma_4(k_x^2 + k_y^2)$. The second term corresponds to the growth strain Hamiltonian if we replace the deformation potential ε_s in Eq. (2.35) with the factor $-\frac{\hbar^2}{m}\gamma_4 k_x k_y$ and allow the reference energy shift indicated by $3\mathbf{I}$.

As we know from our analysis presented in the next chapter, the growth strain has negligible contribution to the in-plane magnetic anisotropy. Hence, we can conclude that on the level of Hamiltonian matrix structure, the microscopic potential $V = xy\xi$ induces the same modification of the $\boldsymbol{k} \cdot \boldsymbol{p}$ Hamiltonian as the in-plane strain e_{xy}^{int} and is expected to induce a similar in-plane uniaxial anisotropy component despite its k dependence. The microscopic simulations presented in Fig. 2.2 confirm that the in-plane anisotropy energy profile due to the local potential V can indeed be accurately obtained by the mapping on the effective shear strain Hamiltonian. (For the particular set of material parameters and $e_{xy}^{int} = 0.01\%$ we considered the new Luttinger parameter $\gamma_4 \approx \gamma_2/100$.)

As we discuss in the following section, effective modelling using the strain Hamiltonian with the constant e_{xy}^{int} term is sufficient to capture semiquantitatively many of the observed experimental trends. Here we have demonstarted, that the model effectively describes a microscopic symmetry-breaking mechanism yielding quantitatively the same in-plane anisotropy energy profiles without the presumption of a macroscopic lattice distortion.

2.2 Magnetocrystalline anisotropy in metals

We use the Slater-Koster tight-binding approach [125, 41] which is a variant of the Linear Combination of Atomic Orbitals (LCAO) method implemented using the Bloch's theorem. For describing the valence electrons of transition metals the basis functions are written in the form of Bloch sums,

$$\Phi_{\boldsymbol{k}a\alpha}(\boldsymbol{r}) = N^{-1/2} \sum_{n=0}^{N-1} e^{i\boldsymbol{k}\cdot(\boldsymbol{R}_n+\boldsymbol{p}_a)} \phi_{a\alpha}(\boldsymbol{r} - \boldsymbol{R}_n - \boldsymbol{p}_a), \tag{2.41}$$

where $\boldsymbol{k}$ is the Bloch wave vector, a is the atom index in the unit cell, α is the atomic orbital quantum number, N is the number of atoms a (unit cells), n is the unit cell index, $\boldsymbol{R}_n$ is the unit cell vector, and $\boldsymbol{p}_a$ is the position vector of the atom a in the unit cell. The wavefunctions $\phi_{a\alpha}(\boldsymbol{r} - \boldsymbol{R}_n - \boldsymbol{p}_a)$ are centred around the atom a in unit cell n and are orthonormal, i.e., assumed to be constructed from the atomic orbitals $\psi_{a\alpha}$ following Löwdin's orthonormalisation procedure:

$$\phi_{a\alpha}(\boldsymbol{r} - \boldsymbol{R}_n - \boldsymbol{p}_a) = \psi_{a\alpha}(\boldsymbol{r} - \boldsymbol{R}_n - \boldsymbol{p}_a) - \frac{1}{2}\sum_m \psi_{a\alpha}(\boldsymbol{r} - \boldsymbol{R}_m - \boldsymbol{p}_a) S_{mn} + \ldots\ , \tag{2.42}$$

where S_{mn} are the overlap integrals,

$$S_{mn} = \int d\boldsymbol{r} \psi^*_{a\alpha}(\boldsymbol{r} - \boldsymbol{R}_m - \boldsymbol{p}_a)\psi_{a\alpha}(\boldsymbol{r} - \boldsymbol{R}_n - \boldsymbol{p}_a), \tag{2.43}$$

and consequently to fulfil:

$$\int d\boldsymbol{r} \phi^*_{a\alpha}(\boldsymbol{r} - \boldsymbol{R}_m - \boldsymbol{p}_a)\phi_{b\beta}(\boldsymbol{r} - \boldsymbol{R}_n - \boldsymbol{p}_b) = \delta_{mn}\delta_{ab}. \tag{2.44}$$

The functions $\psi_{c\alpha}(\boldsymbol{r})$ are eigenstates of a Hamiltonian describing an isolated atom labelled c (denoting the chemical identity of the atom or later its position in the unit cell of a crystal):

$$\left(\frac{p^2}{2m} + V^{at}_c(\boldsymbol{r})\right)\psi_{c\alpha}(\boldsymbol{r}) = E_{c\alpha}\psi_{c\alpha}(\boldsymbol{r}) \tag{2.45}$$

so they are in general not orthogonal to atomic functions of neighbouring atoms in the crystal. We assume that the bound states $\psi_{c\alpha}(\boldsymbol{r})$ are well localised and that the full crystal Hamiltonian, H, can be approximated by the atomic Hamiltonian in the vicinity of each lattice point. The crystal Hamiltonian includes a periodic single-particle potential first mentioned in Eq. (2.3) which can be written without approximation as

$$V_0(\boldsymbol{r}) = \sum_{nc} V^{at}_c(\boldsymbol{r} - \boldsymbol{R}_n - \boldsymbol{p}_c), \tag{2.46}$$

where the indices n and c run through all unit cells and all atoms in a unit cell, respectively.

Our aim is to find eigenstates of the crystal Hamiltonian as linear combinations of the Bloch sums $\Phi_{\boldsymbol{k}a\alpha}(\boldsymbol{r})$ introduced in Eq. (2.41). Therefore we solve the Schrödinger equation:

$$H\Phi_{\boldsymbol{k}}(\boldsymbol{r}) = \varepsilon(\boldsymbol{k})\Phi_{\boldsymbol{k}}(\boldsymbol{r}), \tag{2.47}$$

where $\Phi_{\boldsymbol{k}}(\boldsymbol{r}) = \sum_{a\alpha} w_{\boldsymbol{k}a\alpha}\Phi_{\boldsymbol{k}a\alpha}(\boldsymbol{r})$ and $w_{\boldsymbol{k}a\alpha}$ are the coefficients to be determined. The corresponding matrix elements of the crystal Hamiltonian can be written using the expansion of Eq. (2.41):

$$H_{a\alpha,b\beta}(\boldsymbol{k}) = \sum_n e^{i\boldsymbol{k}\cdot(\boldsymbol{R}_n - \boldsymbol{p}_a + \boldsymbol{p}_b)} \int d\boldsymbol{r}\phi^*_{a\alpha}(\boldsymbol{r}-\boldsymbol{p}_a)H\phi_{b\beta}(\boldsymbol{r}-\boldsymbol{R}_n-\boldsymbol{p}_b), \tag{2.48}$$

where we have used the translation symmetry of the lattice to remove the sum over the lattice vector $\boldsymbol{R}_m$. Since the Hamiltonian has the same periodicity as the basis function $\Phi_{\boldsymbol{k}a\alpha}$ it is diagonal in the $\boldsymbol{k}$-vector. The matrix $H_{a\alpha,b\beta}(\boldsymbol{k})$ has a dimension given by the number of atoms in the unit cell and by the number of valence orbitals considered for each atom.

If we substitute the crystal potential $V(\boldsymbol{r})$ introduced in Eq. (2.46) into Eq. (2.48), then each term of the integral has a contribution from one of three regions: the regions centred around the two atomic-like wavefunctions $\phi_{a\alpha}$ and $\phi_{b\beta}$, and the region centred around the potential at $\boldsymbol{p}_c$. This leads to a classification of the integrals into four categories:

- If all three locations are on the same atom, this is an on-site integral (terms analogous to potential energy, determining the position of an energy band).
- If the location of the potential is the same as the location of one of the wavefunctions, while the other wavefunction is at a separate location, this is a two-centre integral (terms analogous to kinetic energy, corresponding to transition amplitudes between atoms, determining the width of an energy band).
- If the wavefunctions and the potential are all located at different sites, this is a three-centre integral.
- The fourth category occurs when the wavefunctions both come from the same site but the potential is on a different site. This category shares features with both the two-centre and three-centre integrals but is actually a local environment or crystal field correction to the on-site terms. We do not consider this type of integral further in this work.

2.2.1 Slater-Koster approach

Following the Slater-Koster (S-K) approach [125, 92], we now assume that the potentials $V_c(\boldsymbol{r})$ are spherically symmetric. Then the wavefunctions $\phi_{a\alpha}$ and $\psi_{a\alpha}$ can be specified by the usual angular momentum quantum numbers, and the on-site integrals only contribute to the diagonal elements of the Hamiltonian. We further assume that the three-centre integrals can be neglected compared to the two-centre integrals. This is not strictly true but it considerably simplifies the method, and in many cases leads to accurate predictions of the electronic structure and total energy of a system [92]. In this two-centre approximation the integrals in Eq. (2.48) depend only on the displacement $\boldsymbol{d}$ between the two atoms, and have the form

$$E_{a\alpha,b\beta}(\boldsymbol{d}) = \int d\boldsymbol{r}\phi^*_{a\alpha}(\boldsymbol{r})H_2\phi_{b\beta}(\boldsymbol{r}-\boldsymbol{d}), \tag{2.49}$$

where H_2 is the two-centre part of the Hamiltonian, i.e., the kinetic energy operator and a spherically symmetric potential centred on atom a or on atom b. These terms, often called interatomic matrix elements [41], depend on the orientation of $\boldsymbol{d}$, the magnitude of the separation between atoms ($d = |\boldsymbol{d}|$), and the angular momenta contained in the quantum numbers α and β. Eq. (2.48) can be rewritten using $\boldsymbol{d}_n$ running through all relevant neighbours of atom a:

$$H_{a\alpha,b\beta}(\boldsymbol{k}) = \sum_n e^{i\boldsymbol{k}\cdot\boldsymbol{d}_n} E_{a\alpha,b\beta}(\boldsymbol{d}_n), \tag{2.50}$$

In view of modelling transition metals we restrict the atomic orbitals ψ_a to s, p, and d angular momenta. After the symmetry considerations worked out by Slater and Koster, each interatomic matrix element of Eq. (2.49) can be written in terms of 14 parameters (two-centre integrals referred to as S-K parameters in the following text). We will denote these as $V_{\alpha\beta\gamma}(\boldsymbol{d})$, where α and β specify the angular momenta of the orbitals (s, p, d), and $\gamma = \sigma, \pi, \delta$ specifies the component of the angular momentum relative to the direction $\boldsymbol{d}$. In the case where the two atoms are identical, four pairs of the S-K parameters are related by symmetry: $V_{sp\sigma} = -V_{ps\sigma}$, $V_{sd\sigma} = V_{ds\sigma}$, $V_{pd\sigma} = -V_{dp\sigma}$, and $V_{pd\pi} = -V_{dp\pi}$, giving ten independent parameters. Note that the Hamiltonian matrix elements are short range: if the wavefunctions $\phi_{a\alpha}(\boldsymbol{r})$ and $\phi_{b\beta}(\boldsymbol{r})$ do not appreciably overlap, then the integral equation (2.49) will vanish. An example of interatomic matrix elements for s and p orbitals follows:

$$\begin{aligned}
E_{s,s} &= V_{ss\sigma}, \\
E_{s,x} &= lV_{sp\sigma}, \\
E_{x,x} &= l_2V_{pp\sigma} + (1 - l_2)V_{pp\pi}, \\
E_{x,y} &= lmV_{pp\sigma} - lmV_{pp\pi}, \\
E_{x,z} &= lnV_{pp\sigma} - lnV_{pp\pi},
\end{aligned} \tag{2.51}$$

where l, m, and n are the directional cosines of the displacement $\boldsymbol{d}$ and the indices x, y, and z denote the cubic harmonics of the p orbital. Remarkably, the expressions (2.51) are not dependent of the lattice type, only on the mutual displacement of the two atoms. The same holds of the remaining interatomic matrix elements listed, e.g., by W. A. Harrison [41] (page 481). Figure 2.3 presents the construction of the interatomic matrix element $E_{s,x}$ in a diagrammatic way.

In the original work of Slater and Koster the S-K parameters were determined by fitting to ab-initio band structures at high-symmetry points. The parameters were then used as interpolation parameters to describe the band structure throughout the Brillouin zone. We replace the on-site and two-centre integrals $V_{\alpha\beta\gamma}(\boldsymbol{d})$ by parameters which are chosen to reproduce the ab-initio single-particle band structure of a standard crystal as detailed in Subsec. 2.2.3.

The two-centre tight-binding method can be modified to use the atomic orbitals $\psi_{a\alpha}$ which are non-orthogonal. The basis functions Eq. (2.41) are then replaced by the functions

$$\Psi_{\boldsymbol{k}a\alpha} = N^{-1/2} \sum_{n=0}^{N-1} e^{i\boldsymbol{k}\cdot(\boldsymbol{R}_n + \boldsymbol{p}_a)} \psi(\boldsymbol{r} - \boldsymbol{R}_n - \boldsymbol{p}_a), \tag{2.52}$$

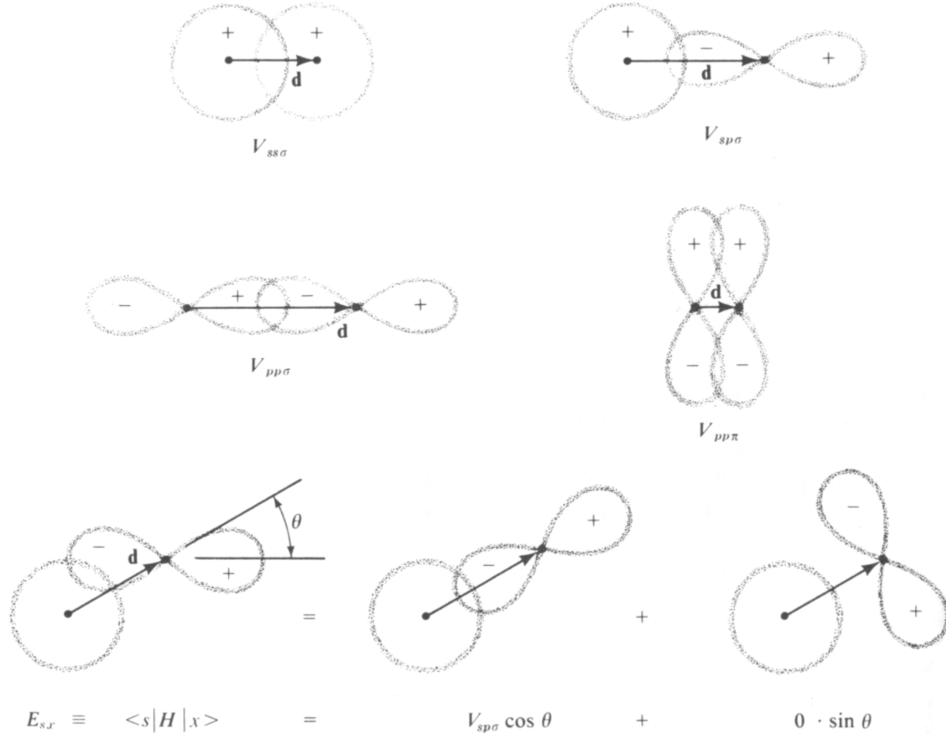

Figure 2.3: Four basic types of interatomic matrix elements of s- and p- bonded systems. When p orbitals are not oriented simply as shown in the upper diagrams, they may be decomposed geometrically as vectors. The interatomic matrix element at the bottom right consists of two contributions that cancel each other out. (Adapted from [41], page 52.)

Consequently, a generalised eigenvalue problem $\boldsymbol{H} - E\boldsymbol{S} = 0$ has to be solved, involving the Hamiltonian matrix elements of Eq. (2.48), with the $\Phi_{a\alpha}$ replaced by the corresponding $\Psi_{a\alpha}$, and a positively definite overlap matrix

$$S_{a\alpha,b\beta}(\boldsymbol{k}) = \sum_n e^{i\boldsymbol{k}\cdot(\boldsymbol{R}_n - \boldsymbol{p}_a + \boldsymbol{p}_b)} \int d\boldsymbol{r} \psi^*_{a\alpha}(\boldsymbol{r} - \boldsymbol{p}_a)\psi_{b\beta}(\boldsymbol{r} - \boldsymbol{R}_n - \boldsymbol{p}_b). \tag{2.53}$$

Since the matrix (2.53) does not include a Hamiltonian term, it can be exactly decomposed into on-site terms (which form a diagonal matrix if the $\psi_{a\alpha}$ are truly atomic-like) and two-centre overlap terms,

$$s_{a\alpha,b\beta}(\boldsymbol{d}) = \int d\boldsymbol{r} \psi^*_{a\alpha}(\boldsymbol{r})\psi_{b\beta}(\boldsymbol{r} - \boldsymbol{d}), \tag{2.54}$$

which have the same symmetry as the corresponding interatomic matrix element given in Eq. (2.49) and can be parametrised in the same way by terms denoted as $s_{\alpha\beta\gamma}(\boldsymbol{d})$. This introduces additional 14 S-K overlap parameters (ten if the atoms are identical) for systems described in terms of s, p, and d orbitals. If the basis functions which generate the overlap are normalised, then the parametrisation is required to fulfil

$$|s_{\alpha\beta\gamma}(\boldsymbol{d})| < 1, \boldsymbol{d} \neq 0 \tag{2.55}$$

and

$$s_{\alpha\beta\gamma}(0) = \delta_{\alpha\beta}. \tag{2.56}$$

The use of the non-orthogonal formalism has two advantages. The most obvious is that the additional parameters make it easier to fit band structures in a large database. A less obvious advantage comes from the nature of the Löwdin transformation of the atomic orbitals $\psi_{a\alpha}$ into orthogonal wavefunctions $\phi_{a\alpha}$. By necessity the $\phi_{a\alpha}$ have a longer range than the atomic wavefunctions. Use of the atomic wavefunctions means that the two-centre matrix elements in Eqs. (2.49) and (2.54) can have a shorter range, usually only a few nearest-neighbour shells. Thus the non-orthogonal matrix elements sample only the local environment of each atom, making the development of transferable S-K parameters easier.

2.2.2 Finite systems

So far we have described infinite periodic crystals with one or more atoms in the unit cell. Our objective is to calculate also anisotropies in multilayers and thin films with periodicity in two directions. Moreover, in very thin films consisting only of a few atomic layers the energy quantisation due to the confinement in the direction perpendicular to the film becomes relevant. Our modelling of systems with periodicity only in the x and y directions is a generalisation of the S-K approach with more atoms per unit cell described in the previous subsection. We describe each layer as an extra atom (or set of atoms) in the unit cell and use only two-dimensional reciprocal space with $\boldsymbol{k} = (k_x, k_y)$. Consequently, the Hamiltonian matrix in Eq. (2.50) enlarges as the atom indices a and b run through all atomic sites of the bulk unit cell and through all considered layers.

Figure 2.4 gives an example of a Hamiltonian matrix describing a system of 6 monoatomic layers with periodic boundary conditions. Each layer has one atom per the 2D unit cell and there are two types of layer/atom which alternate. There is coupling (hybridisation) of a given layer with its first and second nearest layer. An example set of numbers of neighbouring atomic sites considered in the sum of the Hamiltonian matrix element $H_{a\alpha,b\beta}(\boldsymbol{k})$ is given in each block (the neighbours reside in the same layer in case of diagonal blocks or in a different layer in case of off-diagonal blocks). Note that the Hamiltonian schema in Fig. 2.4 can describe also a bulk ordered alloy with two different atomic sites in the 3D unit cell, e.g., to $L1_0$ structure in case of fcc lattice, considering nonzero S-K parameters for the first, second, and third nearest neighbours. (From the numerical point of view, the Brillouin zones of the bulk and layered systems are different and obtaining identical electronic structure such as density of states or total energy is a matter of precise integration in the reciprocal space and of achieving convergence with respected to the number of atomic layers included in the calculation.)

The desired film of finite thickness, here 6 monoatomic layers, is described by a Hamiltonian matrix obtained from the matrix shown in Fig. 2.4 by leaving out the periodic boundary conditions (the three blocks in the upper right and lower left corners). Note that the presented formalism allows for modelling of any system consisting of layers sharing the same periodicity in the x and y directions. The stacking of the layers is limited only by the availability of corresponding S-K parameters which is addressed in the following subsection.

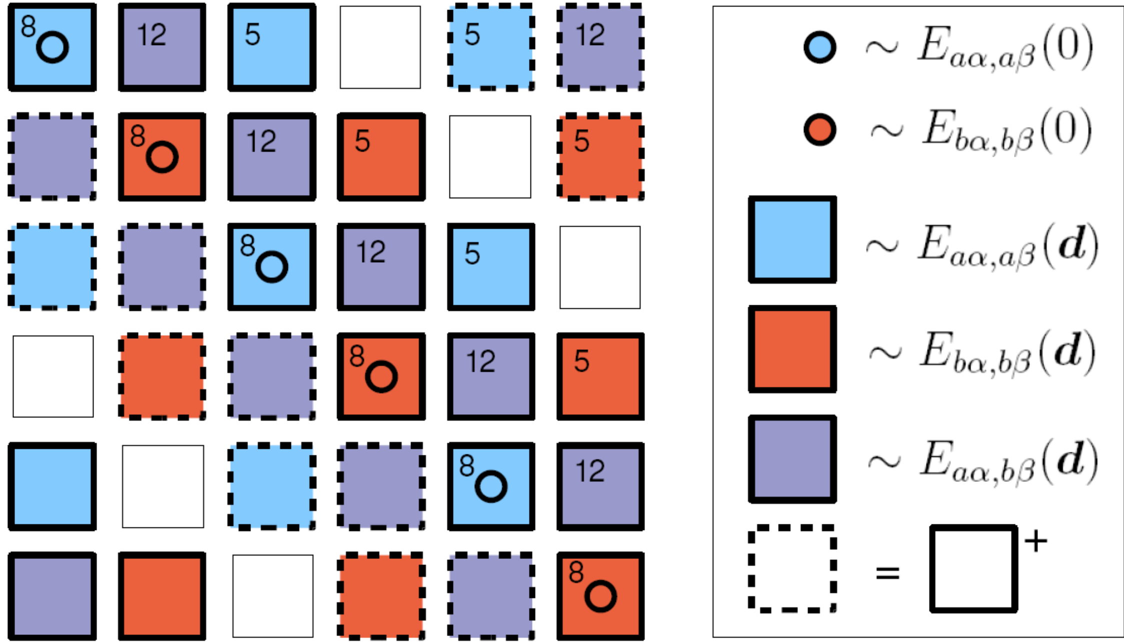

Figure 2.4: An example the block structure of a Hamiltonian matrix (2.50) describing a system of 6 alternating monoatomic layers of two types with periodic boundary conditions. Each layer consists of one type of atom (one atom per the 2D unit cell); the two types of atom/layer are labelled a and b. Each block in the schema represents an 18×18 matrix with indices α and β running through the atomic orbitals. The circles represent the on-site terms which are diagonal in α and β. The squares represent the matrix elements $H_{a\alpha,b\beta}(\boldsymbol{k})$ with fixed atom index a and b, the colour of a square encodes different sets of S-K parameters $V_{\alpha\beta\gamma}(\boldsymbol{d})$ given by the origin of the hybridising orbitals, note that even square blocks of the same colour can differ numerically as the sum in $H_{a\alpha,b\beta}(\boldsymbol{k})$ considers different neighbours; the numbers in the upper left corners of the squares correspond to number of neighbouring atomic sites in the particular layer considered in sum of Eq. (2.50) in case of an fcc lattice with hybridisation of the 1st, 2nd, and 3rd nearest neighbours. The dashed edge of a square with layer indices ij represents Hermitian conjugation to block with layer indices ji. The three blocks in the upper right and lower left corner of the schema correspond to the periodic boundary conditions - hybridisation of the first two and last two sites on the diagonal (the top and bottom layers). If we considered more localised atomic orbitals (hybridisation only to the 1st nearest neighbours) only the violet off-diagonal blocks would suffice.

2.2.3 Parametrisation

Our goal is to describe the ground state properties of transition-metal systems so our minimal basis set is restricted to the atomic orbitals s, p, and d as mentioned earlier. One might think that the on-site and two-centre integrals could be calculated using the tabulated atomic wave functions and estimated potentials. Parameters resulting in much better physical predictions are obtained by empirical methods or by fitting the LCAO band structures to ab-initio calculations.

There are several strategies of parametrising larger groups of standard solids which

range from very simple and therefore universal ones to extensive and less transferable parametrisations giving much more accurate predictions. The transferability of the parameters is crucial to our work as we aim to study systems consisting of different atoms and crystal structures obtained by epitaxial growth which often do not occur naturally for a particular metal. Although, our predictions are not expected to reach the quantitative reliability of ab-initio calculations, we aim to predict subtle quantities such as the anisotropy in density of states in layered multi-element systems. Therefore, starting with a parametrisation giving very accurate results on the level of elemental solids is desirable.

We start our LCAO study by comparing three different parametrisations. All of them use the two-centre Slater-Koster approximation which makes the parameters independent of the lattice structure. The first two follow the Harrison approach [41]. The "Harrison" parametrisation is the most simple and universal of the three. It considers an orthogonal basis set. Harrison expressed the two-centre Slater-Koster integrals $V_{\alpha\beta\gamma}(\boldsymbol{d})$ (using the muffin-tin orbital and pseudopotential theory [41]) as functions of the distance d, an effective radius of the d-orbital r_d which is characteristic to each transition metal, and constants $\eta_{\alpha\beta\gamma}$ which are universal for all elements and lattice structures:

$$\begin{aligned} V_{\alpha\beta\gamma}(d) &= \eta_{\alpha\beta\gamma}\frac{\hbar^2}{md^2}, \\ V_{\alpha d\gamma}(d) &= \eta_{\alpha d\gamma}\frac{\hbar^2 r_d^{3/2}}{md^{7/2}}, \\ V_{dd\gamma}(d) &= \eta_{dd\gamma}\frac{\hbar^2 r_d^3}{md^5}, \end{aligned} \tag{2.57}$$

where α and β run through the orbitals s and p and m is the free electron mass. Values of $\eta_{\alpha\beta\gamma}$ are listed in Appendix A.3. (Note that $V_{sp\gamma}(d)$ scales with $1/d^2 \sim k^2$ so the parameter can be understood as the kinetic energy of band electrons.) In case of transition metals, Harrison uses only the s and d orbitals so there are only two parameters specific to each element, the d-band width given by r_d and the on-site energy of the d-orbitals with respect to the s-orbitals. The parameters are optimised for summation of the interatomic matrix elements to the second nearest neighbours.

The "extended Harrison" parametrisation developed by Shi and Papaconstantopoulos [114] retains much of the universality of Harrison's parameters and improves significantly the accuracy of the results such as the band structure and DOS in transition, alkaline earth, and noble metals. This is accomplished by: (1) Replacing the atomic energies used as on-site parameters which is the main shortcoming of the Harrison's tables by on-site parameters fitted to Augmeted Plain Wave (APW) ab-initio calculations; (2) Including the p-orbitals into the basis set; (3) Modifying of the sp two-centre integrals, by introducing a dimensionless parameter γ_s as follows:

$$V_{\alpha\beta\gamma}(d) = \eta_{\alpha\beta\gamma}\frac{\gamma_s\hbar^2}{md^2}; \tag{2.58}$$

(4) Obtaining new prefactors $\eta_{\alpha\beta\gamma}$ and radii r_d by simultaneously fitting the APW energy bands of 12 transition metals at the equilibrium lattice constants of the structure, which is the ground state of the particular element, and included interactions of nearest, second-nearest, and third-nearest neighbours. The new parameters reproduce APW energy bands

and DOS remarkably well, not only for the 12 elements originally fitted, but also for the rest of the transition metals, the alkaline earth and the noble metals as shown in [114]. The Hamiltonian corresponds to an orthogonal basis set as in Harrison, on the other hand, the on-site and two-centre integrals are exchange-split in case of the ferromagnetic metals. We neglect this ferromagnetic splitting in case of the interatomic matrix elements in our modelling and keep it only in the on-site terms.

The "Mehl" parametrisation developed by Mehl and Papaconstantopoulos [92] resides almost on the opposite side of the spectrum compared to the simple and universal Harrison parametrisation, yet it retains limited transferability. A large set of free parameters is chosen to simultaneously fit band structures and total energies obtained by ab-initio calculations (APW or LAPW) for monoatomic fcc and bcc crystals. Similarly to Harrison, it offers an analytical form of the two-centre integrals but it uses a nonorthogonal basis set and the on-site terms change with the local environment:

$$E_{n\alpha,n\alpha}(0) = a_\alpha + b_\alpha \rho_n^{2/3} + c_\alpha \rho_n^{4/3} + d_\alpha \rho_n^2, \tag{2.59}$$

where α runs through the orbitals s, p, and d. ρ_n is an "embedded-atom-like density" describing the local environment of a particular atom indexed n.

$$\rho_n = \sum_m e^{-\lambda^2 d_{nm}} F(d_{nm}), \tag{2.60}$$

where the sum is over all of the atoms m within a range R_c of atom n, $d_{nm} = |R_n - R_m|$ is the interatomic distance, λ is a fitting parameter (squared to ensure that the contributions are greatest from the nearest neighbours), and $F(d)$ is a cut-off function $F(d) = 1/(1 + exp((d-R_c)/l+5))$. The parameters R_c and l are element specific but their typical values are $R_c = 16.5$ a.u. and $l = 0.5$ a.u. Depending on the structure and lattice constant, this radius will include 80 to 300 neighboring atoms. The two-centre S-K parameters have the form

$$V_{\alpha\beta\gamma}(d) = \left(e_{\alpha\beta\gamma} + f_{\alpha\beta\gamma} d + g_{\alpha\beta\gamma} d^2\right) exp(-h^2_{\alpha\beta\gamma} d) F(d). \tag{2.61}$$

Analogously, the two-centre S-K overlap parameters read

$$s_{\alpha\beta\gamma}(d) = \left(\delta_{\alpha\beta} + p_{\alpha\beta\gamma} + q_{\alpha\beta\gamma} d + r_{\alpha\beta\gamma} d^2\right) exp(-s^2_{\alpha\beta\gamma} d) F(d). \tag{2.62}$$

There are in total 73 parameters (polynomial coefficients) specifying the Slater-Koster tight-binding scheme for a given paramagnetic monoatomic solid (all coefficients available at http://cst-www.nrl.navy.mil/bind). In case of ferromagnetic metals, the number of on-site coefficients doubles. The explicit dependence of the S-K parameters on the interatomic distance facilitates their transferability to structures with different lattice constants or distorted geometry. However, the range of good reliability of the predictions is typically only approx. 0.5 Bohr radii. In our work, we follow the above procedure for elemental crystals of Fe, Co, and Pt, obtain the on-site and S-K parameters considering the nonorthogonal basis and approx. 300 nearest neighbours, and calculate the band structures as well as the magnetic anisotropy energy. The high number of neighbours and sensitivity to lattice structure makes this parametrisation prohibitively complicated to use in layered compounds.

Another extensive database of tight-binding parameters was provided by Papaconstantopoulos [91]. It comprises parameters for both the two-centre and three-centre integrals

in the orthogonal and nonorthogonal basis to the third nearest neighbours. We have not implemented this parametrisation into our modelling since its two-centre part is more complex (higher number of element-specific parameters) than the more recent and comparably accurate “extended Harrison” parametrisation.

We find the S-K parameters coupling two atoms with different chemical identity as a geometric average of the two elemental S-K parameters: $V^{ab}_{\alpha\beta\gamma} = \sqrt{V^{a}_{\alpha\beta\gamma} V^{b}_{\alpha\beta\gamma}}$. The same holds for the overlap parameters. The on-site parameters used in our calculations of bimetallic alloys are optimised to produce band structures in agreement with ab-initio calculations of monoatomic crystals of the constituents rather than the considered alloy. Different choice of averaging of the S-K parameters or further optimisation of the on-site parameters is beyond the initial phase of developing our tight-binding model of composite systems.

There are tight-binding parameters available for certain binary compounds, e.g., GaAs by Jancu et al. [47]. However, such parameters suffer from low relevance to systems with different lattice structure or even layered systems with arbitrary stacking of the atomic layers. (The Jancu parametrisation for GaAs gives directly the interatomic matrix elements for orbitals s, p, d, and s^* rather than the S-K parameters so the explicit dependence of the Hamiltonian on the interatomic distances is lost.)

2.2.4 Modelling of magnetic anisotropy

Following the same lines as in case of our effective Hamiltonian model we incorporate the atomic SOC introduced in Eq. (2.14) to make the band structure sensitive to the magnetisation direction with respect to the crystal geometry. The magnitude of the SOC depends on the orbital angular momentum of the atomic orbitals and it is tabulated for elemental metals [76].

The spin-orbit matrix has to be written in the basis of cubic harmonics for which the S-K parameters are typically tabulated. In analogy to Eq. (2.16), let us relate our basis of cubic harmonics to the angular momentum eigenstates for the p-orbital:

$$\begin{aligned} p_x &= \frac{1}{\sqrt{2}}\big(Y_1^{-1} - Y_1^{1}\big), \\ p_y &= \frac{i}{\sqrt{2}}\big(Y_1^{-1} + Y_1^{1}\big), \\ p_z &= Y_1^{0}, \end{aligned} \tag{2.63}$$

and for the d-orbital:

$$\begin{aligned} d_{xy} &= \frac{i}{\sqrt{2}}\big(Y_2^{-2} - Y_2^{2}\big), \\ d_{yz} &= \frac{i}{\sqrt{2}}\big(Y_2^{-1} + Y_2^{1}\big), \\ d_{xz} &= \frac{1}{\sqrt{2}}\big(Y_2^{-1} - Y_2^{1}\big), \\ d_{x^2-y^2} &= \frac{1}{\sqrt{2}}\big(Y_2^{-2} + Y_2^{2}\big), \\ d_{3z^2-r^2} &= Y_2^{0}, \end{aligned} \tag{2.64}$$

where Y_l^m are the spherical harmonics labelled by the total angular momentum l and its projection m. The orbital angular momentum matrices L_x, L_y, and L_z are typically derived in the basis of Y_l^m, so we have to consider a transformation $L_i' = TL_iT^\dagger$ to obtain the matrix

$$H^{SO}_{a\alpha,a\beta} = \frac{\lambda}{\hbar}\boldsymbol{\sigma} \cdot \boldsymbol{L}'_{\alpha\beta} \tag{2.65}$$

in the basis of cubic harmonics indexed by α and β (same notation as in Eq. (2.50)). λ denotes the SOC magnitude and $\boldsymbol{\sigma}$ is the vector of Pauli spin matrices. The matrix T for orbitals p and d reads

$$T_p = \frac{1}{\sqrt{2}}\begin{bmatrix} -1 & 0 & 1 \\ i & 0 & i \\ 0 & \sqrt{2} & 0 \end{bmatrix}, T_d = \frac{1}{\sqrt{2}}\begin{bmatrix} -i & 0 & 0 & 0 & i \\ 0 & i & 0 & i & 0 \\ 0 & -1 & 0 & 1 & 0 \\ 1 & 0 & 0 & 0 & 1 \\ 0 & 0 & \sqrt{2} & 0 & 0 \end{bmatrix}, \tag{2.66}$$

where the functions Y_l^m are ordered from $m = l$ (first column) to $m = -l$ (last column). The resulting spin-orbit matrix for the p-orbital reads

$$H_p^{SO} = \lambda_p \left[\begin{array}{ccc|ccc} 0 & i & 0 & 0 & 0 & 1 \\ -i & 0 & 0 & 0 & 0 & i \\ 0 & 0 & 0 & -1 & -i & 0 \\ \hline 0 & 0 & -1 & 0 & -i & 0 \\ 0 & 0 & i & i & 0 & 0 \\ 1 & -i & 0 & 0 & 0 & 0 \end{array}\right]. \tag{2.67}$$

For the d-orbital we obtain

$$H_d^{SO} = \lambda_d \left[\begin{array}{ccccc|ccccc} 0 & 0 & 0 & -2i & 0 & 0 & 1 & i & 0 & 0 \\ 0 & 0 & -i & 0 & 0 & -1 & 0 & 0 & i & i\sqrt{3} \\ 0 & i & 0 & 0 & 0 & -i & 0 & 0 & -1 & \sqrt{3} \\ 2i & 0 & 0 & 0 & 0 & 0 & -i & 1 & 0 & 0 \\ 0 & 0 & 0 & 0 & 0 & 0 & -i\sqrt{3} & -\sqrt{3} & 0 & 0 \\ \hline 0 & -1 & i & 0 & 0 & 0 & 0 & 0 & 2i & 0 \\ 1 & 0 & 0 & i & i\sqrt{3} & 0 & 0 & i & 0 & 0 \\ -i & 0 & 0 & 1 & -\sqrt{3} & 0 & -i & 0 & 0 & 0 \\ 0 & -i & -1 & 0 & 0 & -2i & 0 & 0 & 0 & 0 \\ 0 & -i\sqrt{3} & \sqrt{3} & 0 & 0 & 0 & 0 & 0 & 0 & 0 \end{array}\right], \tag{2.68}$$

where the first and second diagonal blocks correspond to spin up and down ($S_z = \pm 1/2$), respectively. The total H^{SO} matrix is added to the on-site Hamiltonian terms, whereas the interatomic matrix elements remain unchanged.

Ferromagnetic solids can be parametrised by different values of on-site or S-K parameters for the two spin states as mentioned in the previous subsection. In all three parametrisations considered in this work the spin quantisation axis is assumed to have arbitrary orientation (absence of SOC). However, we introduce the SOC to obtain the magnetocrystalline anisotropy. The alignment of the magnetisation direction with respect to the crystal becomes relevant. We set our coordinate systems in the orbital space

and in the spin space to coincide and have the z-axis perpendicular to the described atomic layers. We add a term to our Hamiltonian which depends on the magnetisation direction in the following way:

$$H^{exch}_{a\alpha,a\beta}(\hat{\boldsymbol{m}}) = \Delta E_{a\alpha,a\beta}\hat{\boldsymbol{m}}\cdot\boldsymbol{\sigma}, \tag{2.69}$$

where $\Delta E_{a\alpha,a\beta} = E_{a\alpha\uparrow,a\beta\uparrow} - E_{a\alpha\downarrow,a\beta\downarrow}$ (difference of the on-site or interatomic matrix elements for opposite magnetisation directions) and $\hat{\boldsymbol{m}}$ is the magnetisation unit vector. Including $H^{exch}(\hat{\boldsymbol{m}})$ allows for simultaneous rotation of magnetic moments with constant magnitudes present on each ferromagnetic atom site. Our exchange splitting is therefore symmetric around the paramagnetic band energy and independent on the k-vector. This approximation is not ideal in case of band ferromagnets but we consider it a good starting point for our simulations. Moreover, we neglect the contribution of the exchange-split S-K parameters, which would increase the numerical complexity of the calculation and keep only the on-site energy splitting:

$$H^{exch}_{a\alpha,a\alpha}(\hat{\boldsymbol{m}}) = \Delta E_{a\alpha,a\alpha}\begin{bmatrix} m_z & m_x - im_y \\ m_x + im_y & m_z \end{bmatrix}. \tag{2.70}$$

2.2.5 Integration in k-space

The physical quantities of our interest such as the MAE and ADOS are obtained from the band structure by integration in the reciprocal space. In contrast to (Ga,Mn)As, the integration has to consider the full Brillouin zone ($B.z.$). In general, we evaluate numerically the following integrals:

$$I(E) = \frac{1}{NV_{B.z.}}\sum_{i=1}^{18N}\int_{B.z.} d\boldsymbol{k} f_i(\boldsymbol{k})\delta(E - E_i(\boldsymbol{k})), \tag{2.71}$$

$$J(E) = \frac{1}{NV_{B.z.}}\sum_{i=1}^{18N}\int_{B.z.} d\boldsymbol{k} f_i(\boldsymbol{k})\theta(E - E_i(\boldsymbol{k})), \tag{2.72}$$

where the sum is over all eigenstates of the Hamiltonian. We have 18 atomic orbitals in our basis including spin. N is the number of inequivalent atoms or layers and $V_{B.z.}$ is the volume of the Brillouin zone, hence, the results are quantified per atom or layer. ($\delta(E)$ selects only states with eigenvalues equal to E and $\theta(E)$ selects all states from the lowest band up to E.) If the scalar function $f_i(\boldsymbol{k})$ is set to unity then $I(E)$ becomes the DOS and $J(E_F)$ enumerates the occupied states in the ground state with Fermi energy E_F. If $f_i(\boldsymbol{k}) = E_i(\boldsymbol{k})$ then $J(E_F)$ gives the total energy of the ground state. We find MAE as a difference in total energies obtained for two different magnetisation directions. Note that our model does not consider any finite temperature effects.

The formalism above allows for straight forward calculation of expectation values of any operator $S(\boldsymbol{k})$ which is diagonal in k-vector (or k independent such as the spin operator) and its matrix elements are known in the basis of cubic harmonics. We can then set $f_i(\boldsymbol{k}) = \langle\xi_i(\boldsymbol{k})|S(\boldsymbol{k})|\xi_i(\boldsymbol{k})\rangle$, where ξ_i are the eigenvectors of the tight-binding Hamiltonian.

Finally, quantities specific to fractions of the whole system such as spin up/down density of states or local DOS can be readily evaluated using a projector P onto the basis states belonging to the chosen spin polarisation or layer:

$$f_i(\boldsymbol{k}) = \langle \xi_i(\boldsymbol{k}) | P S(\boldsymbol{k}) P^{\dagger} | \xi_i(\boldsymbol{k}) \rangle. \tag{2.73}$$

E.g., a diagonal matrix with $P_{ii} = 1$ for $1 \leq i \leq 9$ and $P_{ii} = 0$ otherwise together with $S(\boldsymbol{k}) = \mathbf{1}$ correspond to spin-up-DOS of the first monoatomic layer. ADOS at an interface of a metal and a tunnel barrier is a ground state property related to the TAMR.

2.3 Shape anisotropy

We conclude this theoretical modelling chapter by briefly discussing the role of shape anisotropy in microstructures and compare its magnitude to the magnetocrystalline anisotropy in case of (Ga,Mn)As.

Magnetic shape anisotropy is due to the long range dipolar interaction. Surface divergence of magnetisation $\mathbf{M}$ gives rise to demagnetising field $\mathbf{H}^D(\mathbf{M}, \mathbf{r})$. In homogeneously magnetised bodies of general shape the demagnetising field is a function of magnetisation magnitude and direction with respect to the sample. In ellipsoidal bodies the function becomes linear in $\mathbf{M}$ and $\mathbf{H}^D(\mathbf{M})$ is uniform in the body:

$$H_i^D(\mathbf{M}) = -\sum_j N_{ij} M_j. \tag{2.74}$$

Tensor N_{ij} is the so called demagnetising factor. In rectangular prisms the linear formula (2.74) is a good approximation and the non-uniform demagnetising factor can be replaced by its spatial average. For the magnetostatic energy density of a homogeneously magnetised rectangular prism we get:

$$E^D(\mathbf{M}) = -\frac{1}{2}\mu \sum_{ij} N_{ij}(a, b, c) M_i M_j, \tag{2.75}$$

where we assume a prism extending over the volume $-a < x < a$, $-b < y < b$ and $-c < z < c$ in a Cartesian coordinate system. Ref. [2] shows the expression for $N_{ij}(a, b, c)$ in such prism.

Fig. 2.5 shows the calculated shape anisotropy energy $E_A = E^D(M_1) - E^D(M_2)$ for a (i) thin film with $a = b > c$ and with magnetisation out-of-plane or in-plane ($M_1 = (0, 0, M)$, $M_2 = (M, 0, 0)$), and (ii) for a bar with $a > b \sim c$ and with magnetisation in-plane ($M_1 = (0, M, 0)$, $M_2 = (M, 0, 0)$). In the former case the shape anisotropy favours in-plane easy axis direction while in the latter case the easy axis tends to align along the bar.

As a result of the relatively low saturation magnetisation of the DMSs, the in-plane vs. out-of-plane shape anisotropy E_A is only about 1.4 kJ/m^3 (0.06 T) for Mn doping $x = 5\%$ and $c < a/100$. This is in agreement with the limit of infinite two-dimensional sheet, where the formula for shape anisotropy energy per unit volume simplifies to $E_A = \frac{\mu_0}{2}\mathbf{M}^2 \cos^2 \theta$. θ is the angle that the saturation magnetisation $\mathbf{M}$ subtends to the plane normal. The

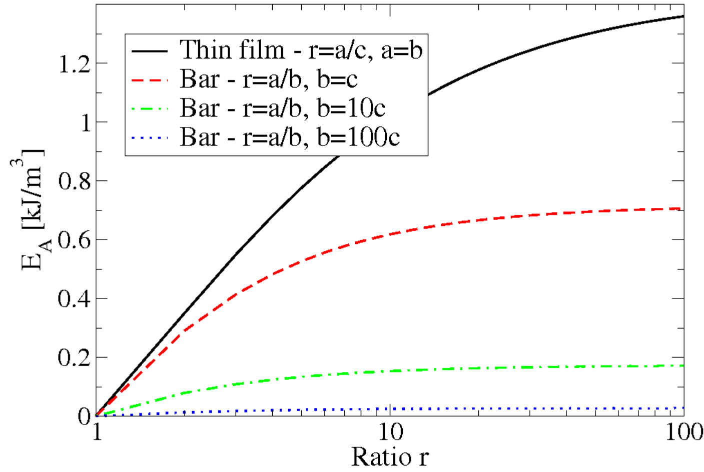

Figure 2.5: Shape anisotropy $E_A = E^D(M_1) - E^D(M_2)$ of a film of a thickness c and a long bar of length a and width b as a function of the dimension-less ratio r as defined in the caption. The curves were obtained using the demagnetising factor approximation of Ref. [2] for $|\mathbf{M}| = 0.06$T which corresponds to Mn doping of $x = 5\%$ at $T = 0$K.

in-plane anisotropy of a bar is even weaker and decreases with relative widening of the bar.

In general, the shape anisotropies in the (Ga,Mn)As dilute-moment ferromagnet are weak compared to the SOC induced magnetocrystalline anisotropies and can be often neglected. In the dense-moment metal ferromagnet structures the shape anisotropy can play an important role. Nevertheless in structures containing the strongly spin-orbit coupled Pt we consider, the magnetocrystalline anisotropy will typically dominate as in the case of (Ga,Mn)As.

Chapter 3

Results and analysis

3.1 Overview of theoretical results in (Ga,Mn)As and comparison to experiments

A large amount of experimental data on magnetic anisotropy in (Ga,Mn)As has accumulated over the past years. Comparison of these results with predictions of the effective Hamiltonian model is not straightforward due to the presence of unintentional compensating defects in (Ga,Mn)As epilayers. Most importantly, a fraction of Mn is incorporated in interstitial positions. These impurities tend to form pairs with Mn_{Ga} acceptors in as-grown systems with approximately zero net moment of the pair, resulting in an effective local-moment doping $x_{eff} = x_s - x_i$ [57]. Here x_s and x_i are partial concentrations of substitutional and interstitial Mn, respectively. In as-grown materials, the partial concentration x_i increases with the total Mn concentration, $x_{tot} = x_s + x_i$. For $x_{tot} > 1.5\%$, $dx_i/dx \approx 0.2$ [57]. We emphasise that in theory the Mn local-moment doping labelled as "x" corresponds to the density of uncompensated local moments, i.e., to x_{eff} in the notation used above. Mn doping "x" quoted in experimental works refers typically to the total nominal Mn doping, i.e., to x_{tot}. When comparing theory and experiment this distinction has to be considered.

Although interstitial Mn can be removed by low-temperature annealing, x_{eff} will remain smaller than the total nominal Mn doping. The interstitial Mn impurities are double donors. Assuming no other sources of charge compensation the hole density is given by $p = (x_s - 2x_i)4/a_0^3$ [57].

The concentration of ferromagnetically ordered Mn local moments and holes is not accurately controlled during growth or determined post growth [52]. We acknowledge this uncertainty when comparing available magnetometry results with theory. Throughout this section we test the relevance of our model over a wide parameter range, focusing on general trends rather than on matching results directly based on the material parameters assumed in the experimental papers.

3.1.1 In-plane vs. out-of-plane magnetic easy axis

In this subsection we study the switching between in-plane and perpendicular-to-plane directions of the magnetic easy axis. (Anisotropies within the growth plain of a sample

are studied in Subsec. 3.1.2.) Early experiments were suggesting that the in-plane vs. perpendicular-to-plane easy axis direction is determined exclusively by the sign of the growth induced strain in the sample. The in-plane easy axis (IEA) develops for compressive growth strain $e_0 = (a_s - a_0)/a_0 < 0$. Tensile growth strain, $e_0 > 0$, results in the perpendicular-to-plane easy axis (PEA). This simple picture was subsequently corrected by experimental results reported for example in Refs. [109, 111, 134, 135]. Sign changes in the magnetic anisotropy for the same sign of the growth strain were observed with varying Mn concentration, hole density, and temperature.

An overview of theoretical easy axis reorientations driven by changes in the material parameters is given in Fig. 3.1. In the plots we show the difference ΔE between total hole energy density for the magnetisation lying in-plane ($E_{tot}(M_{||})$) and out of plane ($E_{tot}(M_{\perp})$) as a function of the hole density and temperature. ($E_{tot}(M_{||})$ is always the smaller of E_{tot} for magnetisation along the [100] and the [110] axis.) We include calculations for four Mn local-moment concentrations to facilitate the comparison with experimental data of different nominal Mn concentrations and different degree of annealing, which also increases the number of uncompensated local moments as discussed above. We note that the calculated magnetocrystalline anisotropies are almost precisely linear in the growth strain and therefore the boundaries between IEA and PEA in Fig. 3.1 depend only very weakly on the magnitude of the growth strain, certainly up to the typical experimental values $|e_0| < 1\%$. magnetocrystalline anisotropy diagrams presented in this subsection for a compressive strain $e_0 = -0.2\%$ are therefore generic for all typical strains, with the IEA and PEA switching places for tensile strain.

Solid arrows in Fig. 3.1 mark easy axis behaviour as a function of temperature and doping that has been observed experimentally. The dashed arrows correspond to theoretical anisotropy variations that have not been observed experimentally. At low hole densities, increasing temperature (marked by arrow (1)) induces a reorientation of the easy axis from a perpendicular-to-plane to an in-plane direction. With decreasing x this transition shifts to lower hole densities; at $x = 2\%$ the theoretical densities allowing for such a transition reach unrealistically low values for a ferromagnetic (Ga,Mn)As material with metallic conduction. Warming up the partially compensated samples (marked by arrow (2)) has no reorientation effect and the easy axis stays in-plane. There are no exceptions to this behaviour at different Mn concentrations. Finally, increasing temperature of a very weakly compensated (fully annealed) sample can cause switching of the theoretical easy direction from in-plane to perpendicular-to-plane (marked by arrow(3)), with the exception of the low Mn concentrations.

The techniques used to increase the hole density in the experimental works discussed in this subsection are the postgrowth sample annealing and annealing followed by hydrogen passivation/depassivation [134]. The latter method yields solely a change in hole density, whereas the former is associated also with an increase in the effective Mn concentration and a decrease in the growth strain. The growth strain is caused to a large extent by Mn atoms in interstitial positions [73], which are removed by the annealing. The simultaneous increase of hole density and effective Mn concentration due to annealing implies a transfer between the phase diagrams of Fig. 3.1 accompanying the transitions marked by arrows (4) - (6). We argue that the remarkable similarity of the four diagrams assures a meaningful qualitative comparison with the effect of annealing even within a given diagram.

We now discuss individual measurements and compare with theoretical diagrams in

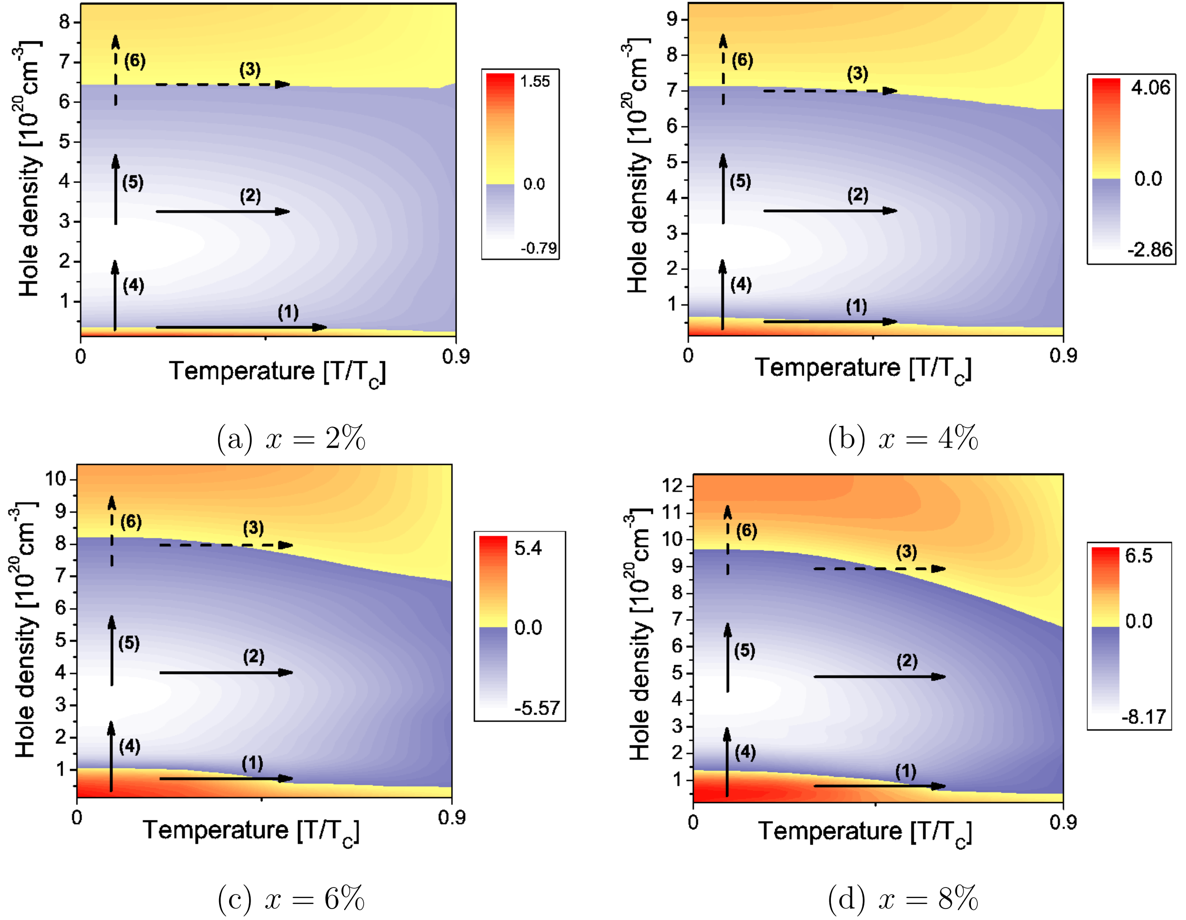

Figure 3.1: Anisotropy energy $\Delta E = E(M_{||}) - E(M_{\perp})$ [kJm^{-3}] calculated for $e_0 = -0.2\%$, $e_{xy} = 0$, and four Mn concentrations. Positive(negative) ΔE corresponds to PEA(IEA). Arrows mark anisotropy transitions driven by change of temperature or hole density.

Fig. 3.1. Ref. [134] reports experiments in a 50 nm thick (Ga,Mn)As epilayer nominally doped to $x = 6-7\%$ and grown on a GaAs substrate under compressive strain. The sample is first annealed to lower the number of interstitial Mn, then hydrogenated to passivate virtually all itinerant holes, and finally depassivated in subsequent steps by annealing. The hole density was not measured, but for the given Mn doping we expect the density in the range of $p \sim 10^{20} - 10^{21}\text{cm}^{-3}$ after depassivation. The low temperature ($T =$ 4 K) reorientation from PEA to IEA induced by successive depassivations and detected indirectly by anomalous Hall effect measurement in Ref. [134] matches the transition marked by arrow (4) in Fig. 3.1(b)-(d).

Magnetic hysteresis loops measured by the Hall resistivity in Ref. [135] reveal easy axis reorientations induced by annealing or increasing temperature in material with nominal Mn doping $x = 7\%$. This (Ga,Mn)As epilayer was grown on a (In,Ga)As buffer which leads to a tensile strain. (Recall that the anisotropy energy ΔE is an odd function of the growth strain so the IEA and PEA regions have to be interchanged in Fig. 3.1 when considering tensile strain.) Again, the hole density is not known and can be estimated to $p \sim 10^{20} - 10^{21}\text{cm}^{-3}$. After annealing, the material exhibits perpendicular-to-plane easy axis at 4 K and no reorientation occurs during heating up to 115 K ($T_C \approx 120 - 130$ K

in this material). Such behaviour corresponds to arrow (2) of Fig. 3.1(c) or (d). The as-grown sample has IEA at 4 K and PEA at 22 K. This easy axis reorientation corresponds to arrow (1), again considering a tensile strain. The as-grown and annealed samples both share PEA at elevated temperature. Such a stability of the easy axis while changing the hole density corresponds to arrow (5). Theoretical anisotropy variations described by arrows (3) and (6) are not observed in Ref. [135]

Ref. [109] presents measurements in compressively strained (Ga,Mn)As epilayers grown on a GaAs substrate. The reported nominal Mn concentrations are $x = 5.3\%$ and $x = 3\%$ with compressive growth strain $e_0 = -0.27\%$ and $e_0 = -0.16\%$, respectively, as inferred from x-ray diffraction measurement of the lattice parameter. The higher doped material was partially annealed for several different annealing times. The hole density was not measured but likely increases substantially with annealing. The as-grown $x = 5.3\%$ sample at 5 K exhibits PEA, which changes to IEA upon warming up to 22 K. This anisotropy variation is not observed for samples subject to long annealing times. Such a result is consistent with Ref. [135] and corresponds to the theoretical predictions marked by arrows (1) and (2) of Fig. 3.1(b) for increasing temperature of the as-grown and annealed samples, respectively. Again, the effect of annealing is in good agreement with anisotropy behaviour predicted for low (high) temperature represented by arrow (4) (arrow (5)), however, there is no experimental counterpart of transitions marked by arrows (3) and (6). The sample doped to $x = 3\%$ was not annealed and no transition from PEA to IEA is observed upon warming. The behaviour corresponds to arrow (2) in Fig. 3.1(a) or (b).

Ref. [108] already reports a successful comparison of measured magnetic anisotropy and theoretical predictions [26]. Among other samples, it presents a compressively strained (Ga,Mn)As epilayer with nominal Mn concentration $x = 2.3\%$ (inferred from x-ray diffraction measurement). A superconducting quantum interference device (SQUID) measurement of this as-grown sample shows PEA at 5 K and IEA at 25 K, corresponding to anisotropy variation marked by arrow (1) in Fig. 3.1(a) (occurring only for a very narrow hole density interval).

Ref. [67] presents (Ga,Mn)As epilayers with compressive and tensile strain grown on GaAs and (In,Ga)As buffers, respectively, with nominal Mn concentration $x = 3\%$ inferred from reflection high energy electron diffraction (RHEED) oscillations measured during the MBE growth. Two of the samples were annealed and magnetic anisotropy was investigated at 5 K. The tensile strained sample has its easy axis aligned perpendicular to the growth plane and the compressively strained sample has an in-plane easy axis. This observation is in good agreement with our theoretical modelling.

We conclude this subsection by discussing magnetic anisotropies in low doped ferromagnetic (Ga,Mn)As samples which are in the vicinity and on both sides of the transition into a degenerate semiconductor. Transport measurements [54] in the epitaxial (Ga,Mn)As reveal insulating characteristics and the presence of the impurity band for $x \lesssim 0.1\%$. For higher concentrations, $0.5 \lesssim x \lesssim 1.5\%$, no clear signatures of activation from the valence band to the impurity band have been detected in the dc transport, suggesting that the bands have merged, yet the materials remain insulating. When the Mn doping reaches $\approx 1.5\%$, low-temperature conductivity of the film increases abruptly by several orders of magnitude and the system in bulk turns into a degenerate semiconductor. The onset of ferromagnetism occurs on the insulating side of the transition at $x \approx 1\%$.

Magnetocrystalline anisotropy has been measured in an insulating ferromagnetic (Ga,Mn)As/GaAs sample nominally doped to 1% and in an already metallic sample doped to 1.5% (Ref. [137]), and in another insulating but ferromagnetic material with nominal 1.1% doping (Ref. [140]). Note that annealing has only a little effect on magnetic properties in these low doped materials. SQUID measurements in the 1% and 1.1% doped materials reveal PEA for all temperatures below T_C. In the 1.5% doped sample, a transition from PEA to IEA was observed near T_C. All these observations are consistent with our theory results in low doped samples, as shown in Fig. 3.1(a).

Magnetic properties of (Ga,Mn)As epilayers in the vicinity of the metal insulator transition have not yet been thoroughly investigated. The results discussed above nevertheless confirm the perception that magnetic interactions are established on much shorter length scales than the macroscopic scales governing transport properties. Magnetic anisotropy is then expected to evolve smoothly across the metal-insulator transition, as seen in the above experimental data, and our theory has therefore a merit for ferromagnetic (Ga,Mn)As on both sides of the transition. Its quantitative reliability should however not be overstated in the vicinity and on the insulating side of the transition.

3.1.2 In-plane anisotropy: Competition of cubic and uniaxial components

As we discussed in the previous subsection, the magnetic easy axis(axes) is in the plane of (Ga,Mn)As/GaAs films over a wide range of dopings. Experimental works in bare (Ga,Mn)As epilayers discussed in this subsection show that the in-plane magnetic anisotropy has cubic and uniaxial components. Typically, the strongest uniaxial term is along the in-plane diagonal ([110]/[1$\bar{1}$0]) direction. (A weak uniaxial component along the main crystal axes ([100]/[010]) has also been detected [94, 36].) The theoretical model used so far to describe the easy axis reorientation between the in-plane and out-of-plane alignment, assuming the growth strain, can account only for the cubic in-plane anisotropy component. In this case we find two easy axes perpendicular to each other either along the main crystal axes or along the diagonals depending on the Mn concentration and hole density, as shown in Fig. 3.2. In order to account for the uniaxial component of the in-plane [110]/[1$\bar{1}$0] anisotropy in bare (Ga,Mn)As epilayers the elastic shear strain e_{xy} is incorporated into our model as discussed in Sec. 2.1. (For brevity we omit the index "int" in the following text and reintroduce the index only when additional real in-plane strains are present due to micro-patterning or attached piezo-stressors.) The superposition of the two components results in a rich phenomenology of magnetic easy axis alignments as reviewed in Figs. 3.3 - 3.5.

Fig. 3.3 shows an example with easy axes aligned close to the main crystal axes [100] and [010] at Mn local-moment concentration $x = 5\%$, hole density $p = 3 \times 10^{20}\text{cm}^{-3}$, and a weak shear strain $e_{xy} = 0.01\%$. For a stronger shear strain $e_{xy} = 0.03\%$ the cubic anisotropy is no longer dominant and the easy axes "rotate" symmetrically towards the diagonal [1$\bar{1}$0] direction until they merge for $e_{xy} \gtrsim 0.05\%$. As explained in detail in Sec. 2.1, the magnitude and sign of the intrinsic shear strain e_{xy} enter as free parameters when modelling in-plane anisotropies of bare epilayers.

The relative strength of uniaxial and cubic anisotropy terms depends also on the hole density and Mn concentration as shown by Fig. 3.4 and 3.5, respectively. Both

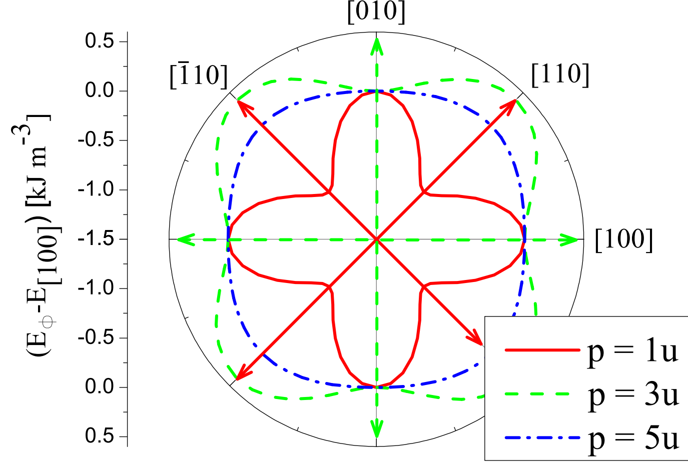

Figure 3.2: Magnetic anisotropy energy $\Delta E = E_\phi - E_{[100]}$ as a function of the in-plane magnetisation orientation $\mathbf{M} = |\mathbf{M}|[\cos\phi, \sin\phi, 0]$ and its dependence on material parameters. Magnetic easy axes (marked by arrows) change their direction upon change of hole density p given in units $\mathrm{u} \equiv 10^{20}$ cm^{-3} at Mn local-moment concentration $x = 5\%$, shear strain $e_{xy} = 0$, and zero temperature.

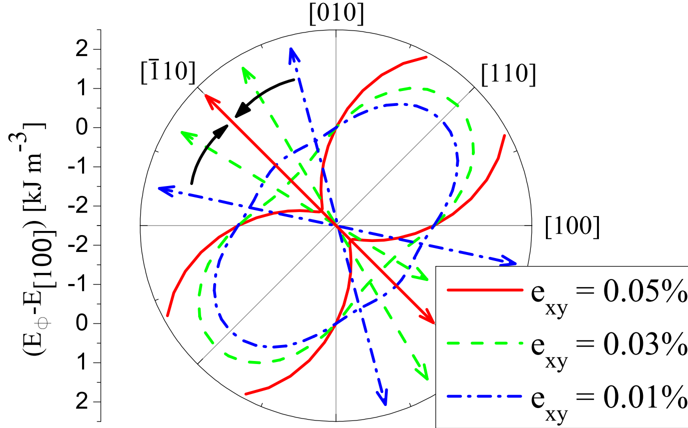

Figure 3.3: Magnetic anisotropy energy $\Delta E = E_\phi - E_{[100]}$ as a function of the in-plane magnetisation orientation $\mathbf{M} = |\mathbf{M}|[\cos\phi, \sin\phi, 0]$ and its dependence on material parameters. Magnetic easy axes (marked by arrows) change their direction upon change of magnitude of shear strain $e_{xy} > 0$ at Mn local-moment concentration $x = 5\%$, hole density $p = 3 \times 10^{20}$ cm^{-3}, and zero temperature.

anisotropies are non-monotonous functions of x and p, compared to the linear dependence of uniaxial anisotropy on the shear strain. We do not show explicitly the effect of increasing temperature which in the mean-field theory is equivalent to decreasing the effective Mn concentration while keeping the hole density constant (as explained in Sec. 2.1).

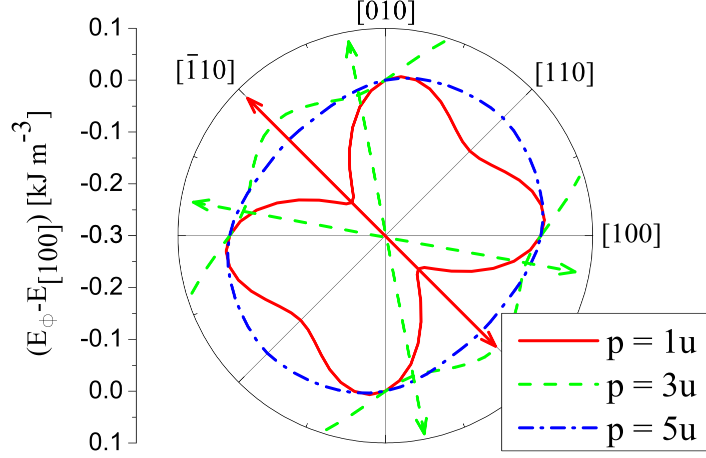

Figure 3.4: Magnetic anisotropy energy $\Delta E = E_\phi - E_{[100]}$ as a function of the in-plane magnetisation orientation $\mathbf{M} = |\mathbf{M}|[\cos\phi, \sin\phi, 0]$ and its dependence on material parameters. Magnetic easy axes (marked by arrows) change their direction upon change of hole density p given in units $\mathrm{u} \equiv 10^{20}$ cm^{-3}, at Mn local-moment concentration $x = 3\%$, shear strain $e_{xy} = 0.01\%$, and zero temperature.

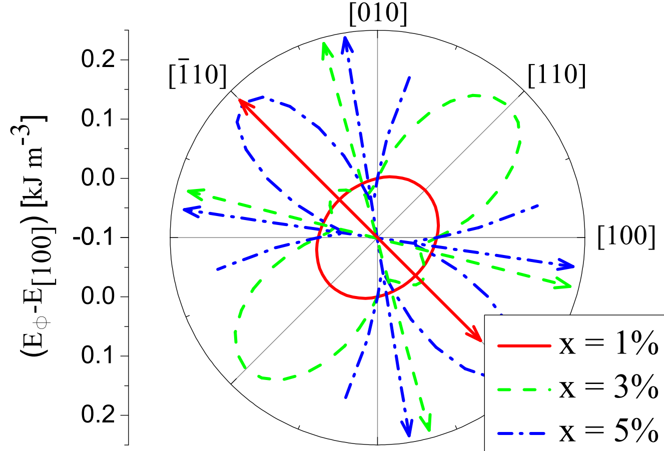

Figure 3.5: Magnetic anisotropy energy $\Delta E = E_\phi - E_{[100]}$ as a function of the in-plane magnetisation orientation $\mathbf{M} = |\mathbf{M}|[\cos\phi, \sin\phi, 0]$ and its dependence on material parameters. Magnetic easy axes (marked by arrows) change their direction upon change of Mn local-moment concentration x at hole density $p = 3 \times 10^{20}$ cm^{-3}, shear strain $e_{xy} = 0.01\%$, and zero temperature.

We begin the comparison of theory and experiment by analysing experimental studies of in-plane magnetic anisotropy in bare samples without lithographically or piezoelectrically induced in-plane uniaxial strain. Experimental results are summarised in Tab. 3.1. Samples are identified by nominal Mn concentration and hole density or anneal-

ing as given by the authors. Typically, the hole density is in the range 10^{20} - 10^{21}cm^{-3}. All samples are thin (Ga,Mn)As epilayers deposited by MBE on a GaAs substrate. According to our calculations, the compressive growth strain has a negligible effect on the interplay of cubic and uniaxial in-plane anisotropies.

Tab. 3.1 shows the largest measured projection of the easy axis (axes) on the main crystal directions ([100], [010], [110], and [$1\bar{1}0$]) in the corresponding sample. (Note that unlike our theoretical calculations of the full in-plane anisotropy profile, most experiments listed in Tab. 3.1 report only projections of the magnetisation to the main crystal directions. Studies using anisotropic magneto-resistance (AMR) to map the easy axis direction precisely are discussed in Subsec. 3.1.3 and 3.1.4.) Tab. 3.1 includes a column labelled as EA_{lT} giving the largest easy axis projection at low temperatures (typically 4 K) and a column labelled as EA_{hT} corresponding to measurements at temperatures close to T_C. This simplified overview of the temperature-dependence of the in-plane anisotropies reflects the nature of available experimental data. The ferromagnetic resonance (FMR) spectra are typically provided only at one high and one low temperature. Moreover, available SQUID data reveal at most one transition between main crystal directions corresponding to the largest projection of the magnetisation in the whole temperature interval. Sample 25 in Tab. 3.1 which shows two transitions is the only exception to this trend.

From Tab. 3.1 we infer the following general trend in the experimentally observed in-plane anisotropies: At low temperatures the in-plane anisotropy is dominated by its cubic component. In most cases, this leads to two equivalent easy axes aligned close to [100] and [010] directions. Only in a few samples the cubic anisotropy yields easy axis directions along the [110]/[$1\bar{1}0$] diagonals at low temperature. The two diagonals are not equivalent, however, due to the additional uniaxial anisotropy component [126, 40, 86, 140]. At high temperatures the uniaxial anisotropy dominates giving rise to only one diagonal easy axis. Finally we note that Refs. [146], and [133] do not identify the correspondence between the in-plane diagonal easy axis and one of the two non-equivalent crystallographic axes [110] and [$1\bar{1}0$] (these measurements are marked as $\otimes$ in Tab. 3.1). This ambiguity does not affect the comparison with our modelling of unpatterned bare films since the shear strain e_{xy} determining which of the two diagonals is magnetically easier is a free effective parameter of the theory. Possibility of error in assigning the two non-equivalent diagonal crystallographic axes is acknowledged by the authors of Ref. [109], where switching roles of the diagonals makes the results consistent with later works of the group.

Following the strategy for presenting experimental data in Tab. 3.1, we plot in Figs. 3.6 and 3.7 theoretical diagrams indicating crystallographic axes ([100],[110] or [$1\bar{1}0$]) with the largest projection of magnetisation as a function of the hole density and temperature. The comparison with experimental results in Tab. 3.1 is facilitated by numbered arrows added to the diagrams, which correspond to switchings between crystallographic directions with the largest projection of the easy axis, driven by increasing temperature (horizontal arrows) and hole density (vertical arrows).

Fig. 3.6 presents diagrams for different Mn concentrations and for $e_{xy} = 0.01\%$. Anisotropy transitions seen in the figures are consistent with majority of the reviewed experimental works, *i.e.*, the arrows correspond to the experimentally observed transitions and their placement in the diagrams is reasonably close to the relevant experimental parameters. Fig. 3.6 also demonstrates how the transition from the [100] to the [$1\bar{1}0$] direction moves to higher temperatures with increasing Mn local-moment concentration.

No.	Ref.	x[%]	p[*]	EA$_{lT}$	EA$_{hT}$	Fig.	A$_p$	A$_{lT}$	A$_{hT}$
1.	[110]	2	ag	+	$\nwarrow$	3.7(a)	(1)	(2)	(3)
2.	[110]	2	an	+	$\nwarrow$	3.7(a)	(1)		
3.	[142]	2	3.5	+	$\nwarrow$	3.7(a)	(1)		
4.	[146]	2	ag	+	$\otimes$	3.7(a)	(1)		
5.	[66]	2	1.1	+	$\nearrow$	3.7(a)	$(1)^n$		
6.	[39]	2	4	+	$\nearrow$	3.7(a)	$(1)^n$		
7.	[109]	3	ag	+	$\nwarrow$	3.6(a)	(1)		
8.	[145]	3	ag	+	$\nearrow$	3.6(a)	$(1)^n$		
9.	[40]	4	3.5	+		3.6(a)		(2)	
10.	[40]	4	5	+		3.6(a)			
11.	[140]	5	ag	+	$\nwarrow$	3.6(b)	(2)	(5)	(6)
12.	[140]	5	an	$\nearrow$	$\nearrow$	3.6(b)	(3)		
13.	[110]	5	ag	+	$\nwarrow$	3.6(b)	(2)	(4)	(6)
14.	[110]	5	an	+	$\nearrow$	3.6(b)	$(2)^n$		
15.	[126]	6	ag	+	$\nwarrow$	3.6(b)	(2)	(5)	(6)
16.	[126]	6	an	$\nearrow$	$\nearrow$	3.6(b)	(3)		
17.	[133]	7	0.75	+	$\otimes$	3.6(c)	(3)		
18.	[133]	7	2	+	$\otimes$	3.6(c)	(3)		
19.	[133]	7	8.8	+	$\otimes$	3.6(c)	(4)		
20.	[133]	7	12	+	$\otimes$	3.6(c)	(4)		
21.	[40]	7	3.6	+		3.6(c)		(6)	
22.	[40]	7	11	$\nearrow$		3.6(c)			
23.	[86]	8	ag	+	$\nwarrow$	3.7(b)	(1)	(3)	(4)
24.	[86]	8	an	$\nwarrow$	$\nwarrow$	3.7(b)	(2)		
25.	[110]	8	an	+	$\nearrow$	3.6(d)	(4)		

Table 3.1: Experimental in-plane magnetocrystalline anisotropies at low temperature EA_{lT}, and high temperature EA_{hT} extracted from SQUID or FMR measurements: largest easy axis projection along [100] and [010] axes (+), along [1$\bar{1}$0] axis ($\nwarrow$), along [110] axis ($\nearrow$), and along one of the [110]/[1$\bar{1}$0] diagonals not distinguished in the experiment ($\otimes$). Nominal Mn concentrations x reported in experimental studies are rounded down to percents. Hole density p [*] is given in units of 10^{20}cm^{-3}. If the hole density is unknown the as-grown and annealed samples are indicated by "ag" and "an", respectively. Samples are ordered according to Mn concentration and hole density (annealed sample follows the as-grown counterpart when it exists). The last four columns label the experimental data in a way which facilitates direct comparison with transitions highlighted by arrows in the theory Figs. 3.6 and 3.7. Numbers in columns A$_p$, A$_{lT}$, and A$_{hT}$ point to corresponding theory transitions marked by horizontal arrows, vertical arrows at low T, and vertical arrows at high T, respectively. The index ^{n} indicates correspondence of the given arrow to modelling with negative value of e_{xy}.

Fig. 3.7 address samples where the observed transition cannot be modelled by $e_{xy} = 0.01\%$. Four of the low doped samples in Refs. [110, 146, 142] are modelled by a weaker strain, whereas one of the highly doped samples in Ref. [86] is modelled by a stronger strain.

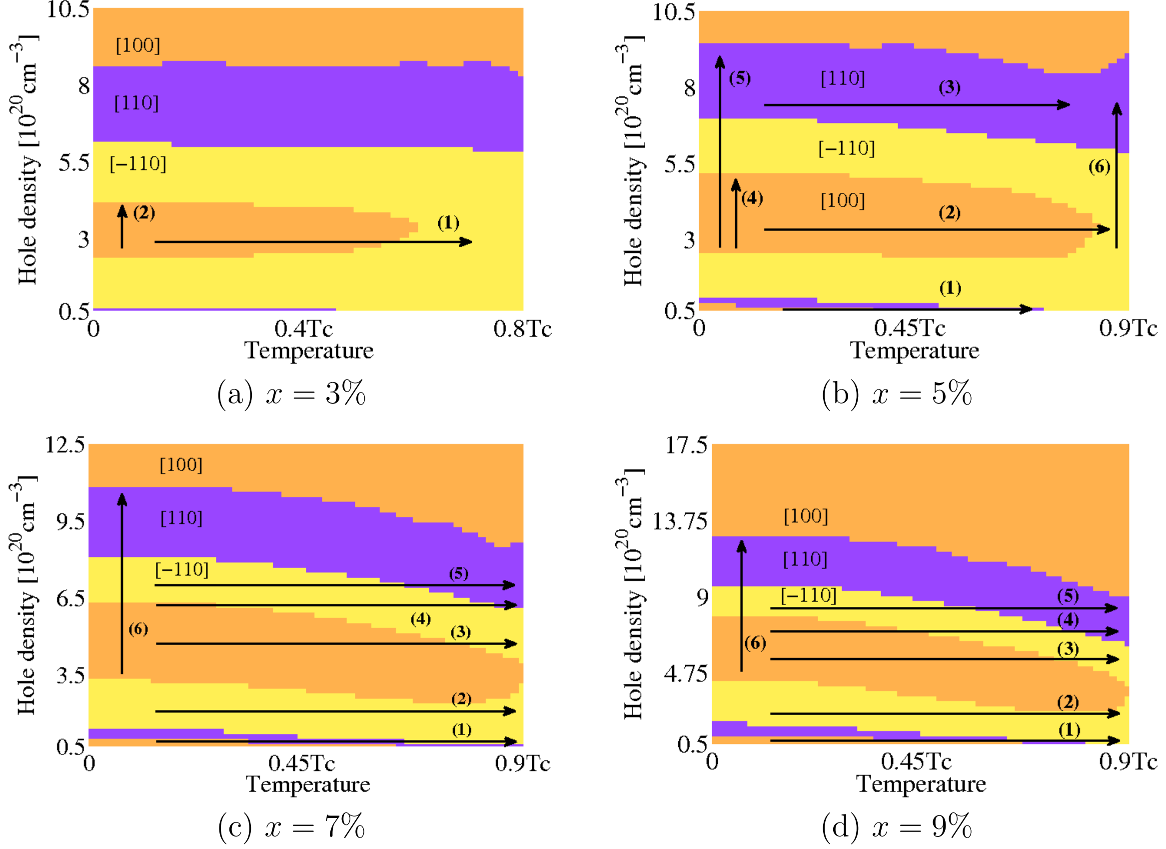

(a) $x = 3\%$ (b) $x = 5\%$ (c) $x = 7\%$ (d) $x = 9\%$

Figure 3.6: Theoretical hole density - temperature diagrams of crystal directions with the largest projection of the magnetic easy axis for $e_{xy} = 0.01\%$, $e_0 = -0.2\%$, and four Mn concentrations. Arrows mark anisotropy behaviour driven by change of temperature or hole density explaining experimentally observed behaviour surveyed in Tab. 3.1.

Now we discuss in detail the theoretical diagrams in Fig. 3.6 and compare to individual samples from Table 3.1, referred to as T3.1-No. Fig. 3.6(a) maps in-plane magnetic anisotropy at Mn local-moment concentration $x = 3\%$ and shear strain $e_{xy} = 0.01\%$. The easy axis reorientation of the as-grown sample T3.1-7 corresponds to arrow (1) in Fig. 3.6(a). Arrow (2) in Fig. 3.6(a) highlights the finite range of hole densities for which the largest projection of the easy-axes stays along the [100] and [010] directions at low temperature, consistent with the behaviour of the as-grown and annealed samples T3.1-9 and T3.1-10. (Note that hole densities in samples T3.1-9 and T3.1-10 were measured by the electrochemical capacitance-voltage profiling.) The transition from the largest easy axis projection along the cube edges to the [110] diagonal observed in as-grown sample T3.1-8 with increasing temperature has no analogy in Fig. 3.6(a) or Fig. 3.6(a). The FMR measurement does not indicate switching of the easy axis alignment between the diagonals at any intermediate temperature. This behaviour can be explained only if the opposite

sign of the shear strain is used to model the intrinsic symmetry-breaking mechanism. Then the easy axis transition of T3.1-8 would correspond to arrow (1) in Fig. 3.6(a).

The behaviour of as-grown samples T3.1-11,13,15 corresponds to arrow (2) in Fig. 3.6(b). The annealed samples T3.1-12,16 exhibit the rarely experimentally observed domination of uniaxial anisotropy for the whole temperature range. This behaviour is also consistently captured by the theory as highlighted by arrow (3) in Fig. 3.6(b). Sample T3.1-14 has a dominant cubic anisotropy preferring [100]/[010] magnetisation directions at low temperature and the easy axis aligns closer to the [110] direction at high temperatures. Similarly to sample T3.1-8, this transition has no analogy in Fig. 3.6(a) or Fig. 3.6(b), however, it can be explained assuming that the [110]/[$1\bar{1}0$] symmetry-breaking mechanism has opposite sign in this material and therefore should be modelled by a negative value of the effective strain e_{xy}. Then the easy axis transition of T3.1-14 would correspond to arrow (2) in Fig. 3.6(b). Another possibility is to assume the same sign of e_{xy} as for the above samples and associate the transition in sample T3.1-14 with arrow (4) in Figs. 3.6(c) and 3.6(d). Note, however, that the intermediate-temperature anisotropy state with the largest magnetisation projection along the [$1\bar{1}0$] diagonal seen when following the theory trend along arrow (4) has not been reported in the experimental study of sample T3.1-14. Arrows (4)-(6) in Fig. 3.6(b) correspond to measured anisotropy behaviour driven by increasing hole density in pairs of as-grown and annealed samples T3.1-11,12, T3.1-13,14, and T3.1-15,16.

At the upper end of the investigated effective Mn concentration interval the theoretical alignment of magnetic easy axes is mapped by Figs. 3.6(c) and 3.6(d). Samples T3.1-17 to T3.1-20 nominally doped to $x = 7\%$ were all annealed after growth, passivated by hydrogen plasma, and then gradually depassivated to achieve different hole densities (measured by high-field Hall effect). Magnetic anisotropies were determined by FMR. The assignment of the in-plane diagonal directions to the non-equivalent [110] and [$1\bar{1}0$] crystallographic axes is not specified in this experimental work; recall that this ambiguity is not crucial for the present discussion. The transition observed in these samples from a cubic ([100]/[010] easy directions) dominated anisotropy at low temperatures to a uniaxial behaviour at high temperatures is captured by arrows (3) and (4) in Figs. 3.6(c) and 3.6(d). Importantly, the depassivated higher hole density samples T3.1-19 and T3.1-20 show an additional switching of the easy axis from one to the other diagonal direction at intermediate temperatures, consistent with the theoretical temperature dependence along arrow (4). This double transition behaviour was also detected in the annealed sample T3.1-25, where the temperature dependent magnetisation projections were measured by SQUID. In this experiment it is identified that the easy axis first rotates towards the [$1\bar{1}0$] direction at intermediate temperatures and then switches to the [110] direction at high temperatures, consistent with the behaviour marked by arrow (4) in Figs. 3.6(c) and 3.6(d).

Samples T3.1-21,22 are measured only at low temperature. Easy axis reorientation from the [100] direction to the [110] direction is driven by an increase in hole density, which corresponds to arrow (6) in Fig. 3.6(c) or 3.6(d). The hole density was measured by the electrochemical capacitance-voltage method.

In-plane anisotropies of samples with $x \approx 2\%$ are modelled in Fig. 3.7(a). To obtain the cubic anisotropy dominated region at low temperatures and a transition to the uniaxial behaviour at high temperatures, as observed in samples T3.1-1 to T3.1-6, we take for

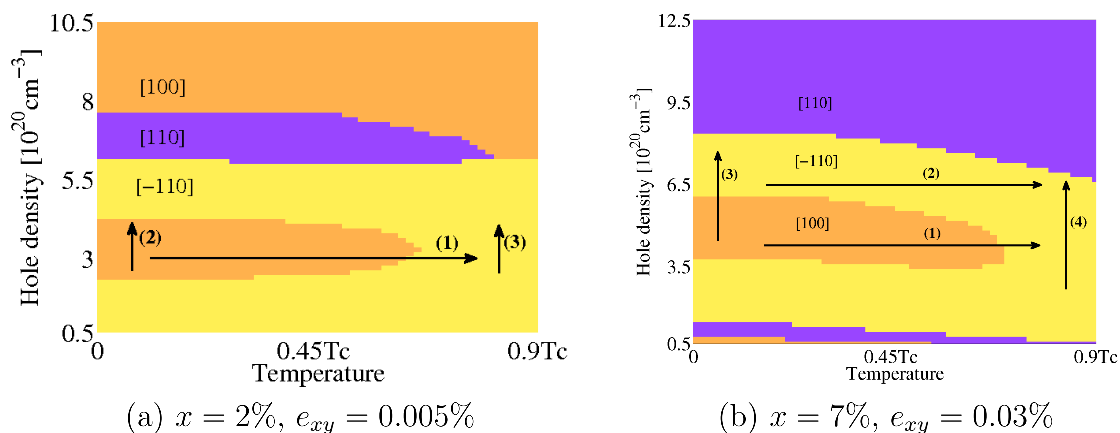

(a) $x = 2\%$, $e_{xy} = 0.005\%$ (b) $x = 7\%$, $e_{xy} = 0.03\%$

Figure 3.7: Theoretical hole density - temperature diagrams of crystal directions with the largest projection of the magnetic easy axis for $e_0 = -0.2\%$ and two combinations of x and e_{xy}. Arrows mark anisotropy behaviour driven by change of temperature or hole density explaining experimentally observed behaviour surveyed in Tab. 3.1.

this low Mn doping $e_{xy} = 0.005\%$. (The effective strain $e_{xy} = 0.01\%$ would lead to easy axis along $[1\bar{1}0]$ over the entire temperature range and for $e_{xy} = 0.001\%$ the cubic anisotropy region would extend up to very high temperatures.) Arrow (1) in Fig. 3.7(a) corresponds to easy axis switching from the [100] to the $[1\bar{1}0]$ direction in samples T3.1-1,2,3. Arrows (2) and (3) in Fig. 3.7(a) mark the behaviour of the easy axis driven by increasing hole density when annealing the sample T3.1-1 to obtain the sample T3.1-2 at low and high temperature, respectively. Sample T3.1-4 assumes the $[1\bar{1}0]$ diagonal always harder than the [110] diagonal. A transition from cubic to uniaxial dominated anisotropy is observed upon increasing the temperature. This behaviour corresponds to arrow (1) in Figs. 3.7(a). (The hole density of sample T3.1-3, $p = 3.5 \times 10^{20}\text{cm}^{-3}$, was determined by low-temperature high-field Hall effect measurements, however, it was not measured for samples T3.1-1,2,4.)

Samples T3.1-5 and T3.1-6 have their easy axis aligned closer to the [100]/[010] directions at low temperatures and to the [110] direction at higher temperatures, similarly to sample T3.1-8. The SQUID measurement of magnetisation projections for the whole range of temperature does not indicate the easy axis alignment close to the $[1\bar{1}0]$ direction at any intermediate temperature. The hole density of the sample T3.1-5, $p = 1.1 \times 10^{20}\text{cm}^{-3}$, is measured by Hall effect (at room temperature) and its Mn concentration is inferred from x-ray diffraction measurement of the lattice constant. The hole density of the sample T3.1-6 is $p = 4 \times 10^{20}$ cm^{-3} (measured by the electrochemical capacitance-voltage method at room temperature), and we estimate the Mn concentration from the reported critical temperature, $T_C = 62$ K, after annealing. The described experimental behaviour does not correspond to predicted anisotropy transitions for relevant hole densities, Mn local-moment concentrations, and positive shear strain. The behaviour can be explained, however, if the opposite sign of the shear strain is used to model the intrinsic symmetry-breaking mechanism at low Mn concentration. Then the easy axis transition of T3.1-5,6 would correspond to arrow (1) in Fig. 3.7(a).

Finally we comment on the less frequent behaviour observed in the annealed sample

T3.1-24. While its as-grown counterpart T3.1-23 shows the commonly seen transition from the cubic dominated anisotropy to the uniaxial anisotropy with increasing temperature, marked by arrow (1) in Fig. 3.7(b), the annealed material has its easy axis aligned close to the $[1\bar{1}0]$ direction over the entire studied temperature range. Arrow (2) in Fig. 3.7(b) provides an interpretation of this behaviour if we increase the magnitude of the effective shear strain. At $e_{xy} = 0.03\%$ the cubic anisotropy dominated region is already strongly diminished and for $e_{xy} = 0.05\%$ it vanishes completely. Arrows (3) and (4) then highlight within the same diagram the consistent description of the evolution of the experimental anisotropies, both at low and high temperatures, from the as-grown low hole density sample T3.1-23 to the annealed high hole density sample T3.1-24.

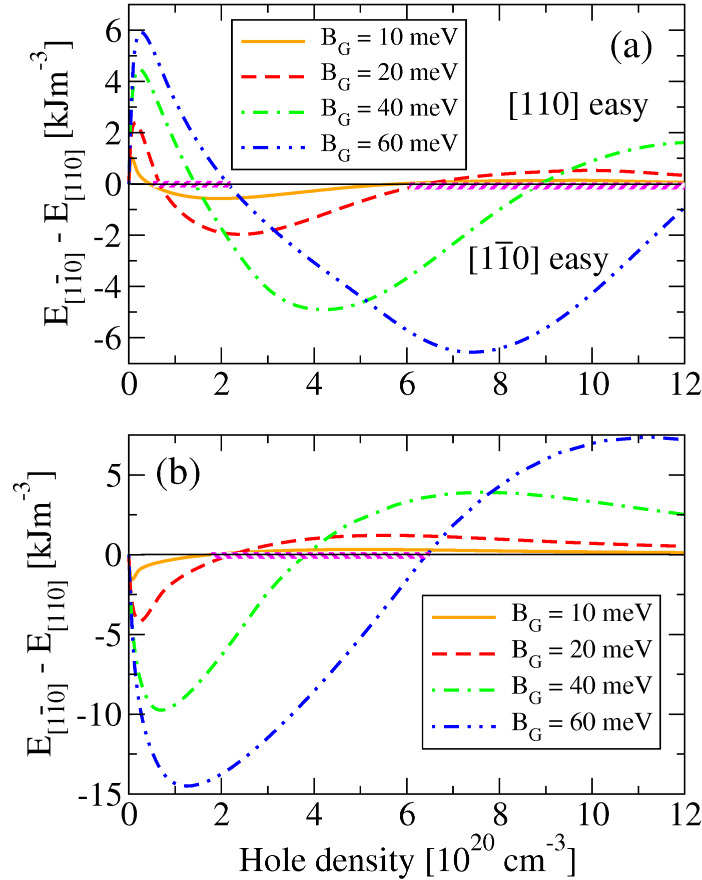

Figure 3.8: In-plane uniaxial anisotropy as a function hole density at zero temperature, $e_{xy} = 0.05\%$, and $e_0 = 0$ calculated in this work (a) and in Ref. [110] (b). Curves are labelled by the valence-band spin-splitting parameter $B_G \equiv J_{pd}N_{Mn}S/6$ to allow for simple comparison with Ref. [110]. ($B_G = 4.98x$ in meV and in percent, respectively.) Dashed intervals of the horizontal axis mark regions where a change of temperature (inversely proportional to B_G) can lead to the $[\bar{1}10] \leftrightarrow [110]$ easy axis reorientation.

To summarise this subsection, our theoretical modelling provides a consistent overall picture of the rich phenomenology of magnetocrystalline anisotropies in unpatterned (Ga,Mn)As epilayers. Our understanding is limited, however, to only a semiquantitative level, owing to the approximate nature of the mean-field kinetic-exchange model, ambiguities in experimental material parameters of the studied films, and unknown mi-

croscopic origin of the in-plane uniaxial symmetry-breaking mechanism. We remark that the effective shear strain we include to phenomenologically account for the experimental $[110]/[1\bar{1}0]$ uniaxial anisotropy scales with Mn doping ($e_{xy} \simeq 0.005x$). It brings additional confidence in this modelling approach as it is most likely the incorporation of Mn which breaks the cubic symmetry of the lattice. The magnitude of the effective strain parameter falls into the range $0.005\% < e_{xy} < 0.05\%$ and the anisotropy behaviour consistent with most experimental works is modelled with positive sign of e_{xy}.

We conclude this subsection by a remark on numerical simulations of the [110] to $[1\bar{1}0]$ easy axis transition performed in Ref. [110]. The physical model employed by the authors of Ref. [110] is identical to ours, nevertheless, the results of the calculations do not quantitatively match ours, as illustrated in Fig. 3.8. We have clarified with the authors of Ref. [110] the numerical origin of the discrepancy. This helpful exercise has provided an independent confirmation of the accuracy, within the applied physical model, of the theoretical results presented in this work. (To compare Fig. 3.8 to the original plot in Ref. [110] use the conversion to units of normalised anisotropy field $H_{un}/M = 2(E_{[1\bar{1}0]} - E_{[110]})/(\mu_0 M^2)$.)

3.1.3 Anisotropy fields

Having analysed the in-plane and out-of-plane anisotropies based on the direction of easy axes, we turn our attention to the relative strength of the anisotropy components, i.e., to the anisotropy energies. The components of magnetocrystalline anisotropy can be described in terms of a simple phenomenological model separating the free energy density $F(\hat{M})$ into components of distinct symmetry. Each component is described by a periodic function with a corresponding coefficient. We find that angular dependencies of the energies obtained from our microscopic modelling can be approximated accurately even in the first and second orders of expansion into periodic functions of uniaxial and cubic symmetry, respectively.

The coefficients can be determined experimentally, e.g., by analysing the FMR spectra [133, 66, 65, 67], from AMR [22, 89] or by fitting SQUID magnetometry data to an appropriate phenomenological formula for anisotropy energy [142, 86]. In this subsection we extract the relevant coefficients from the calculated anisotropies, track their dependence on material parameters and compare theory to experiment on this level.

We start with identifying the types of anisotropy terms considered in our expansion of the anisotropy energy. The cubic anisotropy due to the crystal symmetry of the zinc-blende structure is described using terms invariant under permutation of the coordinate indices x, y, and z. The independent first-, second- and third-order cubic terms read: $K_{c1}\left(n_x^2 n_y^2 + n_x^2 n_z^2 + n_z^2 n_y^2\right)$, $K_{c2}\left(n_x^2 n_y^2 n_z^2\right)$, and $K_{c3}\left(n_x^4 n_y^4 + n_x^4 n_z^4 + n_y^4 n_z^4\right)$, respectively, where $n_x = \cos\phi \sin\theta$, $n_y = \sin\phi \sin\theta$, and $n_z = \cos\theta$ are components of the magnetisation unit vector $\hat{M}$ (the angles θ and ϕ are measured from the [001] and [100] axis, respectively). See Appendix A.1 for details on the mutual independence of all cubic terms.

As mentioned in previous subsections, the cubic anisotropy of the host crystal lattice is accompanied by different types of uniaxial anisotropy. A generic term corresponding to uniaxial anisotropy along a given unit vector $\hat{U}$ depends on the even powers of the dot product $(\hat{M} \cdot \hat{U})$. The first- and second-order terms read: $K_{u1}(\hat{M} \cdot \hat{U})^2$ and $K_{u2}(\hat{M} \cdot \hat{U})^4$.

The particular cases of uniaxial anisotropy terms and their correspondence to lattice strains will be described later in this subsection.

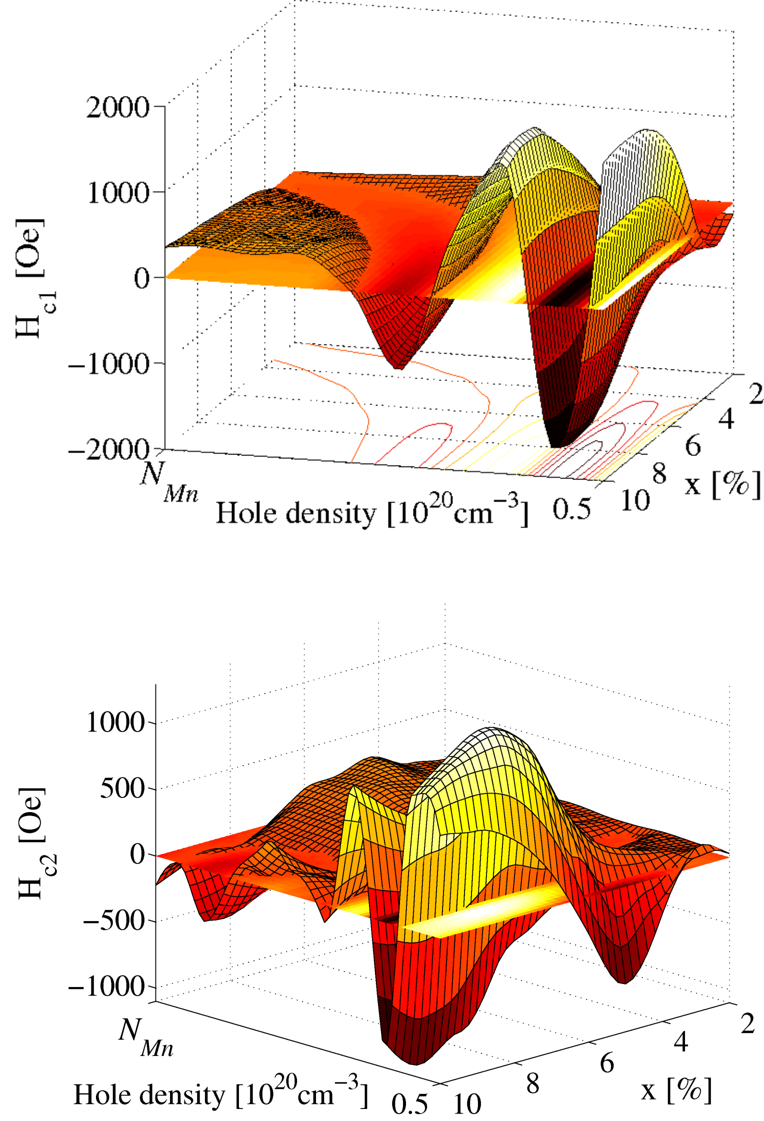

Figure 3.9: Lowest-order cubic anisotropy field H_{c1} and second-order cubic anisotropy field H_{c2} calculated as functions of hole density p (up to zero compensation $p = N_{Mn}$) and Mn local-moment concentration x at zero temperature;

Before we present the calculated values of the cubic anisotropy coefficient, we introduce the so called anisotropy fields, which are often used in literature instead of the energy coefficients. In this subsection we plot the anisotropy fields in Oersteds (Oe) to make the comparison with experiment more convenient. The relation of the anisotropy fields H_a to the energy coefficients K_a reads: $H_a = 2K_a/M$.

Fig. 3.9 shows H_{c1} and H_{c2} as functions of hole density p and Mn local-moment concentration x at zero temperature. Both coefficients oscillate as function of the hole density p. As discussed in detail in Ref. [1] the anisotropies tend to weaken with increasing

population of higher bands, which give competing contributions. Consistent with this trend the amplitude of the oscillations increases with increasing x and decreasing p. The upper limit of the hole density $p = N_{Mn}$ corresponds to no charge compensation (recall, $N_{Mn} \approx 2.21x$ in 10^{20}cm^{-3} for x in percent).

Our modelling predicts the extremal magnitude of the second-order cubic term H_{c2} a factor of two smaller than the extremal magnitude of the first-order term H_{c1}. Upon increasing the hole density the amplitude of oscillations of H_{c2} decreases faster than in case of H_{c1}. The third-order cubic anisotropy field H_{c3} is negligible compared to H_{c1} and H_{c2} for all studied combinations of the material parameters. To our knowledge, H_{c2} and H_{c3} have not been resolved experimentally. We emphasise that the second-order cubic term does not contribute to the anisotropy energy for magnetisation vectors not belonging to the main crystal plains. The dependence of all three calculated cubic terms on the lattice strains of typical magnitudes (up to 1%) is negligible.

Now, we focus on classification of distinct uniaxial anisotropy components and their relation to lattice strains lowering the underlying cubic symmetry of the zinc-blende structure. We have already mentioned that typically the strongest symmetry-breaking mechanism is the growth strain (introduced in Sec. 2.1). It is relevant for the in-plane versus out-of-plane alignment of the magnetic easy axis. We have also mentioned the in-plane uniaxial anisotropy between the [110] and the [1$\bar{1}$0] axes. Its origin is not known, however, we have modelled it using the shear strain which is about a factor of ten weaker than the typical growth strain.

Some (Ga,Mn)As epilayers [94, 36] also show a very weakly broken symmetry between the main crystal axes [100] and [010]. We will introduce here a uniaxial strain that can account for this type of anisotropy; however, our main motivation for introducing this third strain tensor is to complete an in-plane strain basis. This basis is used in Subsec. 3.1.4 to describe all types of lattice in-plane strains induced experimentally by growth and post-growth processing of the (Ga,Mn)As epilayers. Once the strain tensors and corresponding anisotropy contributions to the free energy are introduced, it will be shown that the chosen basis has the advantage of collinearity of the strain and of the resulting anisotropy component. Finally, in this subsection the numerical data and comparison with experiment will be presented for the bare unpatterned epilayers. The patterned structures will be discussed in Subsec. 3.1.4.

First, we recall the growth strain introduced in Eq. (2.21). It is usually referred to as the biaxial pseudomorphic strain as it is due to the lattice mismatch between the substrate and the epilayer. The doped crystal is forced to certain dimensions by the substrate in the two in-plane directions whereas it can relax in the perpendicular-to-plane direction, keeping the requirement of zero net force acting on the crystal: $0 = c_{12}e_{xx} + c_{12}e_{yy} + c_{11}e_{zz}$. The corresponding strain tensor

$$\mathbf{e}^g = \begin{pmatrix} e_0 & 0 & 0 \\ 0 & e_0 & 0 \\ 0 & 0 & -2\frac{c_{12}}{c_{11}}e_0 \end{pmatrix} \quad (3.1)$$

describes an expansion (contraction) along the [100] and [010] axes for positive (negative) e_0 accompanied by a contraction (expansion) along the [001] axis. Parameters c_{11} and c_{12} are the elastic moduli. The growth strain enters our model via the strain Hamiltonian

$\mathcal{H}^{str}$ (see Eq. (2.1)) and induces a uniaxial anisotropy component, which can be described in the lowest order by an energy term $-K_{[001]}n_z^2 = -K_{[001]}\cos^2\theta$.

The shear strain, first introduced in Subsec. 2.1.2, is represented by a tensor

$$\mathbf{e}^s = \begin{pmatrix} 0 & \kappa & 0 \\ \kappa & 0 & 0 \\ 0 & 0 & 0 \end{pmatrix}. \tag{3.2}$$

Positive (negative) κ corresponds to turning a square into a diamond with the longer (shorter) diagonal along the [110] axis. We have used this type of strain as the "intrinsic" shear strain e_{xy}^{int} to model the difference in energy for magnetisation aligned with the two in-plane diagonals. It results in uniaxial anisotropy along the diagonals, described in analogy to the growth strain by a term $-K_{[110]}(n_y - n_x)^2/2 = -K_{[110]}\sin^2(\phi - \pi/4)\sin^2\theta$.

Finally, we write down the third element of the in-plane strain basis,

$$\mathbf{e}^u = \begin{pmatrix} \lambda & 0 & 0 \\ 0 & -\lambda & 0 \\ 0 & 0 & 0 \end{pmatrix}. \tag{3.3}$$

Positive (negative) λ corresponds to turning a square into a rectangle where expansion (contraction) along the [100] axis is accompanied by a contraction (expansion) along the [010] axis of the same magnitude. Much like in case of the growth strain and the shear strain, the requirement of zero net force acting on the crystal is kept but this time it results in $e_{zz} = 0$. The strain $\mathbf{e}^u$ induces uniaxial anisotropy along the main crystal axes, described by a term $-K_{[100]}n_y^2 = -K_{[100]}\sin^2\phi\sin^2\theta$.

Let us remark that strain tensors in Eqs. (3.1)-(3.3) are expressed in Cartesian coordinates fixed to the main crystallographic axes. Strains $\mathbf{e}^s$ and $\mathbf{e}^u$ for $\kappa = \lambda$ are related by a rotation about the [001] axis by $\pi/4$; however, the cubic crystal is not invariant under such rotation so the two strains induce anisotropies with magnitudes $K_{[100]}$ and $K_{[110]}$, which are different in general. The growth strain $\mathbf{e}^g$, the shear strain $\mathbf{e}^s$, and the uniaxial strain $\mathbf{e}^u$ can be characterised by a single direction of deformation and induce uniaxial anisotropy components aligned with that particular direction. We found that higher-order uniaxial terms are small unless we approach experimentally unrealistic large values of exchange splitting (large x) and hole compensation (low p).

In total, we can write our phenomenological formula approximating accurately the calculated free-energy density of an originally cubic system subject to three types of strain as a sum of distinct anisotropy components

$$\begin{aligned} F(\hat{M}) &= K_{c1}\left(n_x^2 n_y^2 + n_x^2 n_z^2 + n_z^2 n_y^2\right) + K_{c2}\left(n_x^2 n_y^2 n_z^2\right) - \\ &- K_{[001]}n_z^2 - \frac{K_{[110]}}{2}(n_y - n_x)^2 - K_{[100]}n_y^2. \end{aligned} \tag{3.4}$$

By definition of the terms, a positive coefficient $K_{[001]}$ prefers perpendicular-to-plane easy axis (PEA); positive $K_{[110]}$ and $K_{[100]}$ prefer easy axis lying in-plane (IEA) aligned closer to $[1\bar{1}0]$ and [010] axis, respectively. Note that the anisotropy terms entering the phenomenological formula follow a sign convention consistent with existing literature [133, 66, 65, 67].

We now provide the microscopic justification for the choice of the elements $\mathbf{e}^s$ and $\mathbf{e}^u$ of the in-plane strain basis and corresponding phenomenological uniaxial terms. This will be

based on symmetries of the Kohn-Luttinger Hamiltonian $\mathcal{H}^{KL}$ and the strain Hamiltonian $\mathcal{H}^{str}$ as shown in Eqs. (2.19) and (2.34), respectively, which relates the band structure to a general in-plane strain with the components e_{xx}, e_{yy}, and e_{xy}.

First let us point out that the basis element $\mathbf{e}^g$ (the growth strain) is invariant under rotation about the [001] axis and according to our calculation does not influence the in-plane direction of the easy axis (in the linear regime of small deformations). We continue by showing that for $\mathbf{e}^s$ and $\mathbf{e}^u$, the strains and the corresponding magnetocrystalline anisotropy components are indeed collinear and that this collinearity applies only for the special cases of uniaxial symmetries along the in-plane diagonals or main axes. Let us assume a rotation of the tensor $\mathbf{e}^u$ by an arbitrary angle φ about the [001] axis,

$$\begin{aligned}\mathbf{e}^u(\varphi) &= R_\varphi^T \begin{pmatrix} \lambda & 0 & 0 \\ 0 & -\lambda & 0 \\ 0 & 0 & 0 \end{pmatrix} R_\varphi \\ &= \begin{pmatrix} \lambda\cos 2\varphi & \lambda\sin 2\varphi & 0 \\ \lambda\sin 2\varphi & -\lambda\cos 2\varphi & 0 \\ 0 & 0 & 0 \end{pmatrix},\end{aligned} \tag{3.5}$$

where R_φ is the rotation matrix and φ is measured from the [100] axis. (The same analysis applies to a rotation of $\mathbf{e}^s$). The parameters $e_{xx} = -e_{yy} = \lambda\cos 2\varphi$ and $e_{xy} = \lambda\sin 2\varphi$ enter the strain Hamiltonian (see Eq. (2.34) in the Appendix) only via the matrix element:

$$\begin{aligned}c^s &= \frac{a_2}{2}\sqrt{3}(e_{yy} - e_{xx}) + i a_3 e_{xy} \\ &= -\lambda\left[a_2\sqrt{3}\cos 2\varphi - i a_3 \sin 2\varphi\right],\end{aligned} \tag{3.6}$$

where $a_2\sqrt{3} \neq a_3$ are strain Luttinger constants. Moreover, the strain component e_{xy} quantifying the shear strain enters only $\mathrm{Im}(c^s)$, whereas the components $e_{xx} = -e_{yy}$ enter only $\mathrm{Re}(c^s)$. According to our calculation the imaginary and real part of c^s generate independent uniaxial anisotropy components along the [110] and [100] axis, respectively. Their combined effect can be understood based on an analogy of the in-plane rotation of the strain tensor $\mathbf{e}^u$ and an in-plane rotation of a k-vector.

As mentioned in Sec. 2.1 the Kohn-Luttinger Hamiltonian $\mathcal{H}^{KL}$ and the strain Hamiltonian $\mathcal{H}^{str}$ have the same structure. We write here explicitly the matrix component c of the Hamiltonian $\mathcal{H}^{KL}$ analogous to c^s as a function of the in-plane angle of the k-vector $\mathbf{k} = |\mathbf{k}|[\cos\phi, \sin\phi, 0]$. The element reads:

$$\begin{aligned}c &= \frac{\sqrt{3}\hbar^2}{2m}\left[\gamma_2(k_x^2 - k_y^2) - 2i(\gamma_3 k_x k_y)\right] \\ &= \frac{\sqrt{3}\hbar^2}{2m}k^2\left[\gamma_2\cos 2\phi - i\gamma_3\sin 2\phi\right],\end{aligned} \tag{3.7}$$

where again $\gamma_2 \neq \gamma_3$ are Luttinger constants describing a cubic crystal. For $\gamma_2 = \gamma_3$ the Hamiltonian $\mathcal{H}^{KL}$ has spherical symmetry. Similarly, if $a_2\sqrt{3} = a_3$, the strain Hamiltonian $\mathcal{H}^{str}$ is spherically symmetric and the contributions of $\mathrm{Im}(c^s)$ and $\mathrm{Re}(c^s)$ to the anisotropy of the system combine in such a way that the resulting uniaxial term is collinear with the strain $\mathbf{e}^u(\varphi)$ rotated with respect to the crystallographic axes by an arbitrary in-plane angle φ.

Clearly, the underlying cubic symmetry of the host crystal causes a non-collinearity of the uniaxial strain along a general in-plane direction and the corresponding anisotropy component. Moreover, the misalignment is a function of Mn local-moment concentration, hole density and temperature. We discuss further this misalignment in more detail in Subsec. 3.1.4. Here we point out the distinct exception when φ is an integer multiple of $\pi/4$ and either the real or the imaginary part of c^s vanish rendering the strain Hamiltonian effectively spherically symmetric. We choose quite naturally the simple forms of $\mathbf{e}^u(\varphi)$ with $\varphi = 0$ and $\varphi = \pi/4$ as elements of the in-plane strain basis. For a different choice of the basis elements than in Eqs. (3.2) and (3.3), setting up the phenomenological formula would be more complicated.

We can now resume our discussion of the interplay of the cubic and uniaxial anisotropy components. Adding the uniaxial terms leads to rotation or imbalance of the original (cubic) easy axes as shown in Sec. 3.1.2 in Fig. 3.2.

Fig. 3.10 shows $H_{[110]} = 2K_{[110]}/M$ and $H_{[100]} = 2K_{[100]}/M$ as functions of hole density p and Mn local-moment concentration x at zero temperature. Both anisotropy fields depend on material parameters in a qualitatively very similar manner. Moreover, we observe similar dependence on the doping parameters also in case of the field $H_{[001]}$ (not plotted). All the three fields oscillate as functions of hole density. The period of the oscillation is longer than in case of H_{c1}. In general, the amplitude of the oscillations decreases with decreasing Mn local-moment concentration.

The uniaxial fields are linearly dependent on the strain from which they originate, unless the strains are very large ($> 1\%$). For the shear strain of the value $e_{xy} = \kappa \approx 0.01\%$, which is the typical magnitude in our modelling, and zero temperature, the extremal values of $H_{[110]}$ are an order of magnitude smaller than the extremal values of $H_{c1} \sim 10^3$ Oe. For typical compressive growth strain $e_0 \approx -0.2\%$ of an as-grown 5% Mn doped epilayer and zero temperature the extremal values of $H_{[001]}$ are of the same order as H_{c1}. When the magnitude of the uniaxial strain along [100] axis is set to $(e_{xx} - e_{yy})/2 = e_{xy}$, or equivalently $\kappa = \lambda$, $H_{[100]}$ is approximately a factor of two smaller than $H_{[110]}$.

To quantify the observed similarity in the calculated dependencies of the uniaxial anisotropy coefficients on x, p, and strains, we can write approximate relationships,

$$\begin{aligned} K_{[001]}(x,p,e_0) &\simeq q_{[001]}(x,p)e_0, \\ K_{[100]}(x,p,\lambda) &\simeq q_{[100]}(x,p)\lambda, \\ K_{[110]}(x,p,\kappa) &\simeq q_{[110]}(x,p)\kappa. \end{aligned} \tag{3.8}$$

Note, that each anisotropy component depends only on one type of strain, which is due to the choice of the basis in the strain space (see Eqs. (3.1)-(3.3)). (Such exclusive dependence of a particular uniaxial anisotropy component on the corresponding strain is, indeed, obtained also from simulations of systems subject to combinations of all three types of strain.) The linearity of anisotropy coefficients as functions of lattice strains is limited to small elastic deformations of the lattice. The approximation cannot be used for strains greater than 1% as revealed also by calculations in Ref. [26]. Experiment confirms the linear behaviour in case of the growth strain up to $e_0 \approx \pm 0.3\%$ [22]. Linear dependence on in-plane uniaxial strains is corroborated by experiments discussed in Subsec. 3.1.4.

In addition to the linearity with respect to strain, we observe universal dependence of the three uniaxial anisotropy coefficients on hole density and Mn local-moment concen-

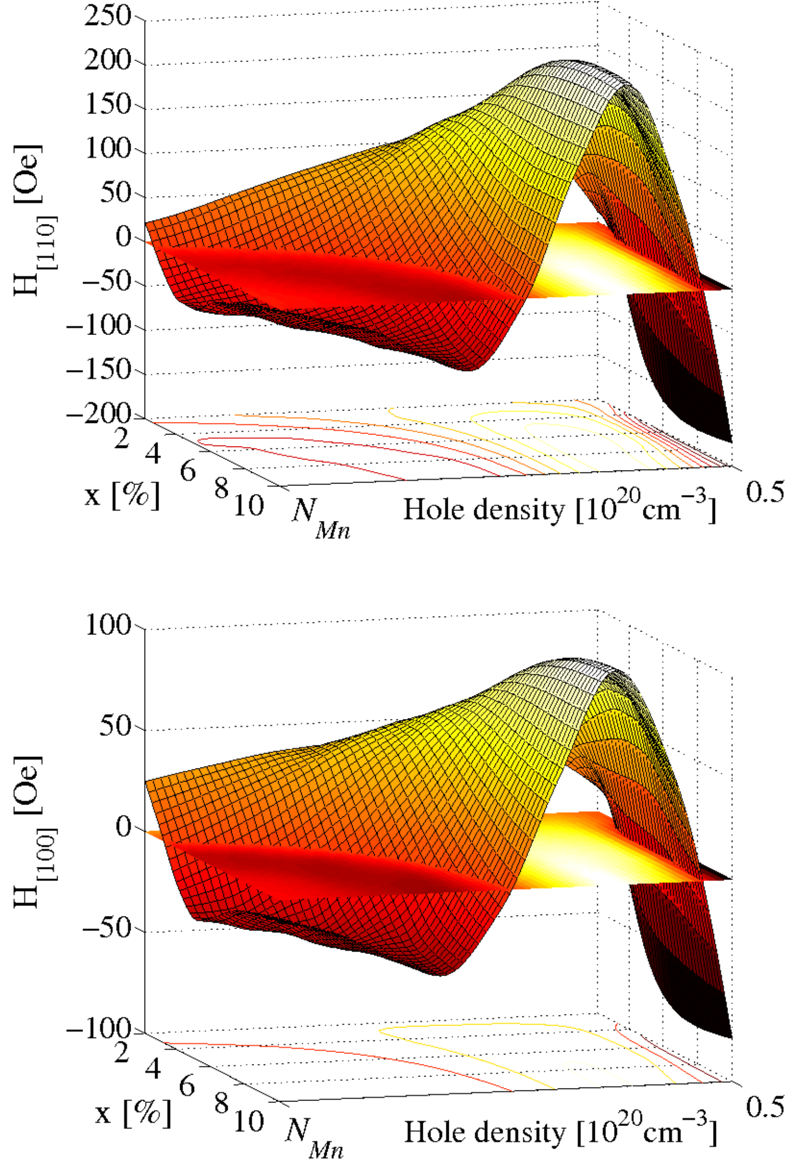

Figure 3.10: Calculated anisotropy fields $H_{[110]}$ and $H_{[100]}$ as functions of hole density p (up to zero compensation $p = N_{Mn}$) and Mn local-moment concentration x at zero temperature and $e_0 = -0.2\%$. For $H_{[110]}$ the in-plane strains are $\kappa = 0.01\%$ and $\lambda = 0$ ($e_{xy} = 0.01\%$, $e_{xx} = e_{yy} = e_0$), while $H_{[100]}$ is found for $\kappa = 0$ and $\lambda = 0.01\%$ ($e_{xy} = 0$, $e_{xx} = e_0 + 0.01\%$, $e_{yy} = e_0 - 0.01\%$).

tration. It can be expressed using the anisotropy functions:

$$q_{[001]}(x, p) \simeq q_{[100]}(x, p) \simeq 0.43 q_{[110]}(x, p). \tag{3.9}$$

The anisotropy function $q_{[110]}(x, p)$ due to shear strain is approximately twice as large as the anisotropy functions $q_{[100]}(x, p)$ and $q_{[001]}(x, p)$. A general property of these functions is that at medium hole densities a relative compression yields a tendency of the easy axis to align with that direction. On the other hand, for very low and high hole densities, the

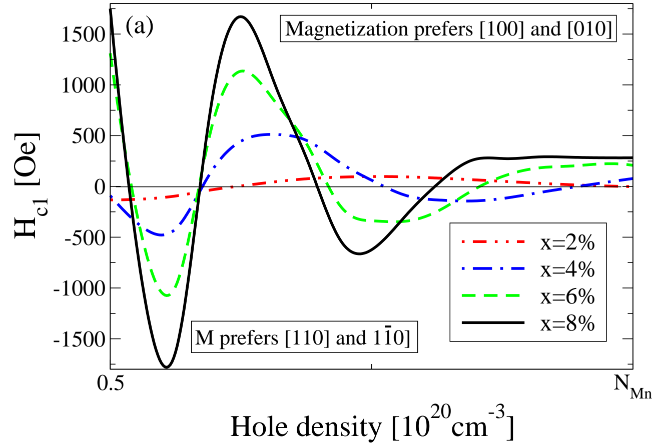

Figure 3.11: Anisotropy field H_{c1} as function of hole density (up to zero compensation $p = N_{Mn}$) at four Mn local-moment concentrations x, zero temperature and growth strain $e_0 = -0.2\%$. (The field H_{c1} is not a function of lattice strains.) "Critical" hole densities,

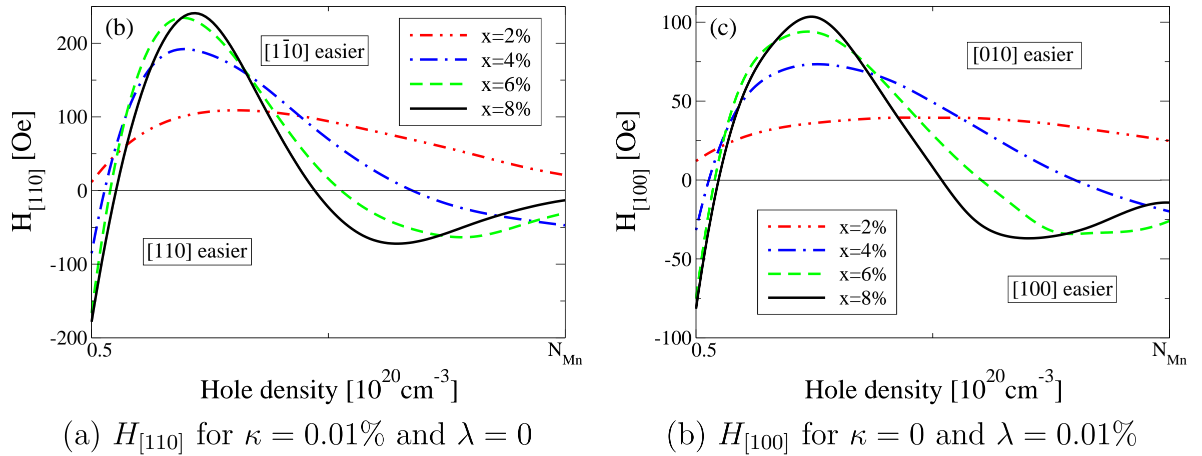

(a) $H_{[110]}$ for $\kappa = 0.01\%$ and $\lambda = 0$ (b) $H_{[100]}$ for $\kappa = 0$ and $\lambda = 0.01\%$

Figure 3.12: Anisotropy fields $H_{[110]}$ and $H_{[100]}$ as function of hole density (up to zero compensation $p = N_{Mn}$) at four Mn local-moment concentrations x, zero temperature and growth strain $e_0 = -0.2\%$. "Critical" hole densities, where the anisotropy fields change sign, are dependent on Mn local-moment concentration.

magnetisation prefers alignment parallel to the direction of lattice expansion.

We caution that Eqs. (3.8) and (3.9) are included to promote the general understanding of the anisotropic behaviour of the strained crystal but are not precise. The relative error of the approximation given by Eq. (3.9) averaged over the $x - p$ space shown in Fig. 3.10 is less than 20%; however, the relative error can be much larger at a given combination of x and p, where the anisotropy coefficients fall to zero.

To finish the analysis of the theoretical results we include Figs. 3.11 and 3.12 to improve the legibility of the data. The individual curves correspond to cuts through the three-dimensional plots in Figs. 3.9 and 3.10 at fixed Mn local-moment concentrations. As already mentioned, the dependence of anisotropy fields on hole density is oscillatory. Note that the critical hole densities, where the sign inversion occurs, shift away

from the extremal values, i.e., zero hole density and zero compensation $p = N_{Mn}$, with increasing x.

Neglecting the complexity of the dependence of the band structure on M (whether changed by doping or temperature), one would expect the cubic anisotropy coefficient K_{c1} to be proportional to M^4 and uniaxial anisotropy coefficients $K_{[001]}$, $K_{[100]}$, and $K_{[110]}$ to M^2. In Figs. 3.11 and 3.12 we can identify intervals of hole density where any change in Mn concentration, and therefore in M, does not induce a sign change in the anisotropy fields and the functional forms of $K_a(M)$ are roughly consistent with the above expectations. For other hole density intervals, however, the behaviour is highly non-trivial and the function $K_a(M)$ can even change sign.

We now proceed to the discussion of how the theoretically expected phenomenology detailed above is reflected in experiments in bare unpatterned (Ga,Mn)As epilayers. The experimental results [133, 66, 65, 67] are often analysed using the following version of the phenomenological formula:

$$\begin{aligned} F(\hat{M}) &= -2\pi M^2 \sin^2\theta - K_{2\perp}\cos^2\theta - \frac{1}{2}K_{4\perp}\cos^4\theta \\ &-\frac{1}{2}K_{4\parallel}\frac{3+\cos 4\phi}{4}\sin^4\theta - K_{2\parallel}\sin^2(\phi-\pi/4)\sin^2\theta, \end{aligned} \tag{3.10}$$

where angle θ and ϕ are measured, as above, from the [001] and [100] axis, respectively. The first term in Eq. (3.10) corresponds to the shape anisotropy described in Sec. 2.3 and not included in Eq. (3.4). The uniaxial anisotropy coefficients $K_{2\perp}$ and $K_{2\parallel}$ correspond to the coefficients $K_{[001]}$ and $K_{[110]}$ in the phenomenological formula Eq. (3.4), respectively. To identify the third and fourth terms in Eq. (3.10) we rewrite those terms as (see also Eq. A.1),

$$\begin{aligned} &-\frac{1}{2}K_{4\parallel}\left(\frac{3+\cos 4\phi}{4}\sin^4\theta + \cos^4\theta\right) - \frac{1}{2}\left(K_{4\perp} - K_{4\parallel}\right)\cos^4\theta = \\ = \;& -\frac{1}{2}K_{4\parallel}\left(n_x^4 + n_y^4 + n_z^4\right) - \frac{1}{2}\left(K_{4\perp} - K_{4\parallel}\right)n_z^4 = \\ = \;& K_{c1}\left(n_x^2 n_y^2 + n_x^2 n_z^2 + n_z^2 n_y^2\right) - \frac{1}{2}K_{[001]_2}n_z^4 + c, \end{aligned} \tag{3.11}$$

where c is an angle-independent constant. From here we see that the coefficient $K_{4\parallel}$ corresponds to the lowest-order cubic coefficient K_{c1} in Eq. (3.4) and $K_{4\perp} - K_{4\parallel} \equiv K_{[001]_2}$ corresponds to the second-order uniaxial anisotropy coefficient K_{u2} for $\hat{U} \parallel [001]$. We point out that omission of the second-order cubic term (and other higher-order terms) can make the determination of $K_{[001]_2}$ from fitting the data to the phenomenological formula in Eq. (3.10) unreliable. Moreover, the accurate extraction of the coefficient $K_{[001]_2}$ can be difficult in samples with large value of the first-order coefficient $K_{[001]}$ [67]. We therefore only note that $K_{[001]_2}$ extracted from the experiment [133, 66, 65] never dominates the anisotropy, consistent with our calculations, and do not discuss the coefficient further in more detail.

The predicted strong dependence of $K_{[001]}$, $K_{[110]}$, and K_{c1} on hole density, Mn local-moment concentration, and temperature is consistently observed in many experimental papers. We start with experiments where the out-of-plane anisotropy is studied. Measurements focusing mainly on the in-plane anisotropies are discussed at the end of this subsection and in Subsec. 3.1.4 for patterned or piezo-strained samples.

The coefficient $K_{[001]}$ is extracted in Ref. [22] using detailed angle-resolved magneto-transport measurements at 4 K for different growth strains in as-grown and annealed, 180 nm thick samples with identical nominal Mn concentration $x \approx 5\%$. The growth strain ranging from $e_0 = -0.22\%$ (compressive) to $e_0 = 0.34\%$ (tensile) is achieved by MBE growth of (Ga,Mn)As on (In,Ga)As/GaAs templates. The observed linear dependence of $K_{[001]}$ on e_0 agrees on the large range of e_0 with the prediction given in Eq. (3.8). The calculated and measured gradients are of the same order of magnitude and sign, and depend on the hole density. The off-set at zero strain in the measured dependence of $K_{[001]}$ on e_0 in Ref. [22] is due to the shape anisotropy.

Ref. [133] presents 50 nm thick, annealed samples with nominal Mn doping $x = 7\%$. All the samples are first passivated by hydrogen and then depassivated for different times to achieve different hole densities while keeping the growth strain the same. The FMR spectroscopy is carried out for in-plane and out-of-plane configurations. There is qualitative agreement of calculation and measurement on the level of the directions of the easy axes as discussed in the previous subsection. The sign change of the uniaxial anisotropy fields driven by increase of temperature is observed. The measured coefficients $K_{[001]}$ and K_{c1} are of the same order of magnitude as the calculated ones and $K_{[001]} \approx K_{c1}$ is consistent with the weaker growth strain in annealed samples.

Ref. [65] presents an as-grown, 6 nm thick film nominally doped with Mn to $x = 6\%$, grown on $Ga_{0.76}Al_{0.24}As$ barrier doped with Be. Increasing the Be doping increases the hole density without changing the Mn local-moment concentration. The fitting of the FMR spectra is done using the coefficients $K_{[001]}$ and K_{c1} and the g-factor of the Mn. The anisotropy field corresponding to the coefficient $K_{[001]}$ reaches value as high as ≈ 6000 Oe at 4 K. Large values of $K_{[001]}$ is consistent with expected large growth strain in a thin as-grown sample [72, 73]. However, for the measured $K_{[001]}$ our calculations would imply strain $e_0 \sim 1\%$ which is an order of magnitude larger than typical strains in as-grown $x = 6\%$ (Ga,Mn)As materials. Other effects are therefore likely to contribute to $K_{[001]}$ in this sample. (Confinement effect or inhomogeneities are among the likely candidates.) The experimental $K_{[001]}$ (K_{c1}) increases (decreases) with increasing hole density which is in agreement with our modelling of highly compensated samples.

Observation of qualitatively consistent behaviour of the anisotropies with the theory but unexpectedly large magnitudes of the anisotropy fields applies also to thick samples studied by FMR in Refs. [66] and [67]. Temperature dependence of the anisotropy fields is studied by FMR in Ref. [66] for a low-doped ($x \approx 2\%$) as-grown 200 nm thick (Ga,Mn)As film. Only the combined contribution of shape anisotropy and $K_{[001]}$ was resolved. The easy axis stays in-plane for all studied temperatures which is consistent with predicted crystalline anisotropy as well as the shape anisotropy dominating at weak growth strains. The uniaxial in-plane anisotropy is of the predicted magnitude but its sign corresponds to modelling by the less frequent negative intrinsic shear strain.

Ref. [67] discussed in Subsec. 3.1.1 on the level of easy axis orientation shows, among other samples, 300 nm thick annealed epilayers with nominal Mn concentration $x = 3\%$ deposited on GaAs and (Ga,In)As substrate under compressive and tensile growth strain, respectively. The strain is measured by x-ray diffraction; however, the predicted linear dependence of $K_{[001]}$ on the growth strain (see Eq. (3.8)) cannot be tested due to different saturation magnetisation and T_C in both samples. Both Refs. [67] and [66] report the coefficient K_{c1} in the 300 nm and 200 nm thick samples an order of magnitude larger

than the calculated one which can [143] be attributed to sample inhomogeneities in these thick epilayers. Ref. [67] studies also 120 nm thick, annealed and as-grown epilayers with $x = 8\%$ deposited on GaAs. The coefficient $K_{[001]}$ doubles its value at low temperature on annealing. Both $K_{[001]}$ and K_{c1} in the thinner samples have values of the order predicted by theory for material with Mn doping $x = 8\%$.

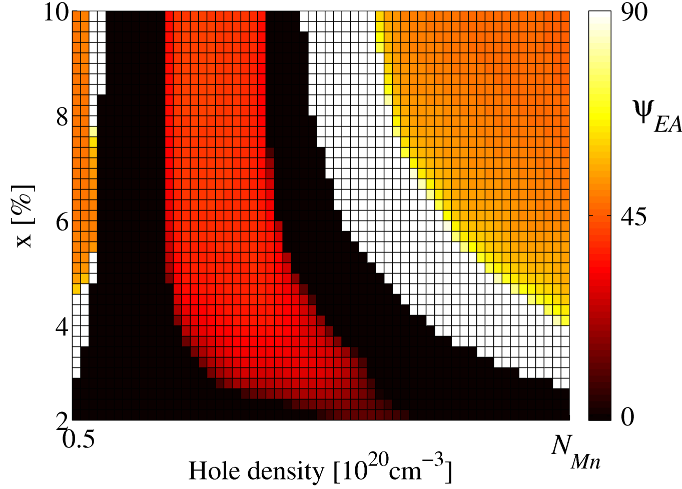

Figure 3.13: Angle ψ of the easy axis with respect to the $[1\bar{1}0]$ axis as function of hole density p (up to zero compensation $p = N_{Mn}$) and Mn local-moment concentration x at zero temperature, $e_0 = -0.2\%$, and $\kappa = 0.01\%$;

Now we analyse experiments focusing on the in-plane anisotropy where the relevant anisotropy coefficients are K_{c1} and $K_{[110]}$. Note that the experimental papers discussed below mostly [142, 130, 89, 101] use the notation with the in-plane magnetisation angle ψ measured from the $[1\bar{1}0]$ axis. To avoid any confusion we write the in-plane form of Eq. (3.4) using the original anisotropy coefficients and the angle $\psi = \phi + \pi/4$,

$$F(\hat{M}) = -\frac{K_{c1}}{4} \sin^2 2\psi + K_{[110]} \sin^2 \psi. \tag{3.12}$$

To facilitate the comparison with experiment we use the notation of Eq. (3.12) consistently in the remaining parts of this section.

The magnetic easy axes lie closer to the [100] or [010] direction than to any diagonal when $K_{c1} > 0$ and $\sqrt{2}K_{[110]} < K_{c1}$. Negative K_{c1} always leads to diagonal easy axes. We include Fig. 3.13 to elucidate the combined effect of K_{c1} and $K_{[110]}$ on the in-plane direction of the easy axes. The angle $\psi_{EA}(x, p)$, plotted as a function of Mn concentration and hole density at zero temperature minimises the free energy $F(\hat{M})$. The local minima at $\psi = 0°$ (black) and $\psi = 90°$ (white) are formed for negative K_{c1}. When $K_{[110]}$ is positive (negative), the global minimum is at $\psi = 0°$ ($\psi = 90°$). The higher energy local minimum disappears for $|K_{c1}| = |K_{[110]}|$. Only one energy minimum forms for $|K_{c1}| < |K_{[110]}|$ and for positive (negative) $K_{[110]}$ the easy axis is at $\psi = 0°$ ($\psi = 90°$). The interface of black and white regions is an evidence of a discontinuity of the function $\psi_{EA}(x, p)$ due to switching of the sign of $K_{[110]}$ when $K_{c1} < 0$. The grey (coloured online) regions in Fig. 3.13 correspond to competition of cubic and uniaxial anisotropy when $K_{c1} > 0$ and

$|K_{c1}| > |K_{[110]}|$. Then there are two easy axes at ψ_{EA} and $180° - \psi_{EA}$ forming "scissors" closing at the $[1\bar{1}0]$ axis. (The darker the colour, the more closed the scissors.)

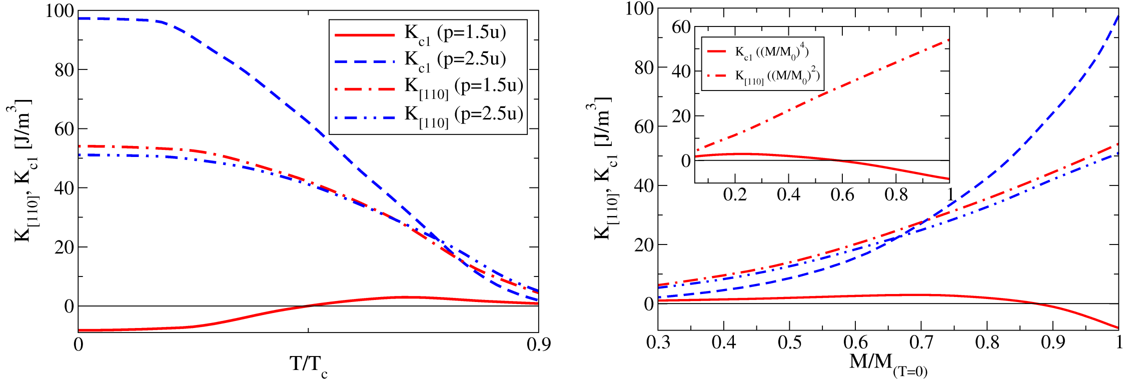

Figure 3.14: Calculated anisotropy fields K_{c1} and $K_{[110]}$ as function of temperature and magnetisation at two hole densities (given in units u $\equiv 10^{20}$ cm^{-3}), Mn concentration $x = 2\%$, strains $e_0 = -0.2\%$, $\kappa = 0.005\%$. Irregular behaviour is observed for the lower hole density.

To demonstrate the typical scaling of in-plane anisotropy components with temperature, we discuss the 50 nm thick as-grown (Ga,Mn)As epilayer with Mn concentration $x = 2.2\%$ determined by x-ray diffraction and secondary ion mass spectrometry, presented in Ref. [142]. The anisotropy coefficients $K_{[110]}$ and K_{c1} are obtained by fitting to the $M(H)$ loop with magnetic field along the hard direction. They can be compared to Fig. 3.14, which shows the calculated anisotropy fields as functions of temperature for two values from the interval of hole densities corresponding to the as-grown sample. For $p = 2.5 \times 10^{20}$ cm^{-3} both the calculated and measured K_{c1} is greater than $K_{[110]}$ at low temperatures but becomes smaller than $K_{[110]}$ at $T \approx T_C$. The calculated K_{c1} is an order of magnitude smaller than the experimental one, however, there is agreement on the level of the temperature dependent ratio of K_{c1} and $K_{[110]}$. On the contrary, Fig. 3.14 shows a non-monotonous dependence of K_{c1} on temperature for $p = 1.5 \times 10^{20}$ cm^{-3}. This singular behaviour is not measured in Ref. [142] but it is reported in a more systematic study in Ref. [133].

The temperature dependence of anisotropy coefficients $K_{[110]}$ and K_{c1} is studied by planar Hall effect in Ref. [117]. The mutual behaviour of the two coefficients observed in the as-grown (Ga,Mn)As epilayer with nominal Mn concentration $x \approx 4\%$ and $T_C = 62$ K is qualitatively the same as in Ref. [142]. K_{c1} becomes smaller than $K_{[110]}$ at $T = 26$ K which is in agreement with our modelling. No sign change of K_{c1} is reported in this experimental work. Again, the calculated K_{c1} is an order of magnitude smaller than the experimental one.

Ref. [133] resolves the in-plane coefficients K_{c1} and $K_{[110]}$ in four samples with nominal Mn doping $x = 7\%$ and different hole densities. In samples with lower hole densities the dependence of K_{c1} and $K_{[110]}$ is qualitatively consistent with Ref. [142], however, both coefficients change sign when temperature is increased in samples with higher hole densities ($p \sim 10^{21}$ cm^{-3}, $T_C = 130$ K). Our model predicts such sign change for a short interval of high hole compensations and a larger interval of low hole compensations as shown in Fig. 3.11.

Another type of temperature scaling of K_{c1} and $K_{[110]}$ is observed in a 50 nm thick, annealed sample with nominal Mn doping $x = 7\%$ and $T_C = 165$ K [86]. $K_{[110]}$ is larger than K_{c1} on the whole temperature interval ($T = 4 - 165$ K). Both coefficients are positive, decrease on increasing temperature, and their magnitudes are of the same order of magnitude as the calculated anisotropies. The stability of sign of $K_{[110]}$ is observed theoretically for higher "intrinsic" shear strain as discussed in Fig. 3.7(b) in Subsec. 3.1.2.

The temperature dependence of domain-wall properties of a 500 nm, as-grown (Ga,Mn)As film with Mn doping $x = 4\%$ is studied by means of the electron holography in Ref. [130]. The width and angle of the domain walls were determined directly from the high-resolution images. The ratio of the anisotropy coefficients $K_{[110]}/K_{c1}$ was extracted from these observations combined with Landau-Lifshitz-Gilbert simulations. The Nèel type domain walls evolve from near-90° walls at low temperatures ($T = 10$ K) to large-angle $[1\bar{1}0]$-oriented walls and small-angle [110]-oriented walls at higher temperatures ($T = 30$ K). The angles of domain-walls aligned with particular crystallographic directions reveal positions of the magnetic easy-axes. The "scissors" of the easy-axes (described in discussion of Fig. 3.13) are closing around the $[1\bar{1}0]$ axis on increasing temperature consistent with our modelling.

The domain-wall width is inversely proportional to the effective anisotropy energy barrier between the bistable states on respective sides of the domain wall: $K^{eff}_{[110]} \equiv K_{c1}/4 - K_{[110]}/2$ ([110]-oriented walls) and $K^{eff}_{[1\bar{1}0]} \equiv K_{c1}/4 + K_{[110]}/2$ ($[1\bar{1}0]$-oriented walls). The width of the $[1\bar{1}0]$-oriented wall in Ref. [130] initially increases with temperature and then saturates at high temperature while the [110]-oriented wall width keeps increasing with temperature until it becomes unresolvable. This observation corresponds well to the theoretical prediction and can be qualitatively understood by considering the approximate magnetisation scaling of $K_{c1} \sim M^4$, $K_{[110]} \sim M^2$, and magnetic stiffness $\sim M^2$. A detailed description of the study [130] is presented in Subsec. 3.2.5.

Finally, Refs. [89] and [19] present (Ga,Mn)As field-effect transistors (FETs), where hole depletion/accumulation is achieved by gating induced changes in the in-plane easy axis alignment. In Ref. [89] the Mn-doped layer is 5 nm thick with Mn doping $x = 2.5\%$ and hole density $p \sim 1\times10^{19} - 10^{20}\text{cm}^{-3}$. The direction of magnetic easy-axes was detected by AMR at $T = 4$K. The 20% variation in the hole density achieved by applying the gate voltage from -1 to 3V is determined from variation of the channel resistance near T_C. This value was a starting point for simulations of the depletion at $T = 4$ K giving hole density changes $\Delta p \approx 5 \times 10^{19}\text{cm}^{-3}$. The measured K_{c1} is negative and its magnitude decreases with depletion. The theoretical magnitude (~ 10 mT) and sign of K_{c1} for the relevant hole density range, as well as the variation of K_{c1} with varying hole density, are consistent with the experiment. Recall that negative K_{c1} corresponds to diagonal easy axes captured by two black/white regions in Fig. 3.13. Samples reported in Refs. [140, 126, 40] and [86] (see also Subsec. 3.1.2) with diagonal easy axes at low temperatures fall into the right region with lower hole compensations, whereas the sample in Ref. [89] is a rarely observed example of diagonal easy axes at high compensation and low temperature corresponding to the left black/white region in Fig. 3.13.

The magnitude of the $K_{[110]}$ constant measured in Ref. [89] was modeled by assuming a small strain parameter e_{xy} and, in agreement with experiment, it was found that $K_{[110]}$ is only weakly dependent on the hole density. In Ref. [19], on the other hand, $K_{[110]}$ changes significantly upon gating. In our modelling, this is explained by the larger Mn

local-moment density $x \approx 10\%$ in the measured film, as compared to the weakly Mn-doped (Ga,Mn)As used in Ref. [89]. We point out, however, that the theoretical constant K_{c1} becomes also more sensitive to the variation of the hole density at higher x, which is not seen in the experimental data in Ref. [19]. This discrepancy can be attributed to the limited reliability of our theory, describing uniform bulk (Ga,Mn)As, for ultra-thin films utilised in the FET structures. Applying the gate voltage does not yield uniform variation in the hole density in the entire film but only affects a ~ 1 nm thick layer of (Ga,Mn)As adjacent to the gate. A more detailed description of the study [89] is presented in Subsec. 3.2.1.

3.1.4 Samples with post-growth controlled strains

In the previous subsection, we discussed three types of lattice strain and calculated corresponding types of uniaxial anisotropy components. In the bare, unpatterned epilayers we could analyse and compare to experiment only anisotropies induced by the growth strain and by the unknown symmetry-breaking mechanism modelled by the "intrinsic" shear strain. The calculations including the model shear strain allow us also to estimate the magnitude of real in-plane lattice strains, controlled post-growth by patterning or piezo-stressing, that can induce sizable changes of anisotropy. In this subsection we investigate samples where these post-growth techniques are used to apply additional stress along any in-plane direction. We will focus primarily on stresses along the main crystal axes and in-plane diagonals. We will also comment on the procedure for determining the lattice strain from specific geometrical parameters of the experimental setup. Where necessary, we distinguish the externally induced strain and the "intrinsic" shear strain, which models the in-plane symmetry-breaking mechanism already present in the bare epilayers. Returning to the notation of Sec. 2.1 we denote the latter strain by the symbol e_{xy}^{int}. For better physical insight and to relate with discussion in previous subsection we will map the anisotropies on the phenomenological formulae by decomposing the total strain matrix into the three basis strains (see Eqs. (3.1)-(3.3)). We will then write the corresponding anisotropy energy terms as in Subsec. 3.1.3, assuming linearity between the respective basis strains and anisotropy energy components (see Eq. (3.8)). Experiments will be discussed based on microscopic anisotropy calculations with the total strain tensor directly included into the Hamiltonian.

We begin this subsection by discussion of the in-plane uniaxial strain induced by post-growth lithography treatment of Mn-doped epilayers grown under compressive lattice strain. Narrow bars with their width comparable to the epilayer thickness allow for anisotropic relaxation of the lattice-matching strain present in the unpatterned film. An expansion of the crystal lattice along the direction perpendicular to the bar occurs while the epilayer lattice constant along the bar remains unchanged. Parameters sufficient for determination of the induced strain are the initial growth strain e_0 and the thickness to width ratio t/w of the bar. In the regime of small deformations the components of the induced strain are linearly proportional to the growth strain. The strain tensor for a bar oriented along the [010] axis reads:

$$\mathbf{e}^{r}_{[100]} = e_0 \begin{pmatrix} -\rho+1 & 0 & 0 \\ 0 & 1 & 0 \\ 0 & 0 & \frac{c_{12}}{c_{11}}(\rho-2) \end{pmatrix}, \qquad (3.13)$$

where the lattice relaxation is quantified by ρ which is a function of t/w and can vary over the bar cross section. We calculate the distribution of ρ over the cross section of the bar using Structural Mechanics Module of Comsol (standard finite element partial differential equation solver, www.comsol.com). Since the macroscopic simulations ignore the microscopic crystal structure, they apply to bars oriented along any crystallographic direction. We therefore introduce a coordinate system fixed to the bar: x' axis lies along the relaxation direction transverse to the bar, y' axis along the bar, and z' axis along the growth direction. We approximate the bar by an infinite rectangular prism with translational symmetry along the y' axis, attached to a thick substrate.

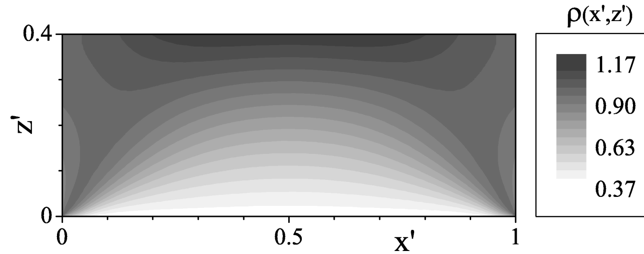

Figure 3.15: Spatial dependence of the strain coefficient ρ due to lattice relaxation in a narrow bar with $t/w = 0.4$ and compressive growth strain $e_0 < 0$, simulated values of ρ are plotted for the cross-section of the bar.

Fig. 3.15 shows the spatial dependence of the function $\rho(x', z')$ for a given thickness to width ratio and compressive growth strain $e_0 < 0$. Only the area of the bar is plotted, whereas the strain induced in the patterned part of the substrate is not shown. (The substrate relaxation is not directly related to the microscopic simulation of the anisotropy energy.) In wide bars ($t/w \ll 1$) the relaxation is very non-uniform, whereas narrow bars ($t/w \gg 1$) are fully relaxed. Fig. 3.16 shows still a fairly non-uniform relaxation for $t/w = 0.4$ with large relaxation at the edges. We point out in this case that the resulting anisotropy can be very sensitive to the details of the etching (vertical undercut/overcut profile).

The non-uniform strain distribution in wider bars can in principle force the system to break into magnetically distinct regions. However, experiments show rather that the whole bars behave as one effective magnetic medium. Because of the linearity between the strain and the anisotropy (see Eq. (3.8)) we can model the mean magnetic anisotropy by considering the spatial average of $\mathbf{e}^r_{[100]}$ over the bar cross section. The inset of Fig. 3.16 shows the averaged value $\overline{\rho}$ as a function of the width to thickness ratio. It confirms that the effect of relaxation can reach magnitudes necessary to generate significant changes in the magnetic anisotropy. In very narrow bars the induced uniaxial anisotropy can override the intrinsic anisotropies of the unpatterned epilayer and determine the direction of the easy axis.

If the bar is aligned with the [100] or [010] crystal axis, the strain $\mathbf{e}^r_{[100]}$ in Eq. (3.13) with the average relaxation magnitude $\overline{\rho}$ can be used directly as input parameter of the microscopic calculation (see Eq. (2.34)). Alternatively, the total strain tensor can be decomposed into the growth basis strain from Eq. (3.1) and the uniaxial basis strain

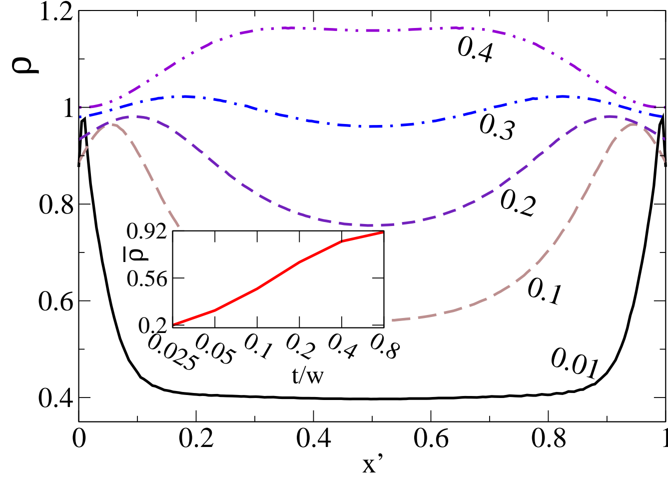

Figure 3.16: Sections of $\rho(x',z')$ in Fig. 3.15 at fixed values of z' (given next to the curves in relative units) of a thin bar. Inset shows the average strain $\overline{\rho}(t/w)$ as a function of the thickness to width ratio.

introduced in Eq. (3.3)

$$\mathbf{e}^r_{[100]}(e_0,\overline{\rho}) = \mathbf{e}^g(\tilde{e}_0) + \mathbf{e}^u(\tilde{\lambda}), \tag{3.14}$$

$$\tilde{e}_0 = e_0\left(1-\frac{\overline{\rho}}{2}\right), \tag{3.15}$$

$$\tilde{\lambda} = -e_0\frac{\overline{\rho}}{2}. \tag{3.16}$$

Their effects on the magnetic anisotropy can be considered separately utilising the results shown in Subsec. 3.1.3.

Now we discuss the introduction of uniaxial in-plane anisotropies by a piezo-actuator attached to the sample. In this case, the (Ga,Mn)As film is assumed to follow the deformation of the stressor. (The substrate is usually thinned to achieve better transmission of the piezo-strain to the studied epilayer. Macroscopic Comsol simulations predict transmission of approximately 70% of the piezo-strain in a substrate with thickness to lateral size ratio $t/l \approx 0.1$ and transmission of approximately 90% of the piezo-strain for $t/l \approx 0.02$.) The net effect of the piezo-stressing on normal GaAs epilayers has been investigated experimentally for example in Ref. [113] for a standard $PbZrTiO_3$ (PZT) piezo-actuator. The induced strain can reach magnitudes $\sim 10^{-4}$ at low temperatures, which are sufficient to induce observable anisotropies in (Ga,Mn)As, as shown in Subsec. 3.1.3. The deformation is linearly proportional to applied voltage on the transducer and increases with increasing temperature.

The dependence of uniaxial anisotropies due to additional piezo-strains is analogous to the behaviour of relaxed microbars, however, the form of the strain tensor induced by the stressor is typically more complex. Let us first assume a strain tensor with components in the Cartesian coordinate system fixed to the orientation of the piezo-stressor: x' axis lies along the principal elongation direction, z' axis is perpendicular to plane of the thin film. We denote the deformation along the x' axis by σ and the simultaneous deformation along the y' axis by σ'. Note that shear strains are typically not considered when describing

the action of a piezo-stressor. The third parameter describing the strained (Ga,Mn)As epilayer is the growth strain e_0. Our analysis takes into account only structures that can be parametrised by these three values. The strain tensor in the dashed coordinate system reads

$$\mathbf{e}^{p}_{[100]} = \begin{pmatrix} \sigma + e_0 & 0 & 0 \\ 0 & \sigma' + e_0 & 0 \\ 0 & 0 & -\frac{c_{12}}{c_{11}}(2e_0 + \sigma + \sigma') \end{pmatrix} \tag{3.17}$$

Components of this tensor are considered uniform in the studied epilayer. If the principal elongation direction of the piezo-stressor is aligned with the [100] crystallographic axis the strain tensor $\mathbf{e}^{p}_{[100]}$ can be used directly as an input of the microscopic simulation. Similarly to the strain induced by lattice relaxation, $\mathbf{e}^{p}_{[100]}$ can be decomposed into the growth basis strain and the uniaxial basis strain

$$\mathbf{e}^{p}_{[100]}(e_0, \sigma, \sigma') = \mathbf{e}^{g}(\tilde{e}_0) + \mathbf{e}^{u}(\tilde{\lambda}), \tag{3.18}$$

$$\tilde{e}_0 = e_0 + \frac{1}{2}(\sigma + \sigma'), \tag{3.19}$$

$$\tilde{\lambda} = \frac{1}{2}(\sigma - \sigma'). \tag{3.20}$$

Again, the results shown in Subsec. 3.1.3 can then be used when analysing the resulting magnetocrystalline anisotropies. Recall that $\mathbf{e}^{g}$ has a minor effect on the in-plane anisotropy and can therefore be omitted when discussing in-plane magnetisation transitions.

So far we have described induced strains aligned with the [100] crystal axis. In case of a lattice relaxation or piezo-stressor aligned at an arbitrary angle ω, the following transformation of the total strain tensor $\mathbf{e}^{r}_{[100]}$ or $\mathbf{e}^{p}_{[100]}$ to the crystallographic coordinate system applies

$$\mathbf{e}^{r(p)}_{\omega} = R^{T}_{\omega}\mathbf{e}^{r(p)}_{[100]}R_{\omega} \tag{3.21}$$

where the rotation matrix reads:

$$R_{\omega} = \begin{pmatrix} \cos(\omega - \pi/4) & \sin(\omega - \pi/4) & 0 \\ -\sin(\omega - \pi/4) & \cos(\omega - \pi/4) & 0 \\ 0 & 0 & 1 \end{pmatrix}. \tag{3.22}$$

The angular shift by $-\pi/4$ is because we measure the angle ω from the $[1\bar{1}0]$ axis. This convention was introduced in subsection 3.1.3 before Eq. (3.12) and is used consistently in this subsection for all in-plane angles. The rotated total induced strain can be used directly as the input strain matrix for the microscopic calculation or it can be decomposed into all three elements of the in-plane strain basis. In case of the relaxation-induced strain, we obtain

$$\mathbf{e}^{r}_{\omega}(e_0, \overline{\rho}) = \mathbf{e}^{g}(\tilde{e}_0) + \mathbf{e}^{u}(\tilde{\lambda}) + \mathbf{e}^{s}(\tilde{\kappa}), \tag{3.23}$$

$$\tilde{e}_0 = e_0\left(1 - \frac{\overline{\rho}}{2}\right), \tag{3.24}$$

$$\tilde{\lambda} = -e_0\frac{\overline{\rho}}{2}\sin 2\omega, \tag{3.25}$$

$$\tilde{\kappa} = e_0\frac{\overline{\rho}}{2}\cos 2\omega. \tag{3.26}$$

In case of the rotated piezo-stressor, the same decomposition follows, however, the effective strain magnitudes $\tilde{\lambda}$ and $\tilde{\kappa}$ depend on different real experimental parameters,

$$\mathbf{e}^p_\omega(e_0,\sigma,\sigma') = \mathbf{e}^g(\tilde{e}_0) + \mathbf{e}^u(\tilde{\lambda}) + \mathbf{e}^s(\tilde{\kappa}), \quad (3.27)$$

$$\tilde{e}_0 = e_0 + \frac{(\sigma+\sigma')}{2}, \quad (3.28)$$

$$\tilde{\lambda} = \frac{(\sigma-\sigma')}{2}\sin 2\omega, \quad (3.29)$$

$$\tilde{\kappa} = -\frac{(\sigma-\sigma')}{2}\cos 2\omega. \quad (3.30)$$

Considering the linear dependence of the anisotropy coefficients on the corresponding strain elements (see Eq. (3.8)), we can write the part due to post-growth induced strains of the phenomenological formula for the free energy as a function of angles ψ and ω,

$$\begin{aligned} F_u(\hat{M}) &= K_{[110]}(\omega)\sin^2\psi + K_{[100]}(\omega)\sin^2(\psi+\pi/4) \quad (3.31)\\ &\simeq q_{[110]}\tilde{\kappa}(\omega)\sin^2\psi + q_{[100]}\tilde{\lambda}(\omega)\sin^2(\psi+\pi/4), \end{aligned}$$

where we use the notation analogous to Eq. (3.8) in Subsec. 3.1.3. The relation of the effective parameters $\tilde{\lambda}$ and $\tilde{\kappa}$ to the experimental parameters of microbars or stressors oriented along arbitrary crystallographic direction is given by Eqs. (3.25) and (3.26) or (3.29) and (3.30), respectively. The linearity of the anisotropy constants $K_{[100]}$, $K_{[110]}$, and $K_{[001]}$ on corresponding strain coefficients and the form of the strain tensors in Eqs. (3.23) and (3.27) allow us to factor out the ω dependence of K_u's. Figs. 3.9, 3.10, 3.11, and 3.12 together with Eqs. (3.23) and (3.27) can therefore be used for analysing magnetic anisotropies induced by micropatterning or piezo-stressors oriented along any crystallographic direction.

The full angular dependencies of the anisotropy energy calculated directly from the total strain tensor included into the Kohn-Luttinger kinetic-exchange Hamiltonian for several combinations of $\tilde{\kappa}$ and $\tilde{\lambda}$ are plotted in Fig. 3.17. Recall that analogous in-plane angular dependencies of the anisotropy energy were presented in Figs. 3.3-3.5, where only the competition of the growth strain $\mathbf{e}^g$ and shear strain $\mathbf{e}^s$ with the cubic anisotropy of the host lattice was considered.

Fig. 3.17(a) shows four angular dependencies of the anisotropy energy for $x = 3\%$ and $p = 3\times10^{20}\mathrm{cm}^{-3}$. The curves are marked by the values of the effective strain components. The solid curve for weak shear strain $\tilde{\kappa} = 0.01\%$ and no uniaxial strain $\tilde{\lambda} = 0$ has two local minima close to the main crystal axes indicating dominant cubic anisotropy with $K_{c1} > 0$ for the considered x and p. The easy axes are shifted due to the positive shear strain towards the $[1\bar{1}0]$ axis which is the direction of relative lattice compression, consistently with the discussion in Subsec. 3.1.3 for samples with medium hole densities. Additional uniaxial strain $\tilde{\lambda} = -0.025\%$ results in only one global minimum easy axis rotating towards the [100] direction which is again the direction of relative lattice compression.

The dashed curve in Fig. 3.17(a) corresponding to strong shear strain $\tilde{\kappa} = 0.09\%$ and no uniaxial strain $\tilde{\lambda} = 0$ has only one global minimum at the $[1\bar{1}0]$ diagonal, indicating domination of the uniaxial anisotropy over the underlying cubic anisotropy. Addition of the uniaxial strain $\tilde{\lambda} = -0.025\%$ leads to rotation of the easy axis towards the direction of relative compression ([100] for $\tilde{\lambda} < 0$).

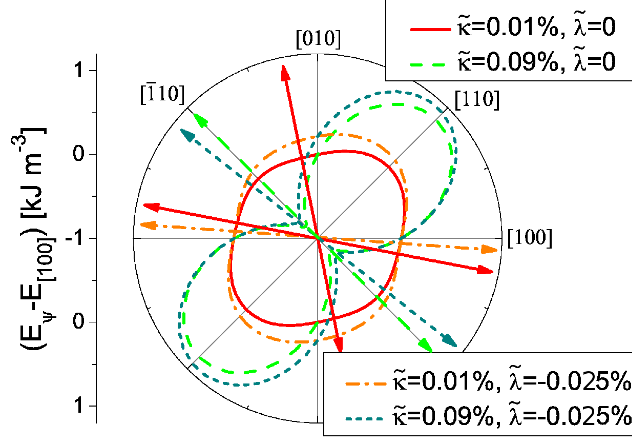

(a) $x = 3\%$, $p = 3 \times 10^{20}\text{cm}^{-3}$, $\tilde{e}_0 = -0.3\%$ when $\tilde{\lambda} = 0$, $\tilde{e}_0 = -0.275\%$ when $\tilde{\lambda} = -0.025\%$

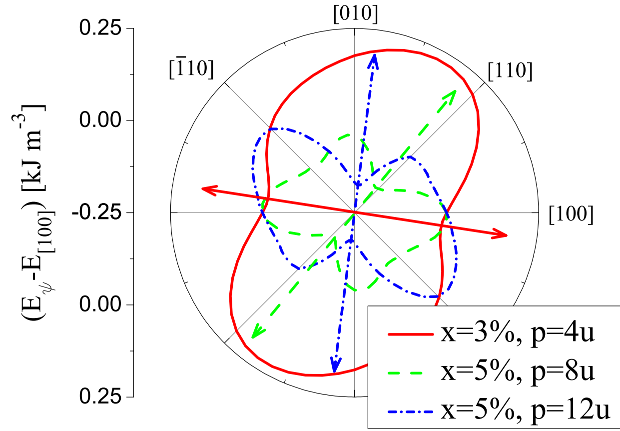

(b) $\tilde{\lambda} = -0.025\%$, $\tilde{\kappa} = 0.01\%$, $\tilde{e}_0 = -0.275\%$

Figure 3.17: Magnetic anisotropy energy $\Delta E = E_\psi - E_{[100]}$ as a function of the in-plane magnetisation orientation $\mathbf{M} = |\mathbf{M}|[\cos\psi, \sin\psi, 0]$ and its dependence on material parameters. Effects of the shear strain and the uniaxial strain combine linearly (a). Magnetic easy axes (marked by arrows) change their direction upon change of Mn local-moment concentration x, and hole density p (in units u $\equiv 10^{20}$ cm^{-3}) for a fixed uniaxial and shear strain (b). Both plots assume zero temperature.

Curves plotted in Fig. 3.17(b) differ in the material parameters but share the same weak shear strain $\tilde{\kappa} = 0.01\%$ and the same uniaxial strain $\tilde{\lambda} = -0.025\%$. The solid curve for $x = 3\%$ and $p = 4 \times 10^{20}\text{cm}^{-3}$ falls into the range of hole densities where the cubic anisotropy coefficient K_{c1} is positive so the easy axes in the absence of in-plane strains align parallel to the main crystal axes. Adding the uniaxial strain $\tilde{\lambda}$ yields only one global minimum along the [100] direction and the shear strain shifts the easy axis towards the [1$\bar{1}$0] diagonal. Again, for both strains the easy axes tend to align along the direction of lattice compression for these medium doping parameters.

The dashed curve in Fig. 3.17(b) for $x = 5\%$ and $p = 8 \times 10^{20}\text{cm}^{-3}$ can be described by a negative K_{c1} corresponding to diagonal easy axes in the unstrained bulk epilayer. The additional shear strain $\tilde{\kappa}$ makes the [110] direction the global minimum easy axis. Note that for these values of x and p the easy axis prefers to align with the direction of lattice expansion. Consistently, the uniaxial strain $\tilde{\lambda}$ rotates the easy axis towards the direction of relative lattice expansion, i.e., towards the [010] axis. Finally, the dash-dotted curve for $x = 5\%$ and high hole density $p = 12 \times 10^{20}\text{cm}^{-3}$ corresponds to positive K_{c1} and again, when the in-plane strains are included the easy axes prefer the direction of relative lattice expansion. To summarise the discussion of Figs. 3.17(a) and 3.17(b), the preferred alignment of the in-plane easy axis with either the lattice contraction or expansion direction depends on x and p. For a given doping it has always the same sense for both the shear strain $\tilde{\kappa}$ and the uniaxial strain $\tilde{\lambda}$ and is uncorrelated with the sign of the cubic anisotropy component. These conclusions are independent of the growth strain, at least for its typical values $|e_0| < 1\%$.

Now we analyse experimental studies that control the in-plane strain by means of post-growth lithography. Refs. [93] and [149] present structures with the shear and uniaxial strain induced locally by anisotropic relaxation of the compressive growth strain. Ref. [149] studies an L-shaped channel with arms aligned along the $[1\bar{1}0]$ and [110] directions patterned by lithography in a 25 nm thick (Ga,Mn)As epilayer with nominal Mn concentration $x = 5\%$. Hole density $p = 5 \times 10^{20}\text{cm}^{-3}$ was estimated from high-field Hall measurements. This patterning allows relaxation of the growth lattice-matching strain in direction perpendicular to the channel. Therefore, the generated uniaxial strains in each arm of the L-shaped channel have opposite signs. The induced shear strain is added to (subtracted from) the intrinsic shear strain in the arm fabricated along the $[1\bar{1}0]$ ([110]) axis. The magnitude of the induced strain increases with decreasing width of the channel. A large effect on magnetic easy axes orientation has been observed in a 1 μm wide channel while only moderate changes have been found in a 4 μm bar. In both cases the easy axes of the unpatterned epilayer rotated in the direction perpendicular to lattice expansion. The sense and magnitude of the easy axis reorientations in the relaxed microbars are consistent with theory prediction for the relevant values of x, p, and microbar geometry. A more detailed description of the study [149] is presented in Subsec. 3.2.3.

Refs. [147] and [46] show lithographically induced uniaxial anisotropy along the [100] or [010] axis in arrays of narrow bars. Ref. [147] presents 200 nm wide bars fabricated in an as-grown 70 nm thick film with Mn concentration $x = 2.5\%$ determined by x-ray diffraction. Ref. [46] reports lattice relaxation in 200 nm wide, 20 nm thick bars in an as-grown material with nominal Mn concentration $x = 4\%$. In both studies the unpatterned epilayers have two equivalent easy axes close to main crystal axes. After the anisotropic relaxation of the growth strain in the nanobars the easy axis corresponding to the relaxation direction is lost, whereas the other easy axis is maintained. This behaviour is in agreement with our simulations on the relevant interval of dopings and patterning induced strains.

Refs. [59] presents two sets of lithographically patterned arrays of (Ga,Mn)As microbars which differ in the thickness to width ratio, Mn doping, hole concentration, and alignment with the crystallographic axes. The two sets were doped nominally to 5%(7%) of Mn, annealed(as-grown), the individual microbars are 750 nm(1 μm) wide, and the (Ga,Mn)As epilayer is 25 nm(200 nm) thick. Structural properties of the (Ga,Mn)As

microbars were investigated by high-resolution x-ray diffraction measurements. The experimental data, showing strong strain relaxation effects, are in good agreement with finite element simulations. SQUID magnetisation measurements were performed to study the control of magnetic anisotropy in (Ga,Mn)As grown under compressive strain on GaAs substrate by the lithographically induced strain relaxation of the microbars. The easy axis can be rotated by the micropatterning by 90° at all temperatures below the Curie temperature. There is semiquantitative agreement between experimental data and theoretical modelling. A more detailed description of the study [59] is presented in Subsec. 3.2.2.

The anisotropies induced in the relaxed structures in Refs. [93, 149, 147] and [46] can be predicted using the results of Subsec. 3.1.3 directly. Bearing in mind the negligible effect of the growth strain, the relevant part of the strain tensor describing the relaxation along the main crystal axes has the form of the uniaxial basis strain $\mathbf{e}^u$, as shown in Eq. (3.14), and corresponds to the anisotropy component with the previously calculated coefficient $K_{[100]}$. The relaxation along the diagonals is described by the strain tensor: $\mathbf{e}^r_{[110]}(e_0, \overline{\rho}) = \mathbf{e}^s(\tilde{\kappa})$ with $\tilde{\kappa} = \pm\frac{1}{2}e_0\overline{\rho}$, where we again neglected the contribution from the growth strain $\mathbf{e}^g$. It induces uniaxial anisotropy component quantified by the coefficient $K_{[110]}$. Note that the "intrinsic" shear strain e^{int}_{xy} in the modelling is independent of the externally introduced lattice distortion and needs to be added to the total strain tensor if the corresponding anisotropy is present in the unpatterned epilayer. As mentioned before, the simulated rotation of easy axis directions in the relaxed microbars is in good agreement with the measured behaviour.

The piezo-strain is also applied in most cases along the main crystal axes or diagonals. In Ref. [35] a PZT piezo-electric actuator is attached to a 30 nm thick (Ga,Mn)As epilayer grown on a GaAs substrate thinned to 100 μm. The principal elongation direction of the actuator is aligned with the [110] crystallographic direction. The nominal Mn concentration of the as-grown epilayer is 4.5%. The relative actuator length change is approximately 4×10^{-4} at $T = 50$ K (measured by a strain gauge) for the full voltage sweep (from -200 to 200 V). Such piezo-strain induces a rotation of the easy axis by $\Delta\psi_{EA} \approx 65°$. Our modelling predicts $\Delta\psi_{EA}$ of the same order for relevant material and strain parameters. The easy axis rotates towards the [110] ([$1\overline{1}0$]) direction upon contraction (elongation) along the [110] axis in agreement with the behaviour observed in the relaxed microbars and with our modelling.

Ref. [10] extends the piezo-stressed (Ga,Mn)As study in Ref. [35] to low temperatures. Again, PZT piezo-actuator is attached to a Hall bar along the [110] crystallographic direction. The 30 nm thick, as-grown (Ga,Mn)As epilayer grown on GaAs substrate has nominal Mn concentration 4.5% and $T_C = 85$ K. A strain gauge measurement shows almost linear dependence of the piezo-strain in the Hall bar on temperature (in the range 5-50 K). The anisotropy coefficients $K_{[110]}$ and K_{c1} are extracted from the angle-dependent magnetoresistance measurement as a function of temperature for three voltages (-200, 0, and 200 V). At high temperatures the relative elongation of the structure is again approximately 4×10^{-4} and the corresponding uniaxial anisotropy dominates over the intrinsic uniaxial anisotropy along the [110] axis. Close to 5 K the action of the piezo-stressor is negligible so the intrinsic uniaxial anisotropy is stronger than the induced one, however, the total in-plane anisotropy is dominated by the cubic anisotropy. The measured and calculated induced anisotropy along the [110] direction are of the same sign and order of magnitude for the considered temperatures.

Ref. [88] presents a 15 nm thick, annealed sample doped to $x = 8\%$, subject to piezo-stressing along the [010] axis. The anisotropy coefficients are extracted from transverse AMR. The PZT actuator induces relative elongation ranging from 1.1×10^{-3} for voltage 200 V to 0.7×10^{-3} for -200 V, measured by a strain gauge. The difference of the limits is again approximately 4×10^{-4} but all values are shifted towards tensile strain most likely due to different thermal dilatation in the sample and the actuator. The lattice expansion along the [010] direction leads to alignment of the easy axis along the [100], in agreement with our modelling and with the experimental studies discussed in this subsection. The extracted cubic anisotropy field is roughly a factor of two lower compared to studies of samples with high hole compensation sharing the value ≈ 1000 Oe at different nominal Mn concentrations [142, 65, 117]. The low critical temperature $T_C = 80$ K suggests lower effective Mn concentration in Ref. [88]. Our calculations for lower Mn local-moment concentration and high hole compensation predict the anisotropy coefficients K_{c1} and $K_{[100]}$ induced by the piezo-strain in correspondence with the measured coefficients.

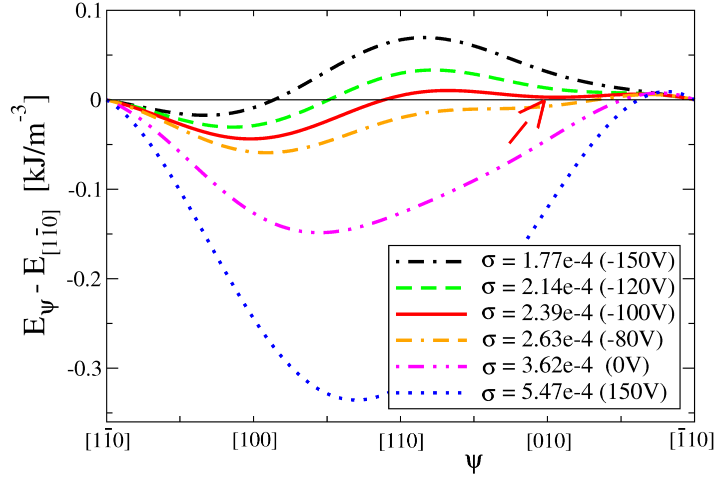

Figure 3.18: Calculated magnetic anisotropy energy $\Delta E = E_\psi - E_{[1\bar{1}0]}$ as a function of the in-plane magnetisation angle ψ measured from the $[1\bar{1}0]$ axis at T= $5/8\mathrm{T}_C$, $e_0 = 0$, $e_{xy}^{int} = 0.017\%$, $x = 5\%$, and $p = 5 \times 10^{20}\mathrm{cm}^{-3}$. The curves are labelled by σ, the induced strain along the principal elongation direction of the piezo-stressor tilted by angle $\omega = -10°$, and by the corresponding voltage. (The relationship of σ and voltage is inferred from Ref. [101] to allow for direct comparison with experiment.) The easy axis rotates smoothly upon sweeping the voltage. For -100 V a shallow local energy minimum forms due to the underlying cubic anisotropy (marked by arrow).

Finally, we discuss a piezo-strain induced along a general in-plane direction. In Ref. [101] the principal elongation direction of the PZT piezo-actuator is tilted by angle $\omega = -10°$ (with respect to the $[1\bar{1}0]$ axis). The 25 nm thick, as-grown (Ga,Mn)As epilayer with nominal Mn concentration $x = 6\%$ is grown on a GaAs substrate, which was thinned before attaching of the stressor to $\approx 150\mu$m. The anisotropies are determined from SQUID and AMR measurements at 50 K. The uniaxial strain caused by differential thermal contraction of the sample and the piezo-stressor on cooling (at zero applied voltage) is of the order 10^{-4}. The uniaxial strains generated at the voltage ± 150 V are $\sigma \approx \pm 2 \times 10^{-4}$ and $\sigma' \approx -\sigma/2$ at 50 K. The tilt of the piezo-stressor with respect to the

crystal diagonal results in a complicated interplay of the intrinsic and induced anisotropy. The easy axis of the bare sample aligns with the $[1\bar{1}0]$ axis due to strong intrinsic uniaxial anisotropy with $K_{[110]} > K_{c1} > 0$. This easy axis rotates to an angle $\psi_{EA} = 65°$ upon attaching of the piezo-stressor and cooling to 50 K. Application of +150 V to the stressor causes the easy axis to rotate further to $\psi_{EA} = 80°$ while for -150 V the axis rotates in the opposite direction to $\psi_{EA} = 30°$. Note that the negative voltage weakens the total piezo-strain and allows domination of the intrinsic anisotropy with easy axis closer to the $[1\bar{1}0]$ axis.

The hole compensations expected in Ref. [101] are in the range $p/N_{\rm Mn} = 0.6 - 0.4$ and the relevant range of effective Mn concentrations is $x = 3 - 5\%$. $K_{[110]}$ measured in the bare epilayer is modelled by $e_{xy}^{int} = 3 - 2 \times 10^{-4}$ (slightly weaker than the strain induced in the structure at zero piezo-voltage). The in-plane anisotropy energies calculated on this parameter interval using the total strain tensor (induced and "intrinsic" components) are in good quantitative agreement with the easy axis orientations measured at the three piezo-voltages. Fig. 3.18 shows calculated curves for one representative combination of x, p, and e_{xy}^{int} from the relevant interval, for the fixed tilt of the stressor $\omega = -10°$, and for a range of induced strains σ. The curves are marked also by the voltages as we infer a simple linear relationship between σ and the voltage to facilitate comparison with the experimental paper.

The anisotropy behaviour shown in Fig. 3.18 can be described as a smooth rotation of the global energy minimum upon increase of σ rather than the "scissors" effect shown in Fig. 3.3 in Subsec. 3.1.2. The total induced strain now contains both components $\mathbf{e}^s$ and $\mathbf{e}^u$ as written in Eq. (3.18). The uniaxial basis strain $\mathbf{e}^u$ present due to the tilt of the stressor diminishes significantly one of the local minima typically occurring because of interplay of a positive cubic and a small uniaxial anisotropy component along a crystal diagonal. The remainder of the weaker local minimum is observed theoretically for σ corresponding to voltages ≈ -100 V when the $\mathbf{e}^s$ component of the induced strain and the "intrinsic" shear strain compensate each other. One would expect domination of cubic anisotropy with two equivalent local minima close to the main crystal axes if the stressor had purely diagonal alignment. The $\mathbf{e}^u$ component of the total strain of the tilted stressor makes the local minimum closer to the [010] axis less pronounced (marked by arrow in Fig. 3.18).

For completeness, we discuss the free energy phenomenological formula used in Ref. [101] to describe the in-plane angular dependence of the induced anisotropy. The decomposition of the total induced strain in Eq. (3.18) into the strain basis introduced in Eqs. (3.1)-(3.3) is not considered in that work. Instead, the induced anisotropy is described by a single uniaxial term $K_\Omega \sin^2(\psi - \Omega)$ added to the phenomenological formula rather than terms with coefficients $K_{[110]}$ and $K_{[110]}$ from Eq. (3.31). Effectively, this corresponds to a change of variables from $K_{[110]}$ and $K_{[110]}$ to K_Ω and Ω. The angle Ω is measured from the $[1\bar{1}0]$ axis and it rotates the additional uniaxial anisotropy term so that it describes the effect due to the tilted stressor. One may assume collinearity of the resulting anisotropy component with the principal elongation direction of the piezo-stressor. However, this simple situation is observed both theoretically and experimentally only when the stressor is aligned with the main crystal axes or diagonals. The misalignment for arbitrary orientation of the induced strain is due to the underlying cubic symmetry of the system incorporated into our microscopic band structure calculation in the form of the band pa-

rameters γ_2, γ_3, a_2, and a_3. It has been explained in Subsec. 3.1.3 that the collinearity of the in-plane strain and corresponding anisotropy occurs only for the strains $\mathbf{e}^s$ or $\mathbf{e}^u$ (see Eqs. (3.2) and (3.3)). For any other stressor orientation, $\Omega \neq \omega$, which is reflected on the level of the anisotropy functions by the inequality, $q_{[100]}(x,p) \neq q_{[110]}(x,p)$. It expresses the difference in the effect on magnetic anisotropy between straining the lattice along the main crystal axis and along the diagonals (see Eq. (3.9) in Subsec. 3.1.3).

The transformation from variables $K_{[110]}(x,p,\omega)$ and $K_{[110]}(x,p,\omega)$ to $K_\Omega(x,p,\omega)$ and $\Omega(x,p,\omega)$ in the phenomenological formula in Eq. (3.31) for $-\pi/2 < \omega < \pi/2$ reads,

$$\begin{aligned} F_u(\hat{M}) &= K_{[110]}(\omega)\sin^2\psi + K_{[100]}(\omega)\sin^2(\psi+\pi/4) \\ &= -K_\Omega \sin^2(\psi-\Omega), \end{aligned} \tag{3.32}$$

where:

$$\begin{aligned} \Omega(x,p,\omega) &= \frac{1}{2}\arctan\left(-\frac{K_{[100]}}{K_{[110]}}\right), \\ K_\Omega(x,p,\omega) &= -K_{[110]}\cos 2\Omega + K_{[100]}\sin 2\Omega. \end{aligned} \tag{3.33}$$

Considering the approximate relation $q_{[100]} = 0.43 q_{[110]}$ the formulae in above simplify to

$$\begin{aligned} \Omega(x,p,\omega) &= \frac{1}{2}\arctan\left(\frac{q_{[100]}(x,p)\sin 2\omega}{q_{[110]}(x,p)\cos 2\omega}\right) \\ &= \frac{1}{2}\arctan\left(0.43\tan 2\omega\right), \\ q_\Omega(x,p,\omega) &\equiv q_{[110]}(x,p)\cos 2\omega\cos 2\Omega + 0.43 q_{[110]}(x,p)\sin 2\omega \sin 2\Omega, \end{aligned} \tag{3.34}$$

where $K_\Omega = q_\Omega(\sigma - \sigma')/2$. The same transformation of variables can be used in case of strains induced along arbitrary in-plane direction by relaxation in a narrow bar (see Eqs. (3.25) and (3.26)). Then we would obtain $K_\Omega = -q_\Omega e_0 \overline{\rho}/2$.

Note that in the representation of $F_u(\hat{M})$ via $K_{[110]}$ and $K_{[110]}$ the dependence on ω can be simply factored out and the dependence on x and p is contained only in the functions functions $q_{[110]}$ and $q_{[100]}$. For our general discussion presented in this work it is therefore the more convenient form than $F_u(\hat{M})$ expressed via K_Ω and Ω.

We conclude that the in-plane alignment of the easy axis in patterned or piezo-stressed samples can be described on a semi-quantitative level by our modelling similarly to the bare (Ga,Mn)As epilayers. A more detailed description of the study [101] is presented in Subsec. 3.2.4.

3.2 Controlling magnetic anisotropy in (Ga,Mn)As - devices

After providing an overview of our calculated results and their comparison to experimental data on a broad range of material parameters reported by numerous groups active in the field, we now present a detailed description of five combined experimental and theoretical studies in which the author of this thesis directly participated. They focus on the control of magnetocrystalline anisotropies in (Ga,Mn)As by applied electric field, temperature, lattice mismatch relaxation due to post-growth lithography, and piezo-straining.

3.2.1 Field Effect Transistor

This subsection presents joint experimental and theoretical study [89] carried out in collaboration with experimentalists from the Department of Spintronics and Nanoelectronics of the Institute of Physics in Prague and from Hitachi Cambridge Laboratory.

Controlling the magnetisation by low-voltage charge depletion in FETs has been a formidable challenge due to the typically large carrier concentrations in ferromagnets compared to semiconductors. Here we demonstrate that this concept is viable in an all-semiconductor, p-n junction transistor utilising a thin-film ferromagnetic (Ga,Mn)As channel. We report experimental observation and detailed theoretical analysis of gate-dependent Curie temperature and magnetoresitance, and persistent magnetisation switchings induced by short electrical pulses of a few volts.

One of the major driving forces in spintronic research is to allow the field to progress from sensors and memories to logic devices which requires development of three-terminal spintronic transistors. Ferromagnetic semiconductors such as (Ga,Mn)As are particularly favourable materials in this research area for their rich phenomenology of magnetoresistive characteristics and the potential to combine and integrate spintronics with conventional semiconductor microelectronics [71, 55]. Only a few works have so far reported electrical gating, via charge depletion, of magnetic properties of (III,Mn)V ferromagnetic semiconductor FETs. Curie temperature and coercive field variations have been demonstrated by applying tens of Volts on a top-gate FET with an AlOx dielectric separating a metal gate from an (In,Mn)As or (Ga,Mn)As channel [81, 20, 18]. The difficulty to achieve efficient depletion in the highly doped ferromagnetic semiconductor films has motivated research in several alternative routes to the field-control of magnetism in (Ga,Mn)As, including the electro-mechanical gating by piezo-stressors [101, 88, 35] or fabrication of small island Coulomb blockade transistors with magnetisation dependent single-electron charging energy [150]. In this work we discuss an all-semiconductor, epitaxial p-n junction FET allowing for a large depletion of (Ga,Mn)As thin films at a few Volts. We demonstrate various gatable magnetic characteristics ranging from the anisotropic magnetoresistance and the Curie temperature to coercivity and magnetisation switchings induced by short electrical pulses.

Device Structure and Simulations

The schematic cross-section of the III-V heterostructure used in our study is shown in Fig. 3.19(a). It is a semiconductor p-n junction FET specially designed to accommodate ferromagnetism in the p-type region and its efficient depletion by low voltages. From the top, the structure comprises a 5 nm thick approximately 2.5% Mn-doped GaAs capped by 2 nm of undoped GaAs to prevent oxidation of the underlying transition metal doped semiconductor film. These two top layers were grown by low-temperature MBE to avoid Mn precipitation. The 2.5% doping was chosen to pass the insulator-to-metal transition threshold which for the moderately deep $\mathrm{Mn_{Ga}}$ acceptor is between 1-2% and to achieve robust ferromagnetic state with Curie temperature $T_c \approx 30$ K, while still minimising the number of unintentional interstitial-Mn impurities [71, 55, 54]. (The interstitial Mn is highly mobile at the growth temperature and its diffusion into the p-n junction would result in detrimental leakage currents.) The Curie temperature measured by SQUID in an unpatterned piece of the wafer is comparable to maximum T_c's achieved at the same

Mn-doping in thicker films, indicating a very good quality of the ultra-thin ferromagnetic semiconductor epilayer.

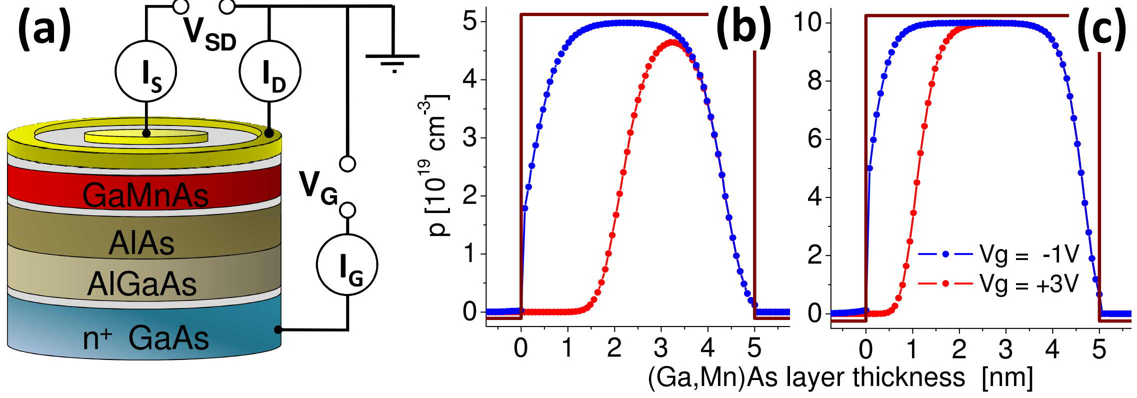

Figure 3.19: (a) Schematic of the ferromagnetic p-n junction FET structure and the Corbino disk geometry of the source and drain contacts. (b) and (c) Numerical simulations of the hole density profile at -1 V (accumulation) and +3 V (depletion), considering a 2×10^{19} cm^{-3} electron doping in the n-GaAs and 5×10^{19} cm^{-3} and 10^{20} cm^{-3} hole doping in the p-(Ga,Mn)As.

The n-type gate electrode is formed by a highly Si-doped (2×10^{19} cm^{-3}) GaAs grown by high-temperature MBE. The large electron doping is required in order to achieve appreciable and voltage dependent depletion of the ferromagnetic p-region with hole doping $\sim 10^{20}$ cm^{-3}. The built-in electrostatic barrier due to the depletion effect at the p-n junction is further supported by inserting a 10 nm $Al_{0.3}Ga_{0.7}As$ spacer layer with a large conduction band off-set to the neighboring n-GaAs and a 10 nm AlAs spacer with a large valence band off-set to the neighboring p-(Ga,Mn)As.

Self-consistent numerical simulations, shown in Fig. 3.19(b), confirm that sizable depletions are achievable by gating the heterostructure with less than 4 Volts. Measurements discussed below were done at voltages between -1 V (forward bias) to $+3$ V (reverse bias) for which the leakage currents between the n-GaAs gate and p-(Ga,Mn)As channel were more than two orders of magnitude smaller than the channel currents. The (Ga,Mn)As channel was lithographically patterned in a low-resistance Corbino disk geometry with the inner contact diameter of 500 μm and the outer diameter of 600 μm.

Voltage control of Curie temperature and magnetoresistance

In Fig. 3.20(a) the measured channel resistances vs. gate-voltage at temperature 4-40 K are plotted. Both at low temperatures and near T_c a marked increase of the channel resistance at positive voltages is observed. It is consistent with the depletion of the (Ga,Mn)As channel as predicted by the simulations in Fig. 3.19(b) and with the vicinity of the metal-insulator transition which causes the superlinear increase of R with V_g. At 4 K, the increase of R between -1 and +3 V is by more than 100%.

Fig. 3.20(b) shows the voltage-dependence of the Curie temperature in the ferromagnetic p-n junction. The measurement technique is distinct from previous studies which relied on approximate extrapolation schemes based on Arrot plot measurements at finite magnetic fields [81, 18, 128]. Recent observation and interpretation [80] of the peak in

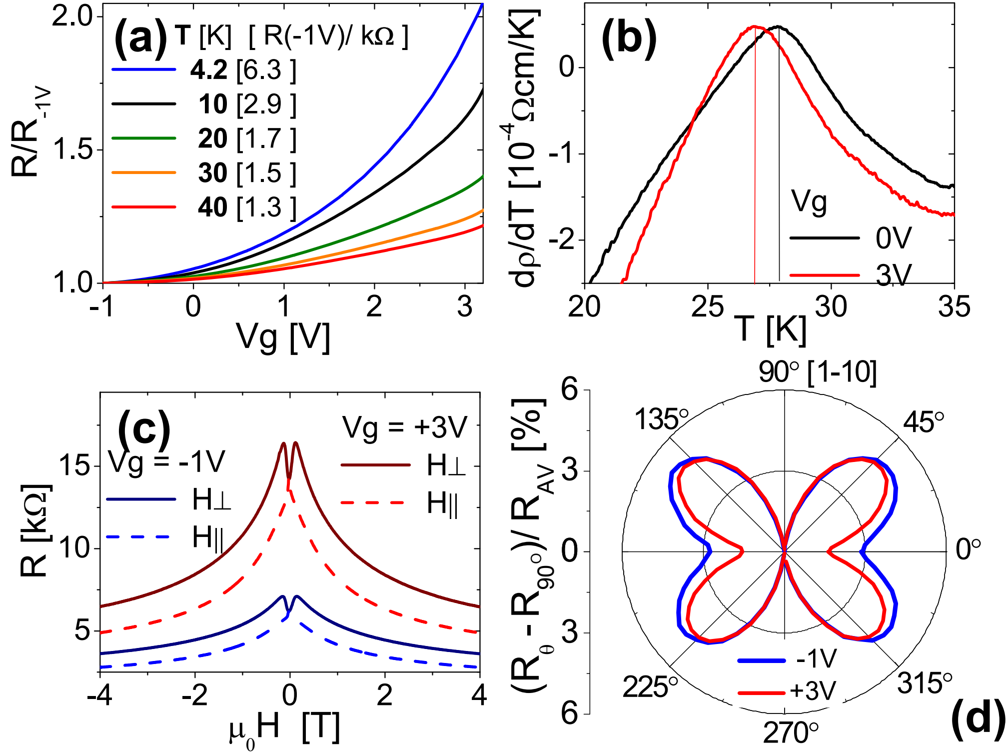

Figure 3.20: (a) Gate voltage dependence of the p-(Ga,Mn)As channel resistance at temperatures 4-40 K. (b) Temperature derivative of the measured channel resistivity at 0 and +3 V. The maximum corresponds to T_c. (c) In-plane ($H_{\|}$) and perpendicular-to-plane ($H_{\perp}$) magnetic field sweep measurements of the channel resistance at -1 and +3 V. The difference between the $H_{\|}$ and $H_{\perp}$ sweeps above the reorientation field of $\approx$ 150 mT corresponds to the out-of-plane AMR. (d) In-plane AMR measured at saturation in a rotating in-plane field at -1 and +3 V.

the zero-field temperature derivative of the resistance at the Curie point in good quality (Ga,Mn)As materials has provided the tool for direct transport measurements of T_c in microdevices without relying on any extrapolation schemes. In Fig. 3.20(b) differentiated resistivity curves obtained in the device at 0 and +3 V are plotted. The data show a clear shift of the Curie temperature, i.e., the magnetisation can be turned on and off in parallel with accumulating and depleting holes in the ferromagnetic semiconductor channel by biasing the p-n junctions with a few Volts.

Curie temperature variations provide the key physical demonstration of the low-voltage control of magnetisation. Nevertheless, for most spintronic functionalities it is not required to destroy the ordered state of spins but only to change their collective orientation. We therefore focus on effects related to reorientations of the unit vector of the macroscopic moment. To avoid thermal fluctuations of the magnetisation, all measurements are done far from the Curie point at 4 K.

Fig. 3.20(c) shows magnetoresistance traces recorded during in-plane and perpendicular-to-plane sweeps of an external magnetic field, at gate voltages of -1 and +3 V. Apart from

the negative isotropic magnetoresistance (IMR), the data indicate a remarkably large anisotropic magnetoresistance (AMR) effect which at saturation reaches $\sim 30\%$. (Note that AMR sensors fabricated in transition metal ferromagnets with AMR ratios of a few per cent [75] marked the dawn of spintronics in the early 1990's.) The resistance is larger for the perpendicular-to-plane magnetisation orientation and the size of the effect is enhanced by depletion. The electrical response of the system to magnetisation rotations is both large and tuneable by low gate voltages.

The magnetoresistance traces in Fig. 3.20(c) indicate that the film has a magnetic anisotropy favouring in-plane magnetisation, which is overcome by an external field of approximately 150 mT. At weaker magnetic fields, magnetisation switching effects are confined to the plane of the ferromagnetic film. The qualitative nature of the in-plane magnetic anisotropy landscape which determines the switching processes can be scanned in the Corbino microdevice by recording the AMR at a rotating in-plane saturation field. Unlike in the out-of-plane rotation AMR, contributions depending on the relative angle between the in-plane magnetisation and current average out over the radial current lines. The in-plane AMR then depends purely on the angle between magnetisation and crystallographic axes [103]. It reflects therefore the same underlying symmetry breaking crystal fields as the magnetic anisotropy. The measurements, shown in Fig. 3.20(d), unveil a cubic anisotropy along the [110]/[$1\bar{1}0$] crystal axes and an additional uniaxial term breaking the symmetry between the [110] and [$1\bar{1}0$] directions. Although the specific responses to these symmetries can be very different for the AMR and for the magnetic anisotropy, the presence of the cubic and uniaxial AMR terms and their sensitivity to the gate voltage observed in Fig. 3.20(d) suggest that the in-plane magnetisation orientation itself can be switched at weak magnetic fields by the low voltage charge accumulation or depletion.

Persistent magnetisation switching with short voltage pulses

A variable width of hysteretic magnetisation loops measured at different constant gate voltages, shown in Fig. 3.21(a), is the prerequisite for observing electrically assisted magnetisation switchings. Note that electrical measurements of magnetisation reorientations utilised in Figs. 3.21 and 3.22 are facilitated in the system by the IMR which responds to abrupt changes of the total magnetic induction upon a 180° reversal, and by a combined effect of the IMR and of the AMR for intermediate switchings by less than 180°. The amplitude of the AMR and the IMR contributions are similar in the experiments of this study. The switchings by short low-voltage pulses are demonstrated in Fig. 3.21(b) and analysed in detail in Fig. 3.22. The experiments were performed at constant field-sweep rate of 0.1 mT per second starting from negative saturation field of 1 T. The gate voltage was set to a base value of -1 V and then after each measurement step spanning 1 second a 10 ms voltage pulse of a fixed magnitude was applied and then returned to the base voltage. The technique allows for the demonstration of the magnetic response to short electric pulses and the persistence of induced reorientations of the magnetisation vector. It also removes potentially obscuring variations among the resistance traces in regions away from magnetisation switchings which are caused by different slopes of the negative IMR at different gate voltages.

Fig. 3.21(b) compares measurement with no pulses (constant -1 V gate voltage) and data acquired at 0 to +4 V peak voltages. The field was swept along the [$1\bar{1}0$] crystal

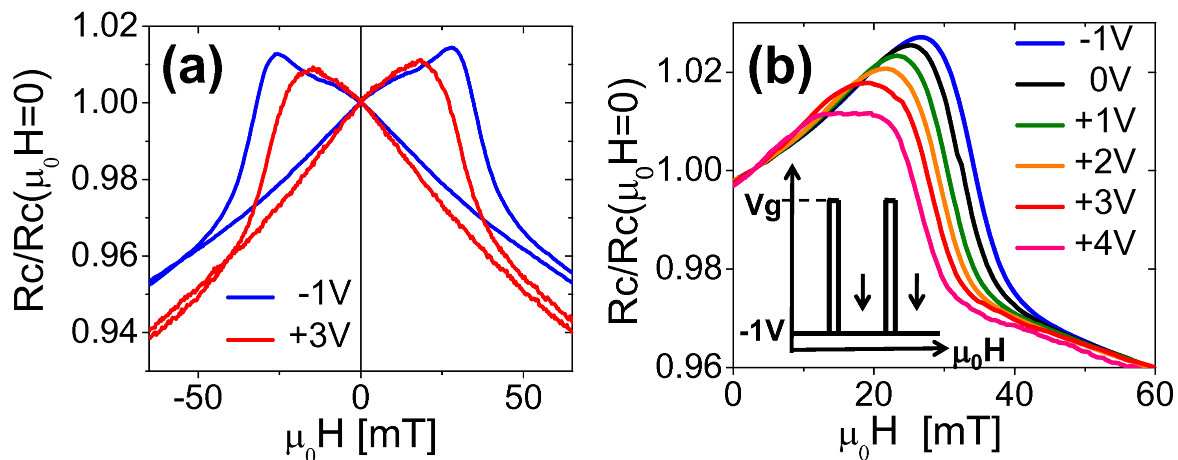

Figure 3.21: (a) Hysteretic field sweep measurements at field angle $\theta = 90°$ for constant gate voltages of -1 and +3 V. (b) Up-sweeps of the $\theta = 90°$ in-plane field at constant -1V gate voltage, and for measurements with the gate voltage set to a base value of -1 V and with short additional voltage pulses corresponding to a total peak voltage of 0, +1 , +2, +3, and +4 V, respectively.

direction ($\theta = 90°$, where θ is the in-plane field angle measured from the [110] direction). As argued in detail in Fig. 3.22 and confirmed by SQUID magnetisation measurements on an unpatterned part of the wafer, $[1\bar{1}0]$ is the main magnetic easy axis. The negative IMR then allows for observation of the drop in R corresponding to a 180° reversal from an antiparallel to a parallel configuration of field and magnetisation and a corresponding increase of the magnetic induction. As the applied peak voltage increases, the magnetisation reversals consistently shift to lower magnetic fields and the magnetisation remains switched when the peak voltage pulse is turned off.

Theoretical analysis

To discuss the detail phenomenology of these persistent low-voltage induced magnetisation switchings field-sweep measurements at fixed field angles spanning the whole interval in 5° steps are presented in Figs. 3.22(a) and (b). Panels (a) and (b) show colour-maps of the resistance as a function of the field magnitude and angle for -1 V constant voltage and for the +3 V peak-voltage measurements, respectively. The main effect observed in these plots is the overall suppression of the magnitude of the switching fields by depletion. Additionally, the relative suppression is stronger at $\theta = 0$ than at 90°, as highlighted in Fig. 3.22(c). This indicates that both the magnitude and ratio between the uniaxial and cubic anisotropy fields is modified by the gate voltage. To quantify the depletion induced modification of the magnetic anisotropy we extracted the anisotropy constants from fitting the measured $\theta = 0$ and 90° switching fields to a single domain anisotropy energy model, $E(\theta, \phi) = K_u \sin^2 \phi - K_c \sin^2 2\phi/4 - MH \cos(\theta - \phi)$, where H and M are the magnitudes of the external field and magnetisation, respectively, and ϕ is the magnetisation angle. The uniaxial constant K_u is relatively weak compared to the cubic constant K_c, as shown in Fig. 3.22(d). They both have a negative sign corresponding to

the magnetic easy directions along the $[1\bar{1}0]$ and [110] axes and the most easy direction along $[1\bar{1}0]$. As shown also apparent from Fig. 3.22(d), the dominant effect of depletion is in reducing the magnitude of K_c. Fig. 3.22(e) shows how the corresponding anisotropy energy profiles at $H = 0$ evolve with depletion.

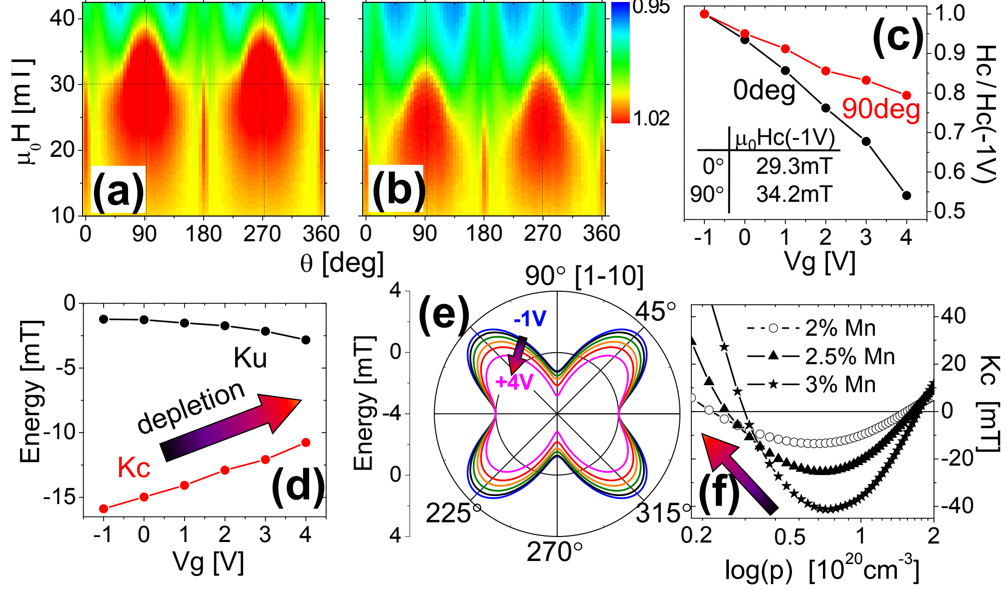

Figure 3.22: (a) and (b) Color maps of channel resistance as a function of the in-plane field angle and magnitude (normalised to $H = 0$ resistance) for -1V constant voltage and +3V peak voltage measurements, respectively. (c) Switching fields at field angles $\theta = 0$ has a stronger suppression than at 90° as a function of the gate voltage. (d) Uniaxial and cubic anisotropy constants and (e) corresponding anisotropy energy profiles derived from the measured $\theta = 0$ and 90° switching fields. (f) Microscopic calculations of the cubic anisotropy constant. Arrows in (d) and (f) highlight the common trend with depletion.

We now discuss the key experimental observations by employing the magnetic anisotropy theory derived from $\boldsymbol{k} \cdot \boldsymbol{p}$ effective Hamiltonian modelling of hole mediated ferromagnetism in (Ga,Mn)As described in sections 2.1 and 3.1. Calculations for 2.5% local moment doping and hole density $p \sim 1 \times 10^{20}$ cm^{-3}, for which the simulations in Fig. 3.19(b) predict hole depletions consistent with the measured variations of the channel resistance at temperatures near T_c, yield $T_c \sim 20$ K and $dT_c/dp \approx 1 \times 10^{-19}$ Kcm^3. Both the absolute value of the Curie temperature and the few Kelvin suppression of T_c at a $\sim 20\%$ hole depletion predicted by the theory are consistent with our p-n junction simulations and the measured gate-dependent T_c values.

As shown in Fig. 3.22(f), the microscopically calculated K_c constant changes sign at hole density of approximately 1.5×10^{20} cm^{-3}. Below this density it favours the $[110]/[1\bar{1}0]$ magnetisation directions, consistent with the experimental data. The typical magnitudes of K_c of ~ 10 mT are also consistent with experiment and considering the large gate

action seen at low temperatures we can also associate, semiquantitatively, the decreasing magnitude of the experimental K_c at depletion with the behaviour of the theoretical K_c at low hole densities.

To conclude, this combined experimental and theoretical work demonstrates low-voltage control of magnetic properties of a p-n junction FET via depletion effect in the ferromagnetic semiconductor channel. The experiments have shown and theory explained variable T_c and AMR, and demonstrated magnetisation switchings induced by short electric field pulses of a few volts. Our concept of the spintronic transistor is distinct from previously demonstrated high-voltage metal-oxide-semiconductor ferromagnetic FETs [81, 18, 128] or electro-mechanically gated ferromagnets by piezo-stressors [58, 63, 12, 13, 101, 88, 35]. It is realised in an all-semiconductor epitaxial structure and offers a principally much faster operation. In basic physics research, we expect broad utility of our results in studies of carrier-mediated ferromagnetism and in interdisciplinary fields combining ferromagnetism and SOC effects with localisation and quantum-coherent transport phenomena [78] controlled by carrier depletion.

3.2.2 Relaxation in arrays of microbars

This subsection presents joint experimental and theoretical study [59]. It was carried out in collaboration with experimentalists from the Department of Spintronics and Nanoelectronics of the Institute of Physics in Prague, Charles University in Prague, University of Nottingham, and Hitachi Cambridge Laboratory.

The control of the magnetocrystalline anisotropy in (Ga,Mn)As epilayers has been achieved by choosing different substrates and therefore different growth induced strain in the magnetic layer, by varying the growth parameters of the (Ga,Mn)As film, and by postgrowth annealing [33, 96]. Reversible electrical control of the magnetocrystalline anisotropy has been demonstrated by utilising piezo-electric stressors [101, 23, 88] or by electrostatic gating in thin-film (Ga,Mn)As field effect transistor structures [19, 89]. Recently, a local control of the magnetocrystalline anisotropy has been reported, which provides the possibility for realising non-uniform magnetisation profiles and which can be utilised, e.g., in studies of current induced magnetisation dynamics phenomena or non-volatile memory devices [149, 93]. In these studies an efficient method of local strain control has been used which is based on lithographic patterning that allows for the relaxation of the lattice mismatch between the (Ga,Mn)As epilayer and the GaAs substrate [147, 46, 149, 93, 103]. The modification of the strain distribution can cause strong changes of the magnetic anisotropy for strains as small as 10^{-4}. The high efficiency and practical utility of the lithographic pattering control of magnetic anisotropy in (Ga,Mn)As, demonstrated in the previous works, have motivated a thorough investigation of the phenomenon which is described in this subsection. The study is based on combined high-resolution x-ray diffraction and magnetisation measurements and on macroscopic modelling of the strain relaxation and microscopic calculations of the corresponding magnetic anisotropies.

We investigate two sets of lithographically patterned (Ga,Mn)As microbars which differ in the thickness to width ratio, Mn doping, and hole concentration. First, the structural properties are studied by high resolution x-ray diffraction of microbars patterned in the thicker, higher Mn doped as-grown (Ga,Mn)As material which has a large growth induced strain. The spatial distribution of the lattice relaxation in the stripe cross-section is de-

termined by comparing the measured intensity maps to maps simulated using the theory of elastic deformations and the kinematic scattering theory. The good agreement of the measurement and simulation shows that the applied model is quantitatively reliable in predicting the local lattice relaxation in patterned epilayers subject to small lattice mismatch. This allows us to infer the much weaker lattice relaxation in stripes fabricated in the thinner and lower Mn concentration (Ga,Mn)As by performing only the elastic theory simulations.

In the next step, the magnetic properties of the samples are measured by SQUID and the anisotropy coefficients are extracted. Stronger focus is on stripes fabricated in the thinner, annealed (Ga,Mn)As epilayer where the SQUID magnetometry data allow for a reliable extraction of the temperature dependence of the anisotropy coefficients and for direct comparison with the microscopic model. A linear superposition of the in-plane uniaxial anisotropies and the presence of a single magnetic domain were assumed when analysing the SQUID magnetometry data. The rotation of the easy axis by 90° caused by the micropatterning, completely over-writing the underlying material anisotropy at all studied temperatures, is demonstrated.

Finally, we calculate the anisotropy coefficients for a range of material parameters and temperatures below T_C. The lattice relaxations determined form the x-ray diffraction measurement and from finite element simulations are the inputs of the microscopic calculations of the magnetocrystalline anisotropy. The microscopic model we use is described in sections 2.1 and 3.1.

Samples

Two sets of patterned (Ga,Mn)As epilayers grown on GaAs substrate are studied. The samples in set A are doped nominally to 5% of Mn, annealed for approximately 75 minutes at 180°C, and the epilayer is 25 nm thick. The Curie temperature $T_C \approx 120$ K corresponds to optimal annealing of the wafer [57]. The control sample A_0 was not patterned. Samples $A_{[1\bar{1}0]}$ and $A_{[110]}$ were patterned into 25 mm^2 arrays of stripes at an angle $\alpha \approx 140°$ and $\alpha \approx 50°$, respectively. Here the angle α is measured from the [100] crystallographic direction. The unintentional 5° misalignment from the crystal diagonals caused by the microfabrication is accounted for when analysing the data. The stripes are 750 nm wide, 100 μm long, and separated by 450 nm gaps, as measured by Atomic Force Microscope (AFM). The fabrication was done by electron beam lithography and wet chemical etching using a solution of phosphoric acid and hydrogen peroxide. The AFM measurements revealed an etch depth of ≈ 60 nm, and cross-sectional Scanning Electron Microscope (SEM) imaging confirmed that the wet etching leads to anisotropic stripe cross-sections, with the $A_{[110]}$ stripes being undercut and the $A_{[1\bar{1}0]}$ stripes overcut, as shown in Fig. 3.23.

The samples in set B are doped nominally to 7%, not annealed, the epilayer is 200 nm thick, and the Curie temperature $T_C \approx 85$ K. The control sample B_0 was not patterned. Samples $B_{[1\bar{1}0]}$ and $B_{[010]}$ were patterned into arrays of 1 μm wide stripes with 1 μm wide gaps along the $[1\bar{1}0]$ and [010] crystallographic directions, respectively. The fabrication was done by electron beam lithography and dry chemical etching with an etch depth ≈ 700 nm ($B_{[1\bar{1}0]}$) and ≈ 900 nm ($B_{[010]}$). The sides of the stripes are slightly overcut in both cases owing to the symmetric dry etching.

With respect to our theoretical modelling of the magnetic anisotropies of the samples,

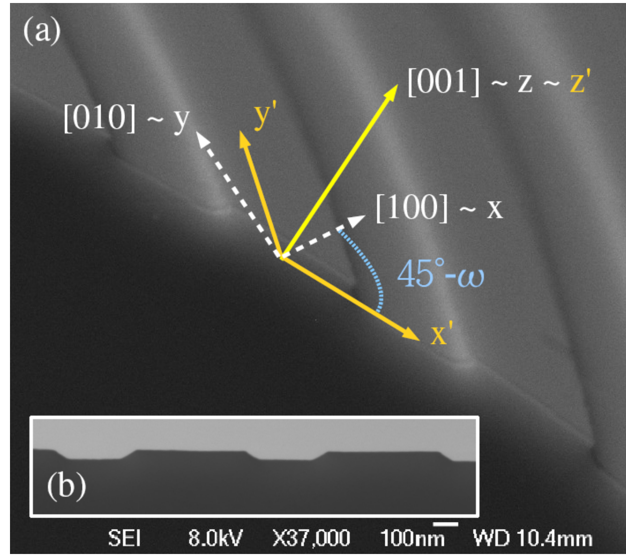

Figure 3.23: Cross-sectional scanning electron microscope (SEM) images of the stripes in set A. (a) Image of sample $A_{[110]}$ showing both the cleaved face and the top surface. Although difficult to discern, the profile is undercut. The curvature is due to the sample stage drifting during the exposure of the image. Introduction of coordinates fixed to the crystallographic axes and dashed coordinates fixed to the stripe geometry: the relaxation direction perpendicular to the stripes, the x' axis, is rotated by angle $\omega - 45°$ with respect to the [100] crystallographic direction, the x axis. The angle $\omega \equiv \alpha - 45°$ describes the rotation of x' with respect to the $[1\bar{1}0]$ axis. (b) Image of sample $A_{[1\bar{1}0]}$ showing a cut through the stripes and substrate in the $x' - z'$ plane revealing the overcut sides of the stripes.

we recall that relating the prediction to the measurement based on the material parameters is not straight forward due to the presence of unintentional compensating defects in the epilayers. We emphasise that in figures presenting calculated data the Mn concentration labelled as x corresponds to the density of uncompensated local moments, i.e., to x_{eff}.

Another input parameter of the theoretical modelling is the lattice mismatch which is different in set A and B as it depends on the partial concentrations of Mn atoms in substitutional and interstitial positions in the lattice and of other unintentional impurities [72]. The lattice mismatch is determined by direct x-ray measurement as detailed in the following section.

Fig. 3.23 introduces the coordinate system fixed to the crystallographic axes: x-axis along the [100] direction, y-axis along the [010] direction, and z-axis along the [001] direction which is the frame of reference for the microscopic magnetocrystalline anisotropies. The dashed coordinate system is fixed to the stripe geometry: x'-axis lies along the relaxation direction transverse to the stripe, y'-axis along the stripe, and z'-axis along the growth direction coinciding with the z-axis. The dashed coordinates are the natural reference for the macroscopic lattice relaxation simulations. (The same notation as in subsection 3.1.4 is used.)

Lattice relaxation

The lattice of thin (Ga,Mn)As films grown epitaxially on GaAs substrates is strained compressively due to a lattice mismatch $e_0 = (a_s - a_0)/a_0 < 0$ where a_s and a_0 are the lattice constant of the substrate and of the relaxed free-standing (Ga,Mn)As epilayer, respectively. The narrow stripes allow for anisotropic relaxation of the compressive strain present in the unpatterned epilayer. An expansion of the crystal lattice along the direction perpendicular to the bar occurs while the epilayer lattice constant along the bar remains unchanged. Parameters sufficient for determination of the induced strain are the lattice mismatch e_0 and the shape of the stripe, mainly the thickness to width ratio of the stripe. In the regime of small deformations the components of the induced strain are linearly proportional to the lattice mismatch. The strain tensor in the coordinate system fixed to the stripe is given in Eq. (3.13) where the lattice relaxation is quantified by $\rho(x', z')$ which varies over the stripe cross-section, c_{12} and c_{11} are the elastic moduli. The strain components in this work are expressed with respect to a relaxed free-standing (Ga,Mn)As epilayer. In this subsection the geometry of the stripes, the size of the lattice mismatch, and the spatial dependence of the lattice relaxation $\rho(x', z')$ are investigated experimentally and theoretically. The results are used as an input of the microscopic modelling of the magnetic anisotropies in subsection 3.2.2.

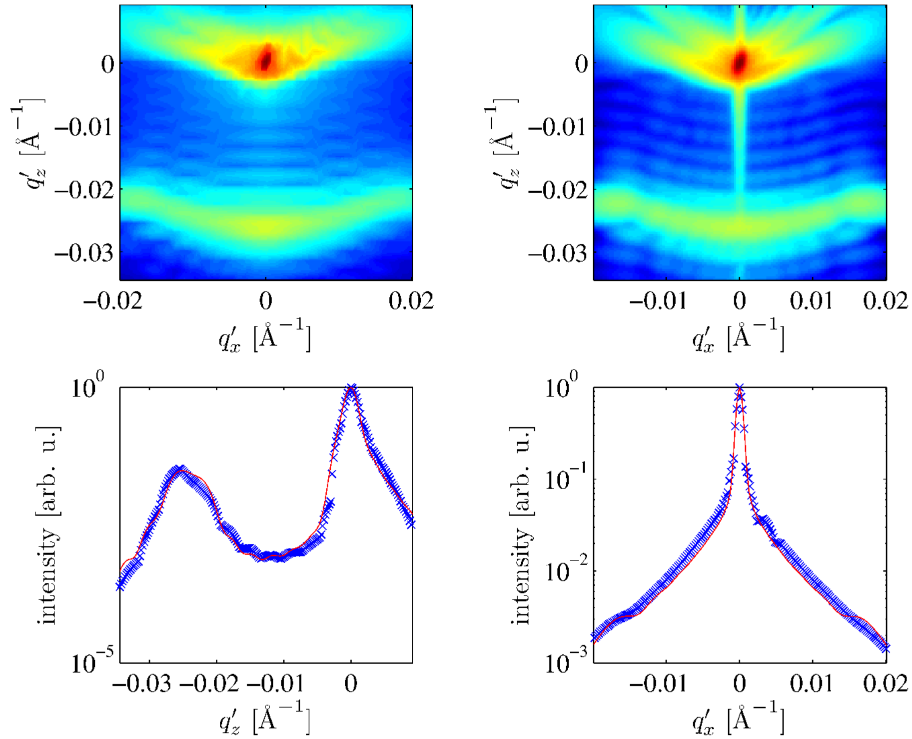

Figure 3.24: The measured (upper left panel) and simulated (upper right panel) reciprocal-space maps in the symmetric 004 diffraction of sample $B_{[010]}$. In the bottom row, the measured (points) and simulated (lines) intensities integrated along the horizontal (left) and vertical (right) directions are plotted. In the intensity maps, the colour scale is logarithmic.

Microbars in set B have larger thickness to width ratio than microbars in set A.

Therefore the relaxation is expected to be larger in set B. At the same time, the (Ga,Mn)As epilayer has larger volume in set B, primarily due to a larger number of interstitial Mn in this higher doped unannealed material. The larger film thickness and larger growth strain in set B make these materials significantly more favourable for an accurate x-ray diffraction analysis of the strain profile in the patterned microbars.

The lattice relaxation in samples $B_{[1\bar{1}0]}$ and $B_{[110]}$ was measured by high-resolution x-ray diffraction using the synchrotron source at ESRF Grenoble (beamline ID10B, photon energy 7.95 keV). For a reliable determination of both in-plane (u'_x) and vertical (u'_z) components of the elastic displacement field the reciprocal-space distribution of the diffracted intensity around the symmetric 004 and asymmetric 404 reciprocal lattice points was measured. The asymmetric diffraction was chosen so that the in-plane component of the corresponding reciprocal lattice vector h was perpendicular to the stripes. The diffracted radiation was measured by a linear x-ray detector lying in the scattering plane.

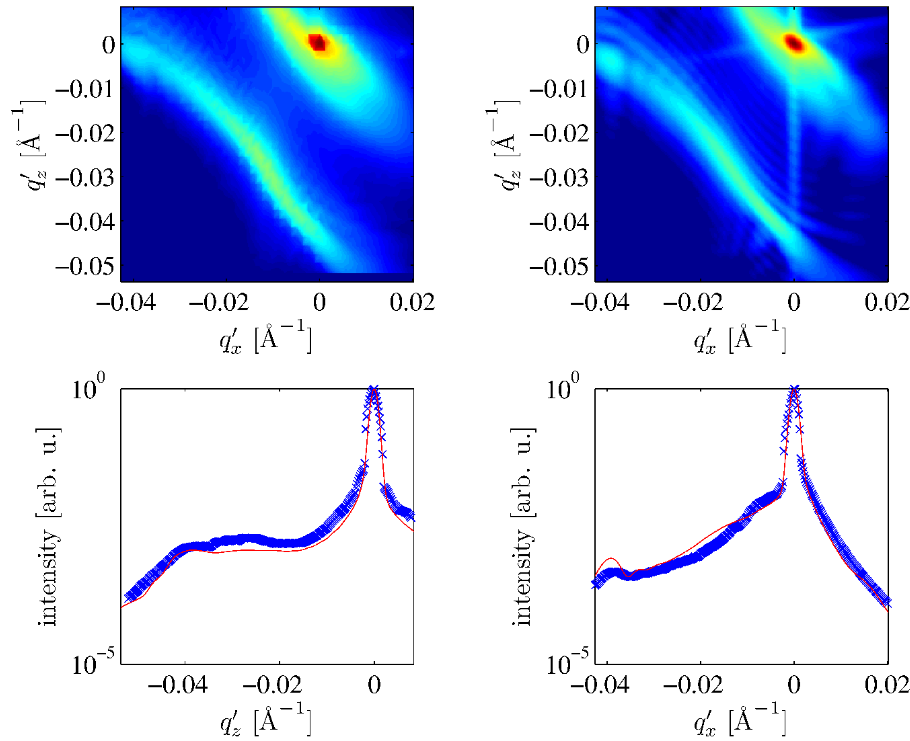

Figure 3.25: The measured (upper left panel) and simulated (upper right panel) reciprocal-space maps in the asymmetric 404 diffraction of sample $B_{[010]}$. In the bottom row, the measured (points) and simulated (lines) intensities integrated along the horizontal (left) and vertical (right) directions are plotted. In the intensity maps, the colour scale is logarithmic.

Figs. 3.24 and 3.25 present examples of the measured (upper left panels) and simulated (upper right panels) reciprocal space maps, showing two maxima corresponding to the reciprocal lattice points of the GaAs substrate and the (Ga,Mn)As layer. The bottom panels show the measured and simulated integrated intensities for two directions in the reciprocal space. Since the lateral stripe period was larger than the coherence width of the primary radiation, different stripes were irradiated incoherently, so that the lateral

intensity satellites stemming from the lateral stripe periodicity could not be resolved. The measured intensity distribution is therefore proportional to the intensity scattered from a single microbar.

We fitted the measured intensity maps to numerical simulations based on the kinematic scattering theory and the theory of anisotropic elastic medium. We used a finite-element simulation (implemented in Structural Mechanics Module of Comsol Multiphysics, standard partial differential equation solver) to obtain the local relaxation distribution $\rho(x', z')$ in the stripes and derived the corresponding reciprocal space map. The angle of the sides of the stripes and the lattice mismatch e_0 of the (Ga,Mn)As and GaAs lattices were the two fitting parameters. The left column of Figs. 3.24 and 3.25 shows the measured diffraction maps and projections. The right column shows the simulated results. The lateral and vertical projections of the measured and simulated intensity maps as well as the whole maps are used in the fitting. The coordinates q'_x and q'_z span the reciprocal space conjugate to the real space with coordinates x' and z' fixed to the stripe. They are measured with respect to the reciprocal lattice point 004 and 404.

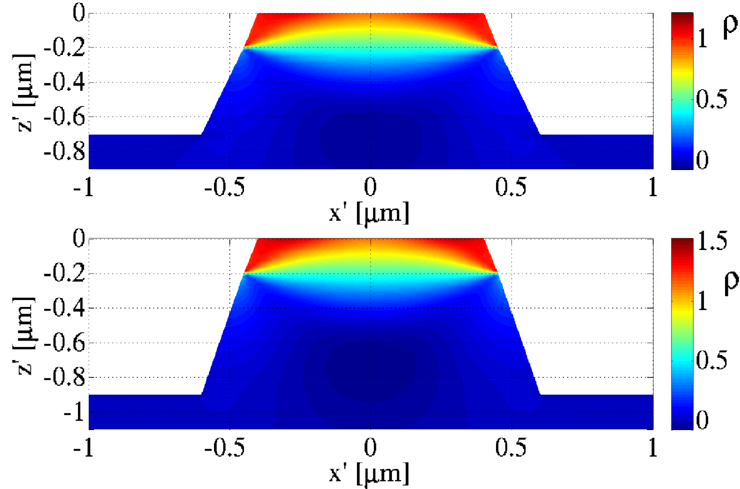

Figure 3.26: Finite element calculation of the lattice relaxation, $\rho(x', z')$, on the cross-section perpendicular to the slightly overcut stripes $B_{[1\bar{1}0]}$ (upper panel) and $B_{[110]}$ (lower panel). The cross-section of one stripe and the underlying substrate is plotted. The relaxation $\rho = 1$ and $\rho = 0$ corresponds to a full relaxation of the lattice and to a lattice under a compressive strain of the unpatterned layer, respectively. Both stripes are close to full relaxation.

The remarkable agreement of the measured and simulated diffraction maps shows that our model of the lattice deformations is quantitatively relevant in determining the local lattice relaxation $\rho(x', z')$ in the stripes shown in Fig. 3.26, the lattice mismatch between the epilayer and the substrate, $e_0 = -0.38 \pm 0.03\%$ for set B, and the stripe geometry, a trapezoidal cross-section of the stripe also shown in Fig. 3.26. The largest relaxation is observed in the corners of the stripes.

The slopes of the sides in set B are few degrees larger than angles typically occurring when dry etching is used during the patterning process. Note that the x-ray diffraction reveals only the regions with regular lattice structure whereas the dry etching can leave a

thin non-uniform amorphous coating on the stripes which leads to the unexpected non-rectilinear shape of the stripe cross-section resulting from the fitting.

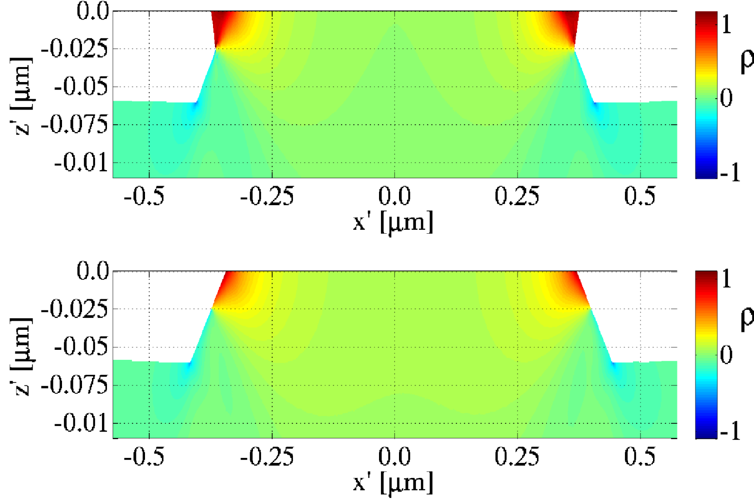

Figure 3.27: Finite element calculation of the lattice relaxation, $\rho(x', z')$, on the cross-section perpendicular to the undercut stripes $A_{[110]}$ (upper panel) and overcut stripes $A_{[1\bar{1}0]}$ (lower panel). The cross-section of one stripe and the underlying substrate is plotted. The relaxation $\rho = 1$ and $\rho = 0$ corresponds to full relaxation of the lattice and to a lattice under a compressive strain of the unpatterned layer, respectively. All stripes show weaker net relaxation than the stripes in set B.

In the next step, we use our modelling of the lattice relaxation also for stripes of set A where the x-ray diffraction would be less accurate due to the small volume of the epilayer, however, the relaxation mechanism should be of the same nature as in set B. Fig. 3.27 shows the spatial dependence of the function $\rho(x', z')$ for two different geometries relevant to samples in set A. The shape of the stripe cross-section cannot be determined from the SEM image of Fig. 3.23 with nanometer accuracy. This uncertainty cannot be neglected in the undercut stripes $A_{[110]}$. Therefore, more geometries (slopes of the sides) were simulated and one representative example is given in the upper panel of Fig. 3.27. On the other hand, the precise shape of the sides does not play such an important role in case of the overcut stripes $A_{[1\bar{1}0]}$ shown in the lower panel of Fig. 3.27. In all geometries, the local induced strain is stronger closer to the edges of the stripes.

The comparison of the macroscopic simulations and x-ray diffraction measurements are done on the level of the full spatial distribution of the relaxation $\rho(x', z')$. The magnetic characteristics, considered in this work in the single domain approximation, are analysed based on the net lattice relaxation. Here we take advantage of the direct proportionality of the magnetocrystalline anisotropy to the corresponding strain [22, 155] and calculate the mean anisotropy from the spatial average of $\rho(x', z')$ over the stripe cross-section. We will denote this average quantity by $\hat{\rho}$ in the rest of the subsection. (We caution that in this study $\hat{\rho}$ is a function of ω, contrary to the approximation used in Subsec. 3.1.4 where the average relaxation is denoted by $\overline{\rho}$.)

The last step in obtaining the input parameters for the microscopic modelling is writing the net in-plane components of the total strain tensor introduced in Eq. (3.13) in the

coordinate system fixed to the main crystallographic axes introduced in Fig. 3.23:

$$\begin{aligned} e_{xx} &= e_0\left(1-\frac{\hat{\rho}}{2}-\frac{\hat{\rho}}{2}\sin 2\omega\right), \\ e_{yy} &= e_0\left(1-\frac{\hat{\rho}}{2}+\frac{\hat{\rho}}{2}\sin 2\omega\right), \\ e_{xy} &= e_0\frac{\hat{\rho}}{2}\cos 2\omega, \end{aligned} \tag{3.35}$$

where the angle ω is measured from the $[1\bar{1}0]$ axis and the angle $\omega - 45°$ describes the rotation of the relaxation direction (the dashed coordinates) with respect to the crystalline coordinate system. Note that the above strain components coincide with those in Eq. (3.13) when $\omega = 45°$, i.e., the relaxation direction is aligned with the [100] axis. We emphasise that the average relaxation $\hat{\rho}$ depends on ω. We rotate the elasticity matrix describing the cubic crystal when simulating the lattice relaxation along different directions.

The strain components e_{xx}, e_{yy}, and e_{xy} for the stripes in set A are obtained from the macroscopic simulations and considering $e_0 \approx -0.22\%$ [158, 57]. Table 3.2 summarises

	$e_0[\%]$	$\hat{\rho}$
$A_{[1\bar{1}0]}$	-0.22 ± 0.03	0.184 ± 0.005
$A_{[110]}$	-0.22 ± 0.03	0.24 ± 0.05
$B_{[1\bar{1}0]}$	-0.38 ± 0.03	0.79 ± 0.01
$B_{[010]}$	-0.38 ± 0.03	0.99 ± 0.01

Table 3.2: The lattice mismatch e_0 and the lattice relaxation $\hat{\rho}$ for the patterned samples as entering the microscopic calculations in subsection 3.2.2. The value of e_0 in set B is determined from the x-ray diffraction experiment, whereas e_0 in set A is inferred from the partial Mn concentrations using the analysis of Refs. [158] and [57].

the parameters determined in this section.

Magnetic anisotropies extracted from experimental data

In-plane magnetic anisotropies in thin (Ga,Mn)As films are often analysed using the lowest order decomposition of the free energy profile into separate terms of distinct symmetry [66, 145, 133]. In this study a variant of the phenomenological formula introduced in Eq. (3.12) is used:

$$F(\psi) = -\frac{K_c}{4}\sin^2 2\psi + K_u \sin^2\psi - K_\Omega \sin^2(\psi - \Omega). \tag{3.36}$$

For simplicity, the cubic coefficient is denoted by K_c and the "intrinsic" uniaxial coefficient along the $[1\bar{1}0]$ axis by K_u. In analogy to Eq. (3.32), a term quantified by K_Ω is added to describe the uniaxial anisotropy with an extremum at an angle Ω induced by the relaxation of the lattice mismatch of the doped epilayer and the substrate. The angle Ω is in general not equal to the angle of the corresponding lattice relaxation ω (see discussion preceding Eq. (3.32) or [155] for details). Both angles are measured from the $[1\bar{1}0]$ axis.

Remanent magnetisation along the main crystallographic directions was measured by SQUID for both sets of samples. The obtained values include the magnetocrystalline anisotropies described in the previous paragraph as well as the shape anisotropy which always prefers the magnetisation alignment with the longest side of a rectangular prism such as the stripes [2].

Fig. 3.28 shows that in the control sample A_0 the intrinsic uniaxial anisotropy dominates over the cubic anisotropy on a large temperature range and the easy axis along the [1$\bar{1}$0] diagonal. The ratio of the remanent magnetisation projections to the [1$\bar{1}$0] and [100] directions below 60 K reveals that the system is almost purely uniaxial. The behaviour of the anisotropy components at $T > 60$ K cannot be described within the single domain approximation. However, the anisotropies of unpatterned samples are relevant to our microscopic analysis of measurements in the microbars only at the lowest temperatures where we extract intrinsic anisotropy coefficients and deduce the material parameters as detailed in subsection 3.2.2.

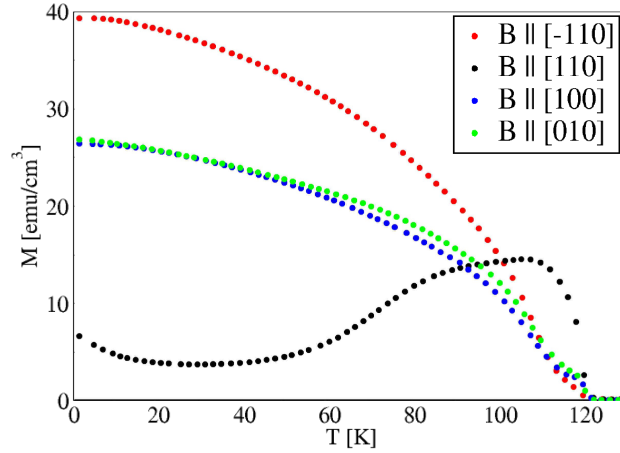

Figure 3.28: Remanent magnetisation along the main crystallographic directions for sample A_0 (25 nm thick unpatterned epilayer).

Fig. 3.29 shows that the patterning of the sample $A_{[1\bar{1}0]}$ strengthens the uniaxial anisotropy present in the parent wafer. The [1$\bar{1}$0] diagonal becomes the easiest of the investigated directions at all temperatures and the [110] diagonal becomes the hardest axis at all temperatures below T_C.

Fig. 3.30 shows that in the sample $A_{[110]}$, the two diagonals switch roles and in analogy with the previous case the easy axis prefers alignment close to the stripe direction, which is the hard axis over most of the temperature range in the parent wafer. This means that a rotation of the easy axis by as much as 90° is achieved by the post-growth patterning. Note that the difference of the projection of the remanent magnetisation to the [100] and [010] directions in the two patterned samples is due to a 5° misalignment between the stripes and the crystal diagonals introduced during the fabrication.

The samples in set B posses stronger cubic anisotropy. Fig. 3.31 shows that in the control sample B_0 the intrinsic uniaxial anisotropy dominates over the cubic anisotropy only at temperatures above 20 K and the [1$\bar{1}$0] diagonal is easier than the [110] diagonal at all temperatures below T_C.

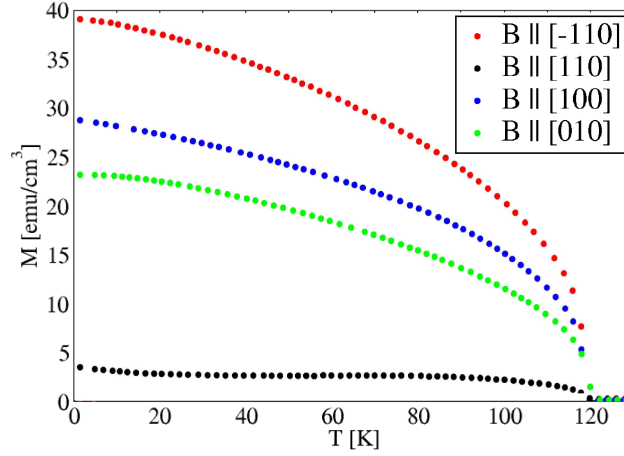

Figure 3.29: Remanent magnetisation along the main crystallographic directions for sample $A_{[1\bar{1}0]}$ (750 nm wide stripes along the $[1\bar{1}0]$ direction).

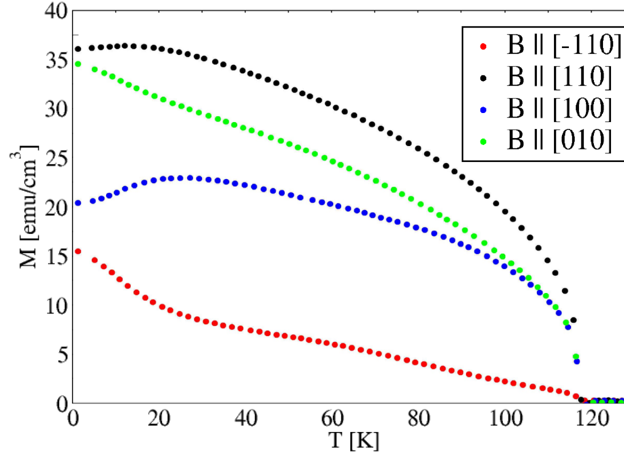

Figure 3.30: Remanent magnetisation along the main crystallographic directions for sample $A_{[110]}$ (750nm wide stripes along the [110] direction).

Fig. 3.32 shows a strengthening of the uniaxial anisotropy along the stripe direction in the sample $B_{[1\bar{1}0]}$, although not large enough to overcome the cubic anisotropy at the lowest temperatures. The transition from cubic to uniaxial anisotropy occurs at a lower temperature than in the control sample. The [110] direction is hardened. The main crystal axes [100] and [010] remain equal due to the more accurate alignment of the stripes with the crystal diagonal.

Fig. 3.33 shows a differentiation of the [100] and [010] projections in the sample $B_{[010]}$. The uniaxial anisotropy along the stripe direction now dominates at all temperatures. The intrinsic anisotropy differentiating the diagonal directions is less pronounced than in case of B_0 as it has to compete also with the induced uniaxial anisotropy.

It can be concluded that the universal effect seen in all patterned (Ga,Mn)As/GaAs samples is the preference of the easy axis to align parallel to the stripe which is the direction in which the growth induced compressive strain cannot relax, i.e., the direction of the relative lattice contraction in (Ga,Mn)As. This is reminiscent of the magnetocrys-

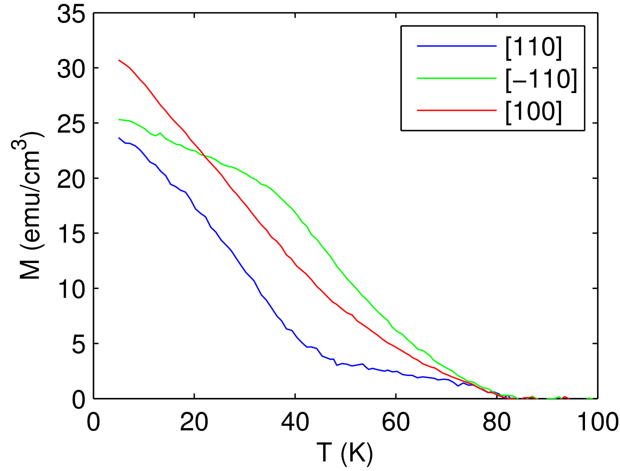

Figure 3.31: Remanent magnetisation along the main crystallographic directions for sample B_0 (200 nm thick unpatterned epilayer).

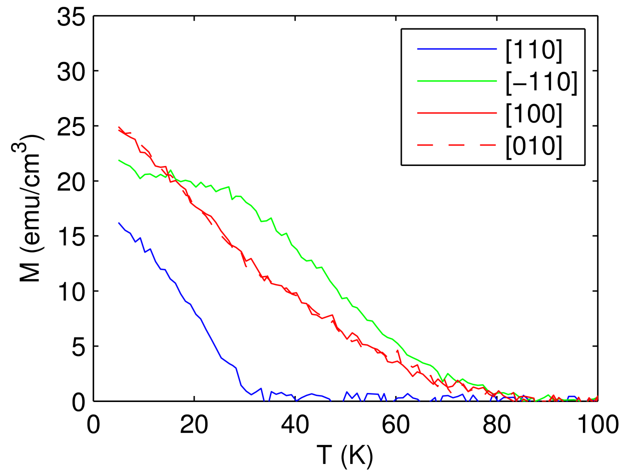

Figure 3.32: Remanent magnetisation along the main crystallographic directions for sample $B_{[1\bar{1}0]}$ (1 μm wide stripes along the $[1\bar{1}0]$ direction).

talline anisotropy of unpatterned (Ga,Mn)As epilayers which typically yields easy-axis oriented also along the direction of contraction, i.e., in-plane for compressively strained (Ga,Mn)As epilayers and out-of-plane for (Ga,Mn)As films grown under tensile strain (as discussed in subsection 3.1.1). We point out that the measured magnitudes of magnetic anisotropies in the microbars are an order of magnitude larger than the shape anisotropy contribution for given concentration of magnetic moments and thickness to width ratio. The microfabrication effects in the (Ga,Mn)As stripes are therefore primarily due to the SOC induced magnetocrystalline anisotropy.

After investigating the reorientations of the easy axis the magnitude of the individual anisotropy components is investigated. The hysteresis loops are measured using the

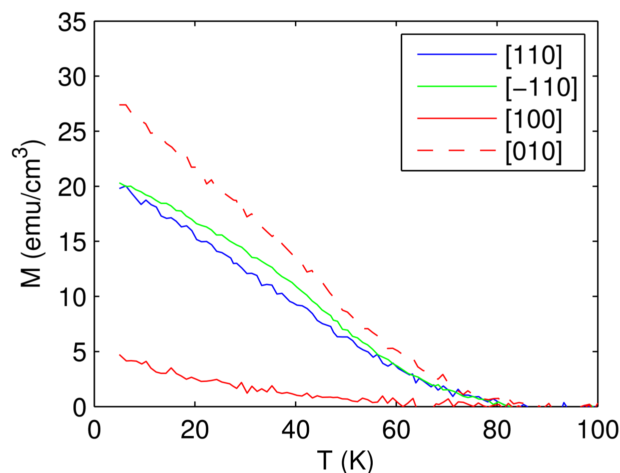

Figure 3.33: Remanent magnetisation along the main crystallographic directions for sample $B_{[010]}$ (1 μm wide stripes along the [010] direction).

SQUID magnetometry and fitted to the following equation:

$$F(\psi)/\mu_0 = -\frac{1}{4}M_S H_c \sin^2 2\psi + M_S H_u \sin^2 \psi - \\ -M_S H_\Omega \sin^2(\psi - \Omega) - M_S H cos(\psi - \phi_H), \qquad (3.37)$$

where $K_i = \mu_0 M_S H_i$ were introduced in Eq. (3.36), M_S is the saturation magnetisation, H is the external magnetic field applied at the angle ϕ_H, and the last term is the Zeeman energy. All angles in Eq. (3.37) are measured from the $[1\bar{1}0]$ axis. In case of a general alignment of the induced uniaxial strain, the angle Ω of the corresponding uniaxial anisotropy is an independent fitting parameter. However, in case of the main crystallographic axes and their small surrounding one can set $\Omega = \omega$, i.e., the anisotropy term is aligned with the corresponding uniaxial strain. An overview of the resulting angles Ω for the different alignments of stripes in sets A and B is given in Table 3.3.

	K_c [kJ/m^3]	K_u [kJ/m^3]	K_Ω [kJ/m^3]	Ω [deg]
A_0	0.412	0.404	0.0	
$A_{[1\bar{1}0]}$	0.412	0.404	0.83	95
$A_{[110]}$	0.412	0.404	1.037	5
B_0	2.213	0.381	0.0	
$B_{[1\bar{1}0]}$	2.213	0.381	0.935	90
$B_{[010]}$	2.213	0.381	0.696	45

Table 3.3: The anisotropy coefficients obtained by fitting the hysteresis loops at $T = 2$ K to Eq. (3.37) and the angular shift of the anisotropy term induced by the lattice relaxation as introduced in Eq. (3.36). Note that the lattice relaxes perpendicular to the stripe direction. The error of the anisotropy coefficients is approximately $10-20\%$, approaching the upper limit in case of the thick inhomogeneous samples in set B.

When determining the anisotropy coefficients in the stripes the assumption of linear superposition of the anisotropies present in the unpatterned samples with the anisotropies

induced by the patterning and lattice relaxation is used: the coefficients K_c and K_u are obtained first in the control samples and kept fixed when fitting the stripes fabricated from the same epilayer. The assumption is justified on the qualitative level by the remanent magnetisation measurement discussed in the previous subsection which revealed the persistence of the bulk anisotropies in all patterned samples. Its validity has been corroborated also by studies of epilayers subject to post-growth piezo straining [101] and lithographic patterning [149]. Note that this approach is appropriate only when the lattice relaxation direction is very close to the main crystallographic axes or when the angle Ω is also treated as a fitting paramater (as mentioned in subsection 3.1.4).

Another assumption concerns the magnetisation reorientation mechanism determining the shape of the hysteresis loops. In case of a dominant uniaxial anisotropy the hysteresis loops obtained for external fields applied along the hard axis are used in the fitting. In case of a dominant cubic anisotropy there is no completely hard direction. Nevertheless, a single domain model is still considered in the fitting.

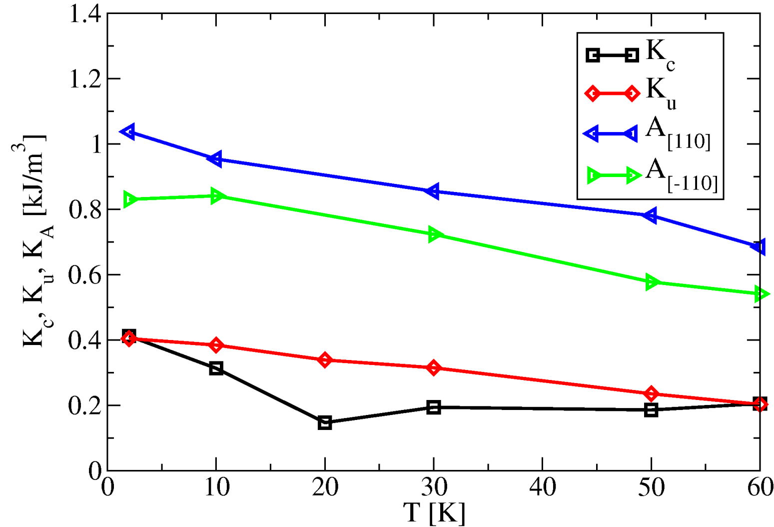

Figure 3.34: Anisotropy coefficients as functions of temperature obtained by fitting the hysteresis loops to Eq.(3.36) for the three samples of set A. The uniaxial coefficients K_Ω (denoted by K_A for set A) due to the growth strain relaxation in the patterned samples dominate the total anisotropy.

Anisotropy coefficients for all six samples at the lowest temperature are summarised in Table 3.3. Recall that these energies include also the contribution of the shape anisotropy which amounts to ~ 0.1 kJ/m^3 in samples $A_{[1\bar{1}0]}$ and $A_{[110]}$ and ~ 0.3 kJ/m^3 in the samples $B_{[1\bar{1}0]}$ and $B_{[010]}$ with the higher thickness to width ratio. Note that the smaller coefficient K_{45} leads to the formation of a strongly uniaxial system as shown in Figs. 3.33, whereas the larger coefficient K_{90} cannot overcome the cubic anisotropy component, at least at low temperatures as shown in Fig. 3.32. It is because in case of sample $B_{[010]}$, the induced anisotropy is added along the [010] axis which was already the easy (together with [100]) direction in the unpatterned epilayer.

For the thinner and more homogeneous epilayers in set A it was possible to extract the temperature dependence of the anisotropy coefficients from the hysteresis loops up to T = 60 K as shown in Fig. 3.34. The uniaxial coefficients due to lattice relaxation

dominate the anisotropy at all temperatures. At low temperatures the relative size of the induced anisotropies corresponds well to the simulated relaxations $\hat{\rho}$: Sample $A_{[1\bar{1}0]}$ with overcut sides (weaker relaxation) shows smaller anisotropy than sample $A_{[110]}$ with undercut sides (stronger relaxation). The cubic anisotropy remains positive for all studied temperatures $T < 60$ K which is in good agreement with the remanent magnetisation data shown in Fig. 3.28. The measurements above 60 K for which, as mentioned above, the single domain model is not applicable, are not discussed here.

Comparison with theory

In this subsection we build on macroscopic calculations of the lattice relaxation presented in subsection 3.2.2, perform the microscopic calculations of the magnetic anisotropy energy, and analyse its correspondence with the experimental results on the level of anisotropy coefficients. We extract the coefficients by fitting the calculated total energies to Eq. (3.36) for different magnetisation directions.

The comparison of the experimental and theoretical results involves a number of material parameters. The most important inputs of the microscopic calculations are the concentration of the ferromagnetically ordered Mn local moments (x) and the hole density (p). Unfortunately, these two parameters cannot be accurately controlled during the growth or determined post growth [52]. The measured saturation magnetisation, the conductivity, and the Curie temperature of the control samples provide only estimates of these input parameters with limited accuracy.

Another independent input parameter of the microscopic simulations is the "intrinsic" shear strain $e_{xy}^{int} \sim 10^{-4}$ (in this study denoted only by e_{in}) which has been used successfully to model [110, 155] the in-plane uniaxial anisotropy in the unpatterned samples. We recall that such modelling for small strains complies well with the assumption that the "intrinsic" uniaxial anisotropy superposes linearly with anisotropy components induced by the lattice relaxation, as mentioned in the previous section. The intrinsic shear strain is added to the off-diagonal element of the total strain tensor written in Eq. (3.35) giving: $e_{xy} = e_{in} + e_0 \frac{\hat{\rho}}{2} \cos 2\omega$.

Fig. 3.35 shows the combinations of x, p, and e_{in} for which the calculated intrinsic K_u and K_c of the control samples A_0 and B_0 agree with the measured values at zero temperature. By this we limit the intervals of x, p, and e_{in} values considered in the modelling of the temperature dependent anisotropy coefficients in all measured samples. Note, that we have also imposed an upper bound to x given by the nominal Mn doping in the particular material and a bound to p ensuring a maximum of one hole per Mn ion and in-plane easy axis (axes). This method allows for predicting the induced anisotropy coefficients in the microbars without any adjustable parameters in the microscopic model.

Using parameter combinations shown in Fig. 3.35 we calculate the induced uniaxial anisotropies in the microbars at zero temperature. The left and right vertical axis of Fig. 3.36 shows the extracted anisotropy coefficients for stripes in sets A and B, respectively. The combinations of x, p, and e_{in} are indexed only by x for simplicity. The plotted values can be compared to the measured coefficients summarised in Table 3.3. The relations $K_{95} < K_5$ and $K_{90} > K_{45}$ hold both in theory and in experiment. We observe a semi-quantitative agreement in samples $A_{[1\bar{1}0]}$ and $A_{[110]}$ where the measured values are roughly a factor of 2 larger than the calculated ones. The ratio of the calcu-

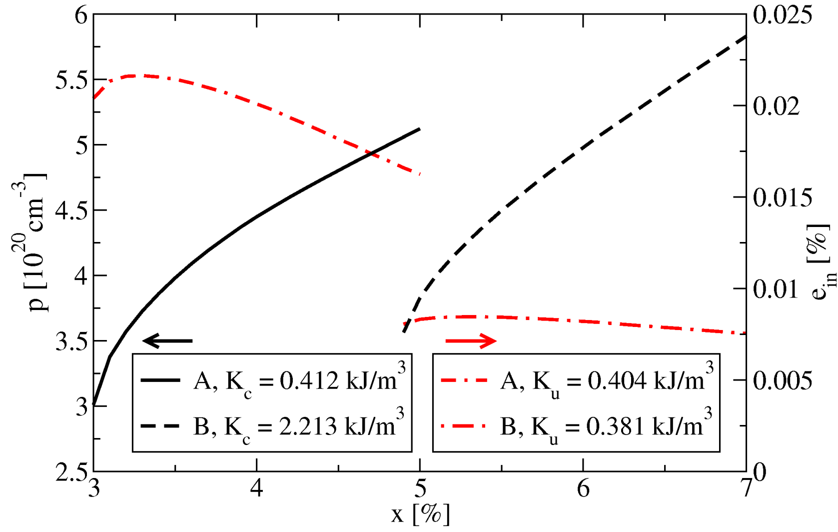

Figure 3.35: Correspondence of the hole density, p, and the intrinsic shear strain, e_{in}, to the effective Mn concentration, x, based on the agreement of the calculated K_c and K_u with the measured values. Samples A and B at zero temperature.

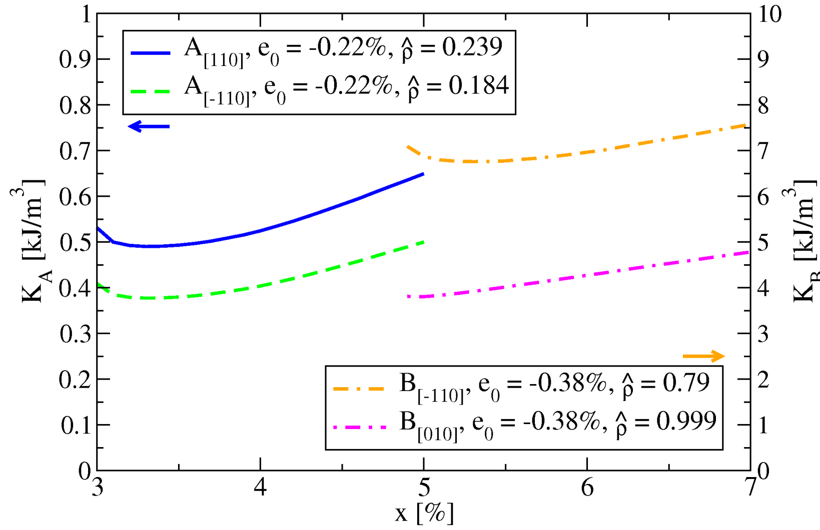

Figure 3.36: Calculated anisotropy coefficients due to the lattice relaxation in the patterned samples A and B at zero temperature for fixed combinations of x and p shown in Fig. 3.35.

lated coefficients K_Ω for samples $A_{[1\bar{1}0]}$ and $A_{[110]}$, K_{95}/K_5, is in excellent agreement with experiment (the difference is only 4%). These agreements justify the interpretation of the measured effects in the microbars based on the strain-relaxation controlled magnetocrystalline anisotropy. Note that they also support the assumption of the linear superposition of individual uniaxial anisotropies terms used in our analysis.

Fig. 3.36 shows also extracted anisotropy coefficients for samples $B_{[1\bar{1}0]}$ and $B_{[010]}$. In this case, the calculated ratio of coefficients extracted for the two stripe alignments, K_{90}/K_{45}, is approximately 20% larger then the corresponding experimental ratio, i.e., still in a very good agreement. We note, however, that the absolute values of the measured

coefficients are about a factor of 10 lower than the calculated ones. A possible source of this discrepancy is the large value of the experimentally inferred K_c due to inaccurate subtraction of the paramagnetic and diamagnetic backgrounds from the measured hysteresis curves. In general, we also expect that the theoretical modelling is less reliable in the thicker, as-grown samples B due to stronger disorder and inhomogeneities in the material.

As a consequence of the almost complete relaxation of the lattice mismatch in the thicker samples the calculated anisotropy coefficients are larger than the cubic coefficient at all studied temperatures which is not in agreement with the measured coefficients in set B at low temperature (see Table 3.3).

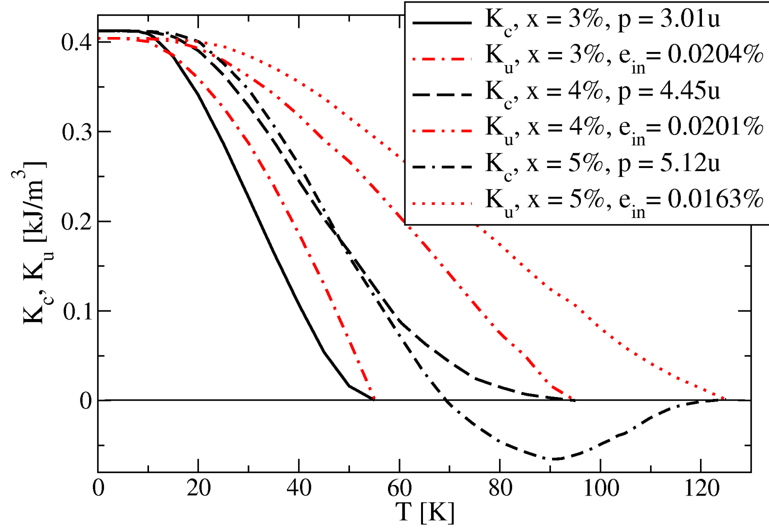

Figure 3.37: Calculated cubic a uniaxial intrinsic anisotropy coefficients present in all samples A as functions of temperature for fixed combinations of x, p, and e_{in} shown in Fig. 3.35.

We now select six representative combinations of x, p, and e_{in} from the relevant interval shown in Fig. 3.35, calculate the temperature dependence of all anisotropy coefficients for each set of parameters, and discuss the comparison with the measured anisotropies. We recall that in our mean-field modelling at finite temperatures the calculated T_C is uniquely determined by x and p. Note that for the entire interval of relevant x and p determined from the low-temperature analysis in the previous section, we obtain Curie temperatures which are in agreement with the experimental values in materials A and B within a factor of 2. This provides an additional support for the overall consistency of our microscopic theoretical analysis of the measured data.

Fig. 3.37 shows the calculated intrinsic anisotropy coefficients K_c and K_u of samples in set A for three fixed parameter combinations. At zero temperature the values coincide with data in Fig. 3.35. The cubic anisotropy component is stronger than the intrinsic uniaxial component at lowest temperatures but it quickly becomes weaker as temperature is increased for all parameter combinations. This temperature dependence is in agreement with the experimental anisotropies measured below 60 K, as shown in Fig. 3.34. The comparison cannot be extended to higher temperatures because, as explained above, the experimental behaviour at these temperatures is not captured by the single domain model.

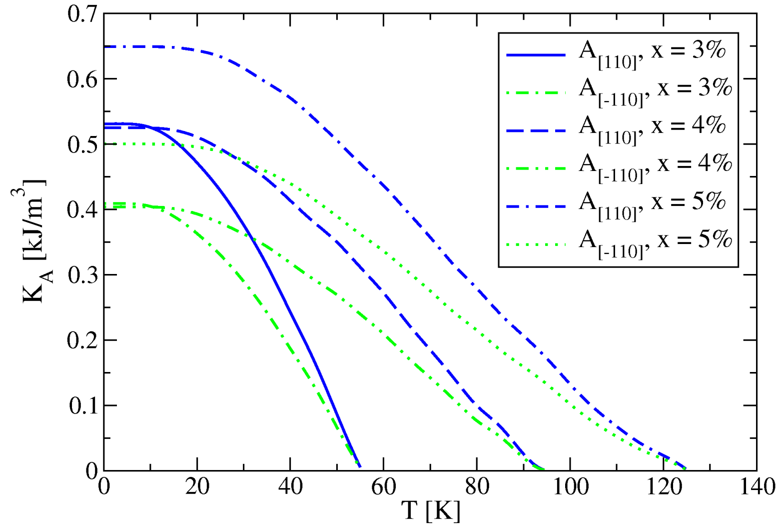

Figure 3.38: Calculated anisotropy coefficients due to the lattice relaxation in the patterned samples A as functions of temperature for fixed combinations of x and p shown in Fig. 3.35 and for the induced strain given in Fig. 3.36.

Fig. 3.38 shows the calculated anisotropy coefficients K_Ω of samples $A_{[1\bar{1}0]}$ and $A_{[110]}$ again for the three fixed parameter combinations. The calculated anisotropy components decrease monotonously with increasing temperature in agreement with the measured dependencies presented in Fig. 3.34. The comparison provides additional support for the interpretation of the experimental data, suggested already by the analysis at low-temperature, which is based on the strain relaxation induced magnetocrystalline ansisotropy effects.

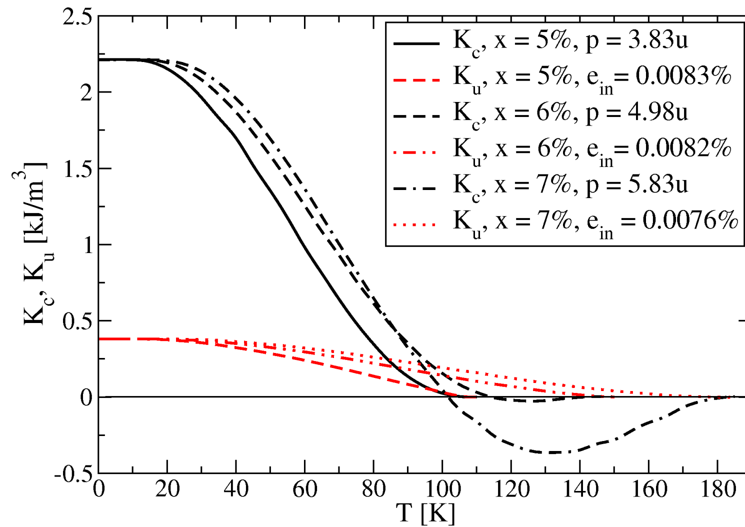

Figure 3.39: Calculated cubic a uniaxial intrinsic anisotropy coefficients present in all samples B as functions of temperature for fixed combinations of x, p, and e_{in} shown in Fig. 3.35.

Fig. 3.39 shows the calculated intrinsic anisotropy coefficients K_c and K_u of samples

in set B again for three fixed parameter combinations. At zero temperature the values coincide with data in Fig. 3.35. The calculated cubic anisotropy dominates over the uniaxial anisotropy at low temperatures in agreement with the experiment. The cross-over in the theory curves to the dominant uniaxial anisotropy occurs at higher temperatures than $T_C/3$ observed in experiment (see Fig. 3.31); at the upper part of the relevant interval of Mn concentrations the theoretical crossover occurs at $T_C/2$. We again attribute this quantitative discrepancy to inhomogeneities and stronger disorder in the thick as-grown material B.

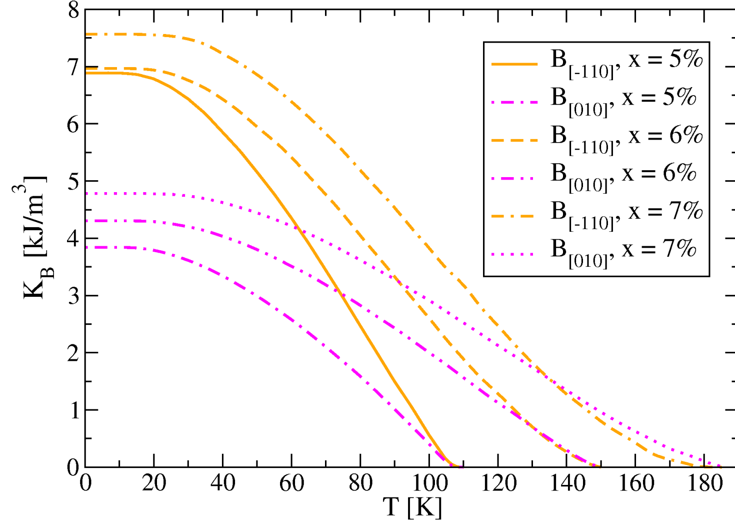

Figure 3.40: Calculated anisotropy coefficients due to the lattice relaxation in the patterned samples B as functions of temperature for fixed combinations of x and p shown in Fig. 3.35 and for the induced strain given in Fig. 3.36.

Fig. 3.40 shows the anisotropy coefficients K_Ω of samples $B_{[1\bar{1}0]}$ and $B_{[010]}$ for the same fixed parameter combinations as in Fig. 3.39. Again, we observe very similar dependence of the uniaxial anisotropy coefficients on temperature as in experiment. The monotonous decrease of the coefficients with growing temperature is in agreement with the measured remanent magnetisation data in Figs. 3.33 and 3.32. Both induced anisotropy coefficients are predicted to be larger than the cubic coefficient at all studied temperatures. This complies with the measured remanence data of sample $B_{[010]}$. Sample $B_{[1\bar{1}0]}$ shows agreement above 20 K. Its behaviour at temperatures below 20 K, is not captured by the theory data as we have already discussed in the previous subsection.

Summary

Detailed analysis of magnetic anisotropies induced in lithographically patterned (Ga,Mn)As/GaAs microbar arrays has been performed. Structural properties of the microbars have been studied by x-ray spectroscopy showing strong strain relaxation transverse to the bar axis. The relaxation induced lattice distortion in stripes with thickness to width ratio as small as ~ 0.1 induces additional uniaxial magnetic anisotropy components which dominate the magnetic anisotropy of the unpatterned (Ga,Mn)As epilayer,

as revealed by SQUID magnetisation measurements. The easy axis can be rotated by the micropatterning by 90° at all temperatures below the Curie temperature.

We have carried out systematic macroscopic and microscopic modelling of the structural and magnetic characteristics of the microbars and analysed in detail the experimental results. The agreement of the measured and simulated x-ray diffraction maps shows that the applied elastic theory model is quantitatively reliable in predicting the local lattice relaxation in patterned epilayers with the growth induced strain. The overall good agreement of the microscopically calculated and measured magnetic anisotropies conclusively demonstrate that the patterning induced anisotropies are of the magnetocrystalline, SOC origin.

3.2.3 Relaxation in L-shaped microbars

This subsection presents joint experimental and theoretical study [149] carried out in collaboration with experimentalists in Hitachi Cambridge Laboratory and Charles University in Prague.

We demonstrate that it is possible to tune and control magnetocrystalline anisotropies in (Ga,Mn)As microchannels by lithographically induced strain relaxation. This result represents the necessary prerequisite for future highly integrated microdevices fabricated in the dilute-moment ferromagnets. It also makes possible a range of new studies of extraordinary magnetotransport and magnetisation dynamics effects in such systems.

Experiment

Fig. 3.41 shows scanning electron micrographs of one of the devices studied. The structure consists of a macroscopic Van der Pauw device and an L-shaped channel patterned on the same wafer, the arms of which are Hall-bars aligned along the $[1\bar{1}0]$ and [110] directions. The trench-isolation patterning was done by e-beam lithography and reactive ion etching in a 25 nm thick $Ga_{0.95}Mn_{0.05}As$ epilayer, which was grown along the [001] crystal axis on a GaAs substrate. Results for two samples are reported: device A(B) has 4(1) μm wide, 80(20) μm long Hall bars. Isolated magnetic elements with the dimensions of these Hall bars and $M_s \sim$50 mT of the $Ga_{0.95}Mn_{0.05}As$ would have in-plane shape anisotropy fields below ~1 mT, which is an order of magnitude lower than the magnetocrystalline anisotropy fields. In-plane shape anisotropies are further reduced in the devices as they are defined by narrow (200 nm) trenches with the remaining magnetic epilayer left in place. The Curie temperature of 100 K was obtained from Arrot plots of anomalous Hall data. Hole density of 5×10^{20}cm^{-3} was estimated from high-field Hall measurements. At this doping the compressive strain in the $Ga_{0.95}Mn_{0.05}As$ epilayer grown on the GaAs substrate produces a strong magnetocrystalline anisotropy which forces the magnetisation vector to align parallel with the plane of the magnetic epilayer [26, 1].

Magnetisation orientations in the individual microbars are monitored locally by measuring longitudinal and transverse components of the AMR at in-plane magnetic fields. The magnetisation rotation experiments at saturation magnetic field measured on device B and on the macroscopic Van der Pauw device are presented in Figs. 3.42(a) and (b). (For the detailed discussion of the origins of the AMR and microscopic modelling of this extraordinary magnetoresistance coefficient in (Ga,Mn)As see Ref. [103].)

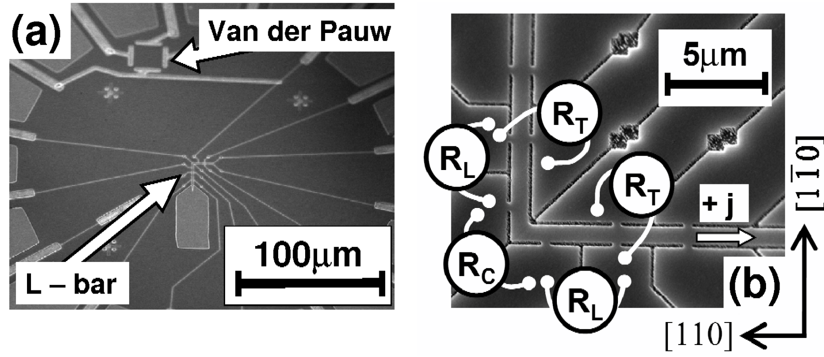

Figure 3.41: (a) Scanning electron micrograph of the L-shaped microdevice B and the macroscopic Van der Pauw device. (b) Detail of the L-shaped microdevice with the longitudinal (L) and transverse (T) resistance contacts in the bars and the corner (C) resistance contacts. Positive hole current in the p-type (Ga,Mn)As is defined to propagate from the [1$\bar{1}$0]-bar to the [110]-bar.

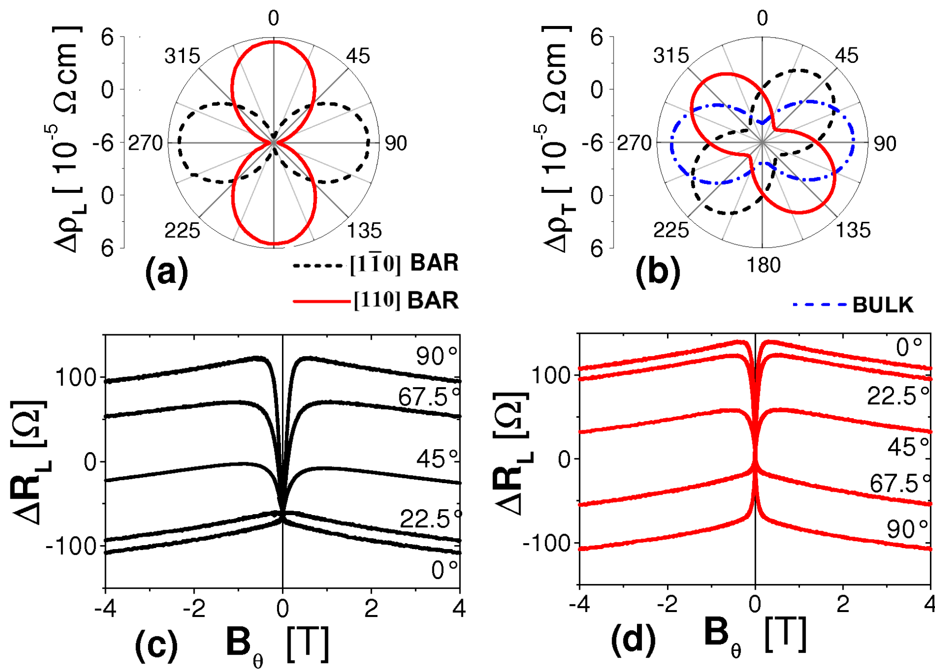

Figure 3.42: Device B longitudinal (a) and transverse (b) AMRs measured at 4.2 K in a rotating 4 T in-plane field with the field angle measured from the [1$\bar{1}$0] axis, and bulk transverse AMR measured in the Van der Pauw device with current lines oriented along the [010] axis. ($\Delta\rho \equiv \rho - \overline{\rho}$ where $\overline{\rho}$ is the average value over all angles.) In-plane, fixed-angle field sweep measurements of the longitudinal magnetoresistances of the (c) [1$\bar{1}$0]-bar and (d) [110]-bar bar of device B. (Same average resistances as in (a) and (b) are subtracted to obtain ΔR)

Examples of magnetoresistance measurements for external magnetic field sweeps in which the field angle θ, measured from the [1$\bar{1}$0] axis, is constant are shown in Figs. 3.42(c)

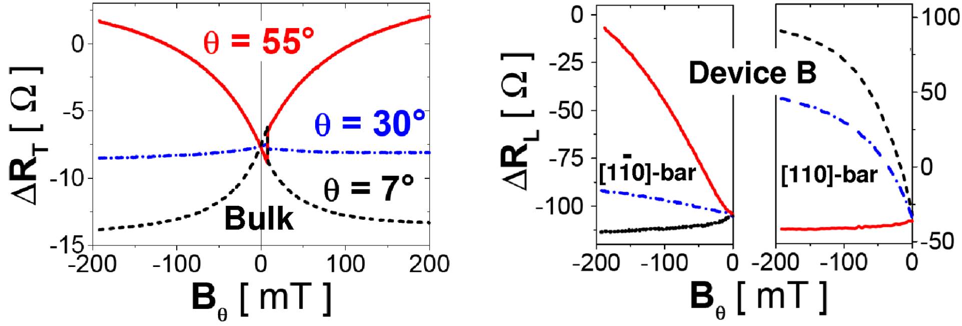

Figure 3.43: Comparison of the low-filed measurements at 4.2 K of the transverse resistance in the bulk Van de Pauw device (left panel) and of the longitudinal resistance of the [1$\bar{1}$0] and [110]-bar in device B (right panel).

and (d). The strongly θ-dependent low-filed magnetoresistance is attributed to magnetisation rotations. At high fields, the magnetoresistance becomes purely isotropic, i.e., the differences between resistances for different angles θ become independent of the magnitude of the external field. This property and the much smaller magnitude of the isotropic magnetoresistance compared to the low-field anisotropic magnetoresistance allows for the use of the high-field measurements in Figs. 3.42(a),(b) for determining the one to one correspondence between a change in the low-field resistance and a change in magnetisation orientation. Note that the 45° phase shift between the longitudinal and transverse AMR traces (see Figs. 3.42(a),(b)) allows for unambiguous determination of the change in the magnetisation angle if both resistance components are measured simultaneously.

The fixed-θ magnetoresistance measurements are used to first determine local magnetic anisotropies in the individual microbars. Values of θ corresponding to easy-axis directions have the smallest low-field magnetoresistance. For values of θ not corresponding to easy-axis directions the magnetisation undergoes a (partially) continuous rotation at low fields resulting in different orientations, and hence different measured resistances, at saturation and remanence. The technique can be used to determine the easy-axis directions within ±1°.

sample	bulk	A [1$\bar{1}$0]	A [110]	B [1$\bar{1}$0]	B [110]
easy-axis angle	±30°	±15°	±36°	+7°,−8°	+55°,−63°

Table 3.4: Easy-axes angles, measured from the [1$\bar{1}$0] crystal direction, determined by magnetoresistance measurements in the macroscopic Van der Pauw device (bulk) and in the [1$\bar{1}$0] and [110]-bars of the L-shaped devices A and B.

The effect of microfabrication on the magnetic anisotropy is apparent in Fig. 3.43. In the bulk, magnetisation angle 30° corresponds to an easy-axis while 7° and 55° are significantly harder. For device B, 7° is an easy-axes in the [1$\bar{1}$0]-bar and 55° is an easy-axis in the [110]-bar. All easy-axes found in devices A and B and in the bulk are summarised in Tab.3.4. The bulk material has the cubic anisotropy of the underlying zincblende structure plus an additional uniaxial [1$\bar{1}$0] anisotropy as is typical (Ga,Mn)As epilayers [110]. This results in two easy-axes tilted by 15° from the [100] and [010] cube edges towards the [1$\bar{1}$0] direction. In the microdevices, the easy-axes are rotated from

their bulk positions towards the direction of the respective bar and the effect increases with decreasing bar width.

Theory

$Ga_{0.95}Mn_{0.05}As$ epilayers grown on GaAs substrate are compressively strained in the (001) plane with the typical value of the lattice mismatch parameter $f \equiv |e_0| \approx 0.2 - 0.3\%$. The strength of the lattice relaxation in the microbars is obtained from numerical elastic theory simulations for the realistic sample geometry. (GaAs values of the elastic constants are considered for the whole wafer including the $Ga_{0.95}Mn_{0.05}As$ epilayer.) Results of such calculations are illustrated in Fig. 3.44 for the $[1\bar{1}0]$-bar of device B. In panel (a) we show the strain component along the growth-direction [001]-axis with respect to the lattice parameter of a fully relaxed cubic GaAs. Since all strain components scale linearly

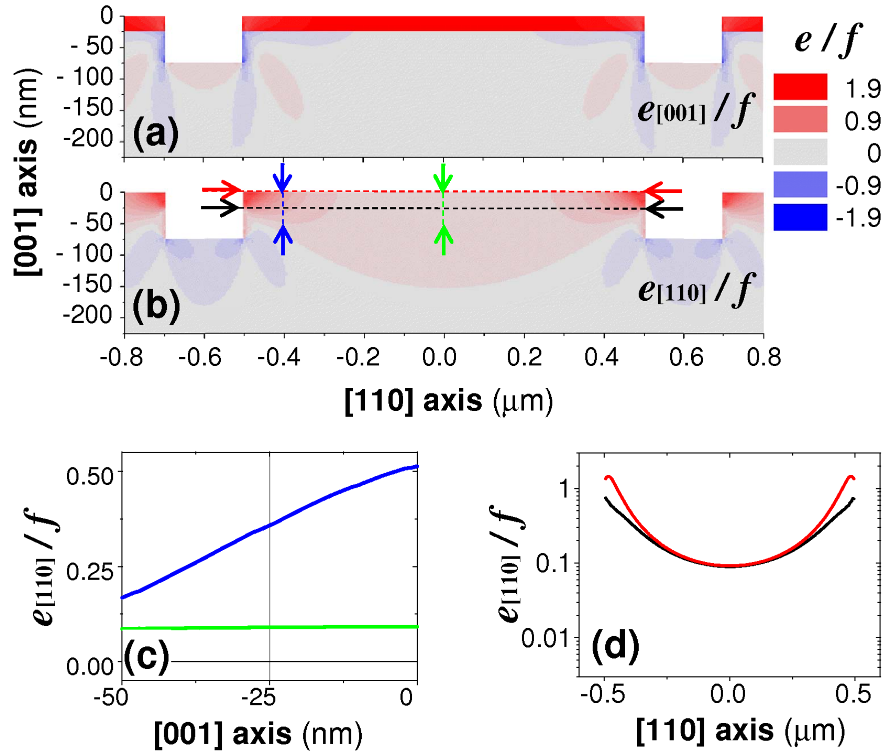

Figure 3.44: Numerical simulations of lattice parameters in the 1 μm wide $[1\bar{1}0]$-bar of device B defined by 200 nm wide and 75 nm deep trenches in the 25 nm thick (Ga,Mn)As film on a GaAs substrate. (a) Strain component along the [001]-axis with respect to the lattice parameter of a fully relaxed cubic GaAs. (b) Same as (a) for in-plane strain component $e_{[110]}$ in the direction perpendicular to the bar orientation. (c) and (d) Strain components $e_{[110]}$ along different cuts through the [001]-[110] plane. The cuts and the corresponding $e_{[110]}/f$ curves are highlighted by coloured arrows in (b) and the corresponding colour coding of curves in (c) and (d).

with f we plot $e_{[001]}/f$. The figure highlights the growth induced lattice matching strain; because of the in-plane compression of the (Ga,Mn)As lattice the elastic medium reacts by

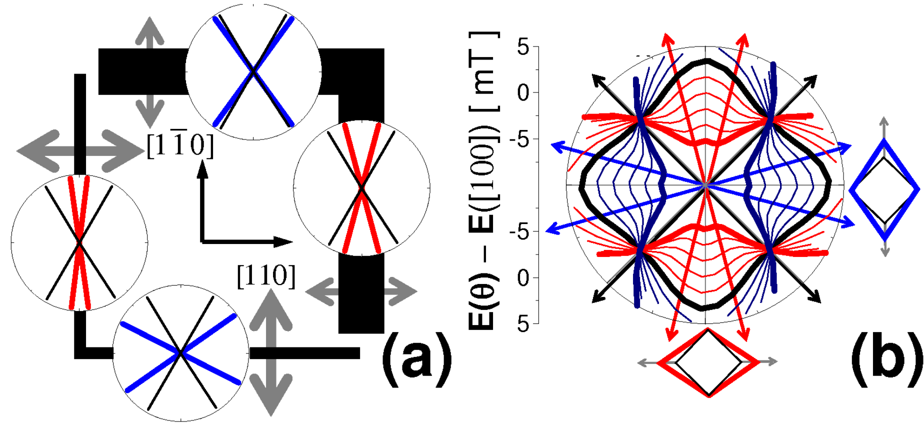

Figure 3.45: (a) Schematics of the easy-axes orientations in the [1$\bar{1}$0] and [110]-bars of the L-shaped devices A and B. Arrows indicate the direction and strength of the patterning induced lattice relaxation. (b) Theoretical magnetocrystalline energies as a function of the in-plane magnetisation angle for zero shear strain (black line), for $e_{xy} = 0.004, .., 0.02\%$ (red lines) corresponding to lattice extension along [110] axis, and for $e_{xy} = -0.004, .., -0.02\%$ (blue lines) corresponding to lattice extension along [1$\bar{1}$0] axis. The magnetic easy-axes at e_{xy} = 0, 0.02% and -0.02% are highlighted by black, red, and blue arrows, resp. Lattice deformations breaking the [1$\bar{1}$0]-[110] symmetry of the microscopic magnetocrystalline energy profile are illustrated by the diamond-like unit cells extended along [110] axis for the [1$\bar{1}$0]-bar (red diamond) and along the [1$\bar{1}$0] axis for the [110]-bar (blue diamond).

expanding the lattice parameter in the growth direction, as compared to the fully relaxed (Ga.Mn)As lattice, i.e., $e_{[001]}/f > 1$.

Within the plane, the lattice can relax only in the direction perpendicular to the microbar orientation. The corresponding strain component, calculated again with respect to the GaAs, is plotted in Fig. 3.44(b) over the entire cross-section of device B and, in Figs. 3.44(c) and (d), along various cuts through the $[001]-[110]$ plane. While in the centre of the bar the in-plane relaxation is relatively weak, i.e., the lattice parameter remains similar to that of the GaAs substrate, the lattice is strongly relaxed near the edges of the bar. Averaged over the entire cross-section of the (Ga,Mn)As bar we obtain relative in-plane lattice relaxation of several hundredths of a per cent. The microscopic magnetocrystalline energy calculations discussed in the following paragraphs confirm that these seemingly small lattice distortions can fully account for the observed easy-axis rotations in the strongly spin-orbit coupled (Ga,Mn)As.

Our microscopic calculations of the magnetisation angle dependent total energies are based again on the effective Hamiltonian theory described in sections 2.1 and 3.1. (As in the above macroscopic simulations we assume that the elastic constants in (Ga,Mn)As have the same values as in GaAs.) Note that the $\boldsymbol{k} \cdot \boldsymbol{p}$ effective Hamiltonian theory describes accurately the sign and magnitude of the AMR data in Fig. 3.42 [103].

For the modelling of the magnetocrystalline energy of the microbars we assume homogeneous strain in the (Ga,Mn)As layer corresponding to the average value of $e_{[110]}$ obtained in the macroscopic elastic theory simulations. The input parameters of the microscopic

calculations are the strain components introduced in Eqs. (3.24) and (3.26), with $\overline{\rho}$ set to the average value of $e_{[110]}$ and $e_0 = -f$.

In Fig. 3.45(b) we plot calculated magnetocrystalline energies as a function of the in-plane magnetisation angle for $f = 0.3\%$ and e_{xy} ranging from zero (no in-plane lattice relaxation) to typical values expected for the $[1\overline{1}0]$-bar ($e_{xy} > 0$) and for the [110]-bar ($e_{xy} < 0$). Consistent with the experiment, the minima at [100] and [010] for $e_{xy} = 0$ move towards the$[1\overline{1}0]$ direction for lattice expansion along [110] direction ($e_{xy} > 0$) and towards the [110] direction for lattice expansion along $[1\overline{1}0]$ direction ($e_{xy} < 0$). Note that the asymmetry between experimental easy-axes rotations in the two bars is due to the a [110]-uniaxial component present already in the bulk material whose microscopic origin is not known but can be modeled by an intrinsic (not induced by micropatterning) strain $e_{xy}^{int} \sim +0.01\%$.

We conclude the the observed easy-axes rotations which depend on the width and crystal orientation of the microchannel can be explained in terms of lattice relaxation induced changes in the magnetocrystalline anisotropy. (Ga,Mn)As microchannels with locally controlled magnetocrystalline anisotropies and inherently weak dipolar fields represent a new favourable class of systems for exploring magneto-electronic effects at microscale.

3.2.4 Piezo-electric stressing

This subsection presents joint experimental and theoretical study [101] carried out in collaboration with University of Nottingham and Hitachi Cambridge Laboratory.

The control of magnetism by electrical means is an important prerequisite for successful implementation of spintronics in information processing technologies, and for advancements in sensor and transducer applications. Multiferroic compounds [100, 42] or layered structures [58, 148, 139, 30] combining piezoelectric/ferroelectric and magnetostrictive/ferromagnetic properties are a promising area of research in this direction. However, due largely to the complex electronic structure and multidomain switching processes giving rise to complicated hysteresis loops, a microscopic theoretical description of the behaviour of these systems is lacking.

(Ga,Mn)As has many favourable characteristics which can be utilised in a hybrid ferromagnetic/piezoelectric structure. Spin polarised holes that mediate ferromagnetic coupling between Mn local moments produce large magnetic stiffness, resulting in a mean-field like magnetisation and macroscopic single-domain characteristics [55, 142]. At the same time, magnetocrystalline anisotropies derived from SOC effects in the hole valence bands are large and sensitive to strains as small as 10^{-4} [149, 147].

In previous subsections the strain effects in (Ga,Mn)As have been controlled by lattice parameter engineering during growth [26, 1] or through post growth lithography [147, 46, 149]. In this subsection we demonstrate that the in-plane uniaxial magnetic anisotropy in (Ga,Mn)As device can be controlled by attaching the epilayer to a piezoelectric transducer. A technique used previously to produce sizeable strains in non-magnetic GaAs structures [113] is followed. Microscopic calculations discussed below describe these effects on an unprecedented level of accuracy compared to rare earth or metal ferromagnet/piezoelectric devices [148, 139, 30, 58].

The 25 nm thick $Ga_{0.94}Mn_{0.06}As$ epilayer was grown by low-temperature molecular-beam-epitaxy on GaAs substrate and buffer layers [15]. The material is under compressive

in-plane strain of $\sim 3 \times 10^{-3}$ [158] due to the lattice mismatch with the GaAs. From SQUID magnetometry on the material the magnetic easy axis is in-plane in a direction determined by competition between biaxial [100]/[010] and uniaxial $[1\bar{1}0]$ anisotropies. At 50 K the cubic and uniaxial anisotropy constants determined from hard axis magnetisation curves are $K_c = 85$ Jm^{-3} and $K_u = 261$ Jm^{-3} $\pm$ 20%.

A (Ga,Mn)As Hall bar, fabricated by optical lithography, and orientated along the $[1\bar{1}0]$ direction, was bonded to the PZT piezo-transducer using a two-component epoxy after thinning the substrate to 150 ± 10 μm by chemical etching. The stressor was slightly misaligned so that a positive/negative voltage produces a uniaxial tensile/compressive strain at $\approx -10°$ to the $[1\bar{1}0]$ direction.

The induced strain was measured by strain gauges, aligned along the $[1\bar{1}0]$ and [110] directions, mounted on a second piece of 150 ± 10 μm thick wafer bonded to the piezo-stressor. Differential thermal contraction of GaAs and PZT on cooling to 50 K produces a measured in-plane, biaxial tensile strain at zero bias of 10^{-3} and a uniaxial strain estimated to be of the order of $\sim 10^{-4}$ [38] which could not be accurately measured. At 50 K, the magnitude of the additional uniaxial strain for a piezo-voltage of ± 150 V is approximately 2×10^{-4}.

The orientation of the in-plane magnetisation of the (Ga,Mn)As Hall bar was determined from the longitudinal and transverse AMR. To a good approximation ($\approx$ 10%), these are given by $\Delta\rho_{xx}/\rho_{av} = C \cos 2\phi$ and $\rho_{xy}/\rho_{av} = C \sin 2\phi$, where ϕ is the angle between the magnetisation direction and the Hall bar direction [103]. Fig. 3.46 shows magnetoresistance measurements at 50 K for external magnetic field sweeps at constant field angle θ measured from the Hall bar direction. The strongly θ-dependent low-field magnetoresistance, which saturates at higher field is due to AMR, i.e., to magnetisation rotations. An isotropic θ-independent magnetoresistance contribution was subtracted from the measured longitudinal resistances. When the external field is close to the magnetic easy axis, the measured resistances at saturation and remanence should be almost the same and a significant magnetoresistance due to rotation of the magnetisation can only be present at very low applied fields. For external fields away from the easy axis, large magnetoresistances corresponding to large rotations of the magnetisation orientation are present. This allows for the determination of the easy axis directions within $\pm 5°$.

The effect of the piezo-stressor is clearly apparent in Fig. 3.46. At 50 K, SQUID measurements show that the magnetic easy axis is oriented along the $[1\bar{1}0]$- direction for the as-grown (Ga,Mn)As wafer, consistent with $|K_c| < |K_u|$. The easy axis for the Hall bar bonded to the stressor rotates to an angle $\phi = 65°$ upon cooling to 50 K due to a uniaxial strain induced by anisotropic thermal contraction of the piezo-stressor [38]. Application of a bias of +150 V to the stressor causes the easy axis to rotate further to $\phi = 80°$ while for -150 V it rotates in the opposite sense to $\phi = 30°$. This directly demonstrates electric field control of the magnetic anisotropy in the (Ga,Mn)As/PZT hybrid system.

The magnetic anisotropy for our system can be described phenomenologically by an energy functional $E(\hat{M}) = -K_c/4 \sin^2 2\phi + K_u \sin^2 \phi + K'_u \sin^2(\phi + \phi_0)$, where the last term is due to the misaligned stressor. (In this study K'_u plays the role of $-K_\Omega$ in Eq. (3.32).) We recall that ϕ_0 is in general not equal to the misalignment of the stressor. Considering Eq. (3.34), the misalignment $\omega \approx -10°$ results is $\Omega \approx -5°$ or in the notation of this study $\phi_0 \approx 5°$.) The observed behaviour is then consistent with the (Ga,Mn)As being in tensile strain along the axis of the stressor on cool down and applied positive (negative) voltage

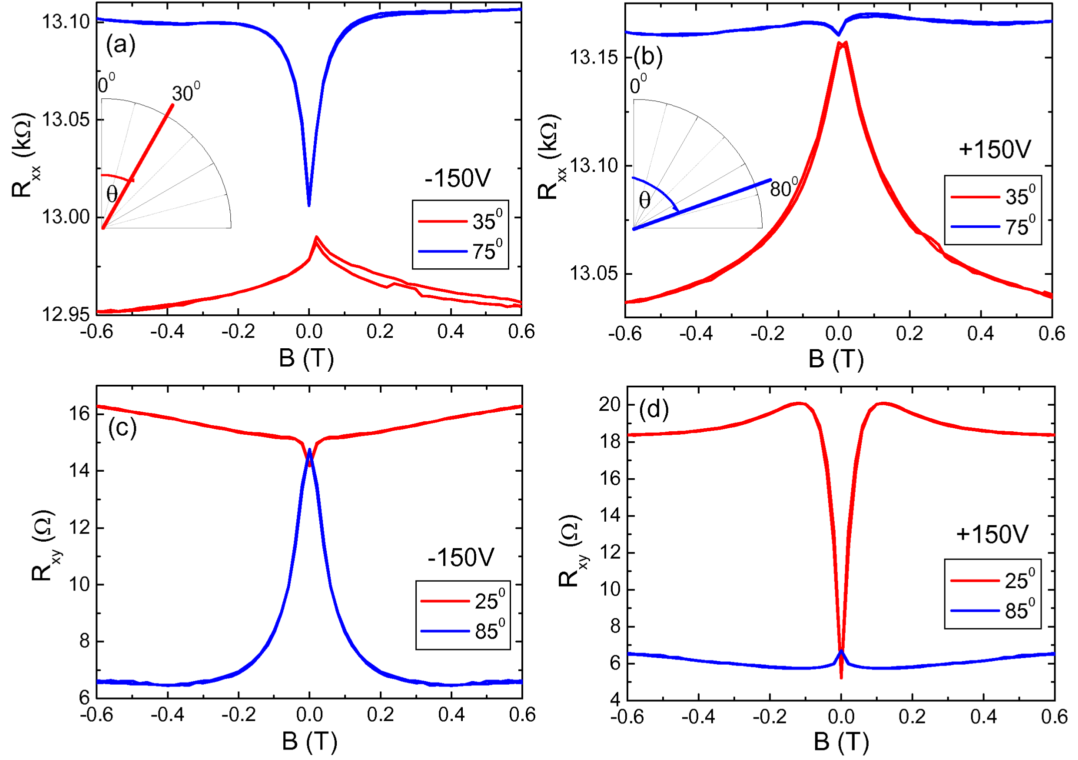

Figure 3.46: The longitudinal resistances, R_{xx} ((a) and (b)) and the transverse resistances R_{xy} ((c) and (d)) as a function of magnetic field for angles close to the easy axes (30° at -150 V and 80° at +150 V). The curves close to the easy axes in each case are relatively flat as a function of field, indicating small rotation of the angle of the magnetisation. T=50 K.

increasing (decreasing) this strain. Note that the misalignment allows smooth rotation of a single easy axis in the experimentally accessible voltage range.

We now calculate the expected magnetic anisotropy characteristics of the studied (Ga,Mn)As/PZT system using the effective Hamiltonian model described in sections 2.1 and 3.1. The magnetocrystalline anisotropy constants are known to be sensitive to the local moment density and the hole compensation ratio p/N_{Mn}. To guarantee that the comparison between theory and experiment does not suffer from an accidental choice of p and N_{Mn} in the calculations, we consider simultaneously $\mathrm{Mn_{Ga}}$ dopings within an interval $x = 3-5\%$ which safely contains the expected value of x in the experimental sample ($N_{\mathrm{Mn}} = 4x/a_{lc}^3$, where a_{lc} is the lattice parameter). For fixed p and N_{Mn}, the cubic term K_c agrees with the measured 50 K value for $p/N_{\mathrm{Mn}} = 0.6-0.4$ across the whole range of $x = 3-5\%$. This narrow range of p/N_{Mn} is in good agreement with the compensation ratio determined from experiment in the studied as-grown material [52].

The origin of the uniaxial anisotropy term in bare (Ga,Mn)As wafers is not known, but it can be modelled [110, 149] by introducing a shear strain e_{xy}^{int} along the $[1\bar{1}0]$ axis. For $p/N_{\mathrm{Mn}} = 0.6-0.4$ we obtain the experimental value of K_u for compressive shear strain $e_{xy}^{int} = 3-2\times10^{-4}$ within the considered range of x's.

The calculations reproduce the measured 0 V easy axis for a tensile strain of $e_{str} = 6-4\times10^{-4}$, along the stressor axis and the experimental easy axes for ±150 V are obtained

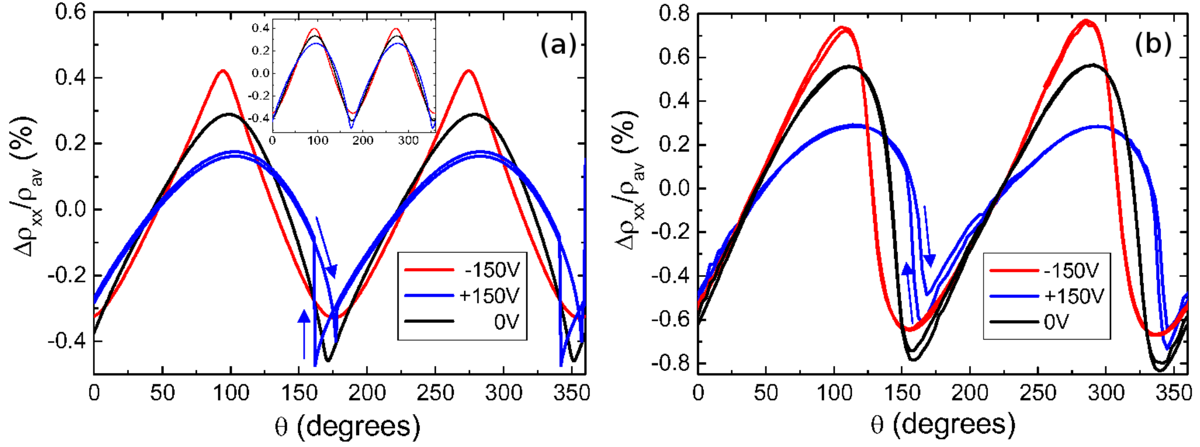

Figure 3.47: (a) The longitudinal AMR from theory calculations with a non saturating magnetic field of 20 mT rotated in the plane of the film. Inset shows the same for a field of 40mT. (b) The experimental AMR curves with a field of 40 mT rotated in the plane of the film. ρ_{av} is the ρ_{xx} averaged over 360° in the low field regime. θ is the angle of the magnetic field with respect to the Hall bar. T=50 K

by increasing/decreasing the e_{str} strain by $3 - 2 \times 10^{-4}$. These changes in strain agree with the measured values for ±150 V, and the 0 V strain due to differential contraction is of the expected order. The resulting microscopic $E(\hat{M})$ curves for relevant voltages are shown in Fig. 3.18.

The magnetoresistance calculated microscopically from the same band structure model combined with Boltzmann transport theory [103] gives AMR at saturation of the same sign and comparable magnitude to the experiment if we assume the above compensation ratios. This allows us to microscopically simulate AMR measurements assuming, as in previous micromagnetics studies of (Ga,Mn)As [142], the single domain behaviour. Fig. 3.47(a) shows the results of simulations and Fig. 3.47(b) the experimental data for the situation where a magnetic field of magnitude smaller than the saturation field is rotated in the plane of the (Ga,Mn)As epilayer. Both theory and experiment show that these AMR traces are no longer sinusoidal since the magnetisation does not track the applied rotating field. Ranges of magnetic field angles θ for which resistance is more slowly varying correspond to angles close to the easy axis, where the magnetisation vector lags behind θ. Rotation around the hard axis is more abrupt, and in this region the AMR can develop hysteretic features whose widths increase with decreasing magnitude of the rotating field. (To highlight the possibility for the hysteretic behaviour in the single domain model we show in Fig. 3.47(a) calculations for 20 mT field with large hysteresis; at 40 mT used in experiment the hysteresis is unresolved in the theory data.) At +150 V the hard axis is close to the Hall bar axis resulting in sharper minima than maxima in the corresponding experimental and theoretical AMR traces, while the trend is clearly opposite for the -150 V bias data, consistent with the easy axis directions obtained from the field sweep measurements.

Our detailed understanding of the piezo-electric stressing effects on magnetic anisotropy in (Ga,Mn)As made it possible to demonstrate electrically induced magnetisation switching. The bias-dependent hysteresis loops which allow for such a reversal process are shown

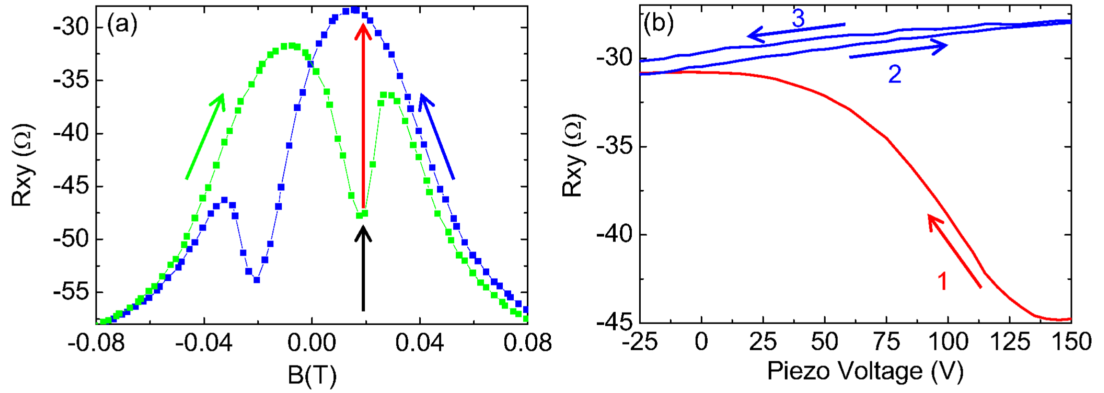

Figure 3.48: (a) Low field magnetic hysteresis curve at +150 V. The field is swept from saturating negative field at 165° to the position show by the black arrow. Then (b) the piezo-voltage is swept inducing a rotation of the angle of the magnetisation, indicated by the red arrows. Numbered arrows represent the order and direction of the voltage sweeps. T=30 K.

in Fig. 3.48(a). With the piezo-voltage at +150V, the initial magnetisation state is prepared by sweeping the external magnetic field from negative saturating field at 165° to the position shown by the black arrow. This causes the magnetisation to rotate from 165° to 260°, at B=0 T (i.e. along the easy axis at +150 V), then to 275° for the small positive field of approximately 18 mT (marked by the black arrow). Then, with the external magnetic field held constant the piezo-voltage is swept (Fig. 3.48(b)) and the magnetisation rotates from 275° to 25° (i.e. close to the easy axis for -150 V) resulting in a change of R_{xy} as shown by the red arrows (The few Ohms discrepancy in the initial value of R_{xy} arises due to the 2 mT resolution of the magnet). This sequence switches the magnetisation from the 4th to the 1st quadrant, where it remains for subsequent voltage sweeps. The magnetisation can be switched back again by reversing the sequence, with the magnetic field set to the opposite polarity.

3.2.5 Domain wall width and angle

This subsection presents joint experimental and theoretical study [130] carried out in collaboration with Hitachi Advanced Research Laboratory in Japan and University of Nottingham.

We investigate magnetic domain walls in an in-plane magnetised (Ga,Mn)As dilute moment ferromagnetic semiconductor. The high-resolution electron holography technique used in the experiments provides direct images of domain wall magnetisation profiles. The experiments are interpreted based on microscopic calculations of the micromagnetic parameters and Landau-Lifshitz-Gilbert simulations. We find that the competition of uniaxial and biaxial magnetocrystalline anisotropies in the film is directly reflected in orientation dependent wall widths, ranging from approximately 40 nm to 120 nm. The domain walls are of the Néel type and evolve from near-90° walls at low-temperatures to large angle $[1\bar{1}0]$-oriented walls and small angle [110]-oriented walls at higher temperatures.

Magnetic domain walls (DWs) are extensively explored for their potential in integrated

memory and logic devices [3, 136] and because of the number of open basic physics questions related to their dynamics in external magnetic and electric fields [132, 157, 6, 32, 127]. DMSs are playing an increasingly important role in this research area [153, 149, 31, 79]. p-type (Ga,Mn)As has a saturation magnetisation (M_s) which is two orders of magnitude lower than in conventional metal ferromagnets, while the magnetocrystalline anisotropy energies (K) and spin stiffness (A) are comparable to the metals [1, 26, 61, 25]. The low M_s is due to the dilute Mn moments while the holes in the spin-orbit coupled valence bands, mediating the long-range Mn-Mn coupling, produce the large K and A.

Among the immediate implications of these characteristics are weak dipolar stray fields which would allow for dense integration of (Ga,Mn)As micro-elements without unintentional cross-links, macroscopic-size domains, square hysteresis loops, and mean-field-like temperature dependent magnetisation [145, 142]. The strong in-plane biaxial and uniaxial magnetocrystalline anisotropies [44, 145, 142] and weak dipole fields lead also to the formation of unique segmented domain structures and spontaneous domain reorganisation with changing temperature [129]. An outstanding feature of DW dynamics in (Ga,Mn)As is the orders of magnitude lower critical current for DW switching than observed for conventional ferromagnets [153, 149].

The basic tool for studying DWs is magnetic structure imaging but here the low saturation moment in (Ga,Mn)As is a problem, greatly reducing the sensitivity of conventional magneto-optical and scanning Hall probe microscopy techniques. For out-of-plane magnetised (Ga,Mn)As films, grown under tensile strain on (In,Ga)As, the resolution achieved with these techniques is limited to $\sim 1\mu$m [119, 153, 141] and the sensitivity is further reduced for (Ga,Mn)As layers grown on GaAs under compressive strain with in-plane magnetisation [145, 97, 98]. Imaging internal DW configurations, which are particularly intriguing in the in-plane materials, requires $\sim 100 - 10$ nm resolution and has therefore remained far beyond the reach of the conventional magnetic microscopy techniques.

We present a detailed study of in-plane DWs in (Ga,Mn)As. Direct images of DW magnetisation profiles were obtained and the type and width of the DWs and their dependence on the wall orientation and temperature were determined. The high sensitivity to in-plane magnetisation is achieved by employing transmission electron microscopy techniques [43] based on the Lorentz deflection of transmitted electrons by the in-plane component of the magnetic induction and on holographic electron phase retrieval. The interpretation of experiments is based on kinetic-exchange-theory [55] calculations of micromagnetic parameters and Landau-Lifshitz-Gilbert (LLG) simulations.

A $Ga_{0.96}Mn_{0.04}As$ (500 nm)/GaAs (1 nm)/AlAs (50 nm)/buffer-GaAs (100 nm) multilayer was deposited on a GaAs(001) substrate using molecular beam epitaxy. Electron transparent uniform (Ga,Mn)As foils with a wide field of view around 100 μm were produced by selectively etching away the substrate using the AlAs as a stop layer. The cubic anisotropy favours magnetisation along the in-plane $\langle 100 \rangle$ crystalline axes, and the uniaxial anisotropy favours magnetisation along one of the $\langle 110 \rangle$ axes. The in-plane uniaxial easy axis is labelled as the $[1\bar{1}0]$ direction, as this was found to be the easy axis in layers grown under similar conditions in the same system [110]. SQUID magnetisation measurements on an unetched part of the wafer yield the cubic anisotropy constant K_c=1.18(0.32) kJ/m^3 and the uniaxial anisotropy constant K_u=0.18(0.11) kJ/m^3 at T=10(30) K, and the Curie temperature $T_c = 60$ K.

Electron holography measurements were performed using a 300 kV transmission elec-

tron microscope equipped with a cold field-emission electron gun (Hitachi High-Technologies, HF-3300X). The specimen was located at a special stage in between the condenser and the weakly-excited objective lens. In this configuration the internal magnetic structures are expected to be undisturbed by the residual magnetic field, which is estimated to be smaller than 10^{-4} T and oriented perpendicular to the specimen. Electron holography experiments were performed within a near-edge sample region, because of the need for a reference electron wave travelling through vacuum. The electrostatic phase gradient associated with slight thickness variations arising from inhomogeneous chemical etching of the sample near edges was compensated for by subtracting a phase image of the sample in the high temperature paramagnetic state together with a linear wedge correction. The sampling resolution of the CCD camera used for image acquisition was 1.6 nm, whilst the numerical phase reconstruction was performed using a low-pass Fourier mask corresponding to the wavelength of 20 nm for holograms acquired with 5 nm-spacing interference fringes.

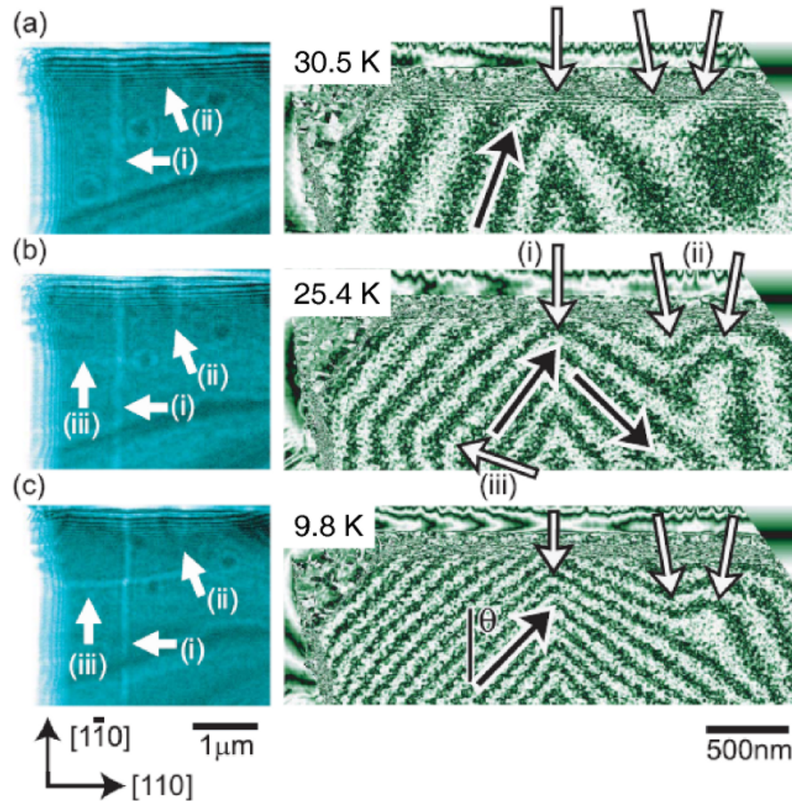

Figure 3.49: Lorentz micrographs (left column) and phase images amplified by a factor of four (right column) acquired at (a) 30.5 K, (b) 25.4, and (c) 9.8 K, respectively. Three different types of DWs are observed, marked by white arrows: (i) a wall parallel to [1$\bar{1}$0] that is near-180° type at high temperature and near-90° type at low temperature; (ii) a pair of DW that is near-180° head-on type at high temperature and near-90° type at low temperature, and (iii) a near-90° type wall parallel to [110] that appeared at low temperature. The local B directions are denoted by black arrows.

Fig. 3.49 shows the DW phase images (right panels) acquired from a 3μm $\times$ 1μm

corner region of the sample foil at 30.5 K, 25.4 K, and 9.8 K, respectively, together with a larger area overviews (left panels) obtained by Fresnel mode Lorentz imaging [129]. The phase (ϕ) is amplified by a factor of 4 for clarity, and its cosine (i.e. $cos(4\phi)$) is displayed in grey-scale. The magnitude and direction of the magnetic induction **B** are determined separately from the relationship between the phase gradient and magnetic induction, $\partial\phi/\partial\mathbf{r} = 2\pi et/h\,\mathbf{B}(\mathbf{r})$, where e is the electron charge, t is the film thickness, and h is the Planck constant. The local **B** directions are parallel to the tangent of the equiphase lines, as indicated by black arrows in Fig. 3.49, and the magnitude of **B** is inverse proportional to the spacing of the equiphase lines.

The Fresnel-mode Lorentz and holographic phase reconstructed images show consistently the location of several DWs by bright contrast lines in the former case and by sharply bent equiphase lines in the latter case. The high resolution electron holography then provides the detailed information on the internal structure of the DWs. As expected the magnitude of **B** decreases with increasing temperature. The direction of **B** rotates gradually across the wall boundary for all detected DWs implying the Néel type walls in the studied (Ga,Mn)As film. For the DW denoted as (i) in Fig. 3.49, **B** rotates from the near [100]/[010] directions towards the [1$\bar{1}$0] direction with increasing temperature, i.e., direct images of a transition from the near-90° in-plane DW at low-temperatures to a near-180° wall at higher temperatures are acquired. As discussed below this is a demonstration in DW physics of the competition between cubic and uniaxial anisotropies in the (Ga,Mn)As ferromagnet.

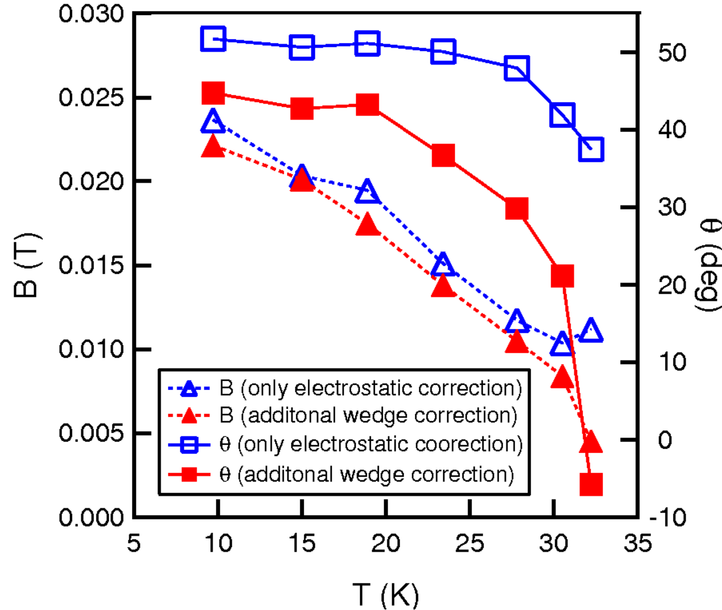

Figure 3.50: Magnitude ($|B|$) and direction (θ) of B as a function of temperature (T). Only results with subtraction of paramagnetic phase images for thickness variation correction and further linear-wedge correction are displayed.

Fig. 3.50 summarises the variation of the magnitude of **B** and the angle θ of **B** measured from the [1$\bar{1}$0]-axis as a function of temperature for the left end of the DW (i). Filled symbols, corresponding to the phase images in Fig. 3.49, include linear wedge cor-

rection for thickness variation near the sample foil edge along the [1$\bar{1}$0]-direction. For comparison the uncorrected data which show similar behaviour (only the variation of θ appears smaller) are plotted. Note that the Lorentz wall contrast observed in the near-edge regions disappeared at temperatures typically 10 K lower than the far-edge region. This suggests that the local temperature near the edges of the sample foil was higher than indicated by the thermal read-out from the liquid helium sample holder, due to restricted or insufficient heat transfer.

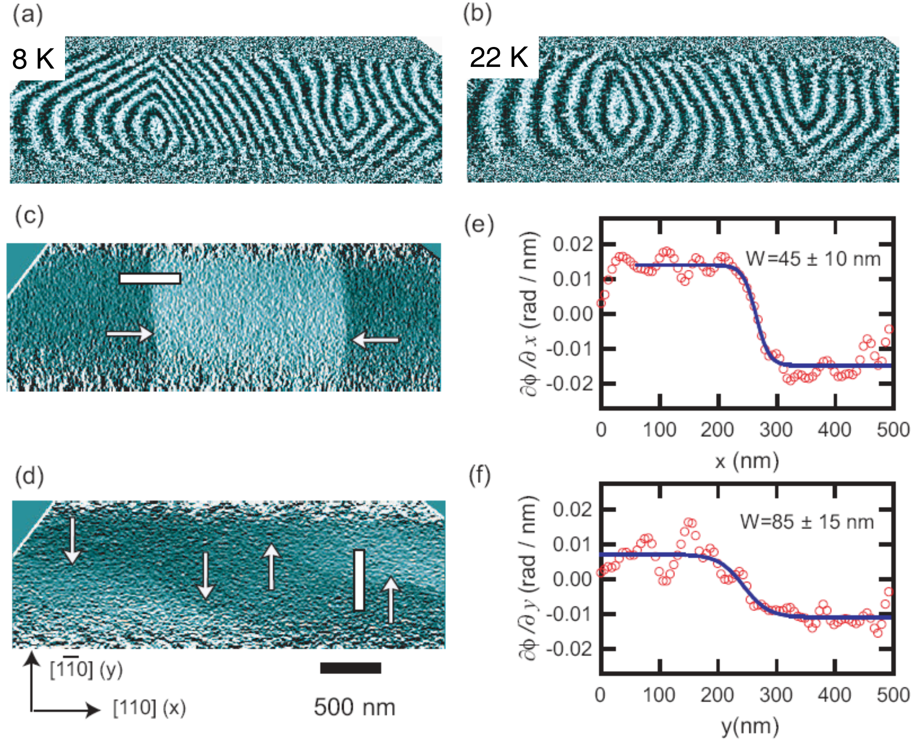

Figure 3.51: Phase image amplified by a factor of 4, acquired at 8 K (a) and 22 K (b). x-differentiated (c) and y-differentiated (d) images of (a). The DW positions are indicated by white arrows. Projected profile of the phase gradient across the [1$\bar{1}$0]-oriented DW (e) and [110]-oriented DW (f) along lines indicated by white rectangles.

Phase images in Fig. 3.51(a),(b) show vortex-like DWs which clearly demonstrate the dependence of the magnetisation rotation angle and width of the DWs on the crystallographic orientation of the wall and temperature. The [110] and [1$\bar{1}$0]-oriented walls evolve from near-90° walls at low-temperatures to a large angle [1$\bar{1}$0]-oriented wall and a small angle [110]-oriented wall at higher temperatures. The width W_m of the walls is obtained by differentiating the phase images with respect to the x ([110]) and y ([1$\bar{1}$0]) directions (see Figs. 3(c)-(f)) and by fitting the measured phase gradient profile with a hyperbolic-tangent function [45]. In particular, the B_y profile along the x-axis for the narrow [1$\bar{1}$0]-oriented wall was fitted by $B_y = B_{y0} \tanh(2(x - x_0)/W_m) + C$, where x_0, and C are the central position of the wall and a compensation term for the phase gradient,

respectively. $W_m = 45 \pm 10$ nm was obtained for the measurement at 8 K and 54 ± 17 nm at 22 K. At 30 K the width is, within the error bar, identical to W_m at 22 K. Analogous fitting procedure for the [110]-oriented walls yield $W_m = 85 \pm 15$ nm for the measurement at 8 K and 117 ± 35 nm at 22 K. At 30 K the [110]-oriented walls have not been resolved.

We now proceed to the theoretical analysis of the measured DW characteristics. On a qualitative or semiquantitative level, the physics underlying the observed phenomenology of in-plane DWs in (Ga,Mn)As can be consistently described using the well established kinetic-exchange model presented in sections 2.1 and 3.1. The SOC in the band states produces the large magnetocrystalline anisotropies and, together with the mixed heavy-hole/light-hole character, the large spin stiffness [1, 26, 61, 25].

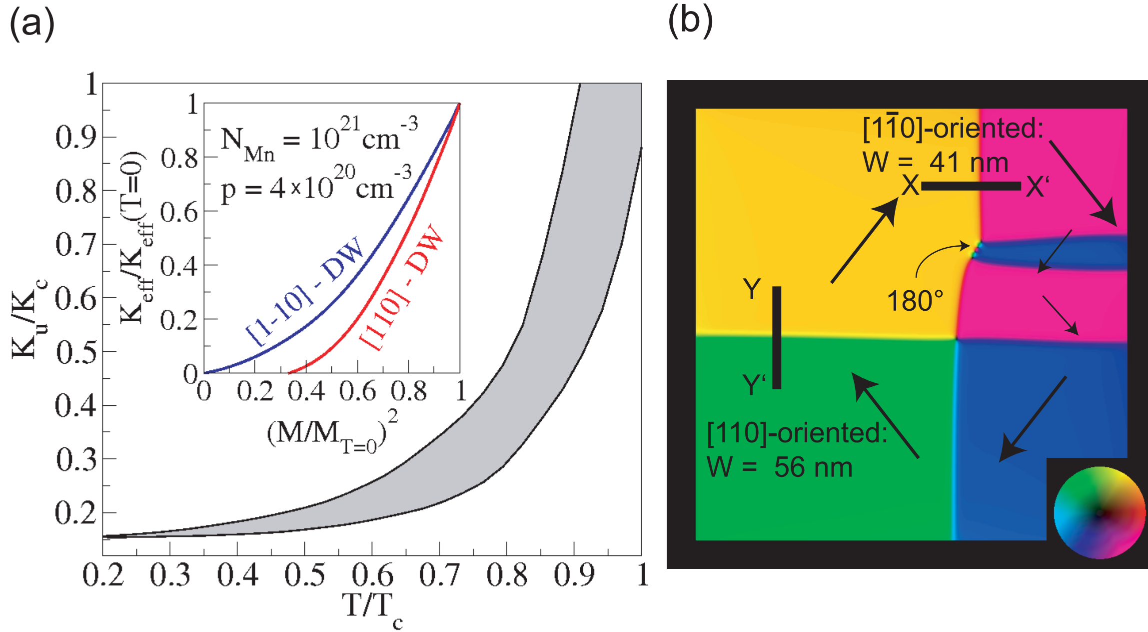

Figure 3.52: (a) Microscopic calculations of K_u/K_c for the whole range of doping parameters considered; inset shows the effective barrier energies for the two walls and the specified hole and local moment densities. (b) LLG simulations for the low temperature micromagnetic parameters of the studied (Ga,Mn)As. Magnetisation orientations in the individual domains are highlighted by arrows.

Based on previous detailed characterisations [57] of the as-grown (Ga,Mn)As materials we assumed in our calculations a range of relevant hole densities, $p = 3 - 4 \times 10^{20}$ cm^{-3} and Mn local moment dopings, $x_{Mn} = 3 - 4.5\%$ ($N_{Mn} = 6 - 10 \times 10^{20}$ cm^{-3}). The corresponding mean-field Curie temperatures are between 50 and 100 K, consistent with experiment. First we inspected the theoretical dependence of in-plane magnetocrystalline anisotropies on growth-induced lattice-matching strains. We found that typical strains in as-grown materials have a negligible effect on the in-plane anisotropy energy profiles and, therefore, releasing the strain during the preparation of the thinned, electron-transparent (Ga,Mn)As foil should not affect significantly the properties of in-plane DWs. The in-plane magnetocrystalline anisotropy energy is accurately described by Eq. (3.12) with the in-plane angle θ measured from the $[1\bar{1}0]$ crystal axis. The microscopic origin of the [110]-uniaxial anisotropy component present in most (Ga,Mn)As materials is not known

but can be modeled by introducing a shear strain $e_{xy} \sim 0.001-0.01\%$. For the considered range of hole and local moment densities we obtained theoretical $T = 0$ values of K_c between approximately 0.5 and 1.5 kJm^{-3}, consistent with the low-temperature SQUID measurement of K_c. The theoretical K_c values were found to be independent of e_{xy}, which is the only free parameter in the theory and whose magnitude and sign was fixed to match the experimental low-temperature K_u/K_c ratio. We then calculated the temperature dependence of K_u/K_c and the corresponding easy-axis angle $\theta = 1/2 \arccos(K_u/K_c)$ (the other easy-axis is placed symmetrically with respect to the $[1\bar{1}0]$-direction.) The results, shown in Fig. 3.52(a), are fairly universal for all p's and N_{Mn}'s considered in the calculations and consistent with experimental data in Fig. 3.50.

An order-of-magnitude estimate of the theoretical DW width is given [61] by the length-scale $\sqrt{A/K_{eff}}$, where K_{eff} is the effective anisotropy energy barrier separating the bistable states on respective sides of the DW. For $N_{Mn} \approx 10^{21}$ cm^{-3}, the mean low-temperature value of $K_{eff} \approx K_c/4 \approx 0.3$ kJm^{-3} (with 20% variation in the considered range of hole densities) and the spin-stiffness $A \approx 0.4$ pJm^{-1} (nearly independent of p), yielding typical DW width $W_m \sim 40$ nm, in agreement with experiment. Despite the relatively small $K_u/K_c \approx 0.15$ and the corresponding small tilt by $\approx 10°$ of the easy-axis from the [100]/[010] directions at low temperatures, $K_{eff}^{[1\bar{1}0]} \approx K_c/4 + K_u/2$ for the larger-angle, $[1\bar{1}0]$-oriented DW is already about twice as large as $K_{eff}^{[110]} \approx K_c/4 - K_u/2$ for the smaller-angle, [110]-oriented DW (see Fig. 3.52(a)), explaining the sizable difference between the respective experimental DW widths at 8 K. The observed temperature dependence of W_m can be qualitatively understood by considering the approximate magnetisation scaling of $K_c \sim M^4$, $K_u \sim M^2$, and $A \sim M^2$ [142, 25]. This implies for the $[1\bar{1}0]$-oriented DW that W_m initially increases with temperature and then saturates at high T while the [110]-wall width steadily increases with T, becoming unresolvable at $K_u(T)/K_c(T) \approx 1/2$. (Note that a more quantitative discussion of the temperature dependence of W_m is also hindered by the relatively large experimental error bars for this quantity.)

Magnetic dipolar fields play a marginal role in the dilute moment (Ga,Mn)As ferromagnets which may explain, together with the $< 180°$ wall-angle, the Néel type of the observed DWs despite their relatively small thickness. We further elaborate on this and on the above qualitative arguments by performing the LLG simulations using micromagnetic parameters of the studied (Ga,Mn)As material. These calculations, shown in Fig. 3.52(b) for $T = 8$ K, confirm the Néel type of the DWs, the evolution from near-90° walls at low-temperatures to larger angle $[1\bar{1}0]$-oriented walls and smaller angle [110]-oriented walls at higher temperatures, and the increasing anisotropy of the DW widths with increasing temperature with W_m ranging from 40 to 100 nm. This leads us to the conclusion that our combined experimental and theoretical work represents an important extension to our understanding of the micromagnetics of in-plane magnetised (Ga,Mn)As down to the smallest relevant length-scale, the individual DW width. Since our findings are likely unaffected by the constraints of the experimental technique on the lateral and vertical sample dimensions, our approach has a generic utility as a basis for DW studies in dilute moment ferromagnets.

3.3 Overview of results in transition metal systems

Now we turn our attention to theoretical results obtained for metallic multilayers using our tight-binding model. As mentioned in the introduction, this work includes the first stage of developing a coherent model of crystalline and transport anisotropies in metallic multilayers. We start with choosing a suitable realistic tight-binding parametrisation, compare results of the newly developed code to ab-initio calculations and check the internal consistency of our numerical predictions focusing on magnetocrystalline anisotropies.

In the next stage, which is beyond the scope of this work, we aim to extend our model to Landauer-Büttiker transport formalism in the framework of equilibrium Green's functions for which a tight-binding parametrisation assuming orthogonal basis set and interactions to the first nearest neighbour would be the most suitable starting point. On the other hand, to our best knowledge, no standard parametrisation of transition metals is restricted only to the first nearest neighbours. Therefore, in this section, we use three standard transferable parametrisations introduced in Subsec. 2.2.3 and analyse the band structures and MAE which they produce for systems with cobalt, platinum, and iron. We select these three elements since they possess room temperature ferromagnetism (Co and Fe) and relatively strong SOC (Pt) and since their compounds have been studied both experimentally and theoretically by relativistic full-potential LAPW methods [115, 116], providing a valuable benchmark for our modelling and code.

After comparing all parametrisations on the level of bulk monoatomic crystals, we resort to the extended Harrison parametrisation as the most suitable for multilayer systems and calculate the DOS and MAE for CoPt and FePt ordered alloys, both for bulk crystals and for thin films. In addition to comparisons to existing results the convergence of our numerical calculations is investigated. We conclude this section by evaluating local MAE and ADOS of a thin film which is a quantity directly related to TAMR, a transport effect that we aim to study in future.

3.3.1 Bulk elemental metals

In this subsection we compare our tight-binding band structures with LAPW results for bulk fcc Co and Pt and for bulk bcc Fe. We do not consider the hcp lattice for Co as our aim is to model the $L1_0$ CoPt structure (alternating Co and Pt layers in fcc lattice), moreover the Mehl parametrisation is only available for fcc and bcc lattices. The comparisons are better visualised on paramagnetic states with fewer bands crossing the Fermi level. Note that the ferromagnetic exchange splitting of the extended Harrison and Mehl tight-binding parameters is optimised to produce ferromagnetic band structures matching the LAPW results. As explained in subsection 2.2.4 we omit the exchange splitting of the S-K parameters included in the extended Harrison parametrisation and keep only exchange-split on-site parameters. Nevertheless, we obtain spin magnetic moments of fcc Co and bcc Fe which differ from ab-initio results by less than 6% [76]. The band structure of Pt considers the SOC with $\lambda_p = 0.05655$ Ry and $\lambda_d = 0.0109$ Ry [76] in case of the tight-binding model. We obtained the LAPW results using the standard WIEN2k package.

Fig. 3.53 compares LAPW band structures of fcc bulk crystals of Co and Pt with results obtained using the Harrison, extended Harrison, and Mehl parametrisations. The

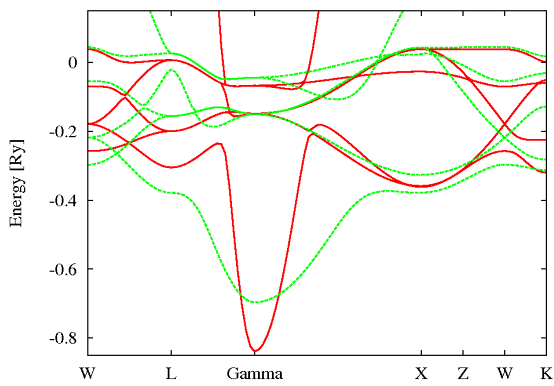

(a) Co, Harrison p.

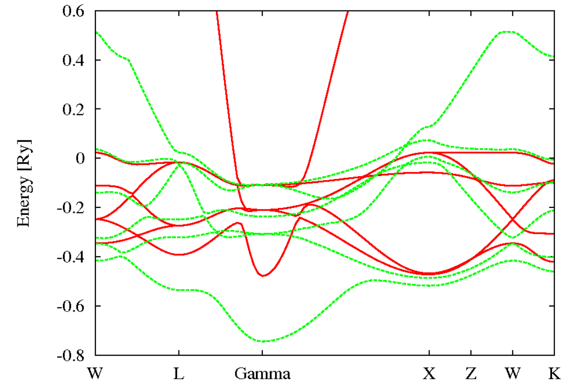

(b) Pt, Harrison p.

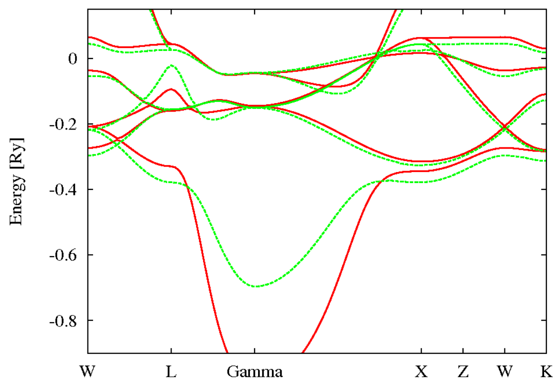

(c) Co, ext. Harrison p.

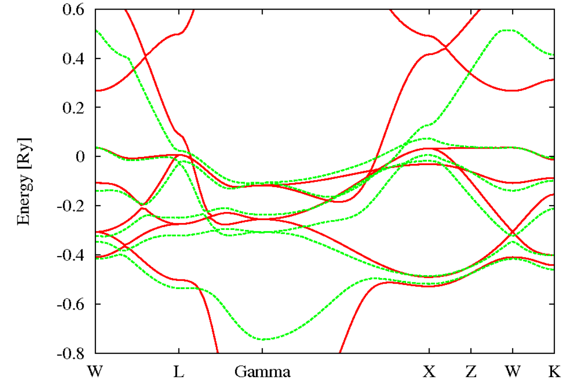

(d) Pt, ext. Harrison p.

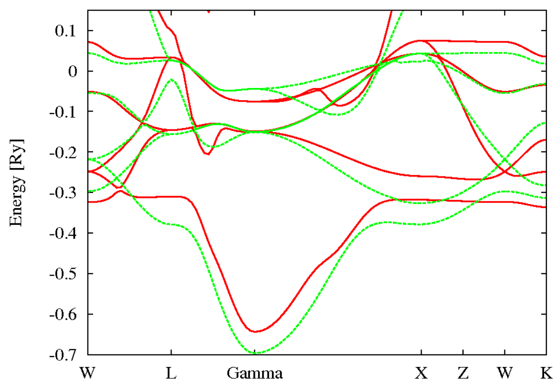

(e) Co, Mehl p.

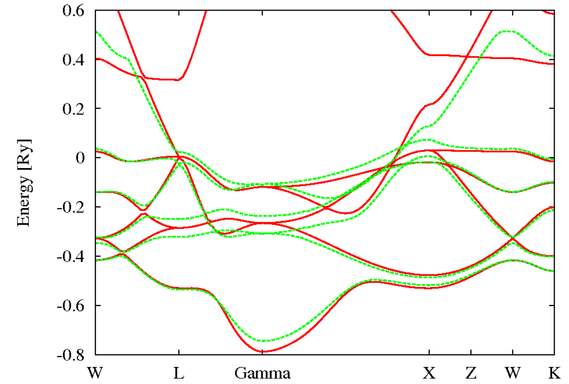

(d) Pt, Mehl p.

Figure 3.53: Band structures of paramagnetic bulk fcc Co and Pt. The red curves are obtained by our tight-binding codes using the parameters given below each panel. The green reference curves obtained by LAPW method are the same in all rows. The lattice constant is 7.45 a.u. for Pt and 6.45 a.u. for Co. The tight-binding band structures were shifted in energy to allow for the most accurate comparison to LAPW in the vicinity of the Fermi energy, 0 Ry. The path through the fcc Brillouin zone connects points of high symmetry with the standard notation (Bilbao Crystallographic server).

same trend can be seen for both metals: The Harrison parametrisation considering only the second nearest neighbours shows the poorest agreement with LAPW. As admitted by Harrison [41], a good result for the s-like band would require consideration of more neighbours which is against the nature of his minimalistic but most elegant parametrisation. The extended Harrison parametrisation considering besides other improvements also the third nearest neighbours shows much better agreement with the LAPW bands in the vicinity of the Fermi energy (origin of the vertical axis) but the bottom of the s-like band remains too low. The best match with LAPW is obtained with the most sophisticated Mehl parametrisation considering in total over 300 neighbours.

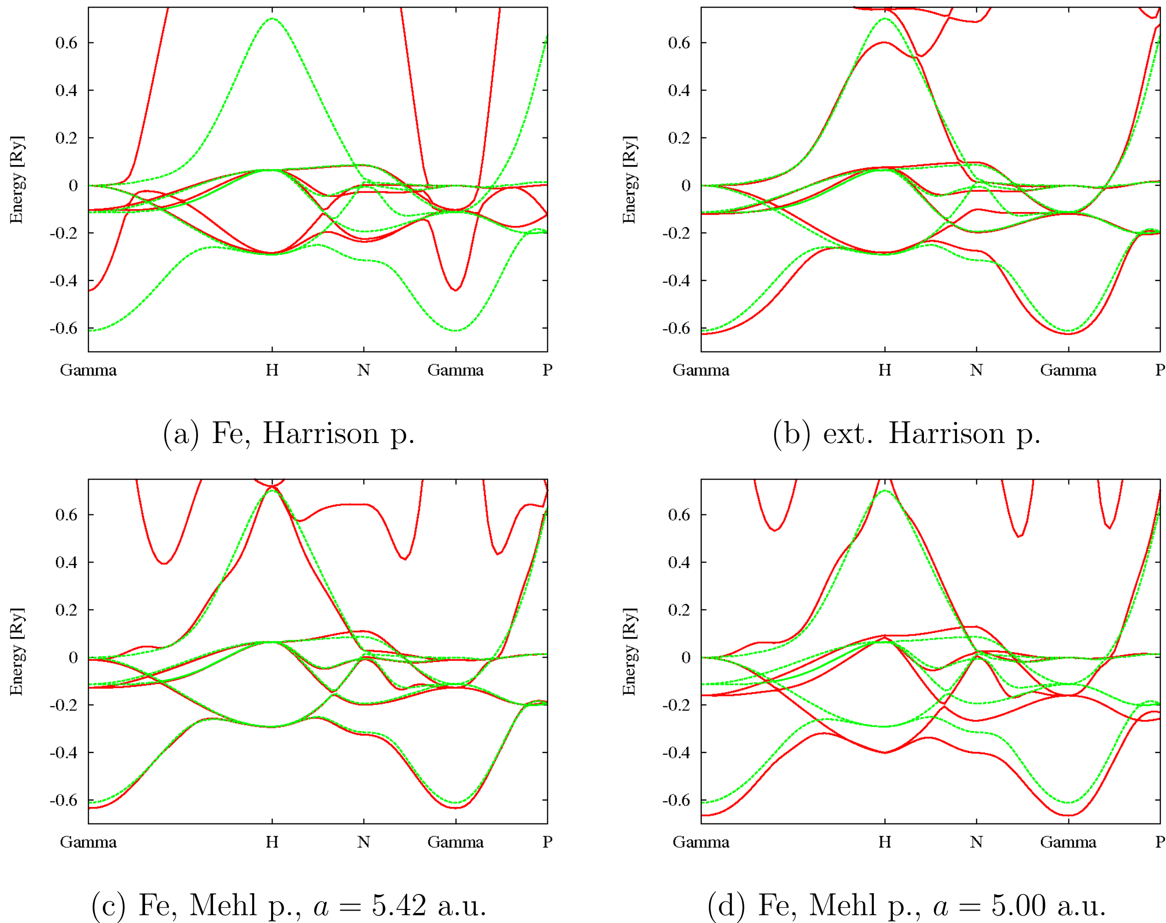

(a) Fe, Harrison p.

(b) ext. Harrison p.

(c) Fe, Mehl p., $a = 5.42$ a.u.

(d) Fe, Mehl p., $a = 5.00$ a.u.

Figure 3.54: Band structures of paramagnetic bulk bcc Fe. The red curves are obtained by our tight-binding codes using the parameters given below each panel. The green reference curves obtained by LAPW method are the same in all panels. The lattice constant is 5.42 a.u. in panels (a,b,c) and 5.00 a.u. in panel (d). The tight-binding band structures were shifted in energy to allow for the most accurate comparison to LAPW in the vicinity of the Fermi energy, 0 Ry. The path through the bcc Brillouin zone connects points of high symmetry with the standard notation (Bilbao Crystallographic server).

Fig. 3.54, in analogy to Fig. 3.53, compares the band structures of bcc bulk Fe. The same trend is seen as in Co and Pt: The Harrison parametrisation shows the poorest agreement with LAPW, whereas the Mehl parametrisations produces bands almost iden-

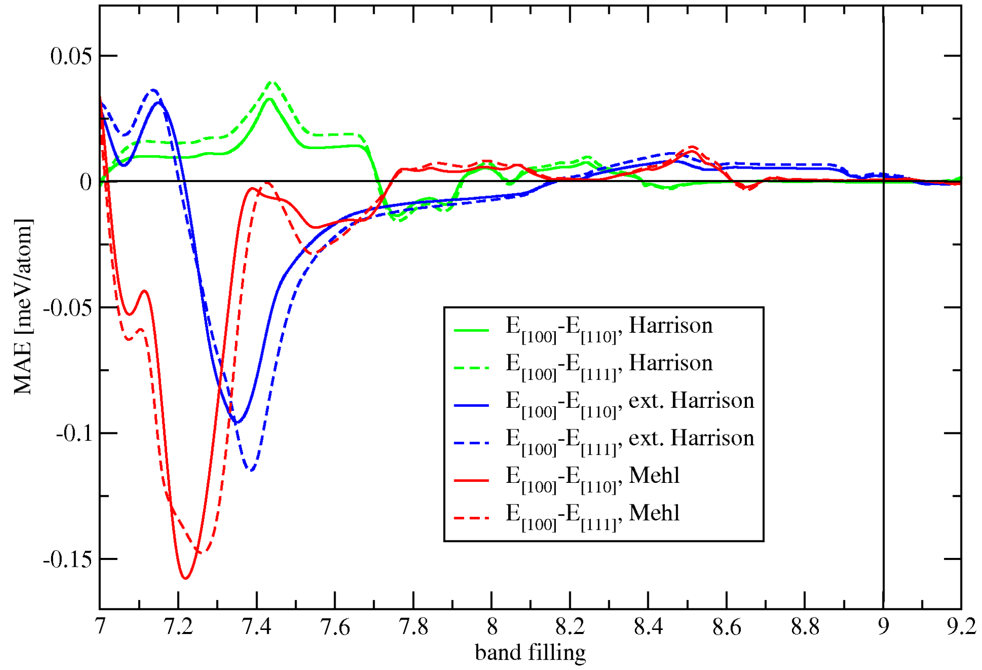

(a) Co, all three parametrisations

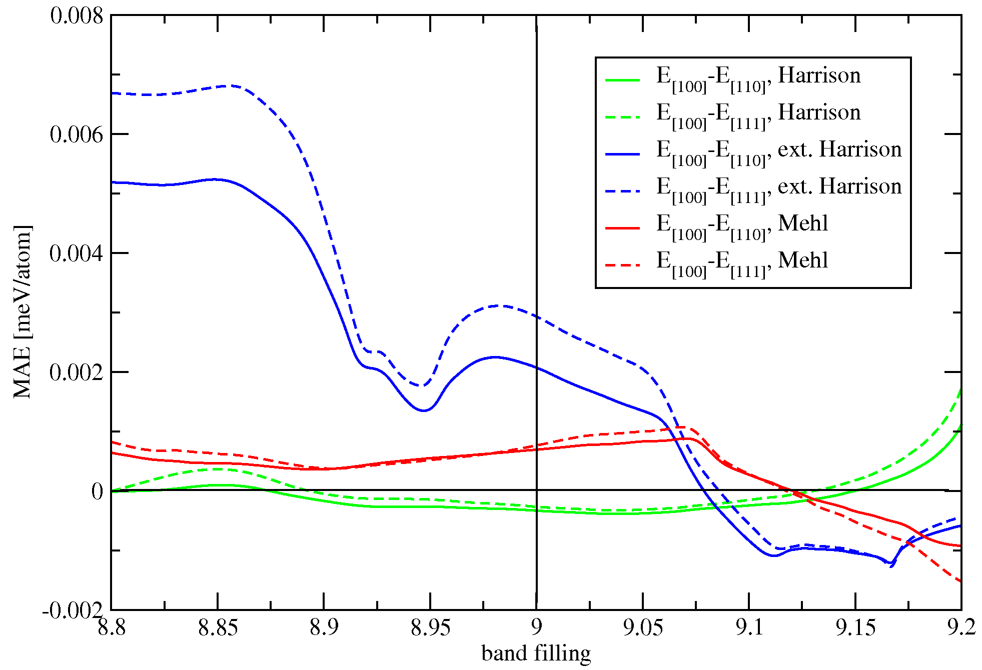

(b) Co, detail of the plot above

Figure 3.55: MAE of bulk fcc Co, $E_{[100]}$ corresponds to total energy with magnetisation along the [100] crystal axis. The vertical line shows the natural number of valence electrons. All data obtained by the tight-binding code.

tical to LAPW for the equilibrium lattice constant. Note that the Mehl parameters are optimised around the equilibrium lattice constant but the method is also quite robust

against physically relevant variations in a. Panel (d) of Fig. 3.54 shows band structures obtained for a reduced by nearly 10% and the agreement between Mehl's parametrisation and LAPW is still very good (similar to the agreement between extended Harrison and LAPW for the equilibrium a shown in panel (b) of Fig. 3.54). However, the lattice constant of the $L1_0$ FePt alloy studied in the next subsection is approximately by 30% larger than the equilibrium lattice constant of bulk Fe so it significantly exceeds the range of reliability suggested by the authors of the Mehl parametrisation.

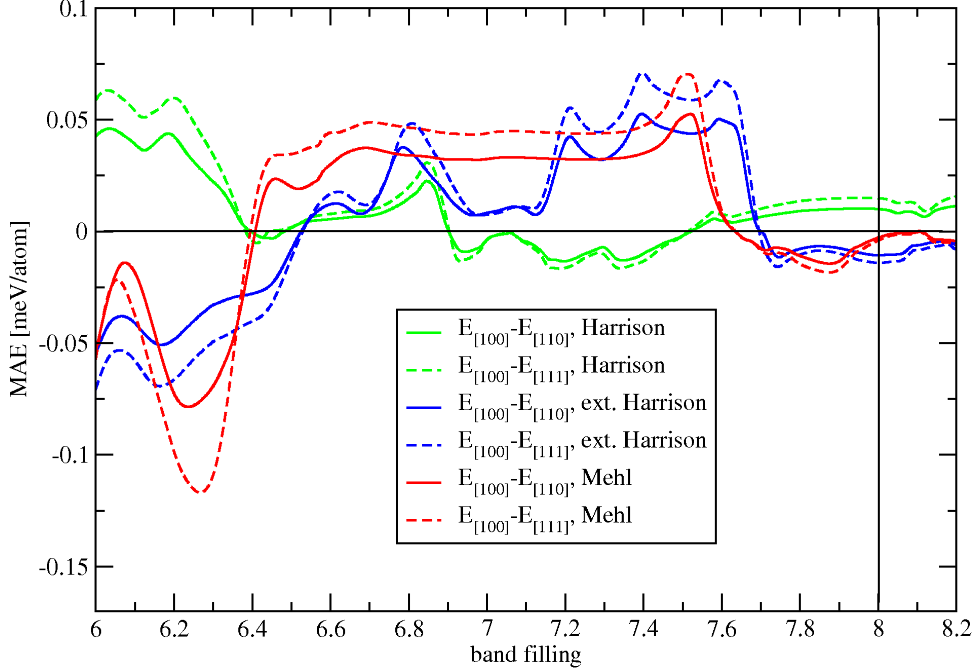

Figure 3.56: MAE of bulk bcc Fe, $E_{[100]}$ corresponds to total energy with magnetisation along the [100] crystal axis. The vertical line shows the natural number of valence electrons. All data obtained by the tight-binding code.

We conclude that the most complex Mehl parametrisation gives band structures which are in the best agreement with the LAPW calculation in case of all three considered metals. Nevertheless, the complexity and lack of transferability of the parametrisation is unfavourable for investigation of more complicated crystal structures of magnetic multilayers. The next candidate for our further use is therefore the extended Harrison parametrisation considering its second best agreement with the LAPW bandstructures.

We continue by a mutual comparison of the parametrisations based on the predicted MAE for Fe and Co. Even though the SOC in Co and Fe is an order of magnitude smaller than in Pt, it gives rise to MAE in the bulk cubic crystals which can be evaluated numerically by our code. Rather than comparing our MAE quantitatively to ab-initio predictions, which would be numerically very demanding, we test whether all three parametrisations produce the same anisotropy in elemental crystals for which they were optimised. The following exchange and spin-orbit parameters are used: $\Delta E_s = -0.038$ Ry, $\Delta E_p = 0.016$ Ry, $\Delta E_d = 0.124$ Ry [114], $\lambda_p = 0.002$ Ry, $\lambda_d = 0.005$ Ry [76] for Co and $\Delta E_s = -0.034$ Ry, $\Delta E_p = 0.037$ Ry, $\Delta E_d = 0.167$ Ry [114], $\lambda_p = 0.0$ Ry, $\lambda_d = 0.004$ Ry [120] for Fe. The lattice constants are $a_{Co} = 6.45$ a.u. and $a_{Fe} = 5.42$ a.u. as in the previous calculations.

Figures 3.55 and 3.56 show the dependence of MAE on the band filling calculated by our tight-binding code using the three parametrisations. In the broader range of band filling, both crystals possess comparable anisotropy with magnitudes reaching ~ 0.1 meV. Closer to the natural filling, the MAE in Co is an order of magnitude smaller than the value obtained by ab-initio calculations for hcp Co and than our value of MAE in Fe. This could be due to different alignment of the magnetisation with the bonds between the 1st nearest neighbours in the fcc lattice. Figures 3.55 and 3.56 show that the extended Harrison and Mehl parametrisations result in similar overall MAE trends, whereas the minimalistic Harrison parametrisation gives different results. Given the small values of MAE in elemental Co or Fe, the similarity we obtained between Mehl and extended Harrison tight-binding results is encouraging and allows us to proceed with the extended Harrison parametrisation to the more complex bimetallic structures. We must, however, also caution that the tight-binding modelling should be regarded only as a qualitative or at most semi-quantitative tool when investigating the subtle relativistic magnetic anisotropy phenomena.

3.3.2 Bimetallic multilayers

We have shown that the extended Harrison parametrisation is capable of predicting MAE in reasonable agreement with the very complex and more accurate Mehl parametrisation. We take advantage of this fact in this subsection where we focus on the $L1_0$ CoPt and FePt alloys and derived multilayer structures of finite thickness. It would be very complicated to implement the Mehl parametrisation for such systems due to the high number of neighbours that it takes into account. Moreover, the unit cell of the CoPt and FePt alloys is not cubic which may compromise the superiority of the Mehl parametrisation optimised for bulk cubic crystals.

In the rest of the subsection we present results obtained using the tight-binding model with the extended Harrison parametrisation (including the exchange splitting) and the experimental lattice constants: $a = 7.19$ a.u., $c = 7.01$ a.u. for CoPt and $a = 7.30$ a.u., $c = 7.15$ a.u. for FePt [116]. For simplicity, we neglect the SOC in Co and Fe and use $\lambda_p = 0.05655$ Ry and $\lambda_d = 0.0109$ Ry [76] for Pt as mentioned earlier. The hybridisation of states belonging to sublattices of the spin-orbit or exchange coupled atoms results in the dependence of the total energy on magnetisation direction.

At first we compare the DOS and the spin moment in ferromagnetic $L1_0$ CoPt alloy obtained by our tight-binding code to LAPW calculation [69] (see also Ref. [116] for details of the LAPW calculation in Ref. [69]). Fig. 3.57 shows spin-up and spin-down DOS calculated for three magnitudes of the exchange splitting. (The SOC is not considered in this particular comparison.) The first value of the exchange splitting assumed in our tight-binding calculation is taken from the extended Harrison on-site parameters for bulk ferromagnetic Co which produce the spin moment of bulk Co in reasonable agreement with the ab-initio result as mentioned in the previous subsection. This default value of the exchange splitting, denoted by "Exch" in Fig. 3.57, produces DOS which is in a poor agreement with the LAPW result. Moreover, it produces a very small spin moment per unit cell $M_s = n_{up}(E_F) - n_{down}(E_F) = 0.96\mu_B/f.u.$, where $n_{up}(E_F)$ is the number of electrons in the spin-up state below the Fermi energy. The spin moment obtained by LAPW is $M_s \approx 2.2\mu_B/f.u.$ [116]. These discrepancies might be due to low relevance of

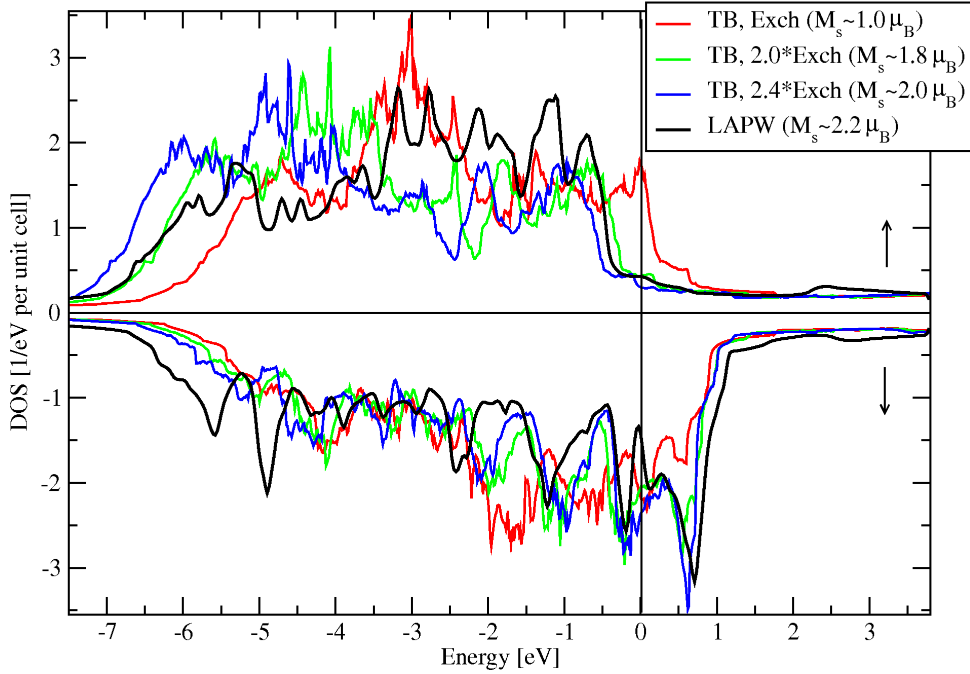

Figure 3.57: Comparison of the density of spin-up and spin-down states calculated by our tight-binding code (denoted by TB) and by the LAPW method for $L1_0$ CoPt alloy. The red curves are obtained for exchange splitting given by the extended Harrison parametrisation and the green curves for an enlarged magnitude. The vertical line marks the Fermi energy. (The unit cell contains two atoms.)

the exchange parameters (optimised for a bulk monoatomic crystal) to $L1_0$ alloys.

There are six independent exchange parameters entering our tight-binding description of the CoPt alloy that could be optimised by fitting our spin moment and DOS to the LAPW results before we would proceed to calculations of the MAE. Instead of such extensive fitting procedure, which is again beyond the scope of the initial stage of our study, we test the stability of our modelling with respect to the exchange splitting on Co atoms. For the sake of simplicity, we multiply all the values ΔE_s, ΔE_p, and ΔE_d of the extended Harrison parametrisation by the same factor α_{Co}. We plot the DOS obtained for $\alpha_{Co} = 2.0$ and $\alpha_{Co} = 2.4$ in Fig. 3.57. The agreement with DOS obtained by LAPW is better for both values of α_{Co} as compared to the default exchange parameter but no further improvement seems to be achievable by tuning the factor α_{Co}. Unfortunately, the corresponding tight-binding prediction of the spin moment ($M_s = 1.81\mu_B/f.u.$ for $\alpha_{Co} = 2.0$ and $M_s = 2.01\mu_B/f.u.$ for $\alpha_{Co} = 2.4$) approaches the LAPW result but remains smaller by almost 10%.

We perform an analogous test for the $L1_0$ FePt alloy for which the spin moment calculated by our tight-binding code for the default exchange splitting on Fe is only $M_s = 2.86\mu_B/f.u.$, whereas the LAPW result is $M_s \approx 3.3\mu_B/f.u.$ [116]. We multiply the default exchange splittings on Fe atoms by the same factor α_{Fe} and obtain $M_s = 3.12\mu_B/f.u.$ for $\alpha_{Fe} = 1.5$ and $M_s = 3.35\mu_B/f.u.$ for $\alpha_{Fe} = 2.0$. In contrast to CoPt, the agreement with the LAPW spin moment is achieved for a reasonably small modification of the exchange splitting optimised for bulk monoatomic Fe.

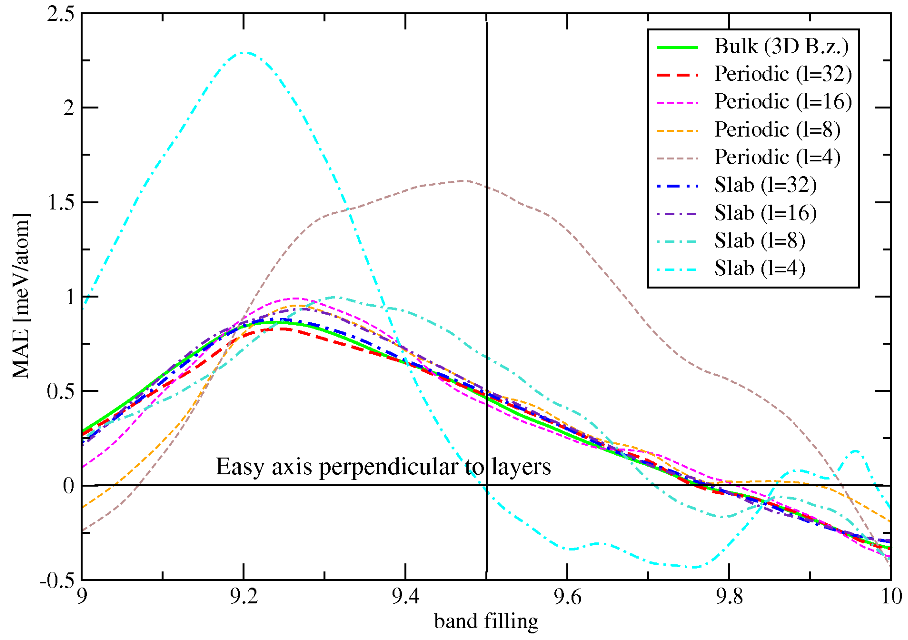

(a) CoPt, convergence to bulk $L1_0$

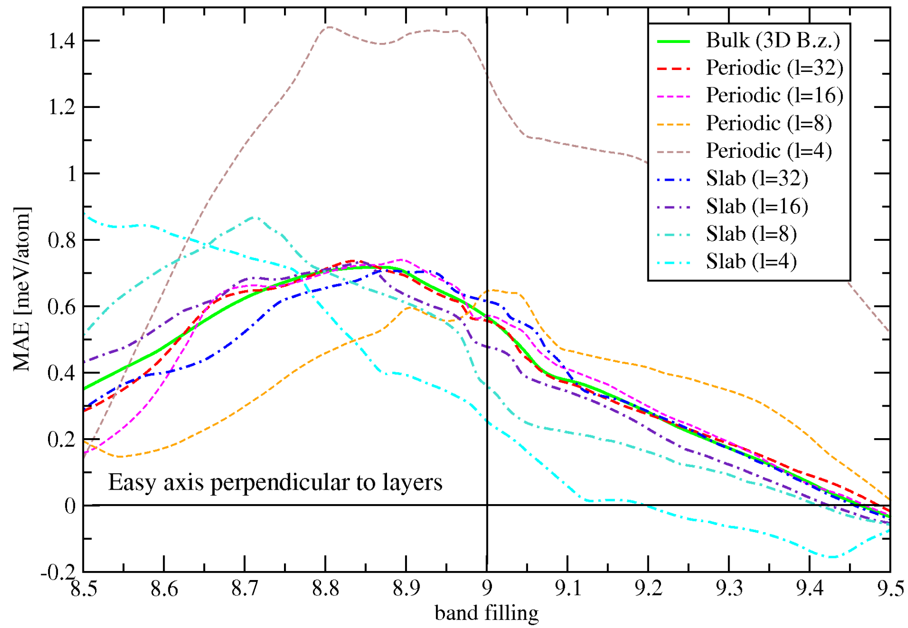

(b) FePt, convergence to bulk $L1_0$

Figure 3.58: MAE $= E_{[110]} - E_{[001]}$ of CoPt and FePt structures: $L1_0$ (bulk), $L1_0$ treated as a sequence of l layers with periodic boundary conditions (periodic), and finite set of l layers (slab). The experimental lattice constants are used in all cases. The vertical line marks the natural number of valence electrons.

We conclude that the extended Harrison parametrisation is relevant in predicting the spin-polarised DOS of the $L1_0$ alloy with modified values of the exchange splitting. Quantitative agreement of the tight-binding and LAPW calculations of the DOS and the

spin moment is not achievable by tuning the exchange parameters on the ferromagnetic atom of the alloy. However, we have determined a range of exchange parameters where the overall agreement with LAPW results is improved significantly as compared to the default exchange splitting. We will continue by testing the stability of our predictions of MAE within this range.

Before the MAE calculated for $L1_0$ alloys is presented, we carry out a check of the implementation of finite multilayers derived from the bulk $L1_0$ structure into our model and code. (We use only the default set of exchange splitting parameters during this check.) The formal description of systems with broken periodicity along the z-axis is provided in Subsec. 2.2.2. Even though our formalism and code are more general, here we only consider multilayers derived from the $L1_0$. In addition to bulk $L1_0$ with a 3-dimensional Brillouin zone, we investigate the same structure treated as a sequence of alternating Pt and Co (or Fe) layers with periodic boundary conditions and a 2-dimensional Brillouin zone (for simplicity referred to as periodic). A finite multilayer is obtained by removing the periodic boundary conditions (for simplicity referred to as slab). Deviations of the numerical predictions for the periodic system, as compared to the 3D $L1_0$ alloy, occur only due to the difference between discretisations of the k-space in the z-direction and of the subband indices, respectively, and between dimensions of the Hamiltonian matrices. The results for bulk and periodic systems should converge to each other with growing number of k-points and number of layers. On the other hand, the electronic structure of a slab is physically different from the bulk structure and the convergence is expected only for properties averaged over the whole multilayer (such as the net MAE) with high number of monoatomic layers.

Fig. 3.58 demonstrates the convergence of MAE obtained for slab and periodic systems to the MAE of bulk $L1_0$ for band filling in the vicinity of the natural values 9.5 (CoPt) and 9 (FePt). The number l counts the monoatomic layers so the dimension of the corresponding Hamiltonians is $18 * l$ (our basis of cubic harmonics has 18 elements including spin). We use the unit meV/atom which can be understood also as meV/layer as we consider monoatomic layers, whereas the unit cell comprises two atoms. Note that good convergence is reached for $l = 32$ in case of the periodic system. The convergence of the slab seems slightly slower and prohibitively demanding to track to higher l. The 2D integration uses $nk = 60$ (14641 k-points in $B.z.$) and the 3D integration gives converged results for $nk = 30$ (226981 k-points in $B.z.$). Calculations of all three structures assume the same lattice constants.

Fig. 3.59 shows the dependence of MAE in a finite CoPt multilayer on the band filling for different sizes of the unit cell. In addition to the reference experimental unit cell, we consider also $c = (c_{Co} + c_{Pt})/2$, $a = a_{Pt}$, and $a = a_{Co}$. (The only calculations in this subsection which do not assume the experimental values.) Note that the result is moderately dependent on the unit cell size but the most important feature which is the sign of MAE at the Fermi level is not affected by small distortions of the lattice geometry. The easy axis prefers the perpendicular-to-plane alignment in all three cases.

After investigating the convergence and stability of our results with respect to material parameters we can present the main results of this section. Fig. 3.60(a) shows the MAE of CoPt and FePt as a function of the band filling. The considered structures are again: bulk, periodic, and slab. In case of the bulk material we obtain MAE = 0.5 meV/atom at the Fermi level both for CoPt and FePt which is in good semiquantitative agreement with

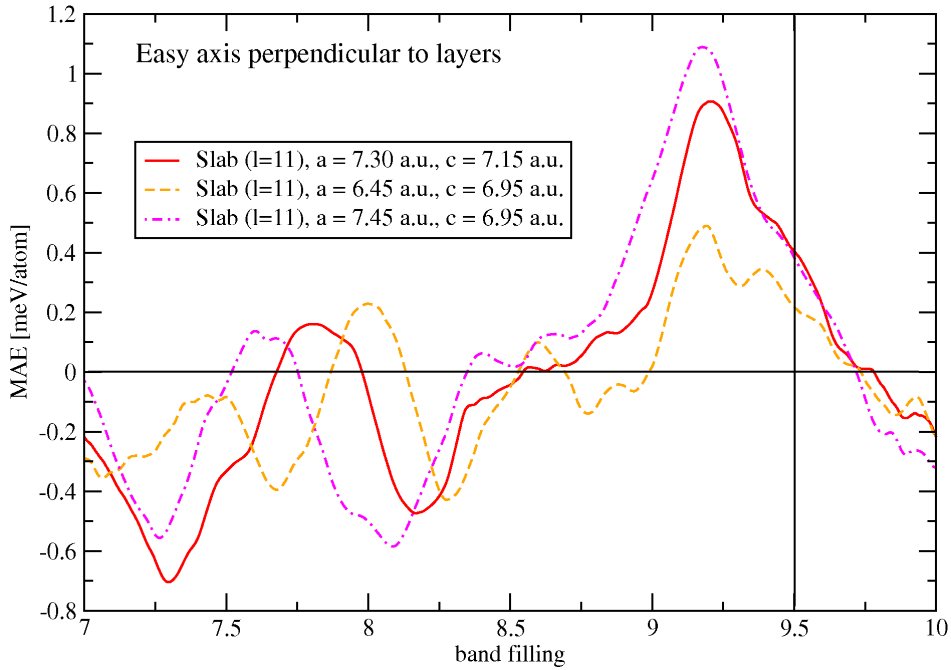

Figure 3.59: MAE $= E_{[110]} - E_{[001]}$ of CoPt thin film comprising 11 layers (slab) with different sizes of the unit cell: a is the in-plane lattice const., c is the distance of two successive layers of the same type. The vertical line marks the natural number of valence electrons.

the experimental and ab-initio theoretical values [116]. According to another theoretical study using the full-potential LAPW with LSDA+U [115], MAE of the finite multilayer comprising 5 Co and 6 Pt layers is approximately a factor of 5 larger than the MAE of bulk $L1_0$ alloy. (To our best knowledge, complementary calculation for FePt is not available). Although we observe an increase of MAE with lowering the number of layers (see slab with $l = 8$ in Fig. 3.60(a)), the factor predicted by LAPW calculation for $l = 11$ is not reproduced. (Note that the natural band filling for Pt terminated multilayer is slightly above 9.5 but this plays negligible role in the comparison.) The most important observation is the alignment of the easy axis perpendicular to the layers which is in agreement with the experiment on a sizable interval of band fillings.

The results presented in Fig. 3.60(a) are obtained for exchange splitting parameters optimised for bulk monoatomic Fe or Co crystals. Earlier in this subsection, we have determined the range of exchange parameters where the agreement of the tight-binding and LAPW predictions of the spin-polarised DOS and the spin moment in the $L1_0$ alloys is improved as compared to the default exchange parameters. Now we test the stability of our predictions of MAE with respect to modifications of the exchange splitting in the relevant range. Fig. 3.60(b) shows that the MAE at the Fermi energy decreases with increasing values of the exchange parameters both for CoPt and FePt. The effect is stronger in case of CoPt but the easy axis remains aligned perpendicular to the layers. It is encouraging to observe that the qualitative agreement with the LAPW and experimental results is preserved for the exchange parameters ranging from the default values to approximately twice the default values. Hence, our tight-binding model predicts

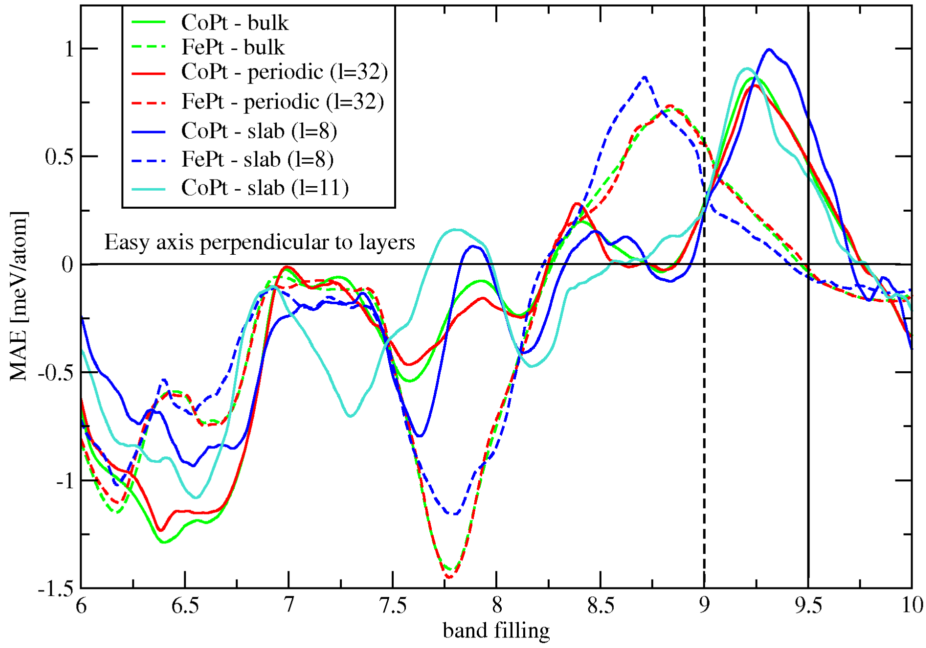

(a) Bulk, periodic, and slab with default exchange splittings

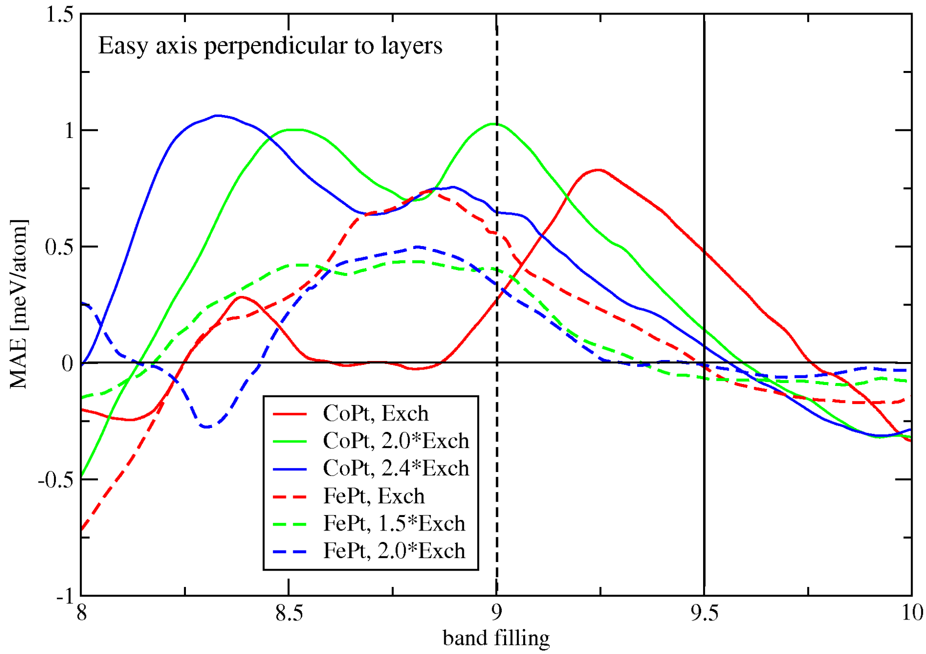

(b) Periodic (l=32) with multiples of default exchange splittings

Figure 3.60: MAE = $E_{[110]} - E_{[001]}$ of CoPt and FePt structures: $L1_0$ (bulk), $L1_0$ treated as a sequence of l layers with periodic boundary conditions (periodic), and finite set of l layers (slab). The experimental lattice constants are used in all cases. The vertical lines mark the natural number of valence electrons.

consistently three ground state magnetic properties (M_s, spin-polarised DOS, and MAE) in qualitative agreement with reference ab-initio results.

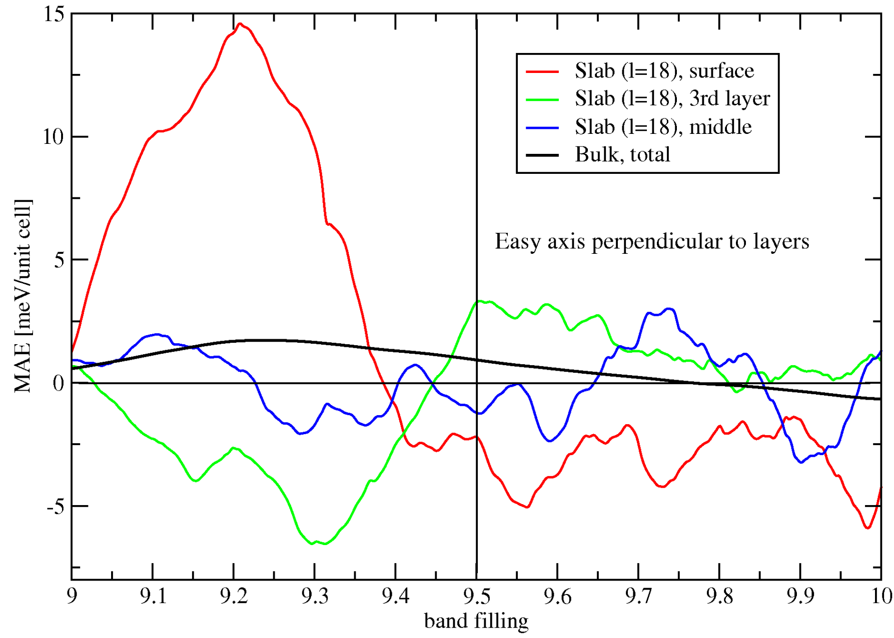

(a) MAE, CoPt slab and $L1_0$ as reference

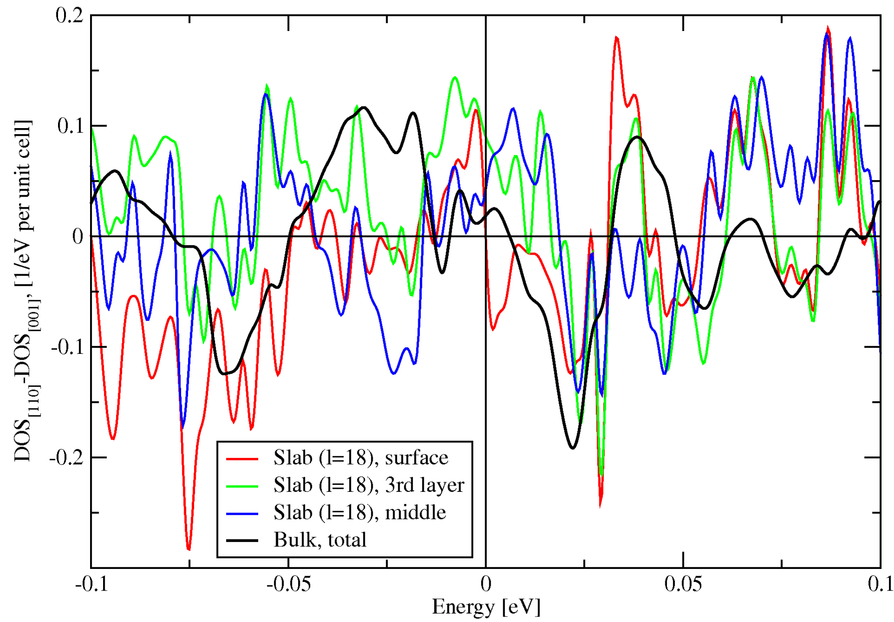

(b) ADOS, CoPt slab and $L1_0$ as reference

Figure 3.61: Local MAE $= E_{[110]} - E_{[001]}$ and ADOS $= \mathrm{DOS}_{[110]}$-$\mathrm{DOS}_{[001]}$ of CoPt thin film and bulk $L1_0$ as reference. The label "surface" denotes the Pt and Co double-layer at one end of the multilayer, "middle" denotes the Pt and Co double-layer in the middle of the structure and "3rd layer" is the double-layer half way in between the previous locations. The experimental lattice constants are used in all cases. The vertical lines mark the natural number of valence electrons and the Fermi energy. (The unit cell contains one Co and one Pt atom as we address the double-layers in contrast to previous plots.)

As an outlook to the next stage of our modelling we calculate the local MAE and ADOS to investigate the distribution of these quantities in the finite multilayer. We choose $l = 18$ (9 Pt-Co double-layers) as the centre of this structure is already approaching bulk material so a noticeable contrast of the surface and middle layers is expected. The local MAE and ADOS are calculated according to Eq. (2.73) as projections onto our basis states localised on the 1st (surface), 3rd (3rd layer), and 5th (middle) double-layer. We observe the largest contribution to the MAE on the surface of the multilayer which gradually decreases and is the smallest in the centre. Similar, yet more oscillatory behaviour is observed in the case of ADOS. Further study of the dependence of ADOS at the Fermi level on the material and tight-binding parameters is desirable as the tunnelling transport properties are directly related to this quantity.

Chapter 4

Summary

4.1 Effective Hamiltonian model

The objective of the first part of this work was to critically and thoroughly inspect the efficiency of a widely used effective Hamiltonian model in predicting magnetocrystalline anisotropies in (Ga,Mn)As. We provided an overview of the calculated anisotropies which show a rich phenomenology as a function of Mn concentration, hole density, temperature and lattice strains, and compared our theoretical results to a wide range of experimental works on the level of the magnetic easy axis direction and on the level of anisotropy fields. The large amount of analysed results has compensated for the common uncertainty in sample parameters assumed in experiment and allowed us to make systematic comparisons between theory and experiment on the level of trends as a function of various tunable parameters. We find this type of comparison between theory and experiment in diluted magnetic semiconductors much more meaningful than addressing isolated samples, given the complexity of these systems and inability of any theoretical approach applied to date to fully quantitatively describe magnetism in these random-moment semiconducting ferromagnets.

In Sec. 2.1 we introduced the mean-field model used throughout the study and discussed the correspondence of the shear strain, modelling the broken in-plane symmetry measured in most (Ga,Mn)As epilayers, with a microscopic symmetry-breaking mechanism. We also estimated the relative strength of the shape anisotropy in Sec. 2.3.

In Sec. 3.1 we focused on modelling and experiments in bare unpatterned epilayers. The in-plane and out-of-plane magnetisation alignments were studied. For compressively strained samples the generally assumed in-plane anisotropy is found to be complemented by regions of out-of-plane anisotropy at low hole densities and low temperatures. This observation is corroborated by available experimental data showing in-plane anisotropy in most of the studied epilayers but also the occurrence of the out-of-plane easy axis in materials with high hole compensation. At the same time, the model predicts out-of-plane easy axis for high hole densities at all Mn concentrations which has yet not been observed experimentally.

Next, the competition of cubic and uniaxial in-plane anisotropy components was investigated. Wealth of experimentally observed easy axis transitions driven by change of temperature or hole density finds corresponding simulated behaviour. The following general trend is observed in most samples: at low temperatures the easy axes are aligned close

to the main crystal axes, while at high temperatures there is always diagonal alignment. This trend is in good agreement with our calculation, however, at low hole densities the calculated and measured easy axis transitions are more consistent than at higher hole densities where the measured phenomena match the predictions assuming hole densities typically a factor of two lower than in the experiment.

We next introduced anisotropy fields corresponding to the crystal symmetry and to three distinct uniaxial strains. We extracted these anisotropy fields from the calculated data and found their dependence on material parameters. We observed linear dependence of the uniaxial anisotropy fields on the corresponding strains. Analysing experiments which determine the anisotropy fields from FMR, AMR, or SQUID measurements allowed for detailed comparison of the cubic anisotropy component and two uniaxial anisotropy components (due to the growth and the $[110/[1\bar{1}0]$ symmetry breaking). The measured and calculated anisotropy fields are of the same order of magnitude ($\sim 10^2 - 10^3$ Oe) in most samples.

In Subsec. 3.1.4 we investigated structures where the post-growth patterning or piezo-electric stressing was used to induce additional strains along any in-plane direction. The interplay of the intrinsic and induced anisotropies was studied. We discussed the procedure for obtaining the strain Hamiltonian from the parameters describing the experimental setup and a finite element solver was employed to find the inhomogeneous lattice relaxation in the patterned epilayers. Induced anisotropies were calculated directly using the total strain tensor. Alternatively, we also introduced a decomposition of the total strain matrix for any of the studied materials and device configurations into three basis strains and their additive effect on the total anisotropy. We found an overall semi-quantitative agreement of theory and experiment on the level of easy axis reorientations due to induced strains.

Finally, in Sec. 3.2 we presented five combined experimental and theoretical projects focused on the control of magnetocrystalline anisotropies in (Ga,Mn)As-based devices by applied electric field, temperature, lattice mismatch relaxation due to post-growth lithography, and piezo-electric straining. In subsection 3.2.1 magnetisation switchings induced by short electric field pulses of a few volts were demonstrated in an all-semiconductor epitaxial structure. In subsections 3.2.2 and 3.2.3 we performed a detailed analysis of magnetic anisotropies induced in lithographically patterned (Ga,Mn)As/GaAs microbars. Structural properties of the microbars were studied by x-ray spectroscopy showing strong strain relaxation transverse to the bar axis. The observed easy-axes rotations which depend on the thickness to width ratio and orientation of the microbar with respect to the crystal can dominate the magnetic anisotropy of the unpatterned (Ga,Mn)As epilayer. The overall good agreement of the microscopically calculated and measured magnetic anisotropies conclusively demonstrate that the patterning induced anisotropies are of the magnetocrystalline, SOC origin. In subsection 3.2.4 the non-volatile switching of the magnetisation direction in (Ga,Mn)As induced by strain applied with a piezo-electric transducer was shown. In subsection 3.2.5 magnetic domain walls in an in-plane magnetised (Ga,Mn)As epilayer were investigated using a high-resolution electron holography technique. We found that the competition of uniaxial and biaxial magnetocrystalline anisotropies in the film is directly reflected in orientation dependent wall width. Both the width and the orientation of the domain walls evolved with temperature and were interpreted successfully based on our microscopic calculations.

The limitations of the theory approach employed in this work have been thoroughly discussed in Ref. [1]. The model, which treats disorder in the virtual-crystal approximation and magnetic interactions on the mean-field level is expected to be most reliable at lower temperatures and in the (Ga,Mn)As materials with metallic conductivity. We have shown that despite the limitations, the model captures on a semi-quantitative level most of the rich phenomenology of the magnetocrystalline anisotropies observed in (Ga,Mn)As epilayers and microdevices over a wide parameter range. We hope that our work will provide a useful guidance for future studies of magnetic and magnetotransport phenomena in (Ga,Mn)As based systems in which magnetocrystalline anisotropies play an important role.

4.2 Tight-binding model

The objective of the second part of this work was to develop a microscopic tight-binding description of complex metallic multilayer structures with strong SOC and compare the results to established ab-initio calculations in case of simpler structures such as $L1_0$ CoPt and FePt alloys. We started with choosing a suitable realistic tight-binding parametrisation introduced in Subsec. 2.2.3 and analysed band structures and MAE which they produce in systems with cobalt, platinum and iron. We compared the predictions of our code to ab-initio calculations for elemental crystals in Subsec. 3.3.1 and for multilayers and thin films in Subsec. 3.3.2. We checked the internal consistency of our numerical predictions focusing on magnetocrystalline anisotropies. We conclude that the extended Harrison parametrisation has proven reasonably reliable in calculations of MAE in $L1_0$ CoPt and FePt, the expected convergence of the finite-system properties to bulk properties was observed with growing number of layers. A more detailed study of the dependence of local ADOS in CoPt and FePt thin films on the tight-binding and material parameters is desirable. Our modelling is ready the for incorporation of the equilibrium Green's function framework for calculating magneto-transport anisotropies in complex metal structures.

Appendix A

Used constants

A.1 Cubic anisotropy coefficients

The angular dependence of the magnetocrystalline anisotropy energy can be approximated by a series of terms of distinct symmetry. In Subsec. 3.1.3 we introduced a simple phenomenological formula consisting of the low-order terms of the cubic and uniaxial symmetry. Here we explain the choice of the independent cubic terms.

We write the terms using the components of the magnetisation unit vector $\hat{M}$: $n_x = \cos\phi\sin\theta$, $n_y = \sin\phi\sin\theta$, $n_z = \cos\theta$, where our angles θ and ϕ are measured from the [001] and [100] axis, respectively. The cubic symmetry requires invariance under the permutation of the coordinate indices x, y, and z. The simplest term satisfying the condition is equal to unity: $n_x^2 + n_y^2 + n_z^2 = 1$. The first-order cubic term can be derived from its second power:

$$\left(n_x^2 + n_y^2 + n_z^2\right)^2 = 2\left(n_x^2 n_y^2 + n_x^2 n_z^2 + n_y^2 n_z^2\right) + n_x^4 + n_y^4 + n_z^4. \tag{A.1}$$

We obtained two lowest-order cubic terms which are mutually dependent. Therefore it is enough to choose only one of them. In case of Eq. (3.4) the lowest-order cubic anisotropy term reads: $K_{c1}\left(n_x^2 n_y^2 + n_x^2 n_z^2 + n_z^2 n_y^2\right)$, where K_{c1} is an energy coefficient.

The second-order term can be derived from the first-order term:

$$\begin{aligned}\left(n_x^2 n_y^2 + n_x^2 n_z^2 + n_y^2 n_z^2\right)\left(n_x^2 + n_y^2 + n_z^2\right) &= n_x^4 n_y^2 + n_x^4 n_z^2 + n_x^2 n_y^4 + n_y^4 n_z^2 + n_x^2 n_z^4 + n_y^2 n_z^4 + \\ &+ n_x^2 n_y^2 n_z^2. \end{aligned} \tag{A.2}$$

The two second-order terms and the first-order term are mutually dependent. Again, only one term describes fully the second-order component of the cubic anisotropy. We choose $K_{c2}\left(n_x^2 n_y^2 n_z^2\right)$ to be included into our approximate formula in Eq. (3.4).

The derivation of the independent third-order term can start from the first-order term:

$$\begin{aligned}\left(n_x^2 n_y^2 + n_x^2 n_z^2 + n_y^2 n_z^2\right)\left(n_x^2 + n_y^2 + n_z^2\right)^2 &= 5(n_x^4 n_y^2 n_z^2 + n_x^2 n_y^4 n_z^2 + n_x^2 n_y^2 n_z^4) + \\ &+ 2(n_x^4 n_y^4 + n_x^4 n_z^4 + n_y^4 n_z^4) \\ &+ n_x^6 n_y^2 + n_x^6 n_z^2 + n_x^2 n_y^6 + n_y^6 n_z^2 + n_x^2 n_z^6 + n_y^2 n_z^6, \end{aligned} \tag{A.3}$$

from the second-order term $(n_x^4 n_y^2 + n_x^4 n_z^2 + n_x^2 n_y^4 + n_y^4 n_z^2 + n_x^2 n_z^4 + n_y^2 n_z^4)(n_x^2 + n_y^2 + n_z^2)$, producing the same three cubic terms as in Eq. (A.3) with different prefactors, or from

$\left(n_x^2+n_y^2+n_z^2\right)^4$, producing an extra third-order term $n_x^8+n_y^8+n_z^8$. Note that these three ways of derivation also represent three constrictions relating the resulting four distinct cubic third-order terms to lower-order terms. Therefore we can choose only one independent third-order term.

This derivation procedure can be continued to higher orders but fitting our microscopic data to the phenomenological formula yields a negligible magnitude even for the third-order term coefficient.

A.2 Effective Hamiltonian parameters

γ_1	γ_2	γ_3
6.98	2.06	2.93
a_1[eV]	a_2[eV]	a_3[eV]
-1.16	-2.0	-4.8
c_{11}[GPa]	c_{12}[GPa]	c_{44}[GPa]
1221	566	600
Δ_{so}[eV]	J_{pd} [eVnm^3]	a_{lc}[nm]
0.341	0.055	0.565325

Table A.1: Luttinger parameters, strain constants, elastic moduli, spin-orbit splitting, and the kinetic-exchange constant for (Ga,Mn)As and the lattice constant of bulk GaAs [138, 55].

Table A.1 lists all material parameters describing (Ga,Mn)As used in our codes implementing the effective Hamiltonian model.

A.3 Tight-binding parameters

	Harrison	ext. Harrison
$\eta_{ss\sigma}$	-1.4	-0.9
$\eta_{pp\sigma}$	3.24	2.19
$\eta_{pp\pi}$	-0.81	-0.03
$\eta_{dd\sigma}$	-16.20	-21.22
$\eta_{dd\pi}$	8.75	12.6
$\eta_{dd\delta}$	0.0	-2.29
$\eta_{sp\sigma}$	1.84	1.44
$\eta_{sd\sigma}$	-3.16	-3.12
$\eta_{pd\sigma}$	-2.95	-4.26
$\eta_{pd\pi}$	1.36	2.08

Table A.2: Constants $\eta_{\alpha\beta\gamma}$ forming the S-K parameters of the Harrison and extended Harrison parametrisations.

Table A.2 lists all universal dimensionless constants $\eta_{\alpha\beta\gamma}$ introduced in Eq. (2.57) for the Harrison parametrisation [41] and in Eq. (2.58) for the extended Harrison parametrisation [114].

	Fe	Co	Pt
r_d [a.u.]	1.5118	1.4362	1.9653
r_d^e [a.u.]	1.3814	1.2966	1.8380
γ_s	0.9392	0.7881	1.0093

Table A.3: The radius of the *d*-orbital in the Harrison (r_d) and extended Harrison (r_d^e) parametrisations and the dimensionless parameter γ_s in the extended Harrison parametrisation.

Table A.3 lists all material specific tight-binding parameters introduced in Eq. (2.57) for the Harrison parametrisation and in Eq. (2.58) for the extended Harrison parametrisation [114]. Note that we use average values instead of the spin-split r_d^e and γ_s parameters in case of Fe and Co.

The extensive set of material specific coefficients forming the Mehl parametrisation is available at http://cst-www.nrl.navy.mil/bind/index.html.

Bibliography

[1] M. Abolfath, T. Jungwirth, J. Brum, and A. H. MacDonald. Theory of magnetic anisotropy in $III_{1-x}Mn_xV$ ferromagnets. *Phys. Rev.*, B 63:054418, 2001.

[2] Amikam Aharoni. Demagnetizing factors for rectangular ferromagnetic prisms. *Journal of Applied Physics*, page 3432, 1998.

[3] D. A. Allwood, G. Xiong, C. C. Faulkner, D. Atkinson, D. Petit, and R. P. Cowburn. Magnetic domain-wall logic. *Science*, 309:1688, 2005.

[4] Nissim Almeleh and Bernard Goldstein. Electron paramagnetic resonance of manganese in gallium arsenide. *Phys. Rev.*, 128:1568, 1962.

[5] P. W. Anderson. Localized magnetic states in metals. *Phys. Rev.*, 124:41, 1961.

[6] S. E. Barnes and S. Maekawa. Current-spin coupling for ferromagnetic domain walls in fine wires. *Phys. Rev. Lett.*, 95:107204, 2005.

[7] David V. Baxter, Dmitry Ruzmetov, Julia Scherschligt, Y. Sasaki, X. Liu, J. K. Furdyna, and C. H. Mielke. Anisotropic magnetoresistance in $Ga_{1-x}Mn_xAs$. *Phys. Rev.*, B 65:212407, 2002.

[8] Anne Bernand-Mantel, Pierre Seneor, Karim Bouzehouane, Stéphane Fusil, Cyrile Deranlot, Frédéric Petroff, and Albert Fert. Anisotropic magneto-coulomb effects and magnetic single-electron-transistor action in a single nanoparticle. *Nat. Phys.*, 5:920, 2009.

[9] A. K. Bhattacharjee and C. Benoit à la Guillaume. Model for the Mn acceptor in GaAs. *Solid State Commun.*, 113:17, 2000.

[10] C. Bihler, M. Althammer, A. Brandlmaier, S. Geprägs, M. Weiler, M. Opel, W. Schoch, W. Limmer, R. Gross, M. S. Brandt, and S. T. B. Goennenwein. $Ga_{1-x}Mn_xAs$/piezoelectric actuator hybrids: A model system for magnetoelastic magnetization manipulation. *Phys. Rev.*, B 78:045203, 2008.

[11] G. L. Bir and G. E. Pikus. *Symmetry and strain-induced effects in Semiconductors*. John Wiley & Sons (New York), 1974.

[12] Bernhard Botters, Fabian Giesen, Jan Podbielski, Peter Bach, Georg Schmidt, Laurens W. Molenkamp, and Dirk Grundler. Stress dependence of ferromagnetic resonance and magnetic anisotropy in a thin NiMnSb film on InP(001). *Appl. Phys. Lett.*, 89:242505, 2006.

[13] H. Boukari, C. Cavaco, W. Eyckmans, L. Lagae, and G. Borghs. Voltage assisted magnetic switching in Co_50Fe_50 interdigitated electrodes on piezoelectric substrates. *J. Appl. Phys.*, 101:054903, 2007.

[14] P. Bruno. Tight-binding approach to the orbital magnetic moment and magnetocrystalline anisotropy of transition-metal monolayers. *Phys. Rev.*, B 39.

[15] R. P. Campion, K. W. Edmonds, L. X. Zhao, K. Y. Wang, C. T. Foxon, B. L. Gallagher, and C. R. Staddon. High quality GaMnAs films grown with as dimers. *J. Cryst. Growth*, 247:42, 2003.

[16] R. A. Chapman and W. G. Hutchinson. Photoexcitation and photoionization of neutral manganese acceptors in gallium arsenide. *Phys. Rev. Lett.*, 18:443, 1967.

[17] Claude Chappert, Albert Fert, and Frédéric Nguyen Van Dau. The emergence of spin electronics in data storage. *Nature Materials*, 6:813, 2007.

[18] D. Chiba, F. Matsukura, and H. Ohno. Electric-field control of ferromagnetism in (Ga,Mn)As. *Appl. Phys. Lett.*, 89:162505, 2006.

[19] D. Chiba, M. Sawicki, Y. Nishitani, Y. Nakatani, F. Matsukura, and H. Ohno. Magnetization vector manipulation by electric fields. *Nature*, 455:515, 2008.

[20] D. Chiba, M. Yamanouchi, F. Matsukura, and H. Ohno. Electrical manipulation of magnetization reversal in a ferromagnetic semiconductor. *Science*, 301:943, 2003.

[21] W. W. Chow and S. W. Koch. *Semiconductor-Laser Fundamentals*. Springer-Verlag, Berlin, 1999.

[22] J. Daeubler, S. Schwaiger, M. Glunk, M. Tabor, W. Schoch, R. Sauer, and W. Limmer. GaMnAs on InGaAs templates: Influence of strain on the electronic and magnetic properties. *Physica*, page 1876, 2008.

[23] E. de Ranieri, A. W. Rushforth, K. Výborný, U. Rana, E. Ahmad, R. P. Campion, C. T. Foxon, B. L. Gallagher, A. C. Irvine, J. Wunderlich, and T. Jungwirth. Lithographically and electrically controlled strain effects on anisotropic magnetoresistance in (Ga,Mn)As. *New J. Phys.*, 10:065003, 2008.

[24] T. Dietl, A. Haury, and Y. Merle d'Aubigne. Free carrier-induced ferromagnetism in structures of diluted magnetic semiconductors. *Phys. Rev.*, B 55:R3347, 1997.

[25] T. Dietl, Jürgen König, and A. H. MacDonald. Magnetic domains in III-V magnetic semiconductors. *Phys. Rev.*, B 64:241201, 2001.

[26] T. Dietl, H. Ohno, and F. Matsukura. Hole-mediated ferromagnetism in tetrahedrally coordinated semiconductors. *Phys. Rev.*, B 63:195205, 2001.

[27] T. Dietl, H. Ohno, F. Matsukura, J. Cibert, and D. Ferrand. Zener model description of ferromagnetism in zinc-blende magnetic semiconductors. *Science*, 287:1019, 2000.

[28] Tomasz Dietl. Origin and control of ferromagnetism in dilute magnetic semiconductors and oxides. *J. Appl. Phys.*, 103:07D111, 2007.

[29] Tomasz Dietl, Fumihiro Matsukura, Hideo Ohno, Joel Cibert, and David Ferrand. Hall effect and magnetoresistance in p-type ferromagnetic semiconductors. In I. Vagner, editor, *Recent Trends in Theory of Physical Phenomena in High Magnetic Fields*, page 197. Kluwer, Dordrecht, 2003.

[30] K. Dorr and C. Thiele. Multiferroic bilayers of manganites and titanates. *Phys. Stat. Sol.*, B 243:21, 2006.

[31] R. A. Duine, A. S. Núñez, and A. H. MacDonald. Thermally-assisted current-driven domain wall motion. *Phys. Rev. Lett.*, 98:056605, 2007.

[32] R. A. Duine, A. S. Núñez, Jairo Sinova, and A. H. MacDonald. Functional Keldysh theory of spin torques. *Phys. Rev.*, B 75:214420, 2007.

[33] K. W. Edmonds, P. Boguslawski, K. Y. Wang, R. P. Campion, N. R. S. Farley, B. L. Gallagher, C. T. Foxon, M. Sawicki, T. Dietl, M. B. Nardelli, and J. Bernholc. Mn interstitial diffusion in (Ga,Mn)As. *Phys. Rev. Lett.*, 92:037201, 2004.

[34] Ion Garate, K. Gilmore, M. D. Stiles, and A. H. MacDonald. Non-adiabatic spin transfer torque in real materials. *Phys. Rev.*, B 79:104416, 2009.

[35] S. T. B. Goennenwein, M. Althammer, C. Bihler, A. Brandlmaier, S. Geprägs, M. Opel, W. Schoch, W. Limmer, R. Gross, and M. S. Brandt. Piezo-voltage control of magnetization orientation in a ferromagnetic semiconductor. *phys. stat. sol.*, (RRL) 2:96, 2008.

[36] C. Gould, S. Mark, K. Pappert, G. Dengel, J. Wenisch, R. P. Campion, A. W. Rushforth, D. Chiba, Z. Li, X. Liu, W. Van Roy, H. Ohno, J. K. Furdyna, B. Gallagher, K. Brunner, G. Schmidt, and L. W. Molenkamp. An extensive comparison of anisotropies in mbe grown (Ga,Mn)As material. *New J. Phys.*, 10:055007, 2008.

[37] C. Gould, C. Rüster, T. Jungwirth, E. Girgis, G. M. Schott, R. Giraud, K. Brunner, G. Schmidt, and L. W. Molenkamp. Tunneling anisotropic magnetoresistance: A spin-valve like tunnel magnetoresistance using a single magnetic layer. *Phys. Rev. Lett.*, 93:117203, 2004.

[38] B. Habib, J. Shabani, E. P. De Poortere, M. Shayegan, and R. Winkler. Anisotropic low-temperature piezoresistance in (311)a GaAs two-dimensional holes. *Appl. Phys. Lett.*, 91:012107, 2007.

[39] K. Hamaya, T. Taniyama, Y. Kitamoto, T. Fujii, and Y. Yamazaki. Mixed magnetic phases in (Ga,Mn)As epilayers. *Phys. Rev. Lett.*, 94:147203, 2005.

[40] K. Hamaya, T. Watanabe, T. Taniyama, A. Oiwa, Y. Kitamoto, and Y. Yamazaki. Magnetic anisotropy switching in (Ga,Mn)As with increasing hole concentration. *Phys. Rev.*, B 74:045201, 2006.

[41] W. A. Harrison. *Electronic Structure and the Properties of Solids.* Freeman, San Francisco, 1980.

[42] J. Hemberger, P. Lunkenheimer, R. Fichtl, H.-A. Krug von Nidda, V. Tsurkan, and A. Loidl. Relaxor ferroelectricity and colossal magnetocapacitive coupling in ferromagnetic $CdCr_2S_4$. *Nature*, 434:364, 2005.

[43] H Hopster and H. P. Oepen. *Magnetic Microscopy of Nanostructures.* Springer-Verlag Berlin, 2004.

[44] D. Hrabovsky, E. Vanelle, A. R. Fert, D. S. Yee, J. P. Redoules, J. Sadowski, J. Kanski, and L. Ilver. Magnetization reversal in GaMnAs layers studied by kerr effect. *Appl. Phys. Lett.*, 81:2806, 2002.

[45] A. Hubert and R. Schäfer. *Magnetic Domains: The Analysis of Magnetic Microstructures.* Springer, Berlin, 1998.

[46] S. Hümpfner, M. Sawicki, K. Pappert, J. Wenisch, K. Brunner, C. Gould, G. Schmidt, T. Dietl, and L. W. Molenkamp. Lithographic engineering of anisotropies in (Ga,Mn)As. *Appl. Phys. Lett.*, 90:102102, 2007.

[47] J. Jancu, R. Scholz, F. Beltram, and F. Bassani. Empirical spds* tight-binding calculation for cubic semiconductors: General method and material parameters. *Phys. Rev.*, B 57:6493, 1998.

[48] W. Jones and N. March. *Theoretical Solid State Physics.* Wiley, New York, 1973.

[49] T. Jungwirth, M. Abolfath, Jairo Sinova, J. Kučera, and A. H. MacDonald. Boltzmann theory of engineered anisotropic magnetoresistance in (Ga,Mn)As. *Appl. Phys. Lett.*, 81:4029, 2002.

[50] T. Jungwirth, W. A. Atkinson, B. Lee, and A. H. MacDonald. Interlayer coupling in ferromagnetic semiconductor superlattices. *Phys. Rev.*, B 59:9818, 1999.

[51] T. Jungwirth, J. König, J. Sinova, J. Kučera, and A. H. MacDonald. Curie temperature trends in (III,Mn)V ferromagnetic semiconductors. *Phys. Rev.*, B 66:012402, 2002.

[52] T. Jungwirth, J. Mašek, K. Y. Wang, K. W. Edmonds, M. Sawicki, M. Polini, Jairo Sinova, A. H. MacDonald, R. P. Campion, L. X. Zhao, N. R. S. Farley, T. K. Johal, G. van der Laan, C. T. Foxon, and B. L. Gallagher. Low-temperature magnetization of (Ga,Mn)As semiconductors. *Phys. Rev.*, B 73:165205, 2005.

[53] T. Jungwirth, Q. Niu, and A. H. MacDonald. Anomalous hall effect in ferromagnetic semiconductors. *Phys. Rev. Lett.*, 88:207208, 2002.

[54] T. Jungwirth, Jairo Sinova, A. H. MacDonald, B. L. Gallagher, V. Novák, K. W. Edmonds, A. W. Rushforth, R. P. Campion, C. T. Foxon, L. Eaves, K. Olejník, J. Mašek, S. R. Eric Yang, J. Wunderlich, C. Gould, L. W. Molenkamp, T. Dietl, and H. Ohno. Character of states near the Fermi level in (Ga,Mn)As: impurity to valence band crossover. *Phys. Rev.*, B 76:125206, 2007.

[55] T. Jungwirth, Jairo Sinova, J. Mašek, J. Kučera, and A. H. MacDonald. Theory of ferromagnetic (III,Mn)V semiconductors. *Rev. Mod. Phys.*, 78:809, 2006.

[56] T. Jungwirth, Jairo Sinova, K. Y. Wang, K. W. Edmonds, R. P. Campion, B. L. Gallagher, C. T. Foxon, Q. Niu, and A. H. MacDonald. Dc-transport properties of ferromagnetic (Ga,Mn)As semiconductors. *Appl. Phys. Lett.*, 83:320, 2003.

[57] T. Jungwirth, K. Y. Wang, J. Mašek, K. W. Edmonds, Jürgen König, Jairo Sinova, M. Polini, N. A. Goncharuk, A. H. MacDonald, M. Sawicki, R. P. Campion, L. X. Zhao, C. T. Foxon, and B. L. Gallagher. Prospects for high temperature ferromagnetism in (Ga,Mn)As semiconductors. *Phys. Rev.*, B 72:165204, 2005.

[58] Sang-Koog Kim, Jeong-Won Lee, Sung-Chul Shin, Han Wook Song, Chang Ho Lee, and Kwangsoo No. Voltage control of a magnetization easy axis in piezoelectric/ferromagnetic hybrid films. *J. Magn. Magn. Mater.*, 267:127, 2003.

[59] C. King, J.Zemen, K.Olejník, L. Horák, J. Haigh, V. Novák, J. Kučera, V. Holý, R. P. Campion, B. L. Gallagher, and T. Jungwirth. Strain control of magnetic anisotropy in (Ga,Mn)As microbars. Submitted to *Phys. Rev.*, B.

[60] W. Kohn and J. M Luttinger. *Phys. Rev.*, 108:590, 1957.

[61] J. König, T. Jungwirth, and A. H. MacDonald. Theory of magnetic properties and spin-wave dispersion for ferromagnetic (Ga,Mn)As. *Phys. Rev.*, B 64:184423, 2001.

[62] R. Lang, A. Winter, H. Pascher, H. Krenn, X. Liu, and J. K. Furdyna. Polar kerr effect studies of $Ga_{1-x}Mn_xAs$ epitaxial films. *Phys. Rev.*, B 72:024430, 2005.

[63] Jeong-Won Lee, Sung-Chul Shin, and Sang-Koog Kim. Spin engineering of CoPd alloy films via the inverse piezoelectric effect. *Appl. Phys. Lett.*, 82:2458, 2003.

[64] M. Linnarsson, E. Janzén, B. Monemar, M. Kleverman, and A. Thilderkvist. Electronic structure of the GaAs:Mn_{Ga} center. *Phys. Rev.*, B 55:6938, 1997.

[65] X. Liu, W. L. Lim, M. Dobrowolska, J. K. Furdyna, and T. Wojtowicz. Ferromagnetic resonance study of free hole contribution to magnetization and magnetic anisotropy in modulation-doped $Ga_{1-x}Mn_xAs/Ga_{1-y}Al_yAs$:Be. *Phys. Rev.*, B 71:035307, 2005.

[66] X. Liu, W. L. Lim, L. V. Titova, M. Dobrowolska, J. K. Furdyna, M. Kutrowski, and T. Wojtowicz. Perpendicular magnetization reversal, magnetic anisotropy, multistep spin switching, and domain nucleation and expansion in $Ga_{1-x}Mn_xAs$ films. *J. Appl. Phys.*, 98:063904, 2005.

[67] X. Liu, Y. Sasaki, and J. K. Furdyna. Ferromagnetic resonance in $Ga_{1-x}Mn_xAs$: effects of magnetic anisotropy. *Phys. Rev.*, B 67:205204, 2003.

[68] J. M. Luttinger. Quantum theory of cyclotron resonance in semiconductors: General theory. *Phys. Rev.*, 102:1030, 1956.

[69] F. Máca. Private communication.

[70] T. Maruyama, Y. Shiota, T. Nozaki, K. Ohta, N. Toda, M. Mizuguchi, A. A. Tulapurkar, T. Shinjo, M. Shiraishi, S. Mizukami, Y. Ando, and Y. Suzuki. Large voltage-induced magnetic anisotropy change in a few atomic layers of iron. *Nature Nanotechnology*, 4:158, 2009.

[71] F. Matsukura, H. Ohno, and T. Dietl. Ferromagnetic semiconductors. In K. H. J. Buschow, editor, *Handbook of Magnetic Materials*, volume 14, page 1. Elsevier, Amsterdam, 2002.

[72] J. Mašek, J. Kudrnovský, and F. Máca. Lattice constant in diluted magnetic semiconductors (Ga,Mn)As. *Phys. Rev.*, B 67:153203, 2003.

[73] J. Mašek and F. Máca. Lattice expansion of (Ga,Mn)As: The role of substitutional Mn and of the compensating defect. *Acta Phys. Pol.*, A 108:789, 2005.

[74] J. Mašek, F. Máca, J. Kudrnovský, O. Makarovsky, L. Eaves, R. P. Campion, K. W. Edmonds, A. W. Rushforth, C. T. Foxon, B. L. Gallagher, V. Novak, Jairo Sinova, and T. Jungwirth. Microscopic analysis of the valence band and impurity band theories of (Ga,Mn)As. 2010.

[75] T. McGuire and R. Potter. Anisotropic magnetoresistance in ferromagnetic 3D alloys. *IEEE Trans. Magn.*, 11:1018, 1975.

[76] V. L. Moruzzi, J. F. Janak, and A. R. Williams. *Calculated Electronic Properties of Metals*. Pergamon, 1978.

[77] J. Moser, A. Matos-Abiague, D. Schuh, W. Wegscheider, J. Fabian, and D. Weiss. Tunneling anisotropic magnetoresistance and spin-orbit coupling in Fe/GaAs/Au tunnel junctions. *Phys. Rev. Lett.*, 99:056601, 2007.

[78] D. Neumaier, K. Wagner, S. Geissler, U. Wurstbauer, J. Sadowski, W. Wegscheider, and D. Weiss. Weak localization in ferromagnetic (Ga,Mn)As nanostructures. *Phys. Rev. Lett.*, 99:116803, 2007.

[79] Anh Kiet Nguyen, Hans Joakim Skadsem, and Arne Brataas. Giant current-driven domain wall mobility in (Ga,Mn)As. *Phys. Rev. Lett.*, 98:146602, 2007.

[80] V. Novák, K. Olejník, J. Wunderlich, M. Cukr, K. Výborný, A. W. Rushforth, K. W. Edmonds, R. P. Campion, B. L. Gallagher, Jairo Sinova, and T. Jungwirth. Curie point singularity in the temperature derivative of resistivity in (Ga,Mn)As. *Phys. Rev. Lett.*, 101:077201, 2008.

[81] H. Ohno, D. Chiba, F. Matsukura, T. Omiya, E. Abe, T. Dietl, Y. Ohno, and K. Ohtani. Electric-field control of ferromagnetism. *Nature*, 408:944, 2000.

[82] H. Ohno, H. Munekata, T. Penney, S. von Molnár, and L. L. Chang. Magnetotransport properties of p-type (In,Mn)As diluted magnetic III-V semiconductors. *Phys. Rev. Lett.*, 68:2664, 1992.

[83] H. Ohno, A. Shen, F. Matsukura, A. Oiwa, A. Endo, S. Katsumoto, and Y. Iye. (Ga,Mn)As: A new diluted magnetic semiconductor based on GaAs. *Appl. Phys. Lett.*, 69:363, 1996.

[84] J. Okabayashi, A. Kimura, T. Mizokawa, A. Fujimori, T. Hayashi, and M. Tanaka. Mn 3d partial density of states in $Ga_{1-x}Mn_xAs$ studied by resonant photoemission spectroscopy. *Phys. Rev.*, B 59:R2486, 1999.

[85] J. Okabayashi, A. Kimura, O. Rader, T. Mizokawa, A. Fujimori, T. Hayashi, and M. Tanaka. Core-level photoemission study of $Ga_{1-x}Mn_xAs$. *Phys. Rev.*, B 58:R4211, 1998.

[86] K. Olejník and V. Novák. Private communication.

[87] K. Olejník, M. H. S. Owen, V. Novák, J. Mašek, A. C. Irvine, J. Wunderlich, and T. Jungwirth. Enhanced annealing, high curie temperature and low-voltage gating in (Ga,Mn)As: A surface oxide control study. *Phys. Rev.*, B 78:054403, 2008.

[88] M. Overby, A. Chernyshov, L. P. Rokhinson, X. Liu, and J. K. Furdyna. GaMnAs-based hybrid multiferroic memory device. *Appl. Phys. Lett.*, 92:192501, 2008.

[89] M. H. S. Owen, J. Wunderlich, V. Novák, K. Olejník, J. Zemen, K. Výborný, S. Ogawa, A. C. Irvine, A. J. Ferguson, H. Sirringhaus, and T. Jungwirth. Low voltage control of ferromagnetism in a semiconductor p-n junction. *New J. Phys.*, 11, 2009.

[90] M. A. Paalanen and R. N. Bhatt. Transport and thermodynamic properties across the metal-insulator transition. *Physica B*, 169:223, 1991.

[91] D. A. Papaconstantopoulos. *Handbook of the band structure of elemental solids.* Plenum, 1986.

[92] D. A. Papaconstantopoulos and M. J. Mehl. The slater-koster tight-binding method: a computationally efficient and accurate approach. *J. Phys.: Condens. Matter*, 15:R413, 2003.

[93] K. Pappert, S. Hümpfner, C. Gould, J. Wenisch, K. Brunner, G. Schmidt, and L. W. Molenkamp. A non-volatile-memory device on the basis of engineered anisotropies in (Ga,Mn)As. *Nature Phys.*, 3:573, 2007.

[94] K. Pappert, S. Hümpfner, J. Wenisch, K. Brunner, C. Gould, G. Schmidt, and L. W. Molenkamp. Transport characterization of the magnetic anisotropy of (Ga,Mn)As. *Appl. Phys. Lett.*, 90:062109, 2007.

[95] B. G. Park, J. Wunderlich, D. A. Williams, S. J. Joo, K. Y. Jung, K. H. Shin, K. Olejník, A. B. Shick, and T. Jungwirth. Tunneling anisotropic magnetoresistance in multilayer-(Co/Pt)/AlO_x/Pt structures. *Phys. Rev. Lett.*, 100:087204, 2008.

[96] S. J. Potashnik, K. C. Ku, S. H. Chun, J. J. Berry, N. Samarth, and P. Schiffer. Effects of annealing time on defect-controlled ferromagnetism in $Ga_{1-x}Mn_xAs$. *Appl. Phys. Lett.*, 79:1495, 2001.

[97] Alexander Pross, Simon Bending, Kevin Edmonds, R. P. Campion, C. T. Foxon, and Bryan Gallagher. Influence of low temperature annealing on the micromagnetic structure of GaMnAs films. *J. Appl. Phys.*, 95:3225, 2004.

[98] Alexander Pross, Simon Bending, Kevin Edmonds, R. P. Campion, C. T. Foxon, and Bryan Gallagher. Magnetic domain imaging of ferromagnetic GaMnAs films. *J. Appl. Phys.*, 95:7399, 2004.

[99] D. Pryia. *Synthesis and characterization of Cobalt-Platinum thin films.* Doctoral thesis, 2002.

[100] R. Ramesh and N. A. Spaldin. Multiferroics: progress and prospects in thin films. *Nature Mat.*, 6:21, 2007.

[101] A. W. Rushforth, E. De Ranieri, J. Zemen, J. Wunderlich, K. W. Edmonds, C. S. King, E. Ahmad, R. P. Campion, C. T. Foxon, B. L. Gallagher, K. Výborný, J. Kučera, and T. Jungwirth. Voltage control of magnetocrystalline anisotropy in ferromagnetic - semiconductor/piezoelectric hybrid structures. *Phys. Rev.*, B 78:085314, 2008.

[102] A. W. Rushforth, K. Výborný, C. S. King, K. W. Edmonds, R. P. Campion, C. T. Foxon, J. Wunderlich, A. C. Irvine, V. Novák, K. Olejník, A. A. Kovalev, Jairo Sinova, T. Jungwirth, and B. L. Gallagher. The origin and control of the sources of amr in (Ga,Mn)As devices. *J. Mag. Magn. Mater.*, 321:1001, 2009.

[103] A. W. Rushforth, K. Výborný, C. S. King, K. W. Edmonds, R. P. Campion, C. T. Foxon, J. Wunderlich, A. C. Irvine, P. Vašek, V. Novák, K. Olejník, Jairo Sinova, T. Jungwirth, and B. L. Gallagher. Anisotropic magnetoresistance components in (Ga,Mn)As. *Phys. Rev. Lett.*, 99:147207, 2007.

[104] C. Rüster, C. Gould, T. Jungwirth, E. Girgis, G. M. Schott, R. Giraud, K. Brunner, G. Schmidt, and L. W. Molenkamp. Tunneling anisotropic magnetoresistance: Creating a spin-valve-like signal using a single ferromagnetic semiconductor layer. *J. Appl. Phys.*, 97:10C506, 2005.

[105] P. Sankowski, P. Kacman, J. Majewski, and T. Dietl. Tight-binding model of spin-polarized tunnelling in (Ga,Mn)As-based structures. *Physica*, page 375, 2006.

[106] P. Sankowski, P. Kacman, J. A. Majewski, and T. Dietl. Spin-dependent tunneling in modulated structures of (Ga,Mn)As. *Phys. Rev.*, B 75:045306, 2007.

[107] Y. Sasaki, X. Liu, J. K. Furdyna, M. Palczewska, J. Szczytko, and A. Twardowski. Ferromagnetic resonance in GaMnAs. *J. Appl. Phys.*, 91:7484, 2002.

[108] M. Sawicki, F. Matsukura, T. Dietl, G. M. Schott, C. Rüster, G. Schmidt, L. W. Molenkamp, and G. Karczewski. Temperature peculiarities of magnetic anisotropy in (Ga,Mn)As: The role of the hole concentration. *J. Supercond.*, 16:7, 2003.

[109] M. Sawicki, F. Matsukura, A. Idziaszek, T. Dietl, G. M. Schott, C. Rüster, C. Gould, G. Karczewski, G. Schmidt, and L. W. Molenkamp. Temperature dependent magnetic anisotropy in (Ga,Mn)As layers. *Phys. Rev.*, B 70:245325, 2004.

[110] M. Sawicki, K-Y. Wang, K. W. Edmonds, R. P. Campion, C. R. Staddon, N. R. S. Farley, C. T. Foxon, E. Papis, E. Kaminska, A. Piotrowska, T. Dietl, and B. L. Gallagher. In-plane uniaxial anisotropy rotations in (Ga,Mn)As thin films. *Phys. Rev.*, B 71:121302, 2005.

[111] Maciej Sawicki. Magnetic properties of (Ga,Mn)As. *J. Magn. Magn. Mater.*, 300:1, 2006.

[112] J. R. Schrieffer and P. A. Wolff. Relation between the anderson and kondo hamiltonians. *Phys. Rev.*, 149:491, 1966.

[113] M. Shayegan, K. Karrai, Y. P. Shkolnikov, K. Vakili, E. P. De Poortere, and S. Manus. Low-temperature, in situ tunable, uniaxial stress measurements in semiconductors using a piezoelectric actuator. *Appl. Phys. Lett.*, 83:5235, 2003.

[114] L. Shi and D. A. Papaconstantopoulos. Modifications and extensions to harrison's tight-binding theory. *Phys. Rev.*, B 70:205101, 2004.

[115] A. B. Shick, F. Máca, J. Mašek, and T. Jungwirth. Prospect for room temperature tunneling anisotropic magnetoresistance effect: density of states anisotropies in CoPt systems. *Phys. Rev.*, B 73:024418, 2006.

[116] Alexander B. Shick and Oleg N. Mryasov. Coulomb correlations and magnetic anisotropy in ordered $L1_0$ CoPt and FePt alloys. *Phys. Rev.*, B 67:172407, 2003.

[117] D. Y. Shin, S. J. Chung, and Sanghoon Lee. Temperature dependence of magnetic anisotropy in ferromagnetic (Ga,Mn)As films: Investigation by the planar Hall effect. *Phys. Rev.*, B 76:035327, 2007.

[118] R. Shioda, K. Ando, T. Hayashi, and M. Tanaka. Local structures of III-V diluted magnetic semiconductors $Ga_{1-x}Mn_xAs$ studied using extended x-ray-absorption fine structure. *Phys. Rev.*, B 58:1100, 1998.

[119] T. Shono, T. Hasegawa, T. Fukumura, F. Matsukura, and H. Ohno. Observation of magnetic domain structure in a ferromagnetic semiconductor (Ga,Mn)As with a scanning hall probe microscope. *Appl. Phys. Lett.*, 77:1363, 2000.

[120] M. Singh, C. S. Wang, and J. Callaway. Spin-orbit coupling, Fermi surface, and optical conductivity of ferromagnetic iron. *Phys. Rev.*, B 11:287, 1975.

[121] Jairo Sinova, T. Jungwirth, and J. Černe. Magneto-transport and magneto-optical properties of ferromagnetic (III,Mn)V semicondcutors: a review. *Int. J. Mod. Phys.*, B 18:1083, 2004.

[122] Jairo Sinova, T. Jungwirth, J. Kučera, and A. H. MacDonald. Infrared magneto-optical properties of (III,Mn)V ferromagetic semiconductors. *Phys. Rev.*, B 67:235203, 2003.

[123] Jairo Sinova, T. Jungwirth, X. Liu, Y. Sasaki, J. K. Furdyna, W. A. Atkinson, and A. H. MacDonald. Magnetization relaxation in (Ga,Mn)As ferromagnetic semiconductors. *Phys. Rev.*, B 69:085209, 2004.

[124] Jairo Sinova, T. Jungwirth, S. R. Eric Yang, J. Kučera, and A. H. MacDonald. Infrared conductivity of metallic (III,Mn)V ferromagnets. *Phys. Rev.*, B 66:041202, 2002.

[125] J. C. Slater and G. F. Koster. Simplified LCAO method for the periodic potential problem. *Phys. Rev.*, 94:1498, 1954.

[126] V. Stanciu and P. Svedlindh. Annealing-induced changes of the magnetic anisotropy of (Ga,Mn)As epilayers. *Appl. Phys. Lett.*, 87:242509, 2005.

[127] M. D. Stiles, W. M. Saslow, M. J. Donahue, and A. Zangwill. Adiabatic domain wall motion and Landau-Lifshitz damping. *Phys. Rev.*, B 75:214423, 2007.

[128] I. Stolichnov, S. W. E. Riester, H. J. Trodahl, N. Setter, A. W. Rushforth, K. W. Edmonds, R. P. Campion, C. T. Foxon, B. L. Gallagher, and T. Jungwirth. Non-volatile ferroelectric control of ferromagnetism in (Ga,Mn)As. *Nature Mater.*, 7:464, 2008.

[129] Akira Sugawara, T. Akashi, P. D. Brown, R. P. Campion, T. Yoshida, B. L. Gallagher, and A. Tonomura. High-resolution observations of temperature-dependent magnetic domain structures within $Ga_xMn_{1-x}As$ by Lorentz microscopy. *Phys. Rev.*, B 75:241306(R), 2007.

[130] Akira Sugawara, H. Kasai, A. Tonomura, P. D. Brown, R. P. Campion, K. W. Edmonds, B. L. Gallagher, J. Zemen, and T. Jungwirth. Domain walls in (Ga,Mn)As diluted magnetic semiconductor. *Phys. Rev. Lett.*, 100:047202, 2008.

[131] J. Szczytko, A. Twardowski, K. Swiatek, M. Palczewska, M. Tanaka, T. Hayash, and K. Ando. Mn impurity in $Ga_{1-x}Mn_xAs$ epilayers. *Phys. Rev.*, B 60:8304, 1999.

[132] G. Tatara and H. Kohno. Theory of current-driven domain wall motion: Spin transfer versus momentum transfer. *Phys. Rev. Lett.*, 92:086601, 2004.

[133] L. Thevenard, L. Largeau, O. Mauguin, A. Lemaître, K. Khazen, and H. J. von Bardeleben. Evolution of the magnetic anisotropy with carrier density in hydrogenated $Ga_{1-x}Mn_xAs$. *Phys. Rev.*, B 75:195218, 2007.

[134] Laura Thevenard, Ludovic Largeau, Olivia Mauguin, Aristide Lemaître, and Bertrand Theys. Tuning the ferromagnetic properties of hydrogenated GaMnAs. *Appl. Phys. Lett.*, 87:182506, 2005.

[135] Laura Thevenard, Ludovic Largeau, Olivia Mauguin, Gilles Patriarche, Aristide Lemaître, Nicolas Vernier, and Jacques Ferré. Magnetic properties and domain structure of (Ga,Mn)As films with perpendicular anisotropy. *Phys. Rev.*, B 73:195331, 2006.

[136] L. Thomas, M. Hayashi, X. Jiang, R. Moriya, C. Rettner, and S. S. P. Parkin. Oscillatory dependence of current-driven magnetic domain wall motion on current pulse length. *Nature*, 443:197, 2006.

[137] Šobáň and V. Novák. Private communication.

[138] I. Vurgaftman, J. R. Meyer, and L. R. Ram-Mohan. Band parameters for III-V compound semiconductors and their alloys. *J. Appl. Phys*, 89:5815, 2001.

[139] J. G. Wan, J.-M. Liu, G. H. Wang, and C. W. Nan. Electric-field-induced magnetization in Pb(Zr,Ti)O_3/Terfenol-D composite structures. *Appl. Phys. Lett.*, 88:182502, 2006.

[140] K. Y. Wang. Private communication.

[141] K. Y. Wang, A. W. Rushforth, V. A. Grant, R. P. Campion, K. W. Edmonds, C. R. Staddon, C. T. Foxon, B. L. Gallagher, J. Wunderlich, and D. A. Williams. Domain imaging and domain wall propagation in (Ga,Mn)As thin films with tensile strain. *J. Appl. Phys.*, 101:106101, 2007.

[142] K. Y. Wang, M. Sawicki, K. W. Edmonds, R. P. Campion, S. Maat, C. T. Foxon, B. L. Gallagher, and T. Dietl. Reorientation transition in single-domain (Ga,Mn)As. *Phys. Rev. Lett.*, 95:217204, 2005.

[143] K. Y. Wang, M. Sawicki, K. W. Edmonds, R. P. Campion, A. W. Rushforth, A. A. Freeman, C. T. Foxon, B. L. Gallagher, and T. Dietl. Control of coercivities in (Ga,Mn)As thin films by small concentrations of mnas nanoclusters. *Appl. Phys. Lett.*, 88:022510, 2006.

[144] M Wang, R P Campion, A W Rushforth, K W Edmonds, C T Foxon, and B L Gallagher. Achieving high curie temperature in (Ga,Mn)As. *Appl. Phys. Lett.*, 93:132103, 2008.

[145] U. Welp, V. K. Vlasko-Vlasov, X. Liu, J. K. Furdyna, and T. Wojtowicz. Magnetic domain structure and magnetic anisotropy in $Ga_{1-x}Mn_xAs$. *Phys. Rev. Lett.*, 90:167206, 2003.

[146] U. Welp, V. K. Vlasko-Vlasov, A. Menzel, H. D. You, X. Liu, J. K. Furdyna, and T. Wojtowicz. Uniaxial in-plane magnetic anisotropy of $Ga_{1-x}Mn_xAs$. *Appl. Phys. Lett.*, 85:260, 2004.

[147] J. Wenisch, C. Gould, L. Ebel, J. Storz, K. Pappert, M. J. Schmidt, C. Kumpf, G. Schmidt, K. Brunner, and L. W. Molenkamp. Control of magnetic anisotropy in (Ga,Mn)As by lithography-induced strain relaxation. *Phys. Rev. Lett.*, 99:077201, 2007.

[148] T. Wu, M. A. Zurbuchen, S. Saha, R.-V. Wang, S. K. Streiffer, and J. F. Mitchell. Observation of magnetoelectric effect in epitaxial ferroelectric film/manganite crystal heterostructures. *Phys. Rev.*, B 73:134416, 2006.

[149] J. Wunderlich, A. C. Irvine, J. Zemen, V. Holý, A. W. Rushforth, E. De Ranieri, U. Rana, K. Výborný, Jairo Sinova, C. T. Foxon, R. P. Campion, D. A. Williams, B. L. Gallagher, and T. Jungwirth. Local control of magnetocrystalline anisotropy in (Ga,Mn)As microdevices: Demonstration in current-induced switching. *Phys. Rev. B*, 76:054424, 2007.

[150] J. Wunderlich, T. Jungwirth, B. Kaestner, A. C. Irvine, K. Y. Wang, N. Stone, U. Rana, A. D. Giddings, A. B. Shick, C. T. Foxon, R. P. Campion, D. A. Williams, and B. L Gallagher. Coulomb blockade anisotropic magnetoresistance effect in a (Ga,Mn)As single-electron transistor. *Phys. Rev. Lett.*, 97:077201, 2006.

[151] A. M. Yakunin, A. Yu. Silov, P. M. Koenraad, J. H. Wolter, W. Van Roy, and J. De Boeck. Charge manipulation and imaging of the mn acceptor state in GaAs by cross-sectional scanning tunneling microscopy. *Superlatt. and Microstruct.*, 34:539, 2003.

[152] A. M. Yakunin, A. Yu. Silov, P. M. Koenraad, J. H. Wolter, W. Van Roy, J. De Boeck, J. M. Tang, and M. E. Flatté. Spatial structure of an individual mn acceptor in GaAs. *Phys. Rev. Lett.*, 92:216806, 2004.

[153] M. Yamanouchi, D. Chiba, F. Matsukura, and H. Ohno. Current-induced domain-wall switching in a ferromagnetic semiconductor structure. *Nature*, 428:539, 2004.

[154] Peter Y. Yu and Manuel Cardona. *Fundamentals of semiconductors.* Springer-Verlag Berlin, 2005.

[155] J. Zemen, J. Kucera, K. Olejnik, and T. Jungwirth. Magneto crystalline anisotropies in (Ga,Mn)As: A systematic theoretical study and comparison with experiment. *Phys. Rev.*, B 80:155203, 2009.

[156] C. Zener. Interaction between the d shells in the transition metals. *Phys. Rev.*, 81:440, 1951.

[157] S. Zhang and Z. Li. Roles of nonequilibrium conduction electrons on the magnetization dynamics of ferromagnets. *Phys. Rev. Lett.*, 93:127204, 2004.

[158] L. X. Zhao, C. R. Staddon, K. Y. Wang, K. W. Edmonds, R. P. Campion, B. L. Gallagher, and C. T. Foxon. Intrinsic and extrinsic contributions to the lattice parameter of GaMnAs. *Appl. Phys. Lett.*, 86:071902, 2005.